Effect of body force on turbulent pipe flow

Kui He

Supervised by

Professor Shuisheng He

The University of Sheffield
Department of Mechanical Engineering

This thesis is submitted to the University of Sheffield in

Partial fulfillment of the requirement for the degree of

Doctor of Philosophy

October 2015

To my families, my girlfriend and my Lord

Acknowledgment

Four years flying away, thousands of words to say to people who make my life in Sheffield happy and easy. They are,

Duan Yu, Akshat Mathur, Sam Gorji, Mehdi Seddighi-Moornani, Zhang Xiao, Miao Xinyi, Muhsin Mohd Amin, Cosimo Trinca, Benjamin S Oluwadare, Zu Yingqing, Xie Jianfei, Wang Wei, Terry and Gill, *et al.*

We studied together and helped each other, during which deep friendship was developed. I would remember all of you in the rest of my life. I am very grateful to Professor Shuisheng He and Dr. Seddighi. Professor He leads me to identify the key thermal fundamental problem in nuclear reactors. His patient tutorial and deep knowledge help me who have only background in Chemical Engineering, to rebuild basical knowledge about heat transfer and turbulent flow in nuclear reactors. Dr. Seddighi, who tutored me in programming, data analysing and paper writing, is a very helpful man and deserves the best appreciation. What make me feel lucky that I study in a top mechanical engineering department in UK. The department provides not only hardware facility but also competitive academic environment, excellent academic staff. I really benefit from the discussion with some of them.

Financially, I would like to express my thanks to the China Scholarship Council and the Department of Mechanical Engineering of Sheffield University.

Last but not the least, I keep the grateful words in my heart for my family and girlfriend. Without their support, it is impossible to finish this thesis.

Abstract

Two non-equilibrium flows, namely, a transient turbulent pipe flow following a sudden change of flow rate and a turbulent pipe flow subjected to a non-uniform body force are systematically studied using direct numerical simulation (DNS). It is revealed that the transient response of a turbulent pipe flow to a sudden increase of flow rate is a laminar-turbulent transition. The response of the flow is not a progressive evolution from the initial turbulence to a new one, but shows a three-stage development, i.e., a pre-transitional stage, a transitional stage and a fully developed stage. This is similar to a typical boundary layer bypass transition with three characteristical regions, i.e., pre-transitional region, transitional region and fully developed region. The results are carefully compared with those of a channel flow of He & Seddighi, J. Fluid Mech. (2013). The statistical and instantaneous behaviours of the two flows are similar in the near-wall region, but there are distinctive differences in the centre of the flow. The transitional critical Reynolds numbers for the transient pipe and channel flow are predicted with the same correlation. The possibility of predicting such transient flow using transitional turbulence modelling, such as $\gamma - Re_\theta$ SST, is discussed. The effect of the rate of the change of the flow is also examined. In a fast ramp-up case, the flow is similar to that of a step-change flow, also showing a three-stage development. In a slow ramp-up case, the flow response is not as clear as that in a fast ramp-up case but the main features of the response are similar.

A series prescribed body forces are used to emulate flows, which contain features similar to those of real buoyancy-aiding flows. It has been shown that the body force with various amplitudes, coverages and distribution profiles can systematically influence the base flow. The body force influenced flows are classified into four groups, namely, partially laminarized flow, 'completely' laminarized flow, partially recovery flow and strongly recovery flow. A new perspective has been proposed for the partially laminarized flow and 'completely' laminarized flow. In contrast to the conventional view, which views the flow to be re-laminarized, the new theory proves that the turbulence of the flow remains largely unchanged following the imposition of the body force. The body force induces a perturbation flow, which lowers the pressure gradient required to maintain the same Reynolds number. This is the mechanism of turbulence relaminarization. The

recovery flows show two-layer turbulence. The outer turbulence is generated by a shear layer in the core of the flow caused by the body force. The inner turbulence is generated in the wall layer, increasing with the outer turbulence. The two layers of turbulence increase hand in hand. The stronger the outer generation, the stronger the inner recovery is. The inner turbulence structure is very similar to an equilibrium turbulent flow. In the region very close to the wall (y^{+0}<10), it shows similar budget patterns and flow structures (sweeps and ejections) to those of the base flow. In the region between y^{+0}=10 and the new shear layer, the turbulence structure is complicated, where the turbulence is a mixture of the inner turbulence and the outer turbulence.

The transient response of the turbulence to the imposition of a non-uniform body force has been examined. The turbulence decay and recovery features of the flows with non-uniform body forces are studied in detail. It is found that the transient features are mainly determined by the total amplitude of the body force. The higher the amplitude, the stronger the turbulence decay is. In some flows, the near wall turbulence is recovered toward the later stage of the transient process. Under such condition, the inner self-sustaining regeneration interacts strongly with the turbulence from the outer shear layer.

Contents

List of figures

List of tables

Nomenclature

Bo^*: Buoyancy number

bf: body force normalized by $0.5\rho {U_{p0}}^2$

b: turbulent stress anisotropic

E_k: integrated kinetic energy

E_{uu}: energy spectrum of streamwise fluctuation velocity

F: integrated body force normalized by shear stress

Fr: Froude number

Gr^*: Grashof number, $=\beta g D^4 q_w''/(\lambda \nu^2)$

H: shape factor based on δ/θ or δ_{du}/θ_{du}

$intbf$: integrated body force

k: wavenumber or kinetic energy

L : The length of pipe

N_z, N_r, N_θ : mesh points in streamwise, wall-normal and spanwise directions

Nu: Nusselt number

p^*: pressure

p: pressure normalized by $\rho {U_{p0}}^2$

$-\frac{dP}{dz}$: mean axial pressure gradient normalized by $\rho {U_{p0}}^2/R$

Pr: Prandtl number

q: flux variable

Q_1: first quadrant, high speed outward motions

Q_2: second quadrant, low speed outward motions

Q_3: third quadrant, low speed inward motions

Q_4: fourth quadrant, high speed inward motions

R : Pipe radius

$Re_p = \frac{RU_{p0}}{\nu}$: Reynolds number based on pipe radius and U_{p0}

$Re_\tau = \frac{Ru_\tau}{\nu}$: Reynolds number based on pipe radius and u_τ

$Re_b = \frac{RU_b}{\nu}$: Reynolds number based on pipe radius and U_b

$Re_\theta = \frac{\theta U_c}{\nu}$: Reynolds number based on momentum thickness and U_c

$Re_\nu = \frac{y^2}{\nu}\frac{d\overline{u_z}}{dy}$: vorticity Reynolds number

t^*: time normalized by H/U_{b1}

$t_k = \left(\frac{\nu}{\varepsilon}\right)^{1/2}$: Kolmogorov time scale

t: time normalized by $\frac{R}{U_{p0}}$

t^+: time normalized by $\frac{\nu}{{u_\tau}^2}$

Δt_{ac}: the period when the flow rate is changed.

U_b: bulk velocity normalized by U_{p0}

U_c: centre line mean velocity

U^+: local mean velocity normalized by u_τ

U_{p0}: centreline velocity of laminar parabolic Poiseuille profile

U_{b0}: bulk velocity at the base flow

$u_\tau = \sqrt{\frac{\tau_w}{\rho}}$: friction velocity at any time

$u_{\tau 0}$: friction velocity of the initial flow

$u_{\tau 1}$: friction velocity of the final flow (chapter 4); an apparent friction velocity (chapter 5 & 6)

u_z, u_r, u_θ : streamwise, wall-normal and spanwise instantaneous velocity

$\overline{u_z}, \overline{u_r}, \overline{u_\theta}$: streamwise, wall-normal and spanwise local mean velocity

u_k: Kolmogorov velocity scale

u'_z, u'_r, u'_θ: streamwise, wall-normal and spanwise *r.m.s* fluctuation velocity

$\overline{u'_z u'_r}$ or $\overline{u'v'}$: Reynolds stress

$\hat{u_z} = \frac{\overline{u_z}(r,t) - \overline{u_z}(r,0)}{\overline{u_z}(0,t) - \overline{u_z}(0,0)}$: differential velocity

y^+ : wall-normal distance normalized by $\frac{\nu}{u_\tau}$

y : wall-normal distance normalized by R

y^{+0}: wall-normal distance normalized by $\frac{\nu}{u_{\tau 0}}$

δ: displacement thickness

δ_{du}: displacement thickness based on differential velocity

θ: momentum thickness

θ_{du}: momentum thickness based on differential velocity

R_{uu}: Correlation of streamwise fluctuation velocity

Greek

τ_T: turbulent stress

τ_w: wall shear stress

ρ: density, kg/m^3

ν: kinematic viscosity, m^2/s

$\mu_t = \frac{1}{\nu} u'v' / \frac{\partial \overline{u_z}}{\partial y}$: turbulent viscosity, m^2/s

ε: energy dissipation

$\eta = \left(\frac{\nu^3}{\varepsilon}\right)^{1/4}$: Kolmogorov length scale

ω: vorticity

ω': vorticity fluctuation

π: circular constant

λ: the eigenvalue of the symmetric tensor $S^2 + \Omega^2$

S: Symmetric part of velocity gradient tensor

Ω: Antisymmetric part of velocity gradient tensor

ϕ: pseudo-pressure in Poisson equation

Subscripts

z: streamwise direction

r: wall-normal direction

θ: spanwise direction

0: initial flow (chapter 4); a base flow (chapter 5)

1: final flow (chapter 4); a higher Reynolds number base flow (chapter 5)

2: a lower Reynolds number base flow (chapter 5)

w: wall

c: centre

max or p: the maximum value

min: the minimum value

Superscripts

$*$: normalization by outer scales (Chapter 4); dimensional variable (Chapter 5 & 6)

Length by R, time by $\frac{R}{U_b}$, velocity by U_b

$+$: normalization by inner scales

Length by $\frac{\nu}{u_\tau}$, time by $\frac{R}{u_\tau}$, velocity by u_τ

Chapter 1

Introduction

Some typical non-equilibrium flows, such as, the flow subjected to a temporal acceleration and the flow with buoyancy, are fundamental and ubiquitous in natural and engineering systems. The understanding of such flows is important. For example, one of the thermal hydraulic issues in supercritical water cooled reactors (SCWRs) is that the fluid properties of the coolant vary dramatically as it flows in the fuel channel. The heat transfer may be significantly impaired in comparison with forced convection of constant property fluids. The mechanism is often very complicated. However, it is with no dispute that the effect of buoyancy (as a non-uniform body force) causing the mean flow to distort and modifying turbulence production is an important phenomenon. In fact, this is the dominant mechanism for the flow 'irregularities' in most mixed convection problems encountered in a vertical tube. Similarly, turbulence production may be suppressed or enhanced in many other situations such as accelerating /decelerating wall bounded flows or a boundary layer flow subject to a favourable or adverse pressure gradient. The flow acceleration and the pressure gradient can be seen as a 'body force' and in this way, the flow behaviour under the influence of the 'body force' can be studied in an unified way.

An investigation is reported here to study the effect of some typified body forces on turbulent pipe flow, which represents the key source of the 'abnormity' of many non-

equilibrium turbulent flows, especially in mixed convection systems. The motivation of this study arises from the need for a better understanding many transient and steady non-equilibrium turbulent flows with the effect of a physical or equivalent body force. Flow statistics and structures generated from direct numerical simulation (DNS) are used to demonstrate the commonality of turbulence features in these flows. The results of the DNS simulations of real flows sometime are difficult to understand since the thermal and hydraulic effects are both complicated and difficult to discern. In present study, the body force effect is studied in isolation from other effects in order to further the understanding of flow physics in many real flows as well as to provide benchmark date for the development of turbulence modelling for these flows.

1.1 Aims and objectives

The aim of the present study is to investigate some typified non-equilibrium flows in a unified way by employing a carefully prescribed body force on a turbulent flow in a pipe. The study focuses on three particular flows:

1. A turbulent flow subjected to a temporal acceleration.
2. A turbulent flow with the imposition of a prescribed non-uniform body force under steady condition.
3. The transient response of a flow following an imposition of a prescribed non-uniform body force.

The results are used to improve the understanding of flow physics of many real flows. The first study is aimed at understanding the turbulence response when the flow rate of a turbulent steady state pipe flow is suddenly increased. The key parameters, such as the acceleration rate, the initial and final Reynolds numbers are carefully varied. The results are compared with those of the channel flow and boundary layer flow with zero pressure

gradients. The mechanism that how the turbulent flow evolves from an original steady state to a new steady state is studied. The statistical and instantaneous similarities and differences among these flows are established. Secondly, detailed flow features and statistics of steady state turbulent pipe flow with non-uniform body force are studied. These data can be used as a benchmark for the development of relative turbulence modelling. A new theory has been proposed to explain the flow laminarization due to a non-uniform body force. This also enables a reliable prediction of the laminarization of such flow. Thirdly, the transient development of turbulent flow following the imposition of a non-uniform body force is studied. The following work has been done in this study in order to complete the above mentioned objectives.

1. The development of a DNS code for the pipe flow based on an initial channel flow version.
2. Detailed investigation of flow physics and turbulence response of unsteady turbulent flow subjected to a temporal acceleration.
3. Investigation of the flow physics and turbulence in a steady state flow subjected to non-uniform body force.
4. Detailed changes of the flow physics and the response of coherent structures are studied after the imposition of a non-uniform body force.
5. The issues of some turbulence modelling on such flows are analysed based on the DNS data.

1.2 Thesis outline

Chapter 1: Introduction

The objectives of the thesis are introduced and the thesis outline is presented.

Chapter 2: Literature review

The literature review is arranged into four parts. They are (i) the research of heat transfer with buoyancy and flow acceleration effects especially in vertical flow channels or pipes, (ii) unsteady accelerating flow in a pipe and channel, (iii) laminar-turbulent transition of a boundary layer with zero pressure gradient, and (iv) the self-sustaining mechanisms of wall bounded turbulence. The studies that are reviewed include experimental, DNS and RANS investigations.

Chapter 3: Numerical methods

An overview of different numerical schemes developed by previous researchers for the solution of three-dimensional incompressible Navier-Stokes equations is presented with an emphasis on the schemes for pipe flows. The method used to treat the singularity at the pipe centre, the time and spatial resolution criteria in relevant DNS simulations are summarized. The numerical methods used in the present study are introduced in detail. Turbulent statistics obtained from the current code for a fully-developed turbulent pipe flow at several Reynolds numbers are validated with available DNS and experiment data inform the literature.

Chapter 4: Pipe flow subjected to an increase of mass flow rate.

A DNS study on a turbulent flow (Re_0=5300) subjected to fast accelerations with a final Reynolds number of Re_1=6000, 10440, 14800 is performed. The results are carefully compared with previous channel and boundary layer data. They are also used to validate a new transition critical Reynolds number correlation, which is based on a recently

proposed new mechanism of the transition of a temporally accelerated flow. Some parameters and correlations used in relevant physical modelling are examined. In the last section of this chapter, the effect of acceleration rate on the flow response is studied.

Chapter 5: DNS of pipe flow with non-uniform body force.

A DNS database of turbulent pipe flow with the imposition of a body force is established and the flows are classified into four types, namely, partially laminarized flow, completely laminarized flow, partially recovery flow and strongly recovery flow. A new mechanism for the 'laminarization' due to the imposition of body force on turbulent flow is proposed. The basic statistics and physical features of the recovery flow are studied in the last section of the chapter.

Chapter 6: The transient response of turbulent pipe flow to a non-uniform body force.

DNS of a transient turbulent flow (Re_0=5300) following the imposition of a non-uniform body force with various distribution patterns and amplitudes is conducted. The transient laminarization and recovery process of the turbulent flow after the imposition of the body force are analysed.

Chapter 7: Conclusions and future work.

Chapter 2

Literature Review

Mixed convection flow with strong heating is characteristic of dramatic fluid property changes in space and time. Especially, the variations of density can affect turbulence production, either by virtue of the flow acceleration due to thermal expansion of the heated fluid or because of the influences of buoyancy. These effects combined with large variations of specific heat and thermal conductivity may have very important consequences in terms of effectiveness of heat transfer (He $et\ al.$ 2008). They often lead to abnormal flow and heat transfer behaviour in mixed convection flows. Some of these effects, such as flow acceleration or buoyancy can be largely attributed to 'body force effect'. The body force distorts the mean flow and establishes a new turbulent state in the flow. The understanding of such flows can be improved not only by the knowledge obtained from direct study on such flows, but also the fundamental knowledge of wall bounded flow, including for example, the self-sustaining mechanisms of wall shear turbulent flow and the transition mechanism of the flow when they are influenced by a body force. Therefore, the review in this chapter is divided into four parts. The first part establishes the basical knowledge about the flow acceleration and buoyancy effect on heat transfer of turbulent flow. The second part is devoted to summarize the study of transient flow with temporal acceleration but without heat transfer. The third part summarizes the

well-established knowledge about bypass transition in boundary layer flow. The last part collects the main knowledge on the self-sustaining mechanism of the wall turbulent flow. This knowledge is important for the understanding of the flow with modified boundary layers. As mentioned before, it is important to know how the self-sustaining process of the turbulent flow is modified by the introduced body force.

2.1 Mixed convection

2.1.1 The general effect of buoyancy and flow acceleration

The effect of buoyancy on heat transfer can be well demonstrated by the experiment of Shitsman (1963). The wall temperature of a heated tube with an upward water flow at supercritical pressures (>22MP) was measured in the experiment. Figure 2.1 shows that the wall temperature experiences a remarkable increase at certain locations at high heat flux.

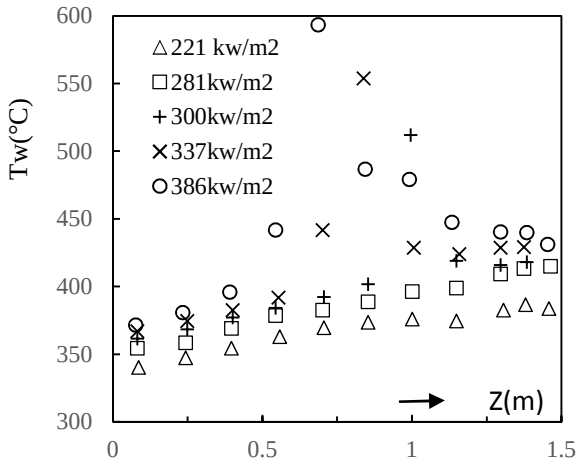

Figure 2.1: Localized impairment of heat transfer due to buoyancy.
(Reproduced from Shitsman 1963)

The effect was initially linked to a film-boiling phenomenon and was given the name "pseudoboiling". But now it is known that the effect was mainly due to buoyancy (Jackson

et al. 1989). Extensive experimental and numerical efforts have been devoted to the study of deteriorated turbulent heat transfer (DTHT) due to buoyancy effect. A detailed review on experimental and numerical research was given by Jackson, *et al*. (2006). The early pioneering work explored the straightforward logical question that under what conditions the buoyancy plays a dominant effect. It is observed through earlier experiments (Shitsman *et al*. 1963; Bishop *et al*. 1962; Styrikovich *et al*. 1967; Yamagata *et al*. 1972) that DTHT usually occurs at a high heat flux and a relatively low mass flux in a vertical channel or pipe. Two kinds of models were intensively investigated to understand such flows. The diagrammatic sketches of them are shown in Figure 2.2. In Figure 2.2(a), the flow is termed as a "buoyancy-aided heated flow (He *et al*. 1998)", which means the flow is counter-current with gravity. On the contrary, the flow shown in Figure 2.2(b) is termed as "buoyancy-opposed heated flow (He *et al*. 1998)'', which means the flow is concurrent with gravity. The two flows are respectively equivalent to downward cooling flow and upward cooling flow. It has been found that the DTHT occurs in "buoyancy-aided heated flow''.

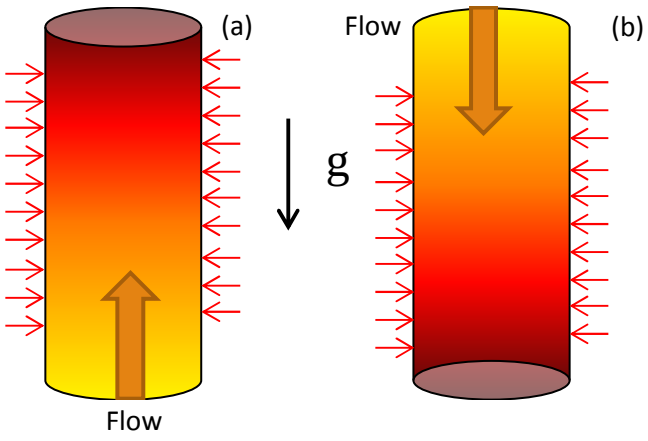

Figure 2.2: The buoyancy-aided (a) and buoyancy-opposed (b) heated flow.

The heat transfer features of the buoyancy-aided flow are reflected on a semi-empirical correlation (Jackson $et\ al.$ 1989), which has been developed to correlate the onset of buoyancy effect in fully-developed pipe flow with a Bo^* parameter which can be written as

$$Bo^* = \frac{Gr^*}{Re^{3.425}Pr^{0.8}} \tag{2.1}$$

where the Re, Pr and Gr^* refer to Reynolds number based on hydraulic diameter, Prandtl number, Grashof number respectively. The data from semi-empirical model of Jackson and experimental data of Li (Jackson $et\ al.$ 1989; Li 1994) are plotted in Figure 2.3. The y-coordinate is Nu/Nu_{fc}, which is a ratio of Nusselt number (Nu) with body force effect (mixed convection) over that without body force effect (forced convection) to characterize the heat transfer behaviour. The x-coordinate is buoyancy number (Bo^*).

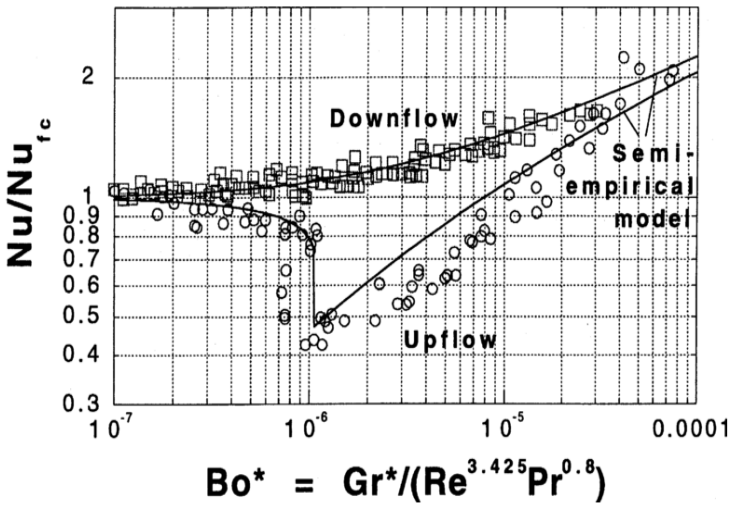

Figure 2.3: The effect of buoyancy on heat transfer of turbulent flow.
(extracted from McEligot $et\ al.$ 2004, where Re is based on the hydraulic diameter)

Qualitatively, heat transfer features of buoyancy-aided flows can be mainly divided into 3 regimes according to (Jackson 1989; He $et\ al.$ 1998; He $et\ al.$ 2008). i) the effect of buoyancy is weak and not noticeable. ii) when buoyancy is strong, it causes a reduction

of the velocity gradient over most of the flow, except in the vicinity of the wall. As a result, turbulence production is reduced and the turbulent diffusion of heat is impaired. If the buoyancy is progressively increased (reducing the flow rate or increasing the heating rate), the impairment of turbulence production and the deterioration of heat transfer become more and more intensified. The turbulence production in the near wall region virtually ceases at certain stage. This is usually described as *laminarization* of the flow (or reversed transition). iii) With further increase of buoyancy influence, negative values of shear stress are generated in the core region and turbulence is reproduced. Consequently, the effectiveness of heat transfer recovers. It is shown in Figure 2.3 that the value of $Bo^{*}\sim 1\times 10^{-6}$ is a reasonable order-of-magnitude estimate of the buoyancy onset threshold for severe laminarization.

Another important effect that may cause local heat transfer deterioration is flow acceleration caused by thermal expansion. Both flow acceleration effect and buoyancy effect are induced by the variation of density. The former is induced by density change in the radial direction resulting in a non-uniformly distributed gravitational force, while the latter is introduced by density change in the axial direction (Yoo 2013). Similarly, the onset of this effect can be correlated with the heat transfer with the K_v parameter (McEligot $et\ al.$ 1970) as following

$$K_v = \frac{v_b}{{u_b}^2}\frac{du_b}{dx} \tag{2.2}$$

where, v_b is the bulk kinematic viscosity and u_b is the local bulk velocity. Moretti and Kays (1965) suggested that for K_v less than about 3×10^{-6} the flow would remain turbulent while for higher values it is likely to laminarize, giving a substantial reduction in heat transfer parameters. This was confirmed by Perkins $et\ al.$ (1973).

2.1.2 The current understanding of DTHT due to acceleration and buoyancy

There are few theoretical analysis on heat transfer with acceleration effect and buoyancy effect. Tanaka $et\ al.$ (1973) studied how the shear-stress is influenced by the buoyancy and acceleration (inertia force). The two effects were considered as a body force in the 1-D momentum analysis, the effect of which on shear stress was analysed. These two effects show similarity in rapidly suppressing the shear stress near the wall under some conditions. A reverse transition may take place when Re<4300 and a certain heating condition is satisfied. The shear stress may continue to decrease to a fairly large negative value, even after it vanishes and changes its sign, leading to what would eventually be called an M-shaped velocity profile.

The shear stress suppression and flow relaminarization due to buoyancy and flow acceleration are summarized as indirect effect by Petukhov & Polyakov (1988). Kurganov & Kaptil'ny (1992) showed a more detailed description of the indirect effect of buoyancy and flow acceleration. The velocity, temperature fields, hydraulic resistance and heat transfer in a supercritical carbon dioxide (carbon dioxide where at or above its critical temperature and critical pressure) flow through a heated vertical circular tube (D=22.7mm) were measured and calculated. The illustrative data is shown in Figure 2.4. Between x/d=17.5 and x/d=62.5, as the Nu_b/Nu_N reduces, the wall temperature increases and reaches a peak. In further downstream, the Nu_b/Nu_N increases and the wall temperature drops. Correspondingly, the mean velocity is flattened and an M-shaped profile develops in the downstream (x/d =62.5). Meanwhile, the shear stress reduces and develops negative shear stress in the core of the flow. The authors attributed the heat transfer deterioration to the deep reconstruction of the velocity field and shear stress under the influence of buoyancy and negative pressure gradient that accelerates the heated flow.

The recovery of the flow was linked to the presence of flow with a structure with analogy to jet flow.

Jackson (2011) also explained that the indirect effect works via changing the force balance. The net shear force at the near wall region reduces as a result of the buoyancy force. The shear stress at the outer edge of the turbulent buffer layer is reduced as balance behaviour. The turbulence production reduces as a response to the change in shear stress and hence the effectiveness of heat transfer is impaired. It has been evident that these indirect effects are essentially the primary reasons that cause the deterioration of the turbulent heat transfer in a vertical passage (Jackson 2006; He *et al*. 2008). However, understanding the indirect effect in detail is not straightforward. The reason can be attributed to a lack of complete turbulence data and the entangled factors influence the mixed convection flow.

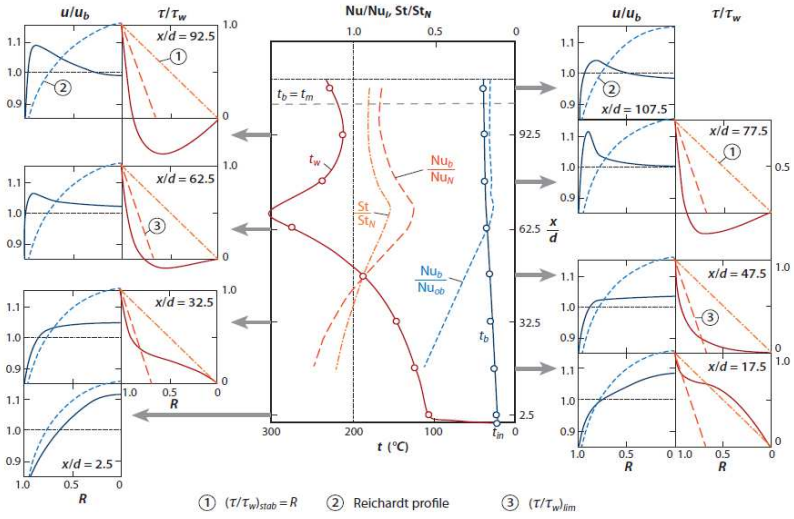

Figure 2.4: Changes in heat transfer, profiles of velocity, and shear stresses in conditions of deteriorated heat transfer. (Figure taken from Yoo 2013, the data original from Kurganov and Kaptil'ny 1992)

The middle column shows the distributions of the wall temperature t_w, the bulk temperature t_b, the normalized Stanton number St/St_N, and the normalized Nusselt numbers Nu_b/Nu_N and Nu_b/Nu_{ob}, t_m is the temperature at the heat capacity maximum and the subscript *N*, *ob* denoting normal heat transfer and the bulk parameter. The left column shows the distributions of dimensionless velocity u/u_b and shear stress τ/τ_w at x/d =2.5, 32.5, 62.5, and 92.5, and the right column shows those at x/d = 17.5, 47.5, 77.5, and 107.5, where x is the axial distance from the entrance and d = 2R is the inner diameter of the tube.

2.1.3 Numerical studies on heat transfer with mixed convection flow

As mentioned before, understanding the effect of buoyancy and flow acceleration requires detailed data, especially these showing the flow structures near the wall. Currently, through experiment, these data cannot be obtained easily. Numerical study, especially DNS study can provide complementary data. Kasagi & Nishimura (1997) studied both buoyancy aided and opposed flows by DNS. The behaviour of the Reynolds stress was linked to interaction of quasi-coherent structures. With buoyancy effect, it was observed by flow visualization that the vortices became weak and appeared less frequently and in larger scales. Satake $et\ al.$ (2000) made use of DNS to understand the laminarization phenomena in DTHT. The normal and Reynolds shear stresses, the budget of turbulent kinetic energy and turbulent structures were presented. The turbulence reduction was clearly observed near y^+=15. Recently, Bae $et\ al.$ (2005, 2008) conducted DNS simulations in order to examine the heat transfer characteristics of turbulence to supercritical fluids flow in vertical pipes and annular channels under strong buoyancy conditions. The work fluid is the supercritical carbon dioxide, with Reynolds numbers of 5400 in pipes and 8900 in annular channels respectively. Bae $et\ al.$ (2008) also found a large reduction in the Reynolds shear stress occurred in the viscous region. The flow visualization revealed that alternating low- and high-speed streaks in the viscous region were not clearly observed when significant heat transfer deterioration was shown.

In addition, the RANS modelling approach is also used to compensate the shortage of experiment. It is not a suitable method to study the detailed mechanism, but it is important to know which models can give better performance in predicting such flows, which is interested by people from industries. Mikielewicz $et\ al.$ (2002) examined 11 ‘simple’ turbulence models and found that the Launder-Sharma model was among the best,

providing predictions in good agreement with the measured velocity and temperature distributions. Youn & Mills (1993) studied heat transfer of forced convection of supercritical carbon dioxide by using low-Reynolds number turbulence models. The main effect to be studied was from the non-uniformity of fluid properties and possibly thermally induced flow acceleration. The turbulence models used were found to be able to reproduce the experiments rather well under many conditions. A number of low-Reynolds number turbulence models have been examined by Koshizuka *et al*. (1995) and He *et al*. (2005). The numerical heat transfer data of mixed convection of supercritical flow (water and carbon dioxide) in vertical tubes were compared with experiments of a wide range of conditions. It is found that most low-Reynolds number turbulence models tested in the study (Koshizuka *et al*. 1995 and He *et al*. 2005) reproduce the trend of flow laminarization and heat transfer deterioration due to buoyancy effect. Some models seem to perform much better than others in terms of giving smaller quantitative derivation with experimental data.

Recently, Cheng *et al*. (2007), Yang *et al*. (2007) and Sharabi *et al*. (2008) employ commercial CFD packages (CFX, StarCD and Fluent) to study heat transfer of supercritical pressure flow. Both low-Reynolds number models and turbulence models with wall-function have been examined. The general trends of the experimental data can be reproduced by the models. These recent computational studies reveal that carefully selected turbulence models can reproduce the general trend of heat transfer enhancement and deterioration exhibited by experiments of supercritical pressure flows. However, the detailed comparison with experiments shows that the performance of models varies significantly at certain conditions and for the same model, varies significantly from condition to condition. It is shown that the low-Reynolds number features of turbulence

models which enable them to respond to local flow distortions is very important to enable the model to reproduce the influences of buoyancy and effects due to large variations of fluid properties. Grötzbach (2007) summarized the fundamental and practical deficiencies of these RANS turbulence models in current commercial CFD codes that can be used for the heat transfer with buoyancy effect. The failure of these models is partially due to that most current turbulence models cannot predict the anisotropic momentum transfer, which characterizes some buoyancy contributions. He suggested more sophisticated models should be used for buoyancy influenced flows.

He *et al*. (2008) assessed the performance of low-Reynolds number turbulence models in predicting mixed convection heat transfer to fluids at supercritical pressure. More attention was paid to the features which enable them to respond to the modifications. It has been found that a group of turbulence models which performed rather well in reproducing mixed convection with constant properties shows an over-response to changes in the flow. Some models' performance that was evaluated less successful previously is improved. The results show that V2F model performs the best among all models tested. Although the turbulence recovery of strong-buoyancy-influenced cases can be reproduced by most models, the heat transfer enhancement phenomenon is not well-captured by them. The inability of turbulence models in reproducing turbulent heat flux using a constant turbulent Prandtl number is one of the reasons.

The above review on turbulence modelling shows that the effects of flow acceleration and buoyancy are not well-captured by most models. For those models, such as the low Reynolds number Launder-Sharma models do show good performance under certain conditions, but they fail under other conditions. The indirect mechanism termed by several researcher (Petukhov & Polyakov 1988; Jackson *et al*. 1989) is proposed for

many years but it has not been studied completely due to the reason mentioned in section 2.1.2. Present thesis is devoted to understand the indirect effects in details. The buoyancy is a non-uniform body force and the flow acceleration can be seen as an apparent 'body force'. The flow behaviour under a variety of different conditions can be studied in an unified way. By isolating the body force effect from other effects in mixed convection heat transfer systems, we will try to answer the following important questions

- How do the shape (spatial distribution), the amplitude (intensity) and the extent of the body force influence the flow and turbulence?
- How and when do the heat transfer deterioration and the recovery of heat transfer occur?

2.2 The accelerating flow in channel and pipe

The needs of study on the non-periodic transient flows comes from vast flows that are encountered frequently in real life situations, for instance, transient flow created by a high speed train going through a tunnel, flows involving rapid changes in mass flow or pressure gradient due to the opening/closing of a valve, etc. A special application is that the unsteady flow data can be used to improve the unsteady shear stress modelling. The detailed studies of such flows also provide valuable wall-bounded flow features that are hidden in the steady state flow (Kataoka $et\ al.$ 1975).

2.2.1 Experimental studies

Comparing to periodic unsteady state flow, such as oscillating and pulsating flows, the research on accelerating/decelerating flow is relatively fewer. The history of experimental study can be traced back to the 1970s. Kataoka $et\ al.$ (1975) studied a transient pipe flows

(starting from the rest) generated by the rapid increasing in flow rate due to sudden opening of a solenoid valve. The final Reynolds number ranged from 1910 to 11900 (based on diameter of the pipe). The velocity profiles of the accelerated flow were measured by electrochemical method and it was found that these profiles are different from those in steady state flows in the entrance region of the circular pipe. They studied the development of the velocity profile: they show a minimum at the axis and a maximum in intermediate region between the axis and the wall. No detailed turbulence data was obtained in this study. A detailed study of an initial turbulent pipe (D=51mm) flow subject to a sudden change in flow rate was conducted by Maruyama $et\ al.$ (1976). The stepwise variation of the flow rate was achieved by suddenly opening or closing one of two identical valves placed in parallel, with which flow rates in the main circuit could be doubled or halved within 0.6s. The low and high Reynolds numbers were 5000 and 10 000 respectively. The streamwise velocity in the fluid and the velocity gradient on the wall were measured using an electrochemical method. The accelerating flow and decelerating flow show apparently different features that the former flow is dominated by the new turbulence generation and its propagation, while the latter one is dominated by decay of old turbulence. Kurokawa & Morikawa (1986) conducted an experiment together with a theoretical study on a transient pipe flow with gradually increasing and decreasing flow rates. They studied the velocity profile development after a laminar flow being accelerated and found that the critical Reynolds number of flow transition was found to increases with the increase in the imposed acceleration. Similar experimental studies were carried out by Lefebvre & White (1989, 1991). These studies also showed that the critical Reynolds number for transition increased with the increase in acceleration

rate. During the transition of low accelerating flow, the wall shear stress & velocity profile & turbulence intensity profile agree well with the quasi-steady turbulent values.

Since 1990s, the research on fully-developed turbulent flow subjected to constant acceleration/deceleration has received more attention. In order to investigate the complex behaviour of flow relaminarization process, Greenblatt & Moss (1999) performed an experimental and RANS investigation of turbulent pipe flow subjected to rapid temporal acceleration. The authors showed that the relaminarization caused a significant reduction of turbulence in the near-wall region (y^+=50) after the acceleration was imposed. Meanwhile, the core region was found in a 'frozen' state, where the turbulence was largely unaffected by the imposed acceleration.

He & Jackson (2000) conducted a series of linearly accelerating and decelerating flow from an initially steady turbulent flow using a two-component laser Doppler anemometer (LDA). Unlike Maruyama $et\ al.$ (1976)'s experiments, the acceleration was maintained at a constant flow rate during the period of the measurement and it was varied systematically. The experiments were carried out with water in a pipe of diameter of 50.8 mm with the Reynolds number varying between 7000 and 42000. By running many repeated identical unsteady flow experiments, ensemble-averaged mean velocity, and all three components of the normal stresses as well as the shear stresses were obtained. Turbulence production, turbulence energy redistribution and the radial propagation of turbulence were also studied carefully. At any locations, turbulence shows two stages response during the transient process. In the first stage (referred as a delay stage), the response of turbulence production, the turbulence energy redistribution among its three components and the propagation of turbulence radially were delayed. In the second stage,

the turbulence is generated at the near-wall region first and propagates quickly towards the centre of the pipe.

Greenblatt & Moss (2004) focused on a higher starting Reynolds number and faster accelerations. The experiments were carried out in a pipe of 48 mm in diameter with water as the working fluid and a one-component LDA was used to measure the instantaneous velocity. The flow was rapidly increased from a Reynolds number of 31000 to 82000 within 0.85, 1.62 and 3 s in three test cases. In each case, the acceleration rate was fast and nearly constant in the first half-period, but was much slower and gradually diminishing in the second half-period. Actually, the first half of the test was similar to that of He & Jackson (2000) where the flow was subjected to a roughly constant acceleration, whereas in the later stage, the flow underwent relaxation in response to an increase of flow rate occurred earlier resembling that of Maruyama $et\ al.$ (1976). Consistent with He & Jackson (2000) and Maruyama $et\ al.$ (1976), the authors found that in a rapidly accelerating flow, turbulence is initially frozen everywhere, but then starts to increase first close to wall, and gradually propagates to other regions. In contrast with early studies, however, a second peak of turbulence response was found in a region further away from the wall at around y^+=300. This phenomenon was not fully understood and was hypothetically associated with the higher starting Reynolds number that was used in the study and hence not observed in earlier studies.

He $et\ al.$ (2011) carried out an experimental study of wall shear stress in an accelerating flow of water in a pipe of a large diameter (100 mm) using flush-mounted hot-film sensors. The development of the wall shear stress shows three stages. In stage 1, the shear stress initially increases rapidly overshooting the pseudo-steady value, but then increases more slowly and eventually falls below the pseudo-steady value. In stage 2, it

increases rapidly again, and finally in stage 3 approaches and fluctuates around the quasi-steady values. Such behaviour of the wall shear was related to turbulence responses. In stage 1, the turbulence is under 'frozen' state, so the turbulent wall shear stress remains largely unchanged except for a very slow accelerated case which was hypothetically associated with the stretching of existing turbulent eddies as a result of flow acceleration. Due to near 'frozen' state of turbulence, the unsteady wall shear stress is driven primarily by flow inertia. To stage 2, there is new turbulence generation, which causes both the mean and turbulent wall shear stress to increase rapidly. The turbulent wall shear, reflecting local turbulent activities near the wall, responds first and the mean wall shear, reflecting conditions across the entire flow field, responds later. The duration of the initial period of the near frozen turbulence response increases with decreasing initial Reynolds number and increasing acceleration. The latter is in contrast with the response of turbulence in the core of the flow, which has been shown by He & Jackson (2000) to be independent of the rate of acceleration.

2.2.2 Numerical studies of transient flow with acceleration

Although, experimental studies accumulate more and more detailed knowledge, the mechanism that how the new turbulence is generated and why the transition Reynolds number increase with the increase of the imposed acceleration and final Reynolds number or decrease in initial Reynolds number are still not fully understood. Direct numerical simulation (DNS) has been used to provide more detailed flow structure data which are unavailable from experiments. Chung (2005) performed a DNS of a fully-developed turbulent channel flow subjected to sudden pressure gradient changes. The Reynolds number ranges employed for flow rate change were relatively low. Recently, Talha (2012)

provided more detailed DNS data in his thesis and the range of Reynolds number between initial and final flow was 7000-15000, which was extended to 7000-22600 by LES. The new turbulence and old turbulence were identified by conditional average. A novel procedure was used to identify regions of new turbulence and it is found that the new turbulence generation is approximately at an exponential rate.

Through DNS, He & Seddighi (2013) established that the transient channel flow following a sudden increase in flow rate from an initial turbulent flow is effectively a laminar-turbulent transition. This process bears striking similarity to the boundary layer bypass transition to turbulence induced by free-stream turbulence (FST). The transient process is divided into three distinct stages, namely, pre-transition, transition, and fully-developed turbulent flow, resembling the buffeted-laminar, intermittent and turbulent regions of a boundary layer bypass transition subject to free-stream turbulence. Later, He & Seddighi (2015) studied the effect of varying the initial and final Reynolds numbers of the transient channel flow. It was shown that the onset of transition is a function of the initial free stream turbulence level, Tu_0, based on the initial turbulence and the final bulk velocity. It has been established through both theoretical and experimental investigations that for spatially developing boundary layer flow, $Re_{cr} \sim {Tu_0}^{-2}$ (Andersson $et\ al.$ 1999; Brandt $et\ al.$ 2004; Fransson $et\ al.$ 2005; Ovchinikov $et\ al.$ 2008). Analogy to boundary layer flow, the onset of transition in transient channel flow has been found to be dependent on Tu_0 as $Re_{t,cr} \sim {Tu_0}^{-1.71}$, where $Re_{t,cr}={t_{cr}{U_{b1}}^2}/{\nu}$ and t_{cr} is the time of the transition onset (He & Seddighi 2015).

The Reynolds Averaged Navier–Stokes (RANS) models have also been used to study unsteady channel/pipe flows by some researchers. Cotton $et\ al.$ (2001) examined the performance of the second moment closure model of Shima (1989) and the $k-\varepsilon$ model

of Launder and Sharma (1974) for both oscillatory flat-plate boundary layer and pulsatile pipe flow. It was found that the second-moment closure schemes generally performed better in comparison with the $k-\varepsilon$ model examined. Scotti & Piomelli (2001) assessed the performance of five turbulence models against their own DNS data on pulsating flows, while Khaleghi $et\ al.$ (2010) investigated the performance of four turbulence models for a ramp-up pipe flow, comparing their results with the experimental data of He and Jackson (2000). In each of these two studies, the performance of an algebraic one-equation model, a $k-\varepsilon$ model, a $k-\omega$ model and a $k-\varepsilon-v^2$ model were examined. It was concluded from both studies that $k-\varepsilon-v^2$ model outperforms the rest. However, these conclusions were based on investigations of only a limited number of models among the various formulations. Gorji (2014) furtherly tested 11 turbulence models, including the recently developed $\gamma - Re_\theta$ transitional modelling (Langtry 2006). The interesting finding was that the $\gamma - Re_\theta$ transitional modelling outperforms the other models, which was mainly designed for bypass transitions.

2.3 Laminar-turbulent transition in boundary layer flow

The problem of how the laminar to turbulent transition occurs in a boundary layer is an attractive topic for more than a century (Reynolds 1883). It is a complicated problem that puzzles the smartest brains in the world. The mechanisms of the transition are related to the flow and the environmental disturbances. There are two kinds of transition, namely, the Tollmien-Schlichting (TS) wave transition and the bypass transition. The former is usually observed in flows with rather small environmental disturbances, which is usually measured using turbulence intensity (Tu). An accepted criterion for this transition scenario is Tu <0.1%. When Tu >1%, another transition scenario is likely to occur,

which is referred to as the bypass transition. The process of the bypass transition of a boundary layer was divided into three regions by Jacobs & Durbin (2001). The first region is dominated by streamwise elongated structures visualized by positive and negative streamwise disturbance velocities (termed as streaks, Kline $et\ al.$ 1967). The amplitude of the disturbance grows in the downstream. In the second region, they breakdown into localized turbulent spots, which increase in size and merge until a third fully turbulent region. There are a large amount of research on this transition, but here only a brief review on the literature in streaks dynamics is provided.

The generation of streaks can be explained by transient growth theory. The theory dates back to the 1970s (Ellingsen & Palm 1975) when 3-D disturbances of infinite streamwise wavelength on a shear flow were found to be able to grow algebraically in the inviscid limit. The theory was extended to viscous flow by Hultgren & Gustavsson (1981), who found that disturbances may undergo considerable transient growth prior to be dampend by viscosity as long as the streamwise wavelength is sufficiently long. In the 1990s, the nonorthogonal nature of the Orr–Sommerfeld and Squire eigenfunctions was found to be the mathematical representation of transient growth (Trefethen $et\ al.$ 1993). Transient growth theory has led to studies on the optimal growth for a combination of modes which form an initial disturbance that experiences the maximum amount of growth. By a temporal formulation of the disturbance equations, Butler & Farrell (1992) determined the optimal disturbance parameters for the maximum transient growth in plane Couette, plane Poiseuille, and Blasius flows. In this case, the optimal disturbances are stationary with a zero frequency and a particular spanwise wave number. A study on the spatial transient growth was later carried out by Schmid & Henningson (1994) for the plane Poiseuille flow. Despite intensive studies on spatial transient growth (Andersson

et al. 1999; Luchini 2000; Zuccher *et al*. 2006), the cause of the breakdown of the streaks is not clear (Schlatter *et al*. 2008).

The physical explanation of the transient growth can be linked to the lift-up mechanism (Reddy & Henningson 1993; Landahl 1980), where a pair of stable, counter-rotating, streamwise-oriented vortices transfer momentum across the boundary layer, creating a 3-D perturbation (streaks). The formation mechanism of streaks has now been well established through theoretical and experimental methods. However, the linear theory is not suitable for the study of the breakdown of streaks which is a non-linear process. The DNS method can be used to study the whole process of transition. The early studies include Wray & Hussaini (1984), Rai & Moin (1991), Gilbert & Kleiser (1986), who focused on developing numerical method and validated them against experiments. Jacobs & Durbin (2001) conducted the first detailed DNS research to simulate the three regions of the bypass transition, demonstrating the behaviour of perturbations with different scales. With the aid of flow visualization, phenomenological flow structures are demonstrated and by linking those structures with corresponding theoretical results, the understanding of bypass transition has been greatly improved. It has been shown that large scale disturbances from the free-stream turbulence (FST) penetrate into the laminar boundary layer which are amplified to produce elongated low- and high- speed streaks, remaining largely stable at this stage. To the end of the first region, the flow reaches a condition such that secondary instability leading to turbulent spots, which evolve and grow, occupying more and more space until they fill the full span of the flow field and then the flow becomes fully turbulent. A recent research (Zaki *et al*. 2010) on bypass transition using DNS provides further result, such as the details on second instability in terms of wavelength response, group velocity and the growth rate of turbulent spots,

which cannot be easily acquired by theoretical and experimental methods. It is observed that the occurrence of turbulent spots is accompanied by the particular state of streaks. Two typical motions of unstable streaks were identified by dye visualization by Mans *et al.* (2005), which led to sinuous instability and varicose instability. The anti-symmetric sinuous mode is caused by the instability of spanwise inflectional velocity, while the anti-symmetric varicose mode is induced by the instability of a wall-normal inflectional velocity. Asai *et al.* (2002), via experiment, established that the spatial growth rate of the varicose mode is very sensitive to the streak width and is rapidly reduced as the velocity defect decreases owing to the momentum transfer by viscous stresses. By contrast, the growth rate of sinuous mode that leads to the spanwise modulation of the streaks, it is not affected by the decrease in the streak width as strongly as that to varicose mode. Schlatter *et al.* (2008) further illustrates that the sinuous mode occurs much more often than the varicose mode. Vaughan & Zaki (2011) predicted theoretically that the critical streak amplitude is ~10% in terms of the ratio of peak r.m.s. and free stream velocity. A similar value was found in the experiments of Mandal *et al.* (2010) for external boundary layer bypass transition.

2.4 The self-sustaining mechanism of wall-bounded turbulent flow

Through a large body of experimental observations and theoretical work is accumulated, a fundamental self-sustaining process modelled for wall-bounded flow has been developed by a number of researchers (Jiménez & Moin 1991; Waleffe *et al.* 1991; Waleffe *et al.* 1993; Hamilton *et al.* 1995; Waleffe 1997; Jiménez & Pinelli 1999). The initial work was inspired by the observations of the wavy streaks and streamwise vortices in the near wall region of turbulent flows, which are ubiquitous features in that region.

Three distinct phases of self-sustaining process were described by Waleffe (1997) as Figure 2.5 shows. The first phase is the redistribution of the streamwise momentum by weak streamwise rolls, which produce streaks.

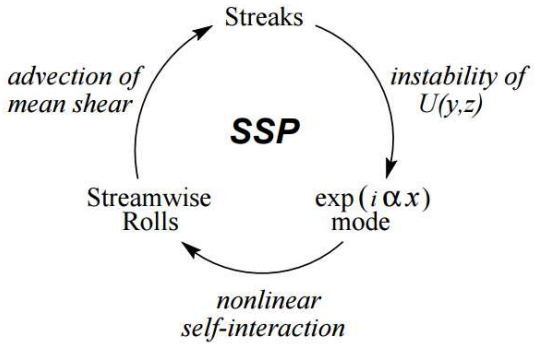

Figure 2.5: The self-sustaining process (Waleffe 1997).

As the spanwise inflections appear, a wake-like instability in which a three-dimensional disturbance of the form $e^{i\alpha x}V(y,z)$ develops (the non-linear development of streaks). The primary nonlinear effect resulting from the development of the instability is to reenergize the original streamwise rolls, leading to a three dimensional self-sustaining nonlinear process. It is shown that this process is remarkably insensitive to whether there is free slip or no-slip at the walls. The involvement of these structures in maintaining the turbulent state was observed in minimal channel simulations in which the streamwise roll and streak structure is observed in a self-sustaining time-dependent state (Jiménez & Moin 1991; Hamilton $et\ al.$ 1995; Waleffe 1997).

Jiménez & Moin (1991) studied the streak spacing that turbulence could not be sustained in their plane channel flow simulations by systematically reducing the spanwise dimension of the computational domain. When it was less than the normally observed streak spacing of about 100 wall units, the turbulence could not be sustained, even though the flow Reynolds number, based on half channel height, was 2000 to 5000. Waleffe

et al. (1991) suggested that the preferred spanwise spacing be the critical Reynolds number. Waleffe *et al.* (1993) went on to show that the critical Reynolds number obtained from the streak spacing, after conversion to the conventional flow Reynolds number, gives the correct critical values for plane Poiseuille, plane Couette, and other shear flows. This suggests that 100 may be a universal critical Reynolds number for near-wall processes. Hamilton *et al.* (1995) studied a highly constrained plane Couette flow. The domain size was reduced to a minimum values which sustain the turbulence. A well-defined quasi-cyclic and spatially organized process of regeneration of near-wall structures is observed. The process is composed of three distinct phases: formation of streaks by streamwise vortices, breakdown of the streaks, and regeneration of the streamwise vortices. The vortex regeneration was found to be a direct result of the breakdown of streaks that were originally formed by the vortices. It was also found that if the width of the domain is further reduced less than typically observed spanwise spacing of near-wall streaks, the turbulence is no longer sustained. Jiménez & Pinelli (1999) showed that a cycle exists which is local to the near-wall region and does not depend on the outer flow. The cycle involves the formation of velocity streaks from the advection of the mean profile by streamwise vortices, and the generation of the vortices from the instability of the streaks. Interrupting any of those processes leads to laminarization.

The similar scenario was also observed in flow with very low Reynolds number. Iida & Nagano (1998) studied the relaminarization mechanisms of turbulent channel flow. By reducing the Reynolds number systematically, they observed in a flow with Re_τ=60 that the streamwise vortices reduces but the scale of them increases. The cores of them are lift slightly up from a typical location at y^+=10. The sweeps are found to be deterred. Tsukahara *et al.* (2005) studied the DNS result of several turbulent flow with very low

Reynolds number (down to Re_τ=64 or Re_b=930 based on half channel height). The authors showed that the spanwise spacing between streaks are about 100 viscous unit even at Re_τ=80. It was observed that the localized turbulence can sustain in the form of periodic oblique band in a low Reynolds number flow (Re_τ=64) as long as the flow domain is large enough to accommodate these basical structures, especially the streaks. It was interesting to observe that the turbulent and laminar bands alternatively distributed with an oblique orientation to the flow direction. Brethouwer $et\ al.$ (2012) indicated that this oblique regime can be shifted up to large values of the Reynolds number Re by increasing the damping by body force (the buoyancy, the Coriolis or Lorentz force). Near wall turbulence structures scale with viscous wall units as in the fully turbulent case.

Chapter 3

Direct Numerical Simulation

The Navier-Stokes equations are a set of equations established on the conservation of mass, momentum, energy and may be coupled with state equations. Direct numerical simulation (DNS) is a numerical method in which the Navier-Stokes equations are directly solved without using any models to resolve the smallest scale motions. The Navier-Stokes equations of incompressible flow without heat transfer read:

$$\frac{\partial u_i}{\partial t} + u_j \frac{\partial u_i}{\partial x_j} = -\frac{1}{\rho}\frac{\partial p}{\partial x_i} + \nu\nabla^2 u \tag{3.1}$$

$$\frac{\partial u_i}{\partial x_i} = 0 \tag{3.2}$$

The scale of motions in turbulent flow varies from the smallest dissipative scales (Kolmogorov 1941) to the integral scale. To resolve the turbulent motions down to the Kolmogorov scale, it is estimated that the number of computation mesh point *N* required (Ferziger & Perié 1996) is

$$N^3 \sim Re^{2.25} \tag{3.3}$$

If a fully explicit method is used for the time integration, the number of time integration step NT required (Ferziger & Perié 1996) is

$$NT \sim Re^{0.75} \tag{3.4}$$

Consequently, the number of operations increases roughly as the cube of the Reynolds number. Therefore, in the early stage, the DNS can only treat very low Reynolds number flows due to the limited capability of computer. Orszag & Patterson (1972) performed a simulation of an isotropic turbulent flow on a 32×32×32 grid with a low Reynolds number of 35. This paper laid a foundation for DNS, after which the work of Kim $et\ al.$ (1987) is classical, focusing on a fully developed channel turbulent flow. This work is a landmark in turbulence research using numerical method and provides many useful physical understanding on a simple shear flow.

3.1 Numerical methods used in DNS

To solve the incompressible Navier-Stokes equations, one is faced with time numerical issue, space numerical issue and the decoupling of velocity and pressure. A detailed review is given by Moin & Mahesh (1998). In this section, some general information on numerical methods is introduced. The most frequently used spatial discretization methods are spectral method, finite difference method and finite volume method. The spectral method has the advantage of exponential spatial convergence, and therefore it can achieve a high spatial accuracy with a lower order scheme. A rule of thumb suggested by Moin & Mahesh (1998) is that the second-order central finite difference schemes require about twice the resolution in each direction to achieve the same results obtained by a spectral DNS. This is one of the reasons that the spectral method is the first choice whenever possible. However, the spectral method is limited to simple geometry applications due to the difficulty in boundary condition treatment. This difficulty can be overcome by finite difference method and finite volume method. Application of finite volume method in DNS can be found in some available CFD softwares, such as *Openfoam*, *StarCD*. Its

advantage is that the Navier-Stokes equations can be solved on a complex geometry generated by commercial grid generation softwares. However, finite volume method cannot be easily extended to higher than second order spatial discretization. The third method, finite difference method is also widely used by many researchers due to its convenience in coding and freedom in raising the accuracy or adjusting to complex geometry. The finite difference method is chosen in this study.

In addition to the spatial discretization, the selection of the time integration method is also very important. There are explicit, implicit or a combination of explicit and implicit methods. Two main factors on the selection of time integration method should be considered, namely, flow physics and numerical stability. The physical restriction is that to resolve the wide range of time scales in turbulent flow, the time steps in DNS have to be limited. Numerical stability depends on the temporal discretization method. When an explicit method is used, a large time step leads to numerical instability. Numerical stability of the time advancement of the unsteady Navier-Stokes equations can be analysed by Cournat instability theory. The time step size is restricted by Cournat-Freidrichs-Lewy (CFL) number. When a full explicit method is used, the requirement of the time step size is very strict in the regions of refined meshes and it makes the simulation significantly more expensive. On the other hand, a fully implicit time advancement method requires either an iterative solver to solve the coupled velocity variables, or making use of the linearisation scheme in decoupling velocity variables. The linearisation scheme is usually expensive in terms of memory. For example, Rosenfeld (1996) proposed a 3-level linearisation method, in which the velocity fields at the previous and current time steps are stored to determine the velocity at the next time step. In addition, when more than 4^{th} order scheme is used for spatial discretization, implicit method is very

difficult to be implemented. In that situation, explicit method is the only choice. Currently, the widely used trade-off method is a combination of explicit and implicit, in which implicit method is usually used to treat the stiff terms, namely, the second order derivative diffusion terms. The representative explicit methods are Runge-Kutta methods (second order, third order, $etc.$), Adams-Bash forth method (second order). A widely used implicit method is Crank-Nicolson method (Ferziger & Perié 1996). The DNS code in current study is based on semi-implicit scheme, i.e., a combination of Runge-Kutta and Crank-Nicolson.

An issue in solving the Navier-Stokes equation is that there is lack of independent equation for the pressure. There are mainly two methods to solve it. The first class is the pressure correction method (Ferziger & Perié 1996). This class method is usually slow since it involves an iterative procedure. It is not used in the present study, therefore it is not explained in detail in this section. The second method is the fractional step method (FSM, Kim & Moin 1985), in which the pressure is taken out of the momentum equations; the momentum equations are first solved for intermediate velocities without consider the continuity constraint. The Poisson equation for the pressure is formulated based on the incompressibility constraint, and the pressure calculated from the Poisson equation is then used to update the velocity at the end of time advancement.

Overall, there are three kinds of fractional step methods (FSM), namely the pressure-correction FSM, the velocity-correction FSM and the consistent splitting FSM (Guermond & Shen 2003). Pressure-correction methods are time-marching techniques composed of two sub-steps for each time step: the pressure is treated explicitly or ignored in the first sub-step and is corrected in the second sub-step by projecting the provisional velocity onto solenoidal vector fields. This strategy became popular after Van Kan (1986)

introduced a second-order version which improved the accuracy. This second-order pressure-correction FSM is further improved by adding a divergence correction to the pressure (Timmermans *et al.* 1996). The improved version was classified by Guermond & Shen (2003) as the rotational form of the pressure-correction FSM. This class of schemes are now widely used in practice and have been rigorously analysed in (Brown *et al.* 2001; E & Liu 2003; Shen 1994). They were used by many researchers (Kim & Moin 1985; Orlandi 2001; *etc.*). The pressure-velocity decoupling method used in current research belongs to this class. A brief pressure-correction FSM (Kim *et al.* 2002) is presented in Subsections 3.3.2. The second type is velocity-correction FSM, in which the role of the velocity and the pressure is switched, i.e., the viscous term is treated explicitly or ignored in the first sub-step and the velocity is corrected accordingly in the second sub-step. The examples are Orszag *et al.* (1986) and Karniadakis *et al.* (1991). The third type is recently introduced by Guermond & Shen (2003). It is termed as consistent splitting FSM, in which the pressure is evaluated by testing the momentum equation against gradients.

The FST algorithms decouple the computations of the velocity and the pressure and this strategy is computationally very efficient. Supposed that the nonlinear terms are made explicit, then at each time step, one only has to solve a set of Helmholtz-type equations for the velocity and a scalar Poisson equation (with a homogeneous Neumann boundary condition) for the pressure. When a fast Poisson solver is used, this method is more efficient than the coupled approach. However, the price for the decoupling is some loss of accuracy on the pressure and the vorticity. The reason is attributed to that the so-called second-order projection schemes provide second-order accuracy on the velocity, while the convergence rates of the pressure and the vorticity are either first-order or 3/2-order

depending on whether it is the standard form or the rotational form (Kim & Moin 1985; Orlandi 2001; Guermond & Shen 2003).

3.2 Special issues in a DNS of pipe flow

Some representative DNS research on channel and pipe flows is summarized by Chin (2011). Comparing to channel flows, papers on DNS of circular pipe flows are fewer. There are two additional problems for DNS solved on cylindrical coordinates. One is the treatment of the singularity on the axis. The other is in a structured mesh system when grid resolution is set to be sufficient near the outer wall of a pipe, it becomes unnecessarily high when the axis is approached.

To overcome the first problem, there are mainly four methods. 1) Introducing a special function for radial derivatives. This method is used by Leonard $et\ al.$ (1975), Stanaway $et\ al.$ (1988). As Verzicco & Orlandi (1996) commented, this method is cumbersome and hence it is not widely used lately. 2) Using finite volume method instead of the finite difference method. Eggels $et\ al.$ (1994) used this method in a LES simulation of turbulent pipe. Because the radial momentum equation is discretized on an extended grid volume at the axis, the evaluation of quantities at r=0 is avoided. But this treatment is first order. 3) Verzicco & Orlandi (1996) introduce a flux quantity $q_r = ru_r$ on a staggered grid, which simplifies the discretization of this region since q_r=0 at r=0. This method is simple and has a second order accuracy at the pole. This method is used in the present code. 4) Overcoming the singularity by coordinate transform. The singularity at the pole is not physical but coordinate originated. This method is used by Morinishi $et\ al.$ (2004).

Very few papers have discussed the second problem because this is a computational cost problem rather than a technical one. The straightforward solution is using a higher order difference scheme for the derivative terms with respect to the azimuthal direction in the near wall region (Morinishi 2004). Quadrio & Luchini (2002) provided a solution to this problem by making the truncation of the azimuthal Fourier series a function of the radial position. This method is designed for spectral scheme. The key of the method is that, whereas in a collocation approach changing the resolution with radius would have involved multiple interpolations and numerical diffusion, in a spectral representation dropping a few Fourier modes at the high end of the spectrum is a smooth operation, which does not introduce any spatially localized error.

3.3 Governing equations and numerical method

A task of this PhD project is to develop a DNS code for the simulation of pipe and channel flows, with a simple flag to switch between the two types of flows. This code has been developed from an existing code developed and thoroughly validated by Seddighi (2011) for Cartesian system. All the main features, including the discretization methods, the solver and the parallelization scheme are kept unchanged whenever possible. The main issues to be addressed are i) the changes in the governing equations due to the use of a cylindrical system; ii) the treatment of the singularity of the equations at the axis; iii) validation against the benchmark data for pipe flow; iv) development of post processing code for pipe flow.

The key features of the DNS code, which has inherited from Seddighi (2011) are summarized as bellowing:

The code is based on a finite difference approach. A second order finite difference method is used to discretize the spatial derivatives of the governing equations on a staggered mesh arrangement. An explicit Runge-Kutta scheme is used for the convection terms and an implicit Crank-Nicholson scheme is used for the diffusion terms. These are coupled with a fractional step approach (Kim & Moin 1985).

In order to explain the scheme for both Cartesian and Cylinder coordinate, the continuity and momentum equations governing a 3D-incompressible turbulent flow are written. The physical problem is described by a coordinate system $x= (x_1; x_2; x_3)$ that can be , Cartesian i.e.$(x_1, x_2, x_3)= (x, y, z)$ or cylindrical, i.e. $(x_1, x_2, x_3) = (z, r, \theta)$. Three flux terms ($q_1$, q_2, q_3, see below) are used to overcome the singularity on the axis of pipe. This method was firstly employed by Verzicco & Orlandi (1996). In Navier-Stokes equations, the length is normalized by H (half channel height) or R (radius of pipe). The velocities are normalized by U_p (the centre line laminar parabolic profile velocity). Therefore, the time is normalized by H/U_p or R/U_p and the pressure is normalized by $\rho {U_p}^2$. The governing equations are listed as follows

$$\eta \frac{\partial q_1}{\partial x_1} + \frac{\partial q_2}{\partial x_2} + \frac{1}{\eta}\frac{\partial q_3}{\partial x_3} = 0 \tag{3.5}$$

$$\frac{\partial q_1}{\partial t} + \frac{\partial q_1 q_1}{\partial x_1} + \frac{1}{\eta}\frac{\partial q_2 q_1}{\partial x_2} + \frac{1}{\eta^2}\frac{\partial q_3 q_1}{\partial x_3} = -\frac{\partial p}{\partial x_1} - \frac{\partial P}{\partial x_1} + \frac{1}{Re_p}\left(\frac{\partial^2 q_1}{\partial {x_1}^2} + \frac{1}{\eta}\frac{\partial}{\partial x_2}\eta\frac{\partial q_1}{\partial x_2} + \frac{1}{\eta^2}\frac{\partial^2 q_1}{\partial {x_3}^2}\right) \tag{3.6}$$

$$\frac{\partial q_2}{\partial t} + \frac{\partial q_2 q_1}{\partial x_1} + \frac{\partial q_2 (q_2/\eta)}{\partial x_2} + \frac{\partial\,(q_3 q_2)/\eta^2}{\partial x_3} - \varepsilon\frac{{q_3}^2}{\eta^2} = -\eta\frac{\partial p}{\partial x_2} + \frac{1}{Re_p}\left(\frac{\partial^2 q_2}{\partial {x_1}^2} + \frac{\partial}{\partial x_2}\eta\frac{\partial (q_2/\eta)}{\partial x_2} + \frac{1}{\eta^2}\frac{\partial^2 q_2}{\partial {x_3}^2} - \varepsilon\frac{q_2}{\eta^2} - \varepsilon\frac{2}{\eta^2}\frac{\partial q_3}{\partial x_3}\right) \tag{3.7}$$

$$\frac{\partial q_3}{\partial t}+\frac{\partial q_3 q_1}{\partial x_1}+\frac{\partial q_2(q_3/\eta)}{\partial x_2}+\frac{1}{\eta^2}\frac{\partial q_3 q_3}{\partial x_3}+\varepsilon\frac{q_3 q_2}{\eta^2}$$
$$=-\frac{\partial p}{\partial x_3}+\frac{1}{Re_p}\left(\frac{\partial^2 q_3}{\partial {x_1}^2}+\frac{\partial}{\partial x_2}\eta\frac{\partial(q_3/\eta)}{\partial x_2}+\frac{1}{\eta^2}\frac{\partial^2 q_3}{\partial {x_3}^2}-\varepsilon\frac{q_3}{\eta^2}+\varepsilon\frac{2}{\eta^2}\frac{\partial q_2}{\partial x_3}\right) \quad (3.8)$$

where $$q_1 = u_z \quad (3.9)$$

$$q_2 = \eta u_r \quad (3.10)$$

$$q_3 = \eta u_\theta \quad (3.11)$$

In eqns.3.6~3.8, P is the mean pressure and p is instantaneous pressure.

when η is set equal to 1 and ε is set to 0, the simulation is for a channel flow. As $\eta = r$ and ε=1, the simulation is for a pipe flow. The flow can be driven by a constant pressure force or kept at a constant mass flow rate. When kept at a constant mass flow rate, the mean pressure gradient is calculated by integrating the streamwise momentum equation, which yields

$$\iiint\frac{\partial q_1}{\partial t}+\iiint\left(\frac{\partial q_1 q_1}{\partial x_1}+\frac{1}{\eta}\frac{\partial q_2 q_1}{\partial x_2}+\frac{1}{\eta^2}\frac{\partial q_2 q_1}{\partial x_3}\right)$$
$$=\iiint\left(-\frac{\partial p}{\partial x_1}-\frac{\partial P}{\partial x_1}\right)+\iiint\frac{1}{Re_p}\left(\frac{\partial^2 q_1}{\partial {x_1}^2}+\frac{1}{\eta}\frac{\partial}{\partial x_2}\eta\frac{\partial q_1}{\partial x_2}+\frac{1}{\eta^2}\frac{\partial^2 q_1}{\partial {x_3}^2}\right) \quad (3.12)$$

The integration is over the flow domain. By making use of periodic condition in streamwise and spanwise, and noticing that on the wall, q_i (i=1, 2, 3) is equal to 0. The integration of the nonlinear and the pressure fluctuation terms are 0. So, we obtain

$$\iiint\frac{\partial q_1}{\partial t}=\iiint\left(-\frac{\partial P}{\partial x_1}\right)+\iiint\frac{1}{Re_p}\left(\frac{\partial^2 q_1}{\partial {x_1}^2}+\frac{1}{\eta}\frac{\partial}{\partial x_2}\eta\frac{\partial q_1}{\partial x_2}+\frac{1}{\eta^2}\frac{\partial^2 q_1}{\partial {x_3}^2}\right) \quad (3.13)$$

To keep a constant mass flow rate for a steady simulation, the left hand side of Eq.3.13 should be 0. Finally, the mean pressure drop term is:

$$\frac{\partial P}{\partial x_1} = \iiint \frac{1}{VRe_p}\left(\frac{\partial^2 q_1}{\partial {x_1}^2} + \frac{1}{\eta}\frac{\partial}{\partial x_2}\eta\frac{\partial q_1}{\partial x_2} + \frac{1}{\eta^2}\frac{\partial^2 q_1}{\partial {x_3}^2}\right) \tag{3.14}$$

where, V is the volume of the flow domain.

3.3.1 Spatial discretization

The second order central finite difference method is used for spatial discretization. The second order scheme on a cylindrical coordinate is outlined to explain the process of spatial discretization. Figure 3.1 shows the definition of position of velocity components and pressure. Uniform mesh is used in streamwise and spanwise directions. Non-uniform mesh is used in wall-normal direction.

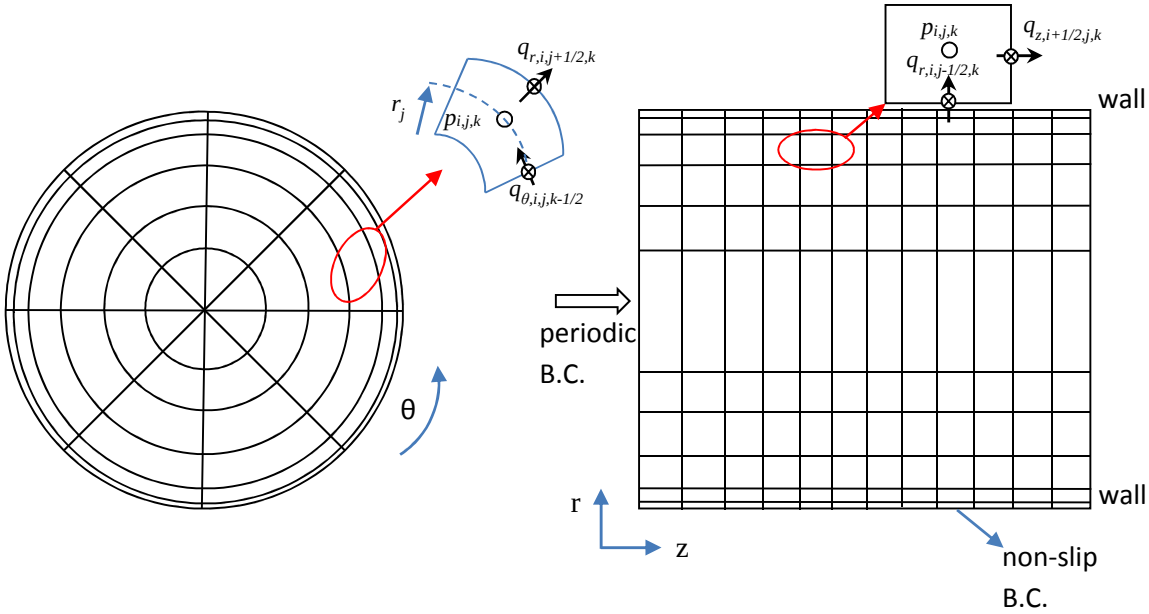

Figure 3.1: Definition points for the velocity and pressure.

In a staggered grid, q_z, q_r and q_θ are defined at $(i+1/2, j, k)$, $(i, j+1/2, k)$, $(i, j, k-1/2)$, respectively. The pressure and other scalars are defined at (i, j, k). More care should be given to the discretization of non-linear term. As suggested by Kleiser & Zang (1991), Kravchenko & Moin (1997), and Blaisdell *et al.* (1996), the aliasing error in non-Galerkin formulations depends upon the analytical form of the nonlinear terms prior to

discretization. There are mainly three forms of the nonlinear term, e.g. the divergence form $(u_i u_i,)_j$, the advection form $u_i(u_i,)_j$ and the skew-symmetric form $\left[(u_i u_i)_j + u_i(u_i,)_j\right]/2$. When the central difference method is used, the skew-symmetric form of the nonlinear terms seems to have lower levels of aliasing error for both incompressible and compressible DNS. The nonlinear terms are discretized in a divergence form in the current code because it is straightforward to implement it. Aliasing error can be indicated by the energy conservation of this scheme. Verzicco & Orlandi (1996) tested the energy conservation of this scheme and it was found that the energy increases only very slightly as long as the time step is small enough. The reason could be attributed to that the aliasing error in finite difference method is not as important as in spectral method.

The z-component *N-S* equation discretization is demonstrated. Other parts are given in Appendix. The non-linear terms in the z-direction are discretized as:

$$\left.\frac{\partial q_z q_z}{\partial z}\right|_{i+\frac{1}{2},\mathrm{j},\mathrm{k}} = \frac{q_{zi+1,\mathrm{j},\mathrm{k}} q_{zi+1,\mathrm{j},\mathrm{k}} - q_{zi,\mathrm{j},\mathrm{k}} q_{zi,\mathrm{j},\mathrm{k}}}{\delta z} \tag{3.15}$$

$$\left.\frac{1}{\mathrm{r}}\frac{\partial q_z q_r}{\partial r}\right|_{i+\frac{1}{2},\mathrm{j},\mathrm{k}} = \frac{1}{\mathrm{r}_j}\frac{q_{zi+\frac{1}{2},\mathrm{j}+\frac{1}{2},\mathrm{k}} q_{ri+\frac{1}{2},\mathrm{j}+\frac{1}{2},\mathrm{k}} - q_{zi+\frac{1}{2},\mathrm{j}-\frac{1}{2},\mathrm{k}} q_{ri+\frac{1}{2},\mathrm{j}-\frac{1}{2},\mathrm{k}}}{\mathrm{r}_{j+1/2} - \mathrm{r}_{j-1/2}} \tag{3.16}$$

$$\left.\frac{1}{\mathrm{r}^2}\frac{\partial q_z q_\theta}{\partial \theta}\right|_{i+\frac{1}{2},\mathrm{j},\mathrm{k}} = \frac{1}{{\mathrm{r}_j}^2}\frac{q_{zi+\frac{1}{2},\mathrm{j},\mathrm{k}+\frac{1}{2}} q_{\theta i+\frac{1}{2},\mathrm{j},\mathrm{k}+\frac{1}{2}} - q_{zi+\frac{1}{2},\mathrm{j},\mathrm{k}-\frac{1}{2}} q_{\theta i+\frac{1}{2},\mathrm{j},\mathrm{k}-\frac{1}{2}}}{\delta\theta} \tag{3.17}$$

With 3.15, 3.16, and 3.17, the nonlinear terms in q_z-component equations are discretized. A linear interpolation is used when the velocity is not defined at the same location, for example:

$$q_{zi+1,\mathrm{j},\mathrm{k}} = \frac{q_{zi+\frac{3}{2},\mathrm{j},\mathrm{k}} + q_{zi+\frac{1}{2},\mathrm{j},\mathrm{k}}}{2} \tag{3.18}$$

$$q_{zi,\mathrm{j},\mathrm{k}} = \frac{q_{zi+\frac{1}{2},\mathrm{j},\mathrm{k}} + q_{zi-\frac{1}{2},\mathrm{j},\mathrm{k}}}{2} \tag{3.19}$$

The discretization of the linear terms is straightforward as bellows:

$$\left.\frac{\partial^2 q_z}{\partial z^2}\right|_{i+\frac{1}{2},\mathrm{j},\mathrm{k}} = \frac{q_{zi+\frac{3}{2},\mathrm{j},\mathrm{k}} - 2q_{zi+\frac{1}{2},\mathrm{j},\mathrm{k}} + q_{zi-\frac{1}{2},\mathrm{j},\mathrm{k}}}{(\delta z)^2} \tag{3.20}$$

$$\frac{1}{\mathrm{r}}\frac{\partial}{\partial r}\mathrm{r}\left.\frac{\partial q_z}{\partial r}\right|_{i+\frac{1}{2},\mathrm{j},\mathrm{k}} = \frac{1}{\mathrm{r}_j(\mathrm{r}_{j+1/2}-\mathrm{r}_{j-1/2})}\left(\mathrm{r}_{j+1/2}\frac{q_{zi+\frac{1}{2},\mathrm{j}+1,\mathrm{k}}-q_{zi+\frac{1}{2},\mathrm{j},\mathrm{k}}}{\mathrm{r}_{j+1}-\mathrm{r}_j} - \mathrm{r}_{j-1/2}\frac{q_{zi+\frac{1}{2},\mathrm{j},\mathrm{k}}-q_{zi+\frac{1}{2},\mathrm{j}-1,\mathrm{k}}}{\mathrm{r}_j-\mathrm{r}_{j-1}}\right) \tag{3.21}$$

$$\frac{1}{\mathrm{r}^2}\left.\frac{\partial^2 q_z}{\partial \theta^2}\right|_{i+\frac{1}{2},\mathrm{j},\mathrm{k}} = \frac{q_{zi+\frac{1}{2},\mathrm{j},\mathrm{k}+1} - 2q_{zi+\frac{1}{2},\mathrm{j},\mathrm{k}} + q_{zi+\frac{1}{2},\mathrm{j},\mathrm{k}-1}}{\left(\mathrm{r}_j\delta\theta\right)^2} \tag{3.22}$$

More words should be given to explain how the singularities on the axis are treated. There is no singularity problem for q_z-component equation due to the use of staggered grid. For q_r-component equation, by using the flux value q_r, most terms at the centre do not need special treatment as they are zero, but there are still two terms that need special treatment. Due to q_r=0 at the axis, the solution of q_r-momentum equation sweeps from j =3/2 to j =$N_r + 1/2$. In this way, most of the singularity terms vanish. There are some special terms at j=3/2 which need information from the axis. They are shown below, in which the subscripts for z- and θ- direction are ignored for simplicity.

$$\left(\frac{\partial q_r\, q_r/r}{\partial r}\right)_{j=3/2} = \frac{q_{r,2}\, q_{r,2}/\mathrm{r}_2 - q_{r,1}\, q_{r,1}/\mathrm{r}_1}{\mathrm{r}_2 - \mathrm{r}_1} \tag{3.23}$$

where,

$$q_{r,1}/\mathrm{r}_1 = \frac{\overbrace{q_{r,1/2}/\mathrm{r}_{1/2}}^{singular} + q_{r,3/2}/\mathrm{r}_{3/2}}{2} \tag{3.24}$$

Similarly, the terms with singularity in the q_θ-component equation are

$$\left(\frac{q_\theta q_r}{r^2}\right)_{j=1} = \frac{q_{\theta,1}}{r_1}\left(\overbrace{q_{r,1/2}/r_{1/2}}^{singular} + q_{r,3/2}/r_{3/2}\right) \tag{3.25}$$

$$\left(\frac{1}{r^2}\frac{\partial q_r}{\partial \theta}\right)_{j=1} = \frac{2}{\mathrm{r}_1}\frac{\left(\overbrace{q_{r,1/2}/\mathrm{r}_{1/2}}^{singular} + q_{r,3/2}/\mathrm{r}_{3/2}\right)}{\delta\theta} \tag{3.26}$$

The L'Hôpital rule is used to evaluate q_r/r at $\left(i,\frac{1}{2},k\right)$. The value of q_r/r is needed at $(i,3/2,k)$, that is:

$$\left(\frac{q_r}{r}\right)_{j=1/2} = \left(\frac{\partial q_r}{\partial r}\right)_{j=1/2}\frac{q_{ri,\frac{3}{2},k+1/2} - q_{ri,\frac{3}{2},k+\frac{1}{2}+\pi}}{2\mathrm{r}_{3/2}} \tag{3.27}$$

These tricks make boundary condition treatment simpler. One of the advantages of this kind scheme is that we do not need to devote much effort on boundary condition treatment as the code is switched between pipe flow and channel flow.

3.3.2 Time integration

A mixed method of the three-step Runge-Kutta and the Crank-Nicolson is used for time integration. All the non-linear terms and the first derivative terms in the diffusion term are explicitly treated using the Runge-Kutta method. The second derivative terms in the diffusion terms are implicitly treated using the Crank-Nicolson method to relax the strict restriction on time step. As mentioned before, the decoupling of pressure-velocity is implemented by pressure-correction fractional step method. The fractional step method was originally developed by Yanenko (1971) and then was used to solve Navier-Stokes equations by Kim & Moin (1985). The method was slightly modified by Orlandi (2001), which is used in the present study. This scheme is more effective than these schemes (like, SIMPLE, SIMPLEC, PISO, $etc.$) using the pressure term to enforce continuity by an iterative method, which is an effective but slow method (Ferziger & Perié 1996).

Taking the q_z-momentum equation for example, by applying Runge-Kutta and Crank-Nicolson method, the equation is split into the following equations:

$$\frac{\widehat{q_z} - {q_z}^k}{\delta t} = \gamma_k {H_z}^k + \beta_k {H_z}^{k-1} - \alpha_k \frac{\delta p^k}{\delta z} + 0.5\alpha_k \left(\frac{\delta^2 \left(\widehat{q_z} + {q_z}^k \right)}{\delta z^2} + \frac{1}{r}\frac{\delta}{\delta r} r \frac{\delta \left(\widehat{q_z} + {q_z}^k \right)}{\delta r} + \frac{\delta^2 \left(\widehat{q_z} + {q_z}^k \right)}{r^2 \delta \theta^2} \right) \tag{3.28}$$

$$\frac{{q_z}^{k+1} - \widehat{q_z}}{\delta t} = -\alpha_k \frac{\delta \emptyset^{k+1}}{\delta z} \tag{3.29}$$

where *H* refers to convection terms and other first derivatives in viscous terms. The $\widehat{q_z}$ is an intermediate velocity that does not satisfy the continuity equation. The solution of $\widehat{q_z}$ require for the inversion of large sparse matrices, these are reduced to three tridiagonal matrices by a factorization procedure with error O(Δt^3) (Orlandi 2001). ${q_z}^k$ is supposed to satisfy the continuity equation. Taking divergence on both sides of eq. 3.29 (the two equations for other components, see Appendix) and making use of $div(q^k) = 0$, we obtain the Poison equation:

$$r^2 \frac{\partial^2 \emptyset^{k+1}}{\partial z^2} + r \frac{\partial}{\partial r} \frac{\emptyset^{k+1}}{\partial r} + \frac{\partial^2 \emptyset^{k+1}}{\partial \theta^2} = \frac{1}{\alpha_k \delta t} \left(r \frac{\partial \widehat{q_z}^k}{\partial z} + r \frac{\partial \widehat{q_r}^k}{\partial r} + \frac{\partial r \widehat{q_\theta}^k}{\partial \theta} \right) \tag{3.30}$$

The Poison equation can be solved by direct (e.g., LU Decomposition, Cyclic Reduction FFT, $etc.$) and iterative methods (e.g., ADI, Conjugate Gradient, Multigrid Methods, SOR methods). In the present case, a uniform mesh is used in the streamwise and spanwise directions which makes it possible to apply FFT in the two homogenous directions with TDMA (tridiagonal matrix algorithm) used in the wall-normal direction. The details are referred to Seddghi (2011). The pressure is updated using the following equation (Orlandi 2001):

$$p^{k+1} = p^k + \emptyset^{k+1} - \frac{\alpha_k \delta t}{2Re} \nabla^2 \emptyset^{k+1} \tag{3.31}$$

The overall solution procedure is to use eqs.3.28-3.31 repeatedly in three steps:

- First step, k=1

$H_z{}^1$ and $H_z{}^0$ are the nonlinear terms at current time step and previous time step (note that at the t=0, $H_z{}^0$ =0). p^1 and $q_z{}^1$ are pressure and velocity at the current time step (p^n and $q_z{}^n$). Constants in eqs. 3.28~3.31 are given as

$$\gamma_1 = \frac{8}{15} \tag{3.32}$$

$$\beta_1 = 0 \tag{3.33}$$

$$\alpha_1 = \frac{(\gamma_1 + \beta_1)}{Re} \tag{3.34}$$

$\widehat{q_z}$ in eq. 3.28 is solved by using factorization technique (Orlandi 2001). The same method is used for q_r- and q_θ-component momentum equations to obtain $\widehat{q_r}$, $\widehat{q_\theta}$. The formulas for $q_r -$ and $q_\theta -$ component momentum equations are given in Appendix. $\widehat{q_z}$, $\widehat{q_r}$, $\widehat{q_\theta}$ are substituted into eq.3.31 to form a Poison equation for $\emptyset^2$, which is solved by using a FFT method combined with the TDMA method (Orlandi 2001). This solved virtual scalar quantity is then used in eq.3.29 to obtain $q_z{}^2$ and similarly, for $q_r{}^2$and $q_\theta{}^2$. p^2 is calculated from eq.3.31.

- Second step, k=2

$H_z{}^2$ are the nonlinear terms calculated with velocities and pressure obtained in the first step ($q_z{}^2$, $q_r{}^2$, $q_\theta{}^2, p^2$). Constants in eq.3.28 and eq.3.29 are given by

$$\gamma_2 = \frac{5}{12} \tag{3.35}$$

$$\beta_2 = -\frac{17}{60} \tag{3.36}$$

$$\alpha_2 = \frac{(\gamma_2 + \beta_2)}{Re} \tag{3.37}$$

$\widehat{q_z}$ in eq. 3.28 is solved by using factorization technique again. The same method is used for q_r- and q_θ-component momentum equations to obtain $\widehat{q_r}$, $\widehat{q_\theta}$. And then $\widehat{q_z}$, $\widehat{q_r}$, $\widehat{q_\theta}$ are substituted into eq.3.32 to form a Poison equation for $\emptyset^3$. This virtual scalar quantity is used in eq.3.29 to get ${q_z}^3$ and similarly, for ${q_r}^3$and ${q_\theta}^3$. p^3 is calculated from eq.3.30.

- Third step, k=3

${H_z}^3$ are the nonlinear terms calculated with the velocities obtained in the second step. $({q_z}^3,\ {q_r}^2,\ {q_\theta}^2, p^3)$ are pressure and velocity solved in second step. Constants in eq.3.28 and eq.3.29 are given by

$$\gamma_3 = \frac{3}{4} \tag{3.38}$$

$$\beta_3 = -\frac{5}{12} \tag{3.39}$$

$$\alpha_3 = \frac{(\gamma_3 + \beta_3)}{Re} \tag{3.40}$$

$\widehat{q_z}$ in eq. 3.28 is solved by using factorization technique again. The same method is used for q_r- and q_θ-component momentum equations to get $\widehat{q_r}$, $\widehat{q_\theta}$. And then $\widehat{q_z}$, $\widehat{q_r}$, $\widehat{q_\theta}$ are substituted into eq.3.32 to form a Poison equation for $\emptyset^4$. This virtual scalar quantity is used in eq.3.29 to get ${q_z}^4$ and similarly, for ${q_r}^4$and ${q_\theta}^4$. p^4 is calculated from eq.3.30. After three above steps, the time is marched. The three step Runge-Kutta method is third order at the limit δt=0. The Crank-Nicolson method is second order. The scheme overall is second order in time.

3.3.3 Boundary condition

The boundary condition is treated as following. In the two periodic directions (streamwise direction and spanwise direction), the periodic condition is easy to be treated

and not to be detailed here. It is referred to Seddghi (2011). More attention needs to be given to the treatment of the boundary condition in the wall-normal direction. The no-slip boundary condition is used at the wall. For q_r, which is defined at the wall, the no-slip boundary condition is defined as

$$q_r(i, nr + 1/2, k) = 0 \tag{3.41}$$

For the velocity components not defined at wall, the no-slip boundary condition is defined as

$$q_z(i + 1/2, nr, k) + q_z(i + 1/2, nr + 1, k) = 0 \tag{3.42}$$

$$q_\theta(i, nr, k + 1/2) + q_\theta(i, nr + 1, k + 1/2) = 0 \tag{3.43}$$

where, q_z and q_θ at n_r+1 are the values at ghost point out of the wall.

3.3.4 Method of parallelization

There are mainly two widely used parallelization methods, namely, OpenMP and MPI (Message Passing Interface). In simple terms, OpenMP makes use of shared memory (all the processors access the same memory), while, MPI is mostly designed for distributed memory architecture. The advantages and disadvantages of OpenMP and MPI are summarized as following:

Advantage of OpenMP

○ easier to program and debug than MPI

○ directives can be added incrementally-gradual parallelization

○ can still run the program as a serial code

○ serial code statements usually don't need modification

○ code is easier to understand and maybe more easily maintained

Disadvantage of OpenMP

- ○ can only be run in shared memory computers
- ○ requires a compiler that supports OpenMP
- ○ mostly used for loop parallelization

Advantage of MPI

- ○ runs on either shared or distributed memory architectures
- ○ can be used on a wider range of problems than OpenMP
- ○ each process has its own local variables
- ○ distributed memory computers are less expensive than large shared memory computers

Disadvantage of MPI

- ○ requires more programming changes to go from serial to parallel version
- ○ can be harder to debug
- ○ performance is limited by the communication network between the nodes

In order to make use of current available cluster, and maintain good extensibility and portability, MPI method is employed. For a message passing methodology, four issues need to be considered, which are the decomposition of the problem, the data structure, appropriate message passing (sending and receiving) between the cores and synchronization of the processes. To parallelize the code by MPI method, the problem must be properly decomposed. There are mainly two ways for problem decomposition, namely domain decomposition and functional decomposition. Domain decomposition is used in the code, because it can be run on arbitrary number of processors. Domain decomposition is implemented in the wall-normal direction only.

3.3.5 Some rules of thumb for DNS study

Till now, more and more knowledge has been accumulated in DNS overtime. It is useful to summarize some of them, especially these about space and time resolutions and the domain size. The spatial resolution should refer to the physical scales. The grid used should capture the smallest scale (Kolmogorov scale, η) in the flow. Some simulation shows this requirement is too restrict. Moser & Moin (1987) shows that most dissipation in the curved channel occurs at scales larger than 15η. This result is obtained from spectrum method. For finite difference method with larger numerical errors, it requires a higher resolution to achieve similar accuracy. A rule of thumb is that second-order central difference schemes require about twice the resolution (in each direction) to achieve the same results as a spectral DNS. The spectrum of the fluctuation velocities is helpful to check the space resolution. If the small scales are not resolved, there will be a tail at the energy spectrum.

As mentioned before, when the time step is considered in a DNS study, one should guarantee the numerical stability of the calculation and resolve the smallest physical time scale. Implicit time advancement for the viscous terms and explicit time advancement for non-linear terms allow as large time steps. However, too large a time step may cause the turbulence decay faster unphysically.

The size of the domain is not emphasized by early researchers. However, it becomes more and more important. It is known that the turbulence cannot be sustained if the spanwise dimension is too small to contain less than two streaks (Hamilton $et\ al.$ 1993). This put some restrictions on spanwise domain length. In the streamwise direction, the requirement comes from the length of domain should be longer enough to contain the longest structure in the flow. The streamwise correlation can be used to check the

suitability of domain size. A criteria that is used often is that the correlation should reduce to 0 within half of the domain. This criteria leads to a ~10δ streamwise length for typical low Reynolds number pipe and channel flows ($Re_\tau = 180$). For a higher Reynolds number flow, it is expected to be reduced as the streaky structures become weaker or absent. However, recently, the importance of the domain length for a high Reynolds number flow is emphasized by many researchers (Marusic $et\ al.$ 2010; Chin $et\ al.$ 2010; Wu $et\ al.$ 2012). These authors suggested that the domain length of the pipe should be longer enough to hold the large structures and very large structures, which is usually several times that of the characteristical length. A length of 8πR is suggested by Chin $et\ al.$ (2010) for pipe flow with Re_τ=500.

3.3.6 Validation of the DNS code against benchmark data

The DNS results of flow at $Re_{\tau 0}$=180 and $Re_{\tau 1}$=437 are compared with benchmark data. These are two representative Reynolds numbers studied in later chapters. The benchmark data of Re_τ=180 is from Fugatama & Kasagi (2002). The details of the two simulations are summarized in table 3-1. The flow with $Re_{\tau 1}$ =437 are compared with the experimental benchmark data of Durst $et\ al.$ (1995) at Re_τ=410, which is the most similar Re that can be found from the literature.

The ensemble-averaged statistical quantities for any location with a distance y_0 from the wall are calculated by averaging in the two homogenous directions as well as in time. For instance, the mean velocity is

$$\bar{u}_s = \frac{1}{N_z N_\theta L}\left(\sum_{k=1}^{L}\sum_{j=1}^{N}\sum_{i=1}^{M} u_s\right) \tag{3.44}$$

and the r.m.s. of the turbulent fluctuating velocity is

$$\bar{u}_{s,rms} = \frac{1}{N_z N_\theta L}\left(\sum_{k=1}^{L}\sum_{j=1}^{N}\sum_{i=1}^{M}(u_s - \bar{u}_s)\right) \tag{3.45}$$

where N_z and N_θ are the numbers of mesh points in the streamwise and spanwise directions, respectively, L is the number of independent flow filed, the index s=1, 2, 3 stands for the streamwise, wall-normal and spanwise velocity components, which are also are denoted u_z, u_r and u_θ. For a pipe flow with two periodic directions, $\bar{u}_z$ is the only non-zero mean velocity. The perturbation velocities $u'_z = u_z - \overline{u_z}$, $u'_r = u_r$ and $u'_\theta = u_\theta$, are referred to as fluctuating velocities and $u'_{z,rms}$, $u'_{r,rms}$, $u'_{\theta,rms}$ are denote the r.m.s of the fluctuating velocities.

Table 3. 1 Simulation detailes of Kasagi's and current DNS

DNS data	Fugata & Kasagi (Pipe)	Current (Pipe)
Method	Finite difference	Finite difference
Mesh size	256×96×128	800×160×240
Domain size	10R×R×2π	18R×R×2π
Δr^+_{min}	0.46	0.09
Δr^+_{max}	2.99	2.4
Δz^+	7.03	4.5
$\Delta (r\theta)^+_{max}$	8.84	2.4
Δt^+	0.18	0.15
Averaging time	2160 (in wall unit)	2400 (in wall unit)
Averaging interval	NA	60 (in wall unit)
$Re_\tau = u_\tau H/\nu$	180	180
$Re_b = U_b H/\nu$	5300	5300

It is shown in Figure 3.2 that the result of current DNS simulation almost collapses with that of benchmark data, especially for the $Re_\tau = 180$. For the higher Reynolds number flow, the mean velocity still agrees with that of Durst *et al.* (1995). The difference detected in r.m.s data of higher Reynolds number flow may be due to lower resolution measurement in experiment.

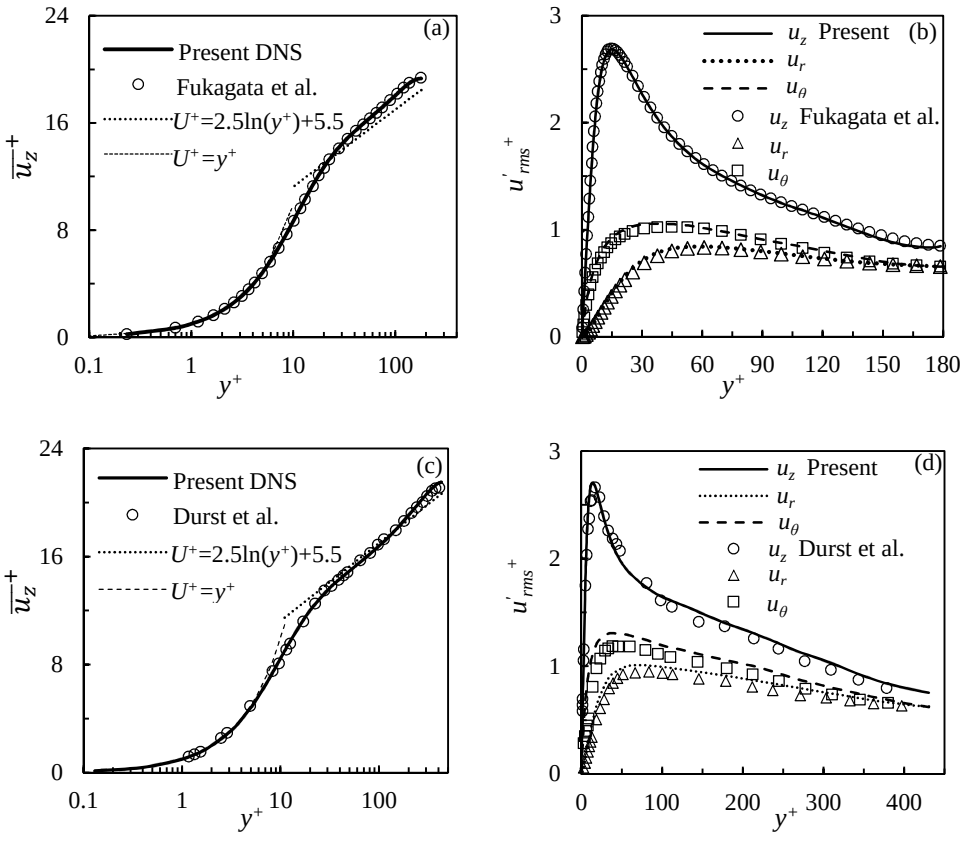

Figure 3.2: Validation of the code: (a)&(b) Re_τ=180; (c)&(d) Re_τ=437.

Chapter 4

Pipe Flow Subjected to an Increase of Flow Rate

Unsteady flows due to a change in flow rate exist in many natural and engineering systems. Sometimes, they are harmful, and may lead to economical loses or safety concerns (Colombo *et al*. 2009). A typical example is a pump on/off event or valve malfunction, which may potentially induce significant transients resulting in strong pressure waves travelling through a pipe network, potentially causing major damages to a civil water system (Ghidaoui *et al*. 2005). Except for the practical relevance, it is also useful in developing a better understanding of turbulent flow in general. In this chapter, DNS studies on a turbulent pipe flow subjected to a slow or sudden increase in flow rate are studied. The result is also compared with the data of corresponding channel flow.

4.1 A introduction for the transient flow subjected to a flow rate change

It has previously been shown that the transient flow in a channel following a step-increase of flow rate is effectively a laminar turbulent bypass transition (He & Seddighi 2013, hereafter referred to HS2013). In response to the rapid increase of flow rate, a new boundary layer is formed. The flow does not progressively evolve from the initial

turbulent structure to a new one, but undergoes a process involving three distinct phases (pre-transition, transition and fully turbulent), which are equivalent to the three regions of the boundary layer bypass transition, namely, the buffeted laminar flow, the intermittent flow and the fully turbulent flow regions. Several parameters are identified which may potentially influence the transition process in the flow. They are,

(1) Re_0, ($=U_{b0}R/\nu$), In this theory, the initial turbulent flow acts as the free stream turbulence (FST). This Reynolds number defines the amplitude and time/length scales of the FST. The higher is the *Re*, the lower the initial turbulence intensity but also the smaller the time/length scales.

(2) Re_1, ($=U_{b1}R/\nu$). U_{b1} is a parameter similar to the "free-stream" velocity U_∞ in boundary layer flow.

(3) (Re_1−Re_0) or ($U_{b1}-U_{b0}$). It defines the varying range of the flow rate and the time-developing boundary layer is characterized by this parameter.

(4) The acceleration rate, $(U_{b1}-U_{b0})/\Delta t_{ac}$, where Δt_{ac} represents the acceleration period. This parameter determines how fast the flow rate is changed and it potentially affects the transient process of the flow.

(5) The initial free-stream turbulence intensity (Tu_0). This is dependent on both Re_0 and Re_1, which can be represented by $(u'_{rms0,max})/U_{b1}$, where $u'_{rms0,max}$ is the peak value of the wall-normal profile of the *r.m.s.* of the streamwise turbulent fluctuating velocity at t=0.

One of the important features needed to study in boundary layer bypass transition is where the transition happens. For boundary layer flow, it is well established that $Re_{cr}\sim Tu_0{}^{-2}$. Through a systematical study (HS2013; Seddighi *et al.* 2014; He & Seddighi 2015), very similar to that of boundary layer flow, the equivalent critical Reynolds number for the

onset of the transition in an unsteady channel flow is strongly correlated with the free-stream turbulence intensity (Tu_0) in a power law, which defines as

$$Re_{t,cr} = ATu_0{}^B \tag{4.1}$$

where $$Re_{t,cr} = \frac{t_{cr}{U_{b1}}^2}{\nu} \tag{4.2}$$

and, t_{cr} is the onset of transition, which is determined by the time when the minimum friction coefficient C_f occurs. However, it is found that the $(u'_{rms0,max})/U_{b0}$ can be correlated by the Reynolds number as $C(U_{b0}/U_{b1})Re^{-0.1}$. With this approximation, the predicted critical Reynolds number can be estimated by pre-known parameters such as Re_0 and Re_1. The constants A, B and C are determined by relative DNS data as 1340, -1.71 and 0.375, respectively. The formula 4.1 is found workable in a Reynolds range (2800-12800) by DNS (HS2013; He & Seddighi 2015) and (2800-42800) by LES (Mathur *et al.* 2015).

In this chapter, the DNS study on the transient pipe flow is conducted to further discuss this new mechanism and the effect of these key parameters. The previous study pays more attention on the Re_0, Re_1 and Tu_0. For the parameter iv, Seddighi *et al.* (2014) found that the acceleration rates does affect the $Re_{t,cr}$ but the general transition process remains similar. However, in this study, only a rapid ramp-up and a slow ramp-up flow were studied. It will be useful to study a series of ramp-up flows with systematically increased acceleration time(Δt_{ac}). This is important because the acceleration rates could be either fast or slow in real life and experiment. Another question to be addressed in this chapter is how is the phenomenon affected by geometry. The differences and similarities between the steady channel and pipe flows are established by many researchers (Wosnik *et al.* 2000; Meseguer & Trefethen 2003; Nagib 2008; Chin 2011). It is generally

accepted that these two flows are similar in near wall region. But there is no dispute that there is unignorable difference in the outer region, where the large turbulence scales are confined in pipe flow but not in a channel and boundary layer flow. In order to address these questions, the following simulations were conducted:

1. A turbulent pipe flow subjected to a sudden change in flow rate. Initial and final Reynolds numbers are 2650 and 7362, respectively. It is similar to those used in HS2013. This is to facilitate the comparison with the corresponding channel flow;
2. Three transient turbulent pipe flows subjected to sudden change in flow rates. The initial bulk flow is kept unchanged at 2650 but final Reynolds numbers are set at 3000, 5220 and 7362;
3. Turbulent pipe flow with a fixed initial and final bulk flow but with systematical increasing acceleration period. The initial and final Reynolds numbers are 2650 and 5300.

The details of these simulations are summarized in corresponding sections.

4.2 Simulation details

The initial and final flow Reynolds numbers of the rapid acceleration of the flow are chosen at 2650 ($Re_{\tau 0}$=180) and 7362 ($Re_{\tau 1}$=437), respectively, which are close to the corresponding channel flow Reynolds numbers, 2825 ($Re_{\tau 0}$=178) and 7404 ($Re_{\tau 1}$=418) used in the reference (HS2013) to facilitate a direct comparison. The subscripts 0 and 1 stand for the initial flow and final flow, respectively.

At time t^*(=$t/(\delta/U_{b1})$)=0, the flow is accelerated rapidly, by a sudden change in mass flow rate. The acceleration period is very short($\Delta t_{ac}{}^* = 0.22$) and hence the change of flow can be seen as a step change. The simulation continues until the flow has become

fully developed again (t^*=97). The calculation of ensemble-averaged statistical quantities follows the method used in HS2013, averaging in the two periodic directions and over 8 realizations. The initial flow for each simulation is selected from one instant of the steady state flow simulation of Re_τ=180 and there is an interval of at least Δt^*=70 between two consecutive realizations, ensuring that the flow fields used in the ensemble averaging are independent of each other. The simulation results are re-scaled using final flow bulk velocity (U_{b1}) or shear velocity ($u_{\tau 1}$) as will be indicated when they are presented. The purpose is to facilitate the discussion of the results and the comparison with the data from HS2013.

The mesh and domain information are summarized in table 4.1.

Table 4. 1 Summary of simulation details

Δt_{ac}	$(\Delta z)_0^+$	$(\Delta z)_1^+$	$\Delta(r\theta)_{max0}^+$	$\Delta(r\theta)_{max1}^+$	$(\Delta r)_{max0}^+$	$(\Delta r)_{max1}^+$	$(\Delta r)_{min0}^+$	$(\Delta r)_{min1}^+$
0.22	4	10	3.2	7.8	1.5	3.6	0.1	0.23

($Re_{\tau 0}$ =180, $Re_{\tau 1}$=437; Re_{b0} =2650, Re_{b1}=7362; $N_z \times N_r \times N_\theta$=800×160×480; Domain: 18R)

4.3 Results and discussion

4.3.1 Three stages of the transient pipe flow

As mentioned in §4.1, the transient process of a channel flow responding to a rapid flow acceleration can be described as a laminar-turbulent transition, comprising three distinct stages namely, pre-transition, transition, and fully turbulent stages. The three-stage process is reflected in the development of the friction coefficient, C_f ($= \frac{\tau_w}{0.5\rho {U_0}^2}$, where $\tau_w = \mu \frac{d\overline{u_z}}{dy}\Big|_{y=0}$) which also reflects the development of wall shear stress. Figure 4.1

shows the development of C_f of the present pipe flow together with that of a channel flow for comparison. Prior to the commencement of the acceleration, the friction coefficient is equal to the value corresponding ($C_{f0} = 0.00928$) to the initial steady-state flow at Re_0 =2650.

Immediately after the commencement of the acceleration, it increases rapidly to a much higher value, reaching a maximum at t^*=0.22 when the acceleration is terminated. The value then reduces gradually, reaching a minimum value at around t^*=~21 or t^{+0}=92 (the corresponding time for the channel flow is t^*=21 or t^{+0}=90).

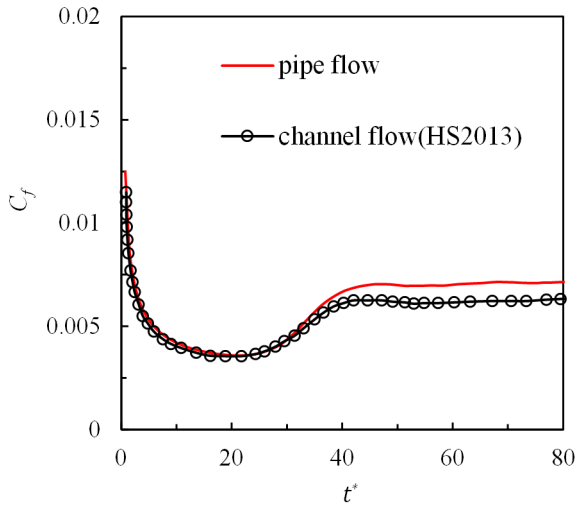

Figure 4.1 : Development of friction coefficient.

Subsequently, C_f recovers and approaches the steady flow value of the final flow around t^*=42. Then, it only changes slightly until t^*=~50, and remains constant afterwards. It is seen that the trend of the development of the friction factor is the same as that of the transient channel flow of HS2013. In fact, the friction factors of the two flows are practically the same before t^*=30. In addition, the time for the transition onset is the same in the two flows. Similar to the channel flow, the response can be characterized into three

stages, namely, pre-transition (t^*<21), transition (t^*=21~42) and fully developed stage (t^*>42).

The pre-transition is characterized by the formation of a thin boundary layer of a high strain rate on the wall, which then grows into the core of the flow with time. The existing turbulence serves as disturbances much like the FST in a boundary layer. The development of the boundary layer is shown in Figs. 4.2(a) & (b) in terms of momentum thickness Reynolds number and shape factor. These are based on the differential velocity $\bar{u}$^ defined in a way similar to that used in HS2013, but it is modified for the cylindrical coordinate.

$$\bar{u}^(r,t^*) = \frac{\overline{u}\,(r,t^*) - \overline{u}\,(r,0)}{\overline{u_c}(t^*) - \overline{u_c}(0)} \tag{4.3}$$

$$R^2 - (R-\delta^*_{du})^2 = \int_0^R (1-\bar{u}^(r,t^*))\,2rdr \tag{4.4}$$

$$R^2 - \ (R-\theta_{du})^2 = \int_0^R \bar{u}^(r,t^*)(1-\ \bar{u}^(r,t^*))\,2rdr \tag{4.5}$$

$$Re_\theta = \frac{\theta_{du}{}^*\overline{u_c}(t^*)}{\nu} \tag{4.6}$$

$$H = \frac{\delta^*_{du}}{\theta_{du}} \tag{4.7}$$

where, $\bar{u}$ and $\overline{u_c}$ are ensemble-averaged of local streamwise mean velocity and the centre velocity of the pipe flow, respectively.

Overall, the boundary layer in a pipe develops in a way similar to that of the channel flow. Re_θ grows almost linearly with time until Re_θ≈240. Afterwards, the growth rate increases as a result of the onset of the transition. The value of Re_θ of the pipe flow is close to, but lower than that of the channel flow during the pre-transition and transition

periods, but diverges from it after the transition is completed (t^*>42). That is, even though the values of Re_θ are significantly different in the two flows they are very close during the transition period. The shape factor of the pipe flow shows a similar developing pattern to that of the channel flow but with a higher value.

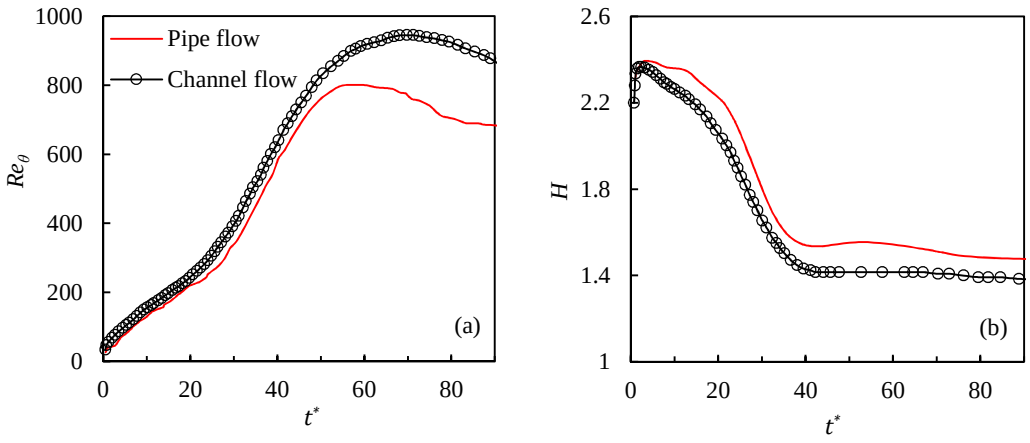

Figure 4.2: Transient boudary layer behavior of pipe flow and channel flow.

4.3.2 Flow structure response during the transient process

Figs.4.3~4.5 shows different flow structure visualization of the transient process. To illustrate the flow structures, Figure 4.3 shows the iso-surface plots of u'_z/U_{b1} =±0.13 and λ_2=-2.0 at t^*=0, 14, 21, and 42. Only the bottom half of the pipe is displayed. λ_2 is the second eigenvalue of the symmetric tensor $S_2 + \Omega_2$ where S and Ω are the symmetric and antisymmetric parts of the velocity gradient tensor ∇u. This value is introduced by Jeong and Hussain (1995) to identify vortex cores, and has been used frequently in studies of transition and turbulence.

At t^*=0, there are few short low- and high-speed streaks. A short time later, at t^* =4, the high speed structure is notably increases but the vortex structure (in red) reduces slightly. At a later pre-transition stage (t^*=10, 17), elongated streaks appear alternately,

which break up at t^*=21 at some isolated places in the pipe. Packets of hairpin-like structures (identified by the iso-surface of the negative λ_2) are observed mostly surrounding the low-speed streaks. There are very few of such structures in the early pre-transition stage, and the size of such packet is small, but at a later stage (t^*=21), large spots of the turbulence start to occur, which signify the onset of transition. To t^*=28 and 35, these spots merge together. At the end of the transition (t^*=42), the vortical structures are full of the flow. The development of the streaky and vortical structures during the transient flow exhibits a great resemblance to that of channel flow of HS2013.

Figure 4.4 shows the contours of the streamwise fluctuating velocity u'_z at an *r*-θ plane (*z*/*R*=5.0) and a *z*-θ plane (y^{+0}=5.4, where y^{+0} is the radial distance from the wall normalized with $\nu/u_{\tau 0}$) at several instants following the rapid increase of flow rate. The first frame (t^*=0) corresponds to the steady flow field just before the start of the transient flow. It is seen from the *z*-θ plane that the values of u'_z are relatively low and the colour is light. Some weak and short patches of high- and low-speed patterns are present in the initial flow field. The *r*-θ plane shows that these streaks appear alternately in the azimuthal direction and the low speed streaks penetrate deeper into the core region of the pipe (Klebanoff $et\ al.$ 1962). During t^*=0~21, elongated streaks of positive and negative u'_z are formed and intensified. The r-θ plane plots on the left show that the low- and high-speed streaks are confined very close to the wall. Later, some highly fluctuating velocities are seen to form, which appear as isolated turbulent patches (or, spots, see panel at t^*=28). The spots spread into the flow and merge with each other until about t^*=42, when the turbulence occupy the z-θ near wall plane.

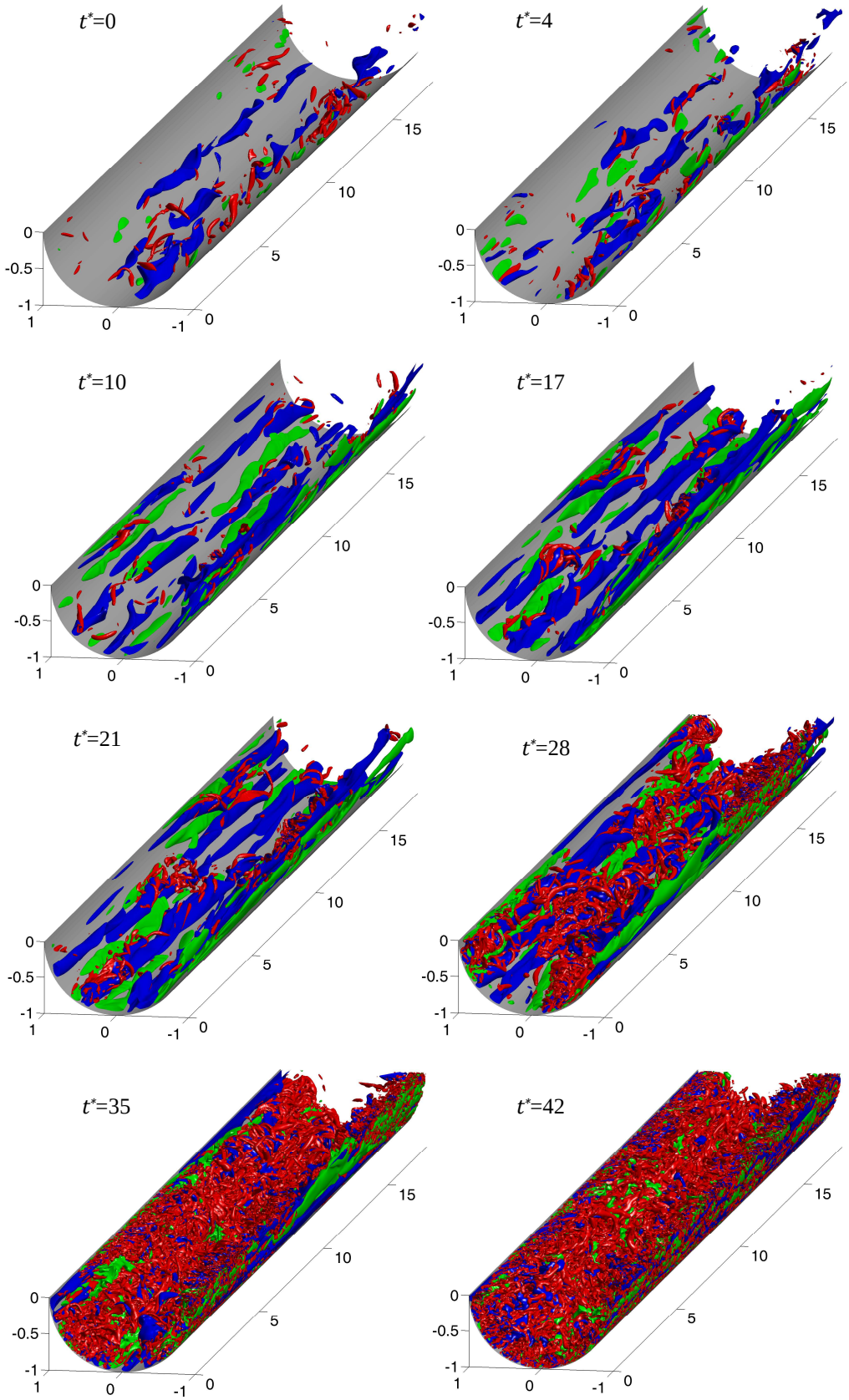

Figure 4.3: Development of flow structures (3-D).

(iso-surfaces: blue for u'_z/U_{b1}=-0.13, green for u'_z/U_{b1} =0.13 and red for λ_2/U_p^2=-2.0)

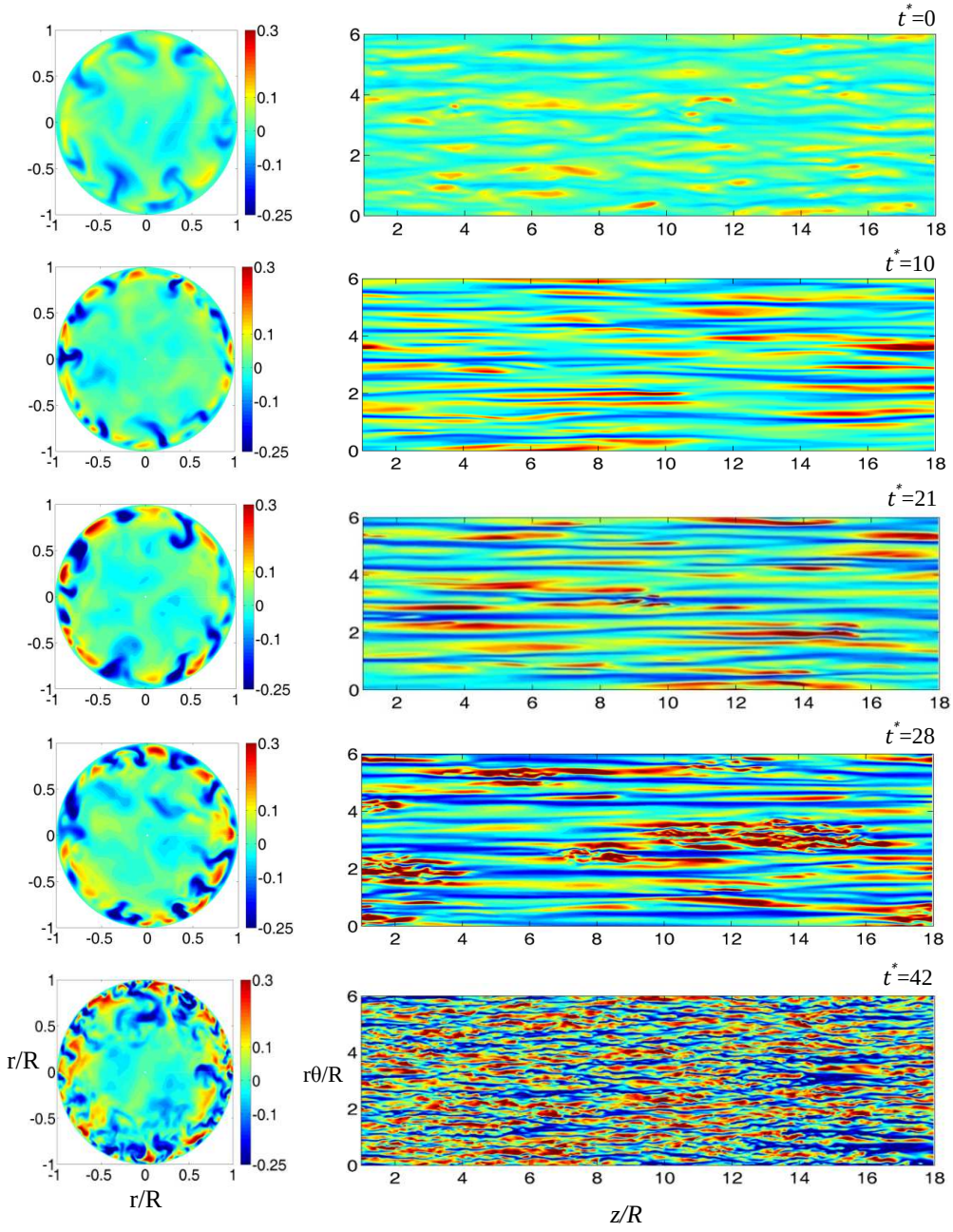

Figure 4.4: Development of flow structures (2-D).

Left: Contour plots of (u'_z/U_{b1}) in a r-θ plane (z/R=5.0); Right: Contour plots of (u'_z/U_{b1}) in a z-θ plane (y^{+0}=5.4)

The streamwise and spanwise correlation coefficients of the streamwise velocity, R_{11}, contain quantitative information of the streaky structures. Figs. 4.5(a) & (b) show the profiles of R_{11} at several instants.

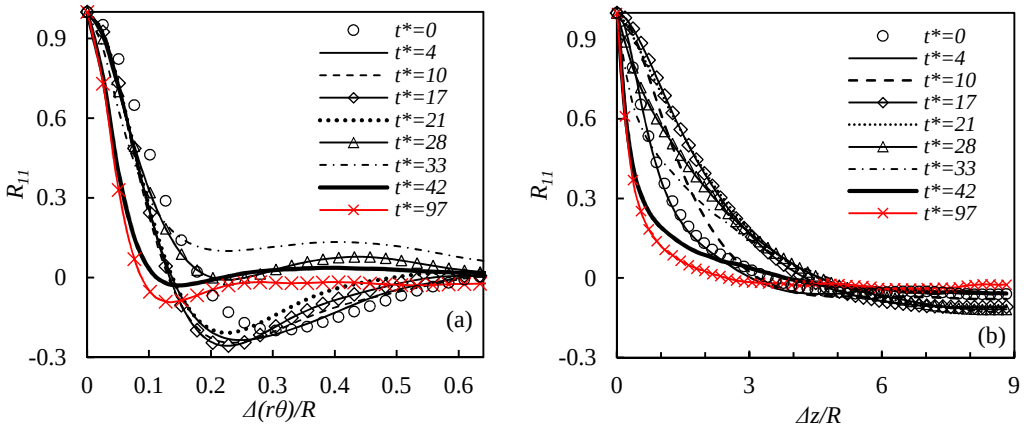

Figure 4.5: Spanwise (a) and streamwise (b) correlations of the streamwise fluctuation velocity at y^{+0} =5.4.

It is seen that the magnitude of the negative value of the spanwise correlation increases slightly first and then remains largely unchanged during the early pre-transitional stage (t^*=4 to 17). The minimum values of the pipe flow at onset of transition are -0.21, whereas those for channel and boundary layer flow are -0.3, and -0.35 respectively (HS2013). The distance at which the minimum R_{11} occurs decreases from the highest value ~0.3R (~50$\frac{\nu}{u_{\tau 0}}$) rapidly to a minimum ~0.23R (~70$\frac{\nu}{u_{\tau}}$, or ~41$\frac{\nu}{u_{\tau 0}}$) at pre-transition stage and it reduces to a value ~0.12R (~50$\frac{\nu}{u_{\tau}}$, or ~122$\frac{\nu}{u_{\tau 0}}$) at final steady stage. The averaged spanwise spacing of the streaks at the onset of transition is therefore approximately 0.46R (~140$\frac{\nu}{u_{\tau 0}}$), which is about twice the boundary thickness (based on $\bar{u}/\bar{u}_c$) and is different from the typical steady flow value of 0.6R (~100$\frac{\nu}{u_{\tau}}$). The growth of the streaks in streamwise can be observed from Figure 4.6(b). The length of the streaks grows from ~3.5R (or ~630$\frac{\nu}{u_{\tau 0}}$) to ~4.5R (or ~1350$\frac{\nu}{u_{\tau}}$) at t^*=21, showing the elongation of the streaks during the pre-transition period. It reduces to ~2.4R (or ~1000$\frac{\nu}{u_{\tau}}$) at the final

stage (t^*=97), commensurate with the features of steady turbulent flow at higher Reynolds number.

Figure 4.6 shows the contours of the wall-normal velocity and iso-surface of spanwise vorticity (in red). It is used to show the development of turbulent spots. During the pre-transition stage (t^*=0~21), the vorticity reduces significantly due to a 'sheltering' effect (Jacobs & Durbin 2001). At t^*=21, some new stronger turbulent spots are observed to appear. These spotty structures then grow in both streamwise and spanwise direction. They connect with each other at t^* =35.

Figure 4.7 furtherly shows the turbulent spot in *z*-*r* plane at several instants by velocity vector. The background is contoured by spanwise vorticity, which is helpful in identifying the turbulent spots. For clarity, a part of the flow domain is selected, i.e., *z*/*R*=10 to *z*/*R*=17.5. In the initial flow (t^*=0), some backward jets are observed in the near wall region of the pipe flow. This is due to the presence of low speed streaks. By contrast, the observed forward jets are weaker. At the interface of backward and forward jets, there are sparse spanwise vorticity. In a short time after the flow rate is changed, at t^*=4, no obvious change is observed. At t^*=14, there are regions where the backward jets are strong and organized. The length of the vectors grows (*z*/*R*=16-17.5), indicating the growth of the amplitude of the low speed streaks. At the onset of transition (t^*=21), very strong backward jets accompanying a local turbulent spot are observed at *z*/*R*=15.8-16.8. High speed fluid is ejected into the free stream (a blue line in the panel is used to show the boundary layer identified by δ_{99} based on $\hat{u}$). At t^*=42, a vorticity forest is formed and developing into the centre region of the pipe. The chaotic vectors here also show that the flow is fully turbulent.

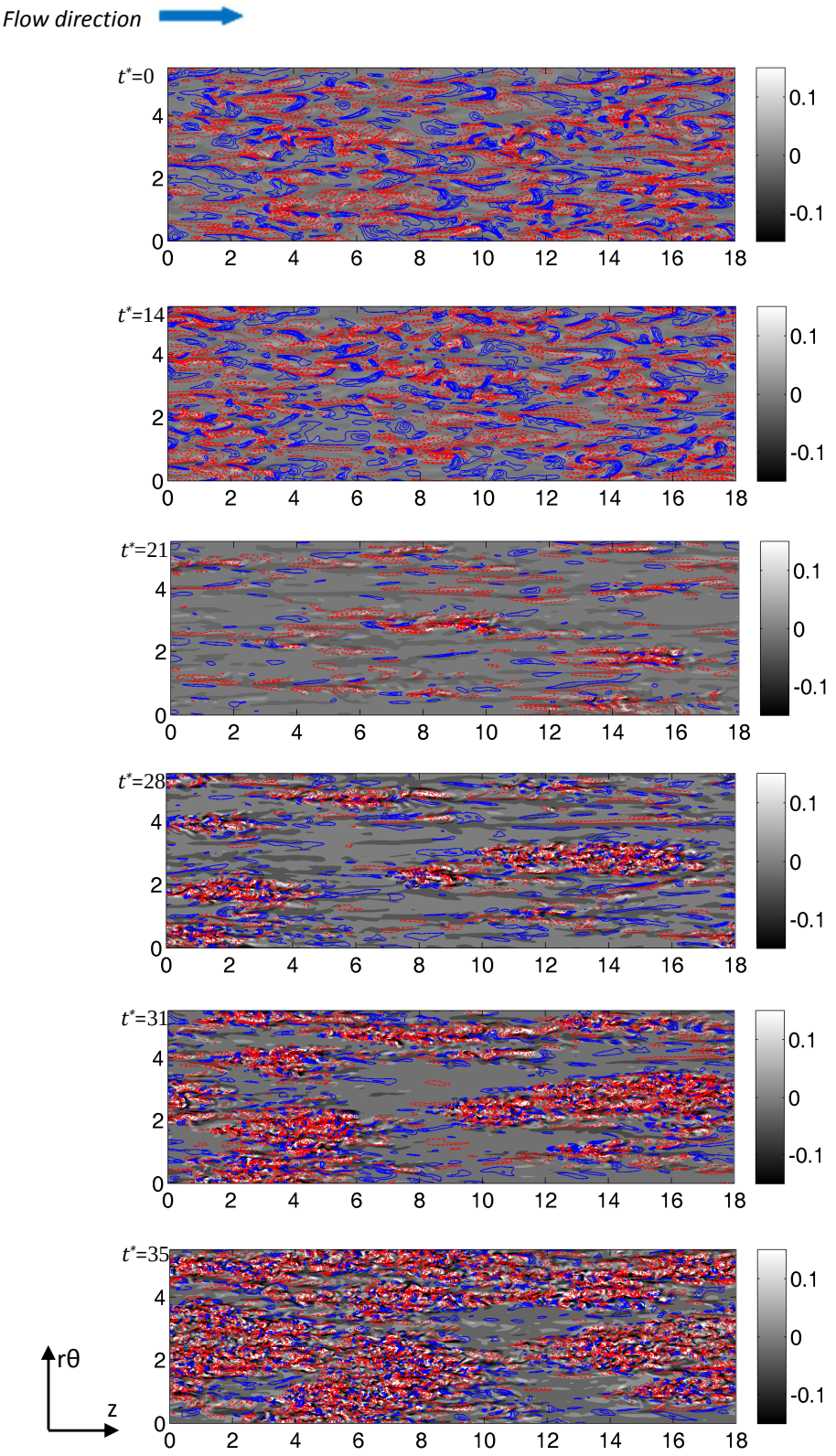

Figure 4.6: The contour of wall-normal velocity(black and white) and spanwise vorticity in z-θ plane (red, negative, $[-\omega'_{\theta,rms,max}, 0]$; blue, positive, $[0, \omega'_{\theta,rms,max}]$, y^{+0}=15).

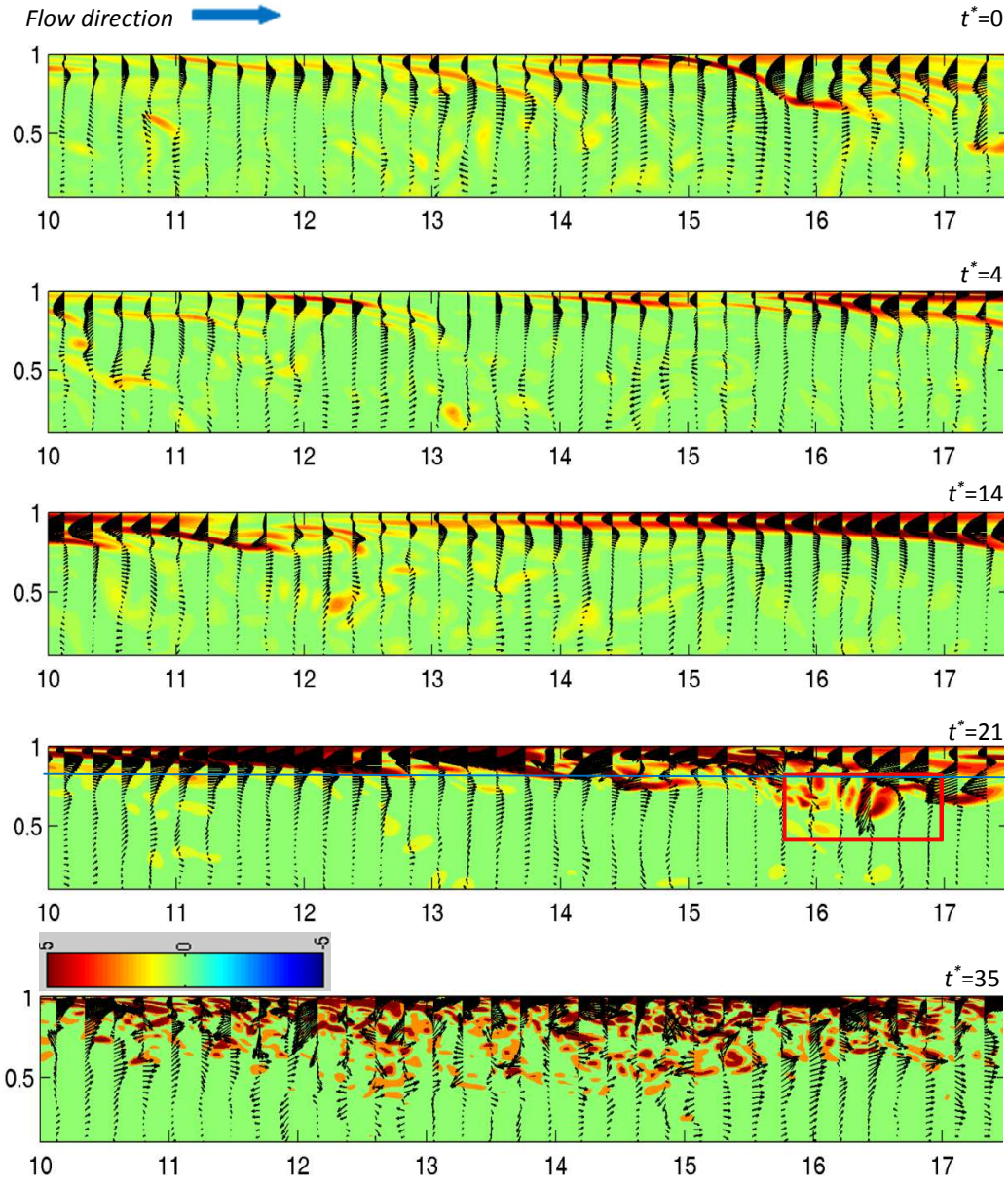

Figure 4.7: Vector and the contour of spanwise vorticity in *z*-*r* plane (θ/R=0.58π).

The above flow visualization shows that during the early stage of the pre-transition period the amplitude of the smaller scale structures (vortices) reduces but the amplitude of large scale structure (streaks) increases. It is interesting to know how the energy of turbulent structure with various scales grows. Figure 4.8 shows the response of pre-multiplied energy spectrum at locations, y^{+0}=5.4, 17, 54, 110. The Figs.4.8 (a), (c), (e)

and (g) are presented in log–linear scales but Figs.4.8 (b), (d), (h), (f) is in log–log scale to facilitate the study of the early responses in the high-wavenumber region.

Following the commencement of the flow transient, the energy spectrum of high wavenumbers ($k_z{}^{+0}$ >0.025) of the streamwise $k_z{}^{0}E_{uu}/u_{\tau 0}{}^{2}$ reduces rapidly reaching a minimum around t^*=4 and remains unchanged till t^*=12.5 at all locations shown. The low wavenumber region ($k_z{}^{+0}$ <0.005) at y^{+0}=5.4 and 17 shows a several times increase in energy. Closer to the centre of the pipe (y^{+0}=54~110), then energy does not change significantly during this period. The increase response of the large scales is observed at t^*=4, 8, 21 and 35 for these locations. It seems that small scale motions show a delay in energy increase. At the centre region y^{+0}=110, the energy increase of small scales starts after t^*=28. As getting closer to the wall, this time decrease to t^*=21 and even early. After the onset of the transition, in the low-wavenumber region of y^{+0} =5.4 and 17, the energy increases till t^*=35, 24 and remains largely unchanged until towards the end of the transition, when it drops to a typical shape for a turbulent flow. At y^{+0} =54 and 110, the energy spectrum shape doesn't change much till the end of the transition.

The changes in energy spectrum further confirms that the energy of the large structures immediately increases near wall after the start of the transient and the typical streaks continue to grow during the early stages of the pre-transitional stage, reaching saturation around the onset of the transition. The energy reduction of large scale motions towards the end of the transition can be interpreted as the breaking up of the elongated streaks. The small turbulent structures are suppressed at the beginning of the flow transient and remains unchanged until the onset of transition which seems to be consistent with the well-established observation of a shear sheltering effect in boundary layer transition, namely, the high-frequency FST can be effectively sheltered by the boundary

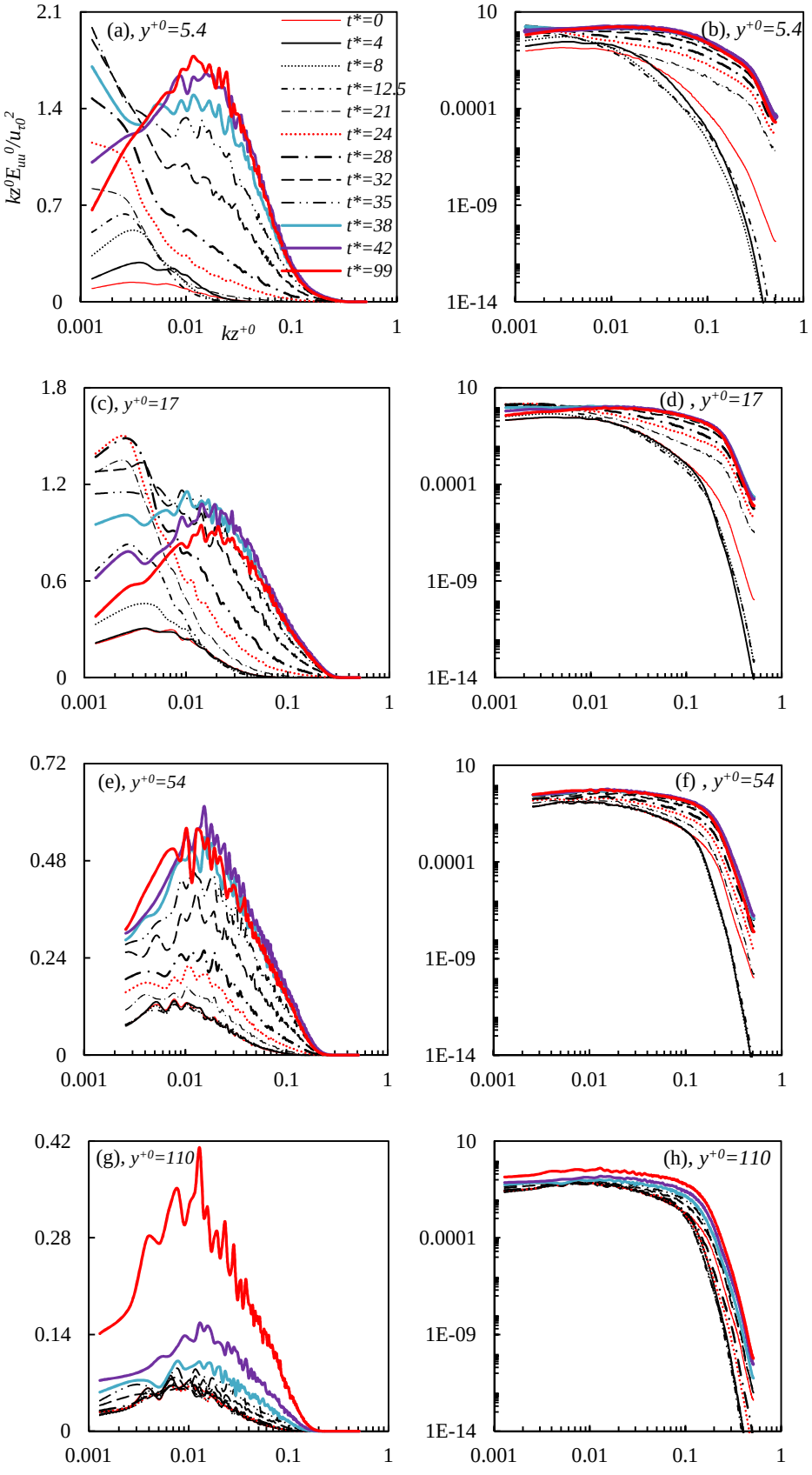

Figure 4.8: The response of energy spectrum at different locations.

layer and the growth of disturbance is due to the penetration of low-frequency FST (Jacobs & Durbin 2001). The several decades' energy increase of small scales at the near wall locations around t^* ≈21 is related to the generation of turbulent spots. The energy increase of large scales in the centre region is more progressive implies that the turbulence growth at this region is mainly due to a diffusion mechanism.

4.3.3 Mean velocity

Figure 4.9 shows the profiles of the ensemble-averaged mean velocity profiles normalized by $u_\tau(t)$ at several instants. Also shown in the plot are the corresponding values of the channel flow. During the pre-transitional period, after a rapid reduction at the very beginning, the velocity gradually increases with time reaching a maximum around the onset of the transition. During this period, the thickness of the sub-layer increases due to the growth of the boundary layer. During the transition period, the velocity in the core progressively reduces and the profile gradually approaches the typical distribution of a steady flow again. It can be seen that the behaviour of the velocity profiles in the pre-transition stage (Figure 4.9a) is very similar to that in the channel flow. There are however some quantitative differences between the two flows. In the initial steady flow, the velocity profiles in the pipe and channel flows overlap each other in y^+<20, but differ beyond this region. During the pre-transition period, the profiles in the two flows are very similar. In a steady pipe flow, the velocity in the centre region is higher than that in the channel flow. The quantitative differences in the centre region still remain during the pre-transition period. This is due to the fact that both flows respond to the increase of the flow rate as a "plug" flow due to the 'inertia effect', namely, the velocity of the fluid is uniform across any cross-section of the pipe perpendicular to the axis of the pipe, and reduces

rapidly to zero in the vicinity of the wall due to no-slip boundary condition on the wall. The turbulence in centre region is frozen so that the mean velocity profile does not change. During the transition period, the profiles of both the pipe and the channel flows reduce significantly in the log law region during t^*=28.8-34.8. At the end, the main differences between the two profiles are in the wake region.

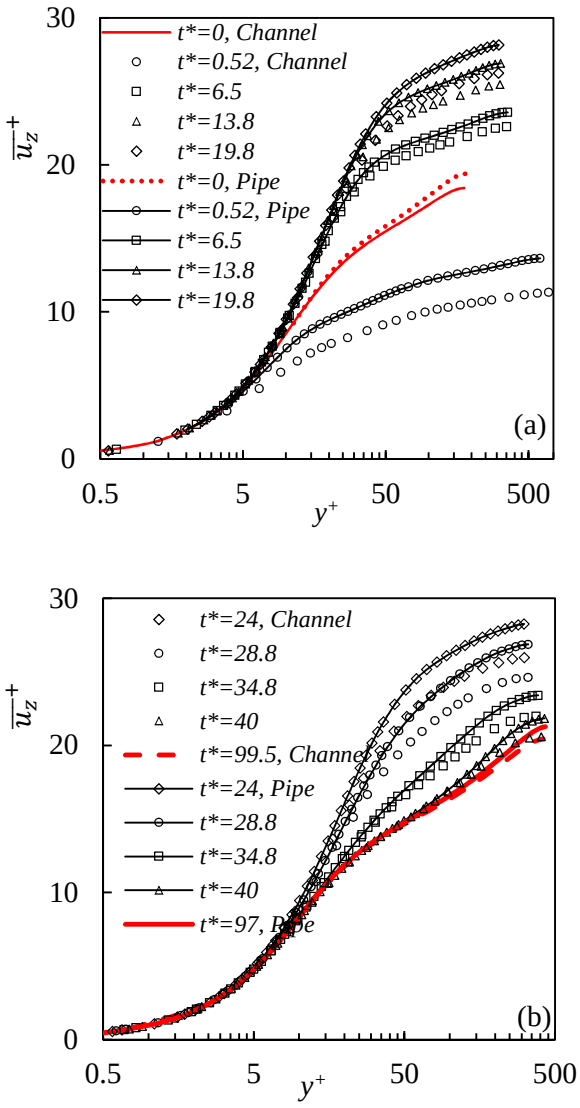

Figure 4.9: Development of ensemble-averaged streamwise mean velocity: (a) pre-transition stage (b) transitional and fully developed stage.

4.3.4 Development of Reynolds stresses

Figure 4.10 shows the development of the ensemble-averaged r.m.s. values of the fluctuating velocities normalized by the final bulk velocity ($u'_{z,rms}/U_{b1}$, $u'_{r,rms}/U_{b1}$, $u'_{\theta,rms}/U_{b1}$), together with the normalized Reynolds stress ($\overline{uv}/{U_{b1}}^2$). The curves with makers are data of a channel flow at corresponding positions. The responses in the wall region (y^{+0}<36) are shown in Figs. 4.10(a) & (c) & (e) and those in the core region are shown in Figs. 4.10 (b) & (d) & (f). It is clear that the response of turbulence is different in the wall and in the core regions. In addition, the response of the streamwise turbulence $u'_{z,rms}$ is characteristically different from those of the other two components. Focusing on the streamwise turbulence first, the values of $u'_{z,rms}$ in the wall region (y^{+0}=8.6, 19.5) increase rapidly with small or no delays until t^*<34, after which they reduce and eventually approach the steady state values. The response of $u'_{z,rms}$ at other locations all have some delays before increasing, the period of which increases with the distance from the wall. In the wall and buffer regions, $u'_{z,rms}$ over-shoots its final steady values at t^*=~30. The responses of $u'_{r,rms}$ and u'_{θ} are similar to each other, but are distinctively different from that of the $u'_{z,rms}$ in the wall and buffer layers (y^{+0}<36). They either reduce then increase slightly or remain more or less unchanged until t^*=~21. They then respond rapidly and reach to their corresponding final steady values (or slightly over-shooting them) just after t^*=~35. In the core region, the response of $u'_{r,rms}$ and $u'_{\theta,rms}$ are similar to that of $u'_{z,rms}$, which show a delay followed by a period of response and the period of the delay is longer as the distance to wall increases. The Reynolds stress in Figs. 4.10(g) & (h) exhibits similar features described for the normal stresses.

The general behaviour of the responses of the various turbulence components is very similar to that observed by He & Jackson (2000) who studied much slower accelerated flows in a pipe experiment, but their measurements were largely limited to the core and the buffer region (up to y^{+0}~17). The turbulence behaviour was explained by relating them to turbulence production, energy redistribution between its components and the radial diffusion. The results in Fig. 8 provide detailed information in the wall region (y^{+0}<36). More importantly, the present results show that the initial response in $u'_{z,rms}$ is due to the formation of elongated streaks which are not conventional turbulence. The rapid increase of $u'_{r,rms}$ and $u'_{\theta,rms}$ at around t^*=~21 is linked to the transition of the flow, from an agitated laminar flow to a turbulent flow. This is to some extend related to the energy redistribution identified by He & Jackson (2000).

Comparing the pipe flow with the channel flow, the overall behaviour identified here is very similar. Especially, in the near wall region, the transient behaviour of $u'_{z,rms}$ is quantitatively similar before t^*<25. However, some notable differences are observed in the centre region. Firstly, $u'_{z,rms}$, $u'_{r,rms}$, $u'_{\theta,rms}$ at y^{+0}=148 increase earlier in pipe flow than in the channel flow. Secondly, the growth rates of $u'_{r,rms}$ and $u'_{\theta,rms}$ are similar before the onset of transition, however they become larger after the onset of transition in the pipe flow. One possible reason for these differences is that the structures are free to grow in spanwise in the channel flow, whereas in the pipe flow, the structures near the core region are constrained in the azimuthal direction. Stronger structure interactions in the pipe core region hence intensify the mixing of the flow, introducing an earlier growth of fluctuation velocities and a higher growth rate.

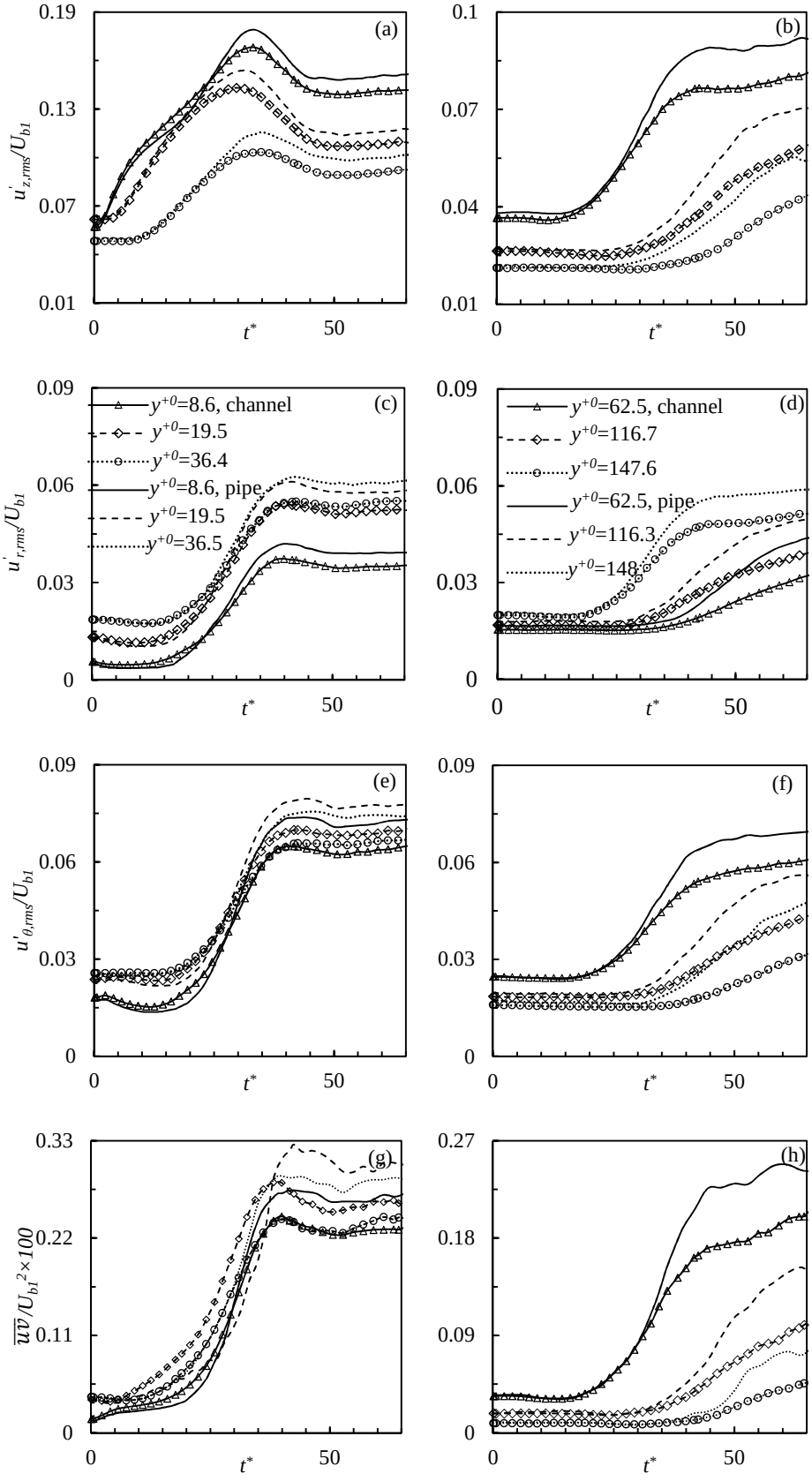

Figure 4.10: Development of the normalized *Reynolds stresses*. (a, c, e, g) near-wall region; (b, d, f, h) core region. Lines: pipe flow, lines with makers: channel flow.

The growth rate of the peak *r.m.s.* of the fluctuating velocity represents the energy growth in the pre-transition stage. Figure 4.11 shows the development of the streamwise fluctuating velocity normalized by its corresponding peak value in pipe flow, against $y/\delta_u{}^*$, where $\delta_u{}^*$ is defined as follows:

$$\bar{u}(r,t^*) = \frac{\overline{u}\,(r,t^*)}{\overline{u_c}(t^*)} \tag{4.8}$$

$$R^2 - (R - \delta_u{}^*)^2 = \int_0^R 2\mathrm{r}(1 - \bar{u}(r,t^*))\,dr \tag{4.9}$$

The position of the peak value moves rapidly outwards at the beginning, then remains almost unchanged at $0.75\delta_u{}^*$during t^*=5-21. It is of interest noting that the location of the peak value of the transient pipe flow is similar to that found for the channel flow, which also remains at $0.75\delta_u{}^*$ unchanged during t^*=5-21. As indicated by HS2013, this behaviour suggests that $u'_{z,rms}$ value varies with the growth of the boundary layer and can be scaled with boundary thickness instead of the inner scaling. This is in fact an important feature of the boundary bypass transition reported (e.g., Cossu *et al*. 2009).

Figs. 4.12(a) & (b) show the growth of square of the peak *r.m.s.* of fluctuating velocities together with the turbulent kinetic energy for both the pipe and channel flows. It is clear that following a short delay, the peak value grows linearly during pre-transition. It is estimated that at the onset of transition, the streak amplitude grows to ~14% of mean flow, which is the same as that of the channel flow (HS2013). The growth rates of the pipe and channel flows are the same before t^*<21. However, after that, and the growth rates of all components are different in the two flows.

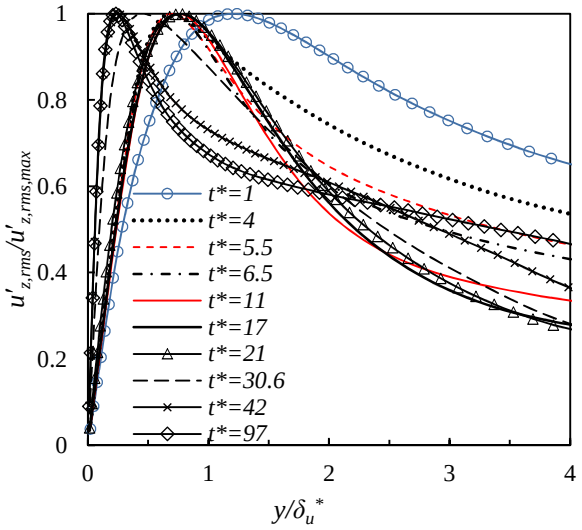

Figure 4.11: Development of u'_{rms} normalized by the peak values.

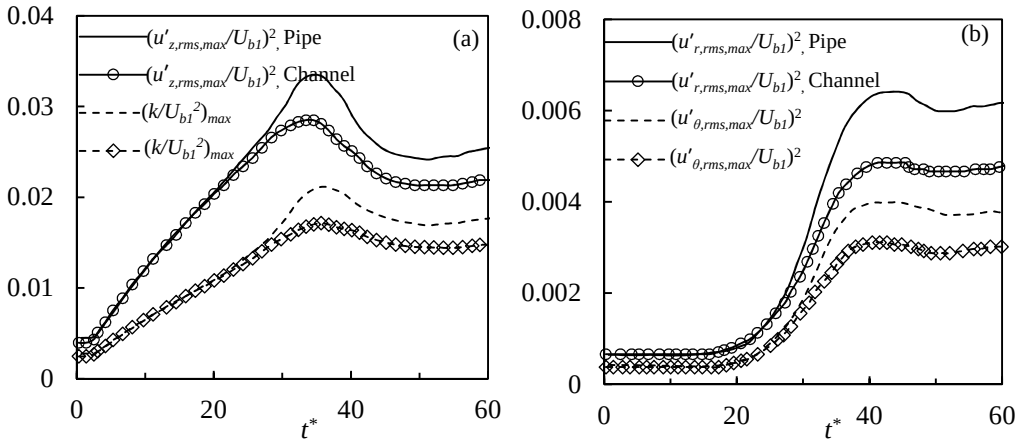

Figure 4.12: History of squared of the peak *r.m.s. fluctuating* velocities.
(a) u'_z and k (b) u'_r and u'_θ.

4.3.5 Turbulent viscosity

Figure 4.13 shows the development of turbulent viscosity calculated from

$$\mu_t = \frac{\rho \overline{u_z u_r}}{d\overline{u_z}/dy} \tag{4.10}$$

The turbulent viscosity reflects turbulent activities and mixing, and a useful parameter in RANS modelling. It can be seen from Figure 4.13(a) that during t^*=0 to 19.5, the value of μ_t/μ in the core region (y^{+0}>60) remains more or less unchanged (except for some fluctuations) but it decreases in the wall region (y^{+0}<60). During the transition period (21<t^*<42), μ_t/μ increases rapidly near the wall (y^{+0}<60), reaching its final steady values towards the end of this period (see Figure 4.13b).

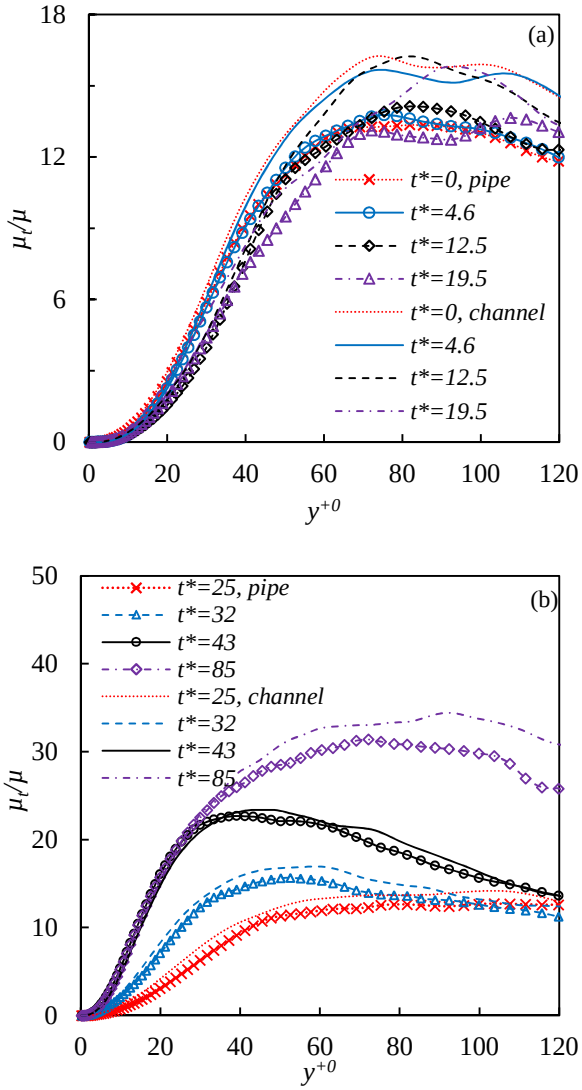

Figure 4.13: Development of turbulent viscosity: (a) Pre-transition stage (b) transition and fully turbulent stages.

The increase of μ_t/μ in the core region is much slower, which continues after the completion of transition (=43). The behaviour of μ_t/μ in the channel is generally the same as that of the pipe flow. The steady state value is slightly lower in the pipe flow than in the channel flow, especially in the centre region (y^{+0}>50). It is interesting to see that this difference in the central region (y^{+0}>50) is reduced during the transition stage (21<t^*<43), but it is regained when the flow is fully developed again. As indicated in section 4.3.5, the growth of turbulent shear stress ($\overline{uv}$) in the central region is different for the two types of flows during the transition stage. The value of $\overline{uv}$ grows faster in the pipe flow at this stage. However, this is not reflected in the turbulent viscosity response, which implies different growth behaviours of velocity gradient in the two flows. This is discussed in the next section.

4.3.6 Vorticity Reynolds number

Gorji *et al.* (2014) showed that the $\gamma - Re_\theta$ transitional model can predict the basic features of a ramp-up flow rather well. However, the predicted onset of the transition in three ramp-up flow cases by this model is noticeably delayed. A key feature of this turbulence model is to make use of the correlation between Re_θ and $Re_{v,\max}$, replacing the former by the latter to trigger the transition. The correlation will be evaluated in this section. The vorticity Reynolds number Re_v was originally defined by van Driest & Blumer (1963) as

$$Re_v = \frac{\rho y^2}{\mu}\frac{d\overline{u_z}}{dy} \tag{4.11}$$

where $\overline{u_z}$ is the local mean velocity. It is known that (Driest & Blumer 1963; Langtry 2006) the maximum value of this local parameter ($Re_{v,\max}$) can be directly linked to the

momentum thickness Reynolds number Re_θ through an empirical correlation. Hence $Re_{v,\max}$ is used in favour of Re_θ to avoid the integration of the boundary layer velocity profile in order to determine the onset of transition in the RANS approaches. In the Blasius boundary layer, the maximum Re_v in the wall-normal direction is proportional to the momentum thickness Reynolds number as $Re_{v,\max}$=2.193Re_θ. For a flat plate boundary layer flow, it is shown that the constant in the correlation is affected by pressure gradient. The error is less than 10% when the flow is subjected to a pressure gradient which causes a variation of the shape factor between 2.3-2.9 (Langtry 2006).

Figs. 4.14(a) and (b) show the developments of the vorticity Reynolds number (Re_v) in the channel and pipe flows respectively. The calculation of Re_v is based on local mean velocity. It is shown in Figure 4.14 (a) that this local parameter increases quickly near the wall (y/R<0.4), forming a local peak. Another peak is observed at the centre, however, it does not respond to the flow rate change. This is consistent with earlier observations that there are no structural changes in central region. Figure 4.14(b) shows that Re_v in the centre (y/R >0.4) increases quickly during the transition stage, whereas Re_v near the wall starts to decrease. In Figure 4.14(c), the development of peak Re_v against the Re_θ in pipe flow is shown, where Re_θ is calculated from the local mean velocity. It is found that the relationship between Re_v, max and Re_θ is not linear. The values of Re_θ and $Re_{v,max}$ at the onset of transition are 395 and 281, respectively.

Let us now consider the differential velocity ($\bar{u}^\wedge$ defined in section 4.3.1). The correlations between $Re_{v,max}(\bar{u}^\wedge)$ and $Re_\theta(\bar{u}^\wedge)$, which are calculated from the differential velocity for both the pipe and channel flows. Figure 4.14(d) shows that the near wall peaks, $Re_{v,max}$ of the pipe and channel flows both increase linearly with the Re_θ for t^*<14. After that, $Re_{v,max}$ in the pipe flow increases slightly slower than Re_θ until

t^*=19.8. In the transitional stage, $Re_{v,max}$ increases significantly slower than Re_θ. It shows that there is a linear relationship between Re_θ and $Re_{v,max}$ at the pre-transition stage if these parameters are calculated from the differential mean velocity.

The linear correlation between the $Re_{v,max}$ and Re_θ in the transient pipe and channel flows are respectively as:

$$Re_{v,max} = 0.99Re_\theta \tag{4.12}$$

$$Re_{v,max} = 0.62Re_\theta \tag{4.13}$$

The differences between the actual momentum thickness Reynolds number and the prediction of equations are less than 22% and 14% respectively for the two equations during the pre-transition region (t^*=0-19.8).

As shown in §4.3.1, the growth of Re_θ is the same in the channel and pipe flows during pre-transition. The difference between the $Re_{v,max}$-Re_θ correlation in the two flows is therefore attributed to the different growth rates of the vorticity Reynolds number, which are in turn due to the different growths of the velocity gradient in these flows. Initially (t^*=0 to 14), the growth of the velocity gradient of the pipe flow is faster than that of channel flow, but later (t^*=14 to 19.8), the growth of velocity gradient of pipe flow slows down dramatically, contrasting to the steady growth of the velocity gradient in channel flow. Consequently, the $Re_{v,max}$-Re_θ correlation is geometry dependent. This may have some implications when the models developed based on the boundary layer correlation are directly used for a channel, pipe or other internal flows. Further studies are required to develop a better understanding.

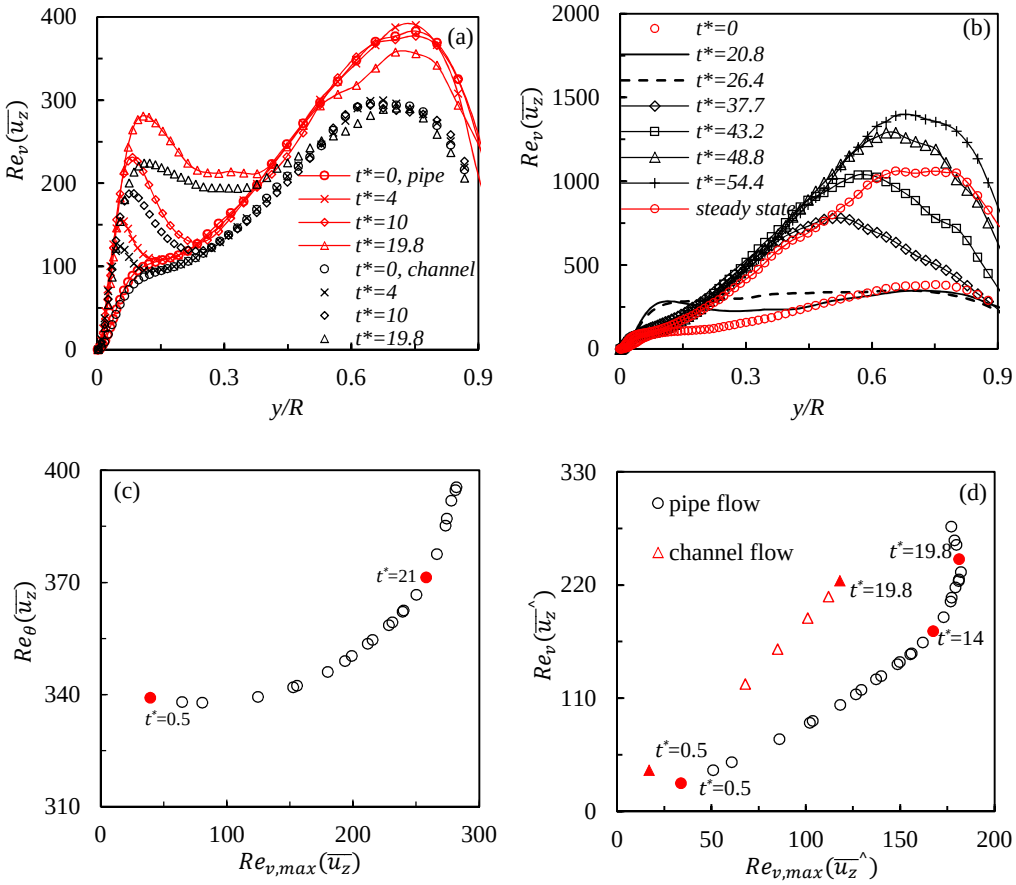

Figure 4.14: Development of vorticity Reynolds number (Re_v).
(a) pre-transition; (b) transition and fully turbulent stages; (c) Relationship between $Re_{v,\max}$ and Re_θ at pre-transition stage (based on local mean velocity); (d) Relationship between $Re_{v,\max}$ and Re_θ at pre-transition stage (based on differential mean velocity). Lines with makers: pipe flow; makers: channel flow.

4.3.7 Budget terms

In this section, we present the variations of the budget terms of $\overline{u'_z u'_z}$ during the transition period. The transport equation of $\overline{u'_z u'_z}$ in a cylindrical coordinate system is as follows:

$$\frac{\partial \overline{u_z'}^2}{\partial t} = -2\overline{u_r' u_z'}\frac{\partial \overline{u_z}}{\partial r} + 2\overline{p'\frac{\partial u_z'}{\partial z}} - 2\overline{\frac{\partial p' u_z'}{\partial z}} - \frac{2}{Re}\left[\overline{\left(\frac{\partial u_z'}{\partial z}\right)^2} + \overline{\left(\frac{\partial u_z'}{\partial r}\right)^2} + \frac{1}{r^2}\overline{\left(\frac{\partial u_z'}{\partial \theta}\right)^2}\right]$$
$$-\frac{1}{r}\frac{\partial r\overline{u_r' u_z'^2}}{\partial r} + \frac{1}{Re}\left[\frac{1}{r}\frac{\partial}{\partial r}\left(r\frac{\overline{u_z'^2}}{\partial r}\right)\right] \quad (4.14)$$

On the right hand side of the equation, the terms from left to right are production, pressure strain, pressure diffusion, dissipation rate, turbulent transport and viscous diffusion, respectively. The pressure diffusion term is 0, which is not studied in the following section. The term on the left is the temporal variation terms, which is less than 10% during the pre-transition stage (not shown).

Figure 4.15 shows the budget terms of $\overline{u'_z u'_z}$ normalized with ${u_\tau}^4/\nu$ at t^*=5.6, 11, 20, 25, 33, 42. The budget terms of the final steady flow (t^*=97) are shown for comparison. Since the data is normalized using the ensemble-averaged friction velocity at the corresponding t^*, the absolute variations during the transitional period cannot be shown. Instead, they show how the distributions deviate from those of a fully developed flow. At the beginning of the transient (t^*=5.6), the budget terms are very low compared to the final flow results. This is due to the rapid increase of the wall shear stress.

There are characteristic differences between the budget distributions in the transient flow and in a steady turbulent wall shear flow. Firstly, the location of the peak production moves from y^+=10 in steady flow to y^+=20. Secondly, the dissipation term remains rather uniform in the wall region (say, y^+<20), whereas a typical feature of the wall shear flow is that the dissipation increases as the wall is approached. Thirdly, as noted before, the pressure–strain term remains very low compared to the production term, which implies that little energy is supplied to u_r and u_θ components. These features of the budget terms are related to the fact that the "turbulence" generated during the pre-

transition stage is not conventional turbulence, but due to the elongated streaky structures (t^*<20).

Figure 4.15(f) shows the response of the production (*P*), pressure strain (*Π*) and dissipation (ε) terms integrated over y^{+0}≈0~50 and y^{+0}≈50~100 respectively. All three terms are normalized with $Ru_{\tau 0}{}^4/\nu$ to show the absolute value of the development of these terms in the two regions. During the pre-transition period (t^*<21), the pressure strain term remains unchanged in both regions. The production and dissipation terms grow steadily in the near wall region, but no significant changes are observed in central region. The production term is mainly balanced by the dissipation term at pre-transition stage in the near wall region, whereas it is balanced by both the pressure strain term and dissipation term in the central region. The values of the three terms in centre region are multiplied by 7 for clearer display.

The growths of the budget terms in the near wall region during the early period (t^*<20) are not associated with conventional turbulence, but a reflection of the streaks developed in the region of y^{+0}≈0~50. Later during the transition period (t^*=21~40), the growth rates of the three terms increase significantly in the near wall region. In the centre region, the growths of these terms are delayed until t^*=30 when the pressure strain term starts to increase significantly. The dominant terms are still production and dissipation in the region of y^{+0}~0 to 50. However, the pressure strain term increases to a significant level in both the near wall and the central regions. It starts to overtake the dissipation for t^*>40 in the region of y^{+0}~50 to 100, where it redistributes a significant amount of energy from the streamwise component to the other two components. The budget terms reach a peak at t^*≈40, and then they drop to the steady state values at t^*≈44.

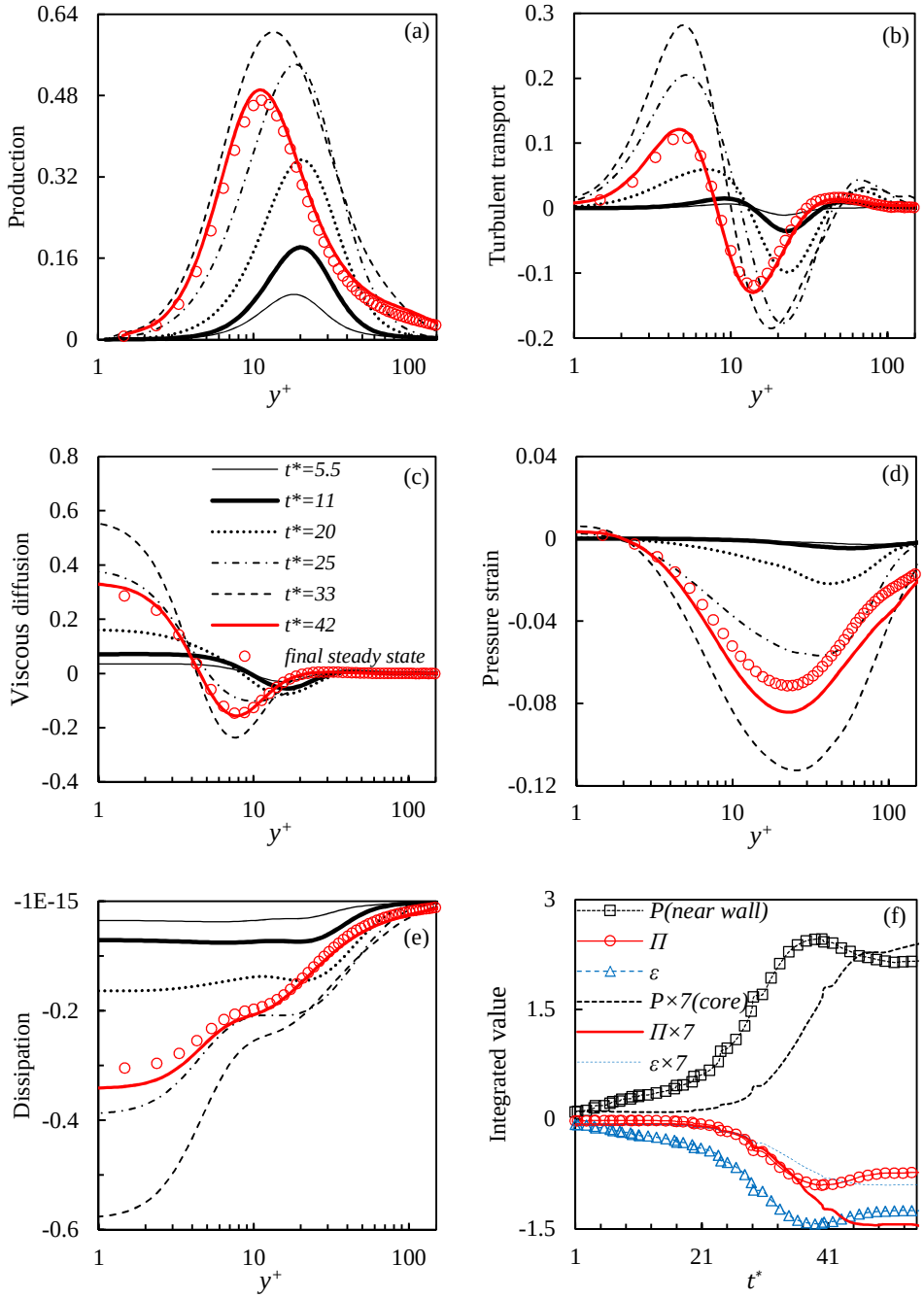

Figure 4.15: Development of budget terms of $\overline{u'_z u'_z}$.

(a) production; (b) turbulence transport; (c) visocus diffusion; (d) pressure strain; (e) disssipation; (f) spatial integration of (a, d, e) in the wall and core regions.

4.3.8 Effect of starting and final Reynolds numbers

The results discussed so far have been for a fixed starting and final Reynolds number. An interesting question to ask is that what will happen if the starting or the final Reynolds numbers are changed. Potentially, the transient process may be affected by a number of factors, including the initial turbulence characteristics (dependent on Re_0), the 'free stream' velocity (dependent on Re_1), the change rate of the mean velocity (dependent on $(U_{b1} - U_{b0})/\Delta t$), and the free stream turbulence level (dependent on Re_0 and Re_1). The rate of change of the mean velocity plays a weak role as long as the acceleration time is much less than the onset time of the transition (HS2013). It was shown that, in a channel flow, the critical Reynolds number $Re_{t,cr}$ (=$t_{cr}{}^{*}Re_1$) is proportional to ${Tu_0}^{-1.71}$, where $t_{cr}{}^{*}$ is the time for the onset of transition, Tu_0 is defined as $(u'_{rms0,max})/U_{b1}$, $u'_{rms0,max}$ is the peak value of the r.m.s. of the streamwise fluctuating velocity of the initial flow. In Fig. 16, the results of 3 cases of pipe flows with the same initial Reynolds number (Re_0=2650) but different final Reynolds numbers (Re_1=3000, 5220, 7362) are plotted against the data obtained from channel flows (He & Seddighi 2015). Those cases are simulated with the same mesh setup described in section 2 for the case (Re=2650-7362).

It can be seen from Figure 4.16 that the critical Reynolds number for the pipe flow collapses extremely well with the correlation of the channel flow. The correlation developed for the channel transient flow, $Re_{t,cr} = 1340{Tu_0}^{-1.71}$, can also be used for the pipe flow. For detailed discussion, the reader is referred to the study on transient channel flow (He & Seddighi 2015).

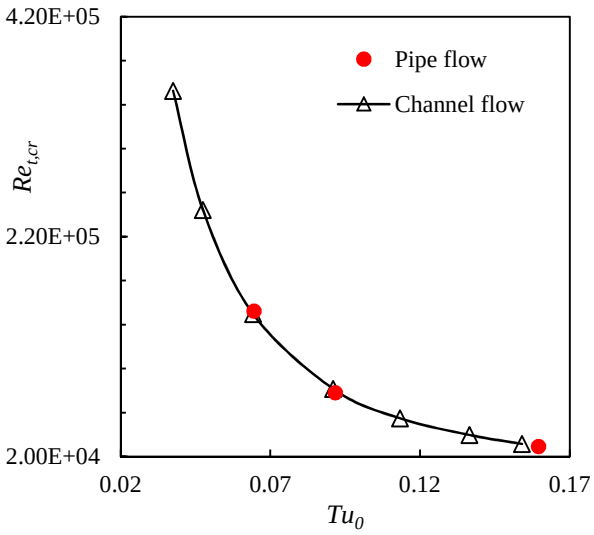

Figure 4.16: Variation of the critical Reynolds number against Tu_0

4.3.9 The effect of acceleration time on the transition

It is shown above that the response of a turbulent flow subjected to a sudden increase in flow rate is a bypass transition process. A question to ask is what will happen if the acceleration is slow, i.e., Δt is large? This question is examined in this section by analysing the results of a series of ramp-up flows with the same initial and final Reynolds numbers but different $\Delta t_{ac.}$ The initial flow and final flow are 2650 and 4770, respectively. The mesh resolution is adjusted to 600×96×240. Other details of these simulations are shown in table 4.2.

To give an impression on how fast the acceleration is in terms of physical time used in experiment, this acceleration time of the test cases are transformed into physical time as 0.13s, 0.63s, 1.25s, 1.95s and 2.5s (the pipe diameter 50.8mm as used in He and Jackson 2000). The fastest acceleration of He & Jackson 2000 was implemented in 2s and it was hard to reduce this acceleration period further due to the limitation of the valve.

Table 4.2 Summary of simulation details

Case	Δt_{ac}	$(\Delta z)_{max0}{}^{+}$	$(\Delta z)_{max1}{}^{+}$	$\Delta(r\theta)_{max0}{}^{+}$	$\Delta(r\theta)_{max1}{}^{+}$	$(\Delta r)_{max0}{}^{+}$	$(\Delta r)_{max1}{}^{+}$	$(\Delta r)_{min0}{}^{+}$	$(\Delta r)_{min1}{}^{+}$
RP1	1	6	10	7.8	4.5	2.2	3.6	0.16	0.23
RP5	5	6	10	7.8	4.5	2.2	3.6	0.16	0.23
RP10	10	6	10	7.8	4.5	2.2	3.6	0.16	0.23
RP15	15	6	10	7.8	4.5	2.2	3.6	0.16	0.23
RP20	20	6	10	7.8	4.5	2.2	3.6	0.16	0.23

($Re_{\tau 0} = 180$, $Re_{\tau 1} = 300$; $Re_{b0} = 2650$, $Re_{b1} = 5300$; $N_z \times N_r \times N_\theta$=600×96×240; Domain: 20R)

The C_f and onset of the transition time are summarized in Figure 4.17(a) and (b). The value of C_f reaches a higher peak but faster in a faster ramp. A clear kink point shows on the C_f curves, which indicates the withdrawing of the applied body force. Before the withdraw of the body force, C_f reduces nearly linearly with time. Without the additional body force, C_f of all cases develops in similar patterns.

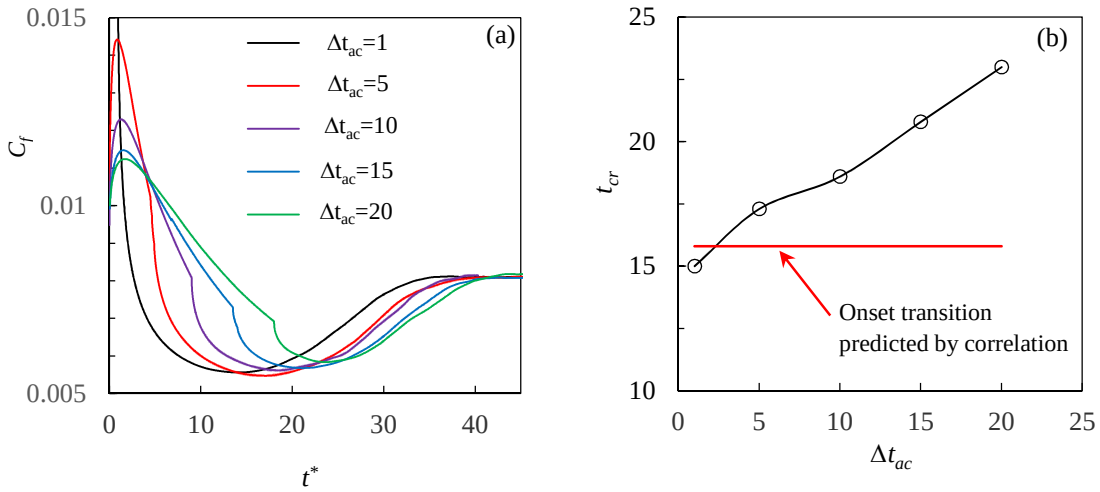

Figure 4.17: The critical transition time againest the accelearation time.
(a): the C_f of differenct flows; (b): the onset of transition time againest accleration time.

The $t_{cr}{}^{*}$ predicted by the formula $t_{cr}{}^{*} = \left(1340Tu_0{}^{-1.71}\right)/Re_1$ is about 16. A larger Δt_{ac} delays the onset of the transition identified by minimum C_f. To $\Delta t_{ac} = 1$, the onset of the transition is converged to the value predicted by the formula. The delay in $t_{cr}{}^{*}$ is not surprising. For a slower ramp, the boundary layer due to the change of flow is established in a slow and gradual manner (Seddighi $et\ al.$ 2014).

The flow structure response of the different cases can be observed in Figure 4.18. In the $RP1$, at t^{*}=10, there is clear low speed and high speed streaks. The low speed streaks and high speed streaks are elongated and grow in size later. To t^{*}=18, large mount vortices show around the streaks. At t^{*}=27, the pipe is full of vortices. This phenomenon is similar in $RP5$ and $RP10$. In slower ramps, $RP15$ and $RP20$, the growth of streaks is not significant and the generation of the new turbulence in the flow is slower.

The spanwise correlation reflects the developing of the streaks. The x-coordinate of minimum peak represents the mean spanwise spacing between streaks, which shows at t^{*}=17 that the streaks spacing are smaller in $RP1$. In other cases, the difference of streaks spacing is not significant. This situation remains to t^{*}=26. The transition is nearly completed at this time in $RP1$, while in other cases the transition is not significant. The y-coordinate of minimum peak represents the strength separation between streaks. It shows that the minimum y coordinate is increased significantly between t^{*}=13.5 to t^{*}=26 in $RP1$, which is associated to the earlier breakdown of streaks. At t^{*}=63, the correlation curves of different cases collapse together, indicating that the transition is finished.

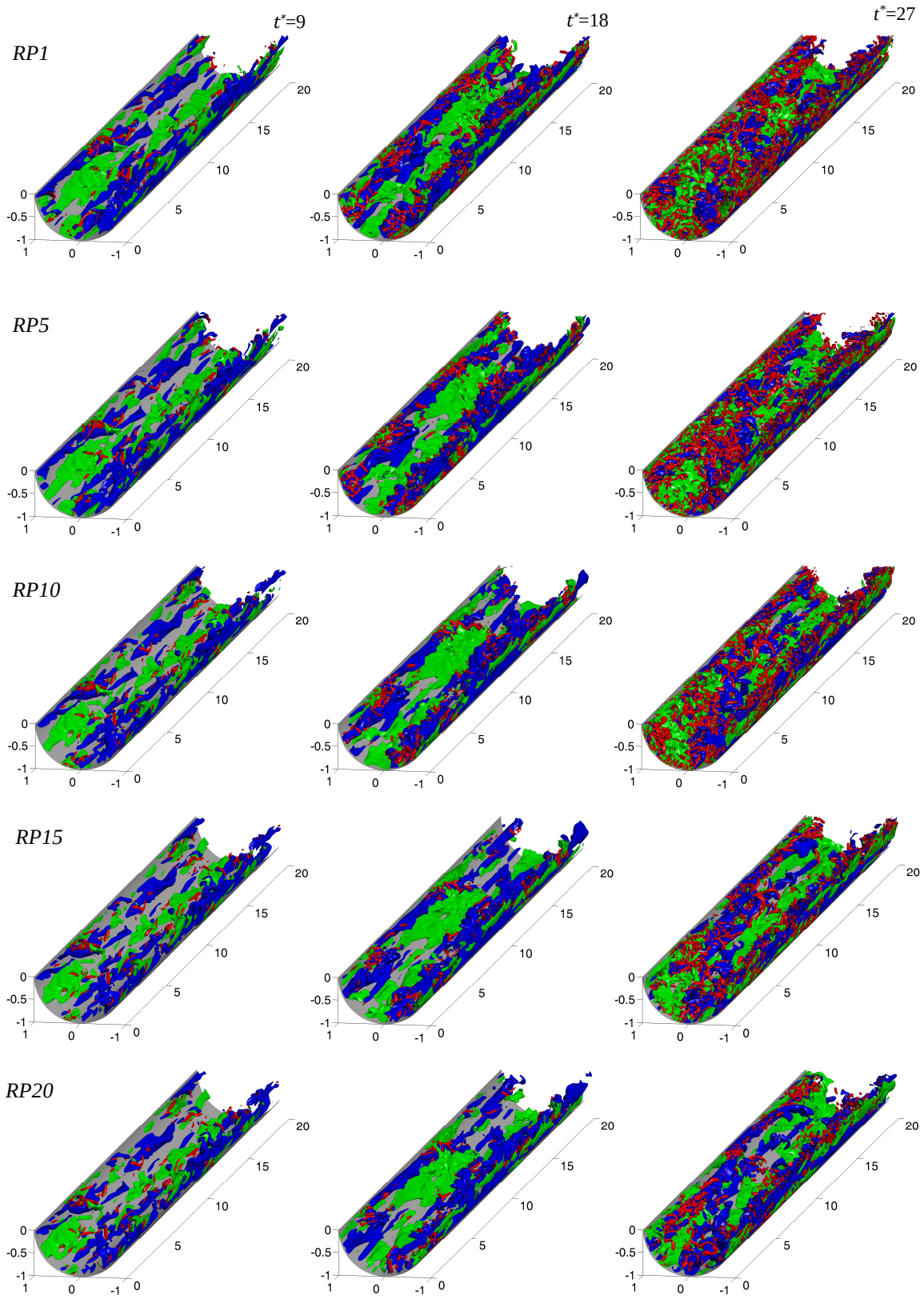

Figure 4.18: Transition scenarios in different cases.

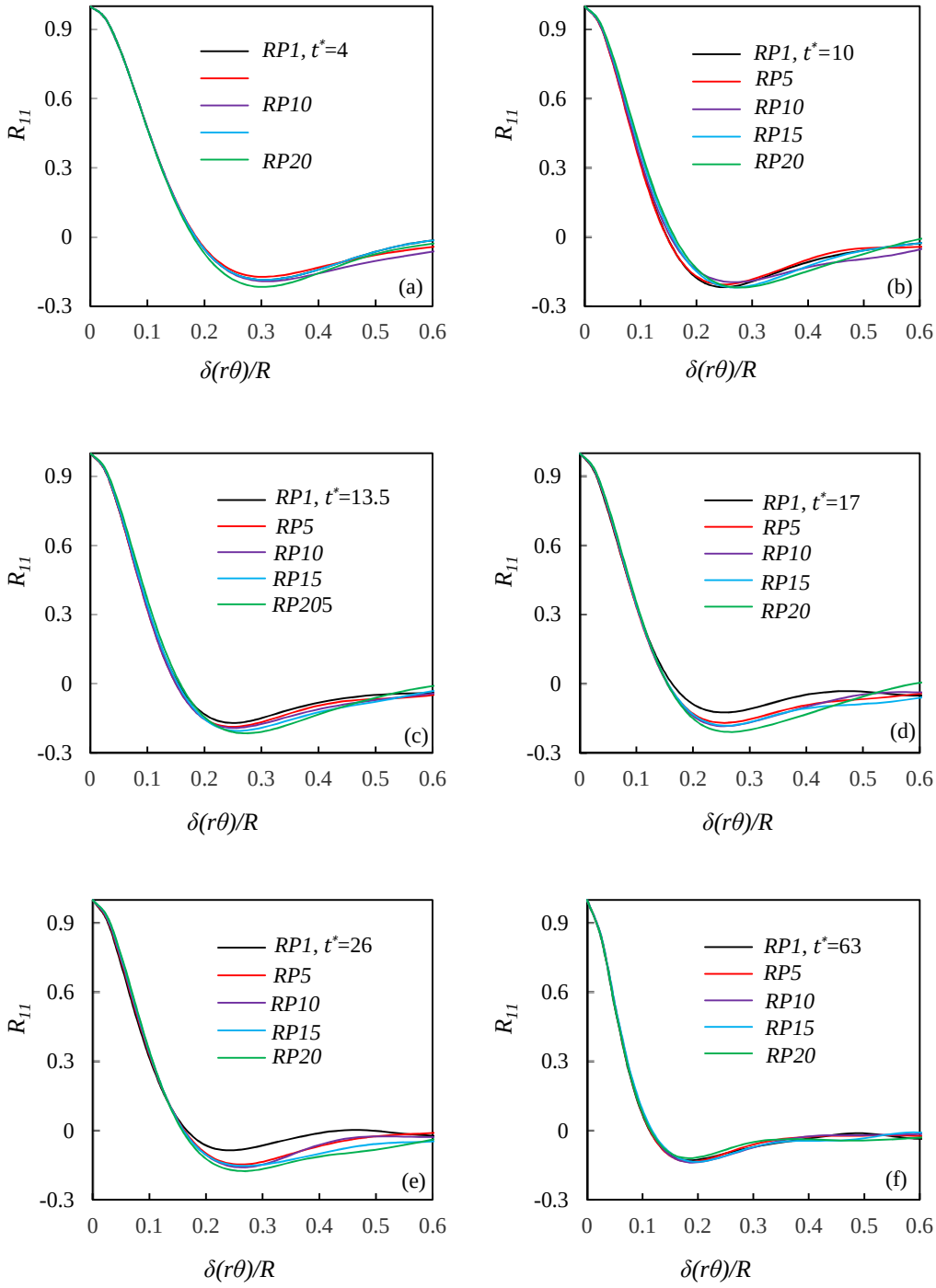

Figure 4.19: The developement of spanwise correlations.

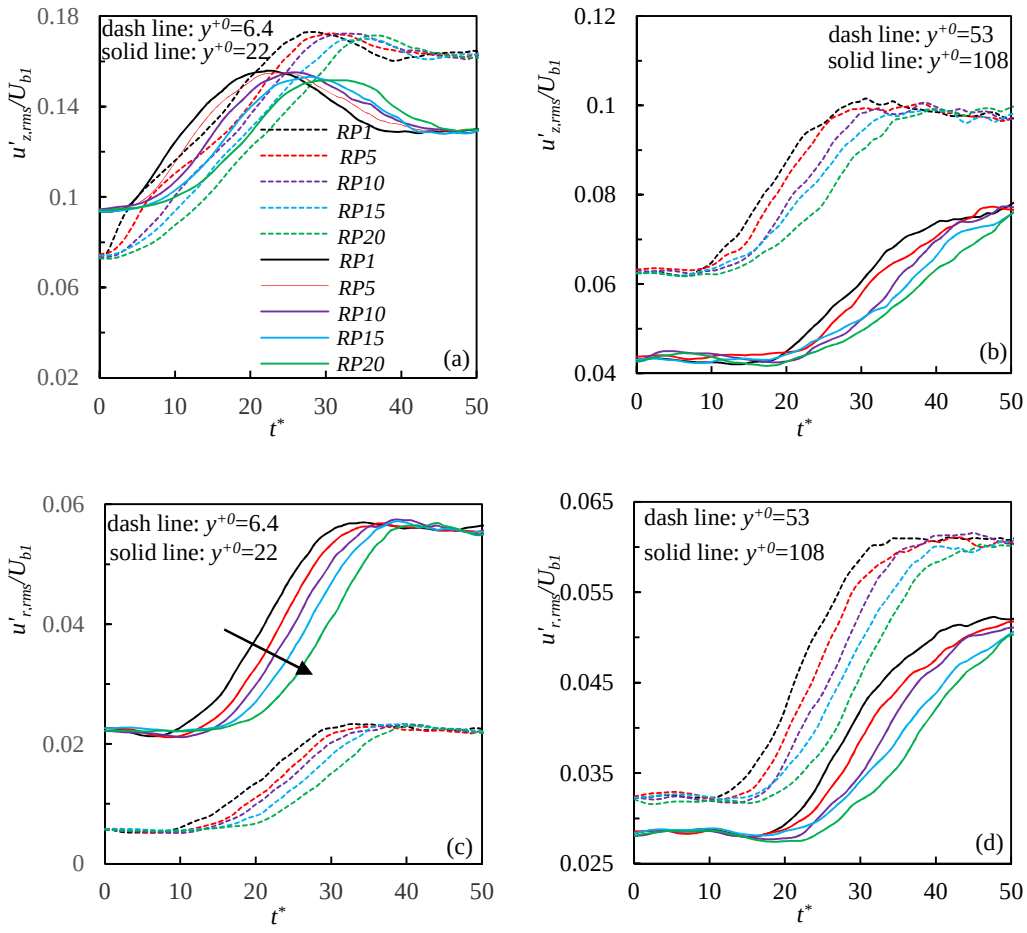

Figure 4.20: Turbulence growth in different cases.

The growth behaviour of turbulence is examined by studying the r.m.s of fluctuating velocities at selected locations in the centre region and the near wall region. It is shown in Figure 4.20 that the growth of $u'_{z,rms}$ is delayed as the observation position moves toward the centre. This phenomenon is found among all cases. The growths of $u'_{z,rms}$ at near wall region are slowed down as the Δt_{ac} increases, which is consistent to the slower growth of streaks in these cases. The delay effect due to slower ramp is decreased as the observation position is close to the centre of the pipe. It is noticed that the maxims of $u'_{z,rms}$ at near wall regions reach a similar level at onsets of transition in different cases. Comparing to the $u'_{z,rms}$, the growth delays of $u'_{r,rms}$ due to increase of Δt_{ac} is more

significant, especially at the near wall region. The slower the ramp is, the later the growth of the $u'_{r,rms}$. Although, there is delay in onset of the growth, the rate of growth in $u'_{r,rms}$ at the near wall region are similar. This phenomenon implies the turbulence generation mechanism in slow ramp is similar to that in fast ramp.

The response of energy spectrum furtherly reveals the flow structure change in different cases. The subplot in Figure 4.21 is used to show the spectrum change in low-wavenumber regions. The steady state spectrum is also included for reference. At t^*<3, the spectrum curves almost collapse. As the t^* increases to t^*=10, the separation of energy spectrum becomes more and more clear. The faster the ramp causes more significant energy growth at low-wave numbers.

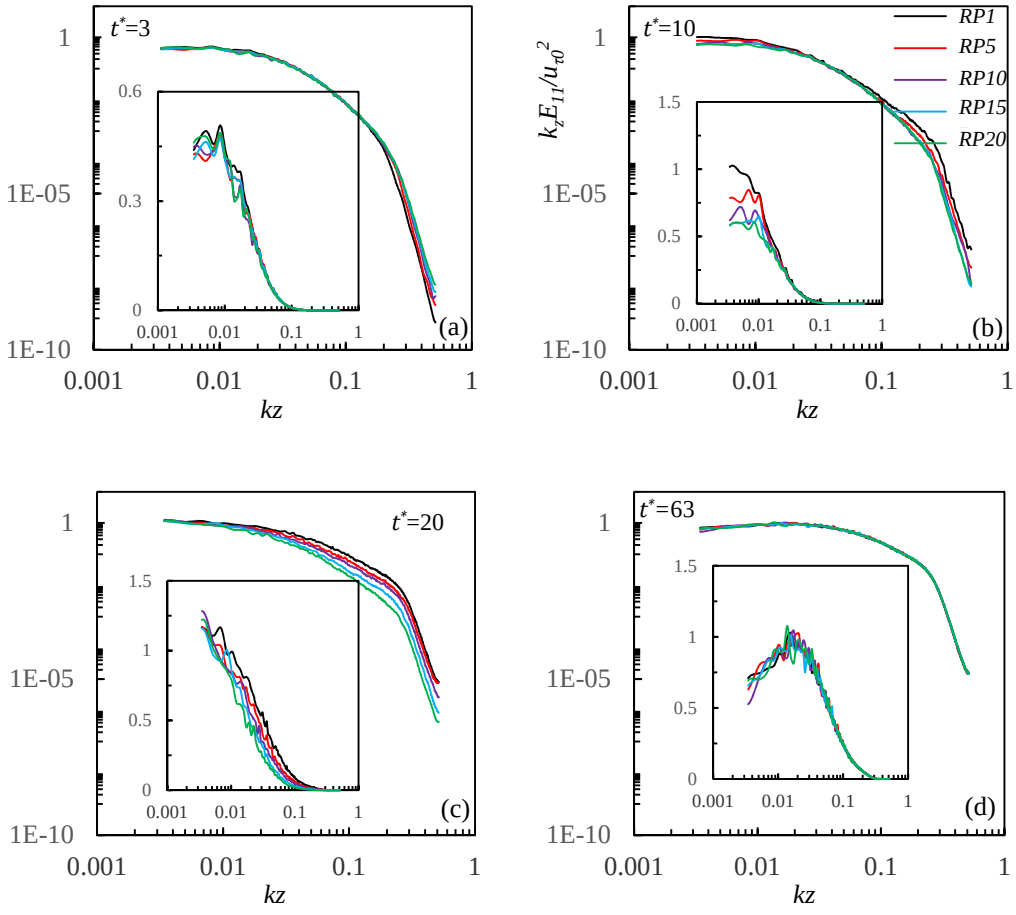

Figure 4.21: The behaviour of energy spectrum in different cases at y^{+0}=15.

The high wavenumber regions, reflecting the response of small scale motions, illustrate energy growth, which increases as Δt_{ac} reduces. The energy in low wavenumber regions starts to reduce at t^*=20 in *RP1*, but in other cases, the energy still grows. The energy spectrums collapse together at t^*=63.

Apart from these turbulence responses, the budget terms' behaviour is important to understand how the turbulence is generated and redistributed. As shown before, there are five terms in the budget of $\overline{u'_z u'_z}$. However, the most important three ones are the production, dissipation and pressure strain terms. Figure 4.22 shows the developments of the three terms at a near wall region (y^{+0}=6.4) and a centre region (y^{+0}=108). The production and dissipation increase immediately after the change of flow rate at the y^{+0}=6.4. The faster acceleration increases the initial growth rate. The growths of pressure strain terms at this region are delayed and the delay is enhanced as the acceleration slow down. In the centre region, all terms start to increase at around t^*=20. The delay effects due to increase of acceleration period are not significant.

As mentioned in section 4.3.8, recent years, turbulence modelling has been developed to a more advanced stage. Some models, like $\gamma - Re_\theta$ transitional modelling, are based on physical transition mechanism, which are believed to be advanced than traditional modelling. However, this modelling is specially designed for the boundary layer flows. The key correlations are mainly obtained from the boundary layer flow data. Its generality in other inner flow should be examined carefully. As shown before, a linear correlation between $Re_{v,max}$ and Re_θ also exist in the transition process of pipe and channel flow, but it depends on the definition of Re_θ and $Re_{v,max}$. Only the definition based on differential velocity shows linear correlation between the two parameters.

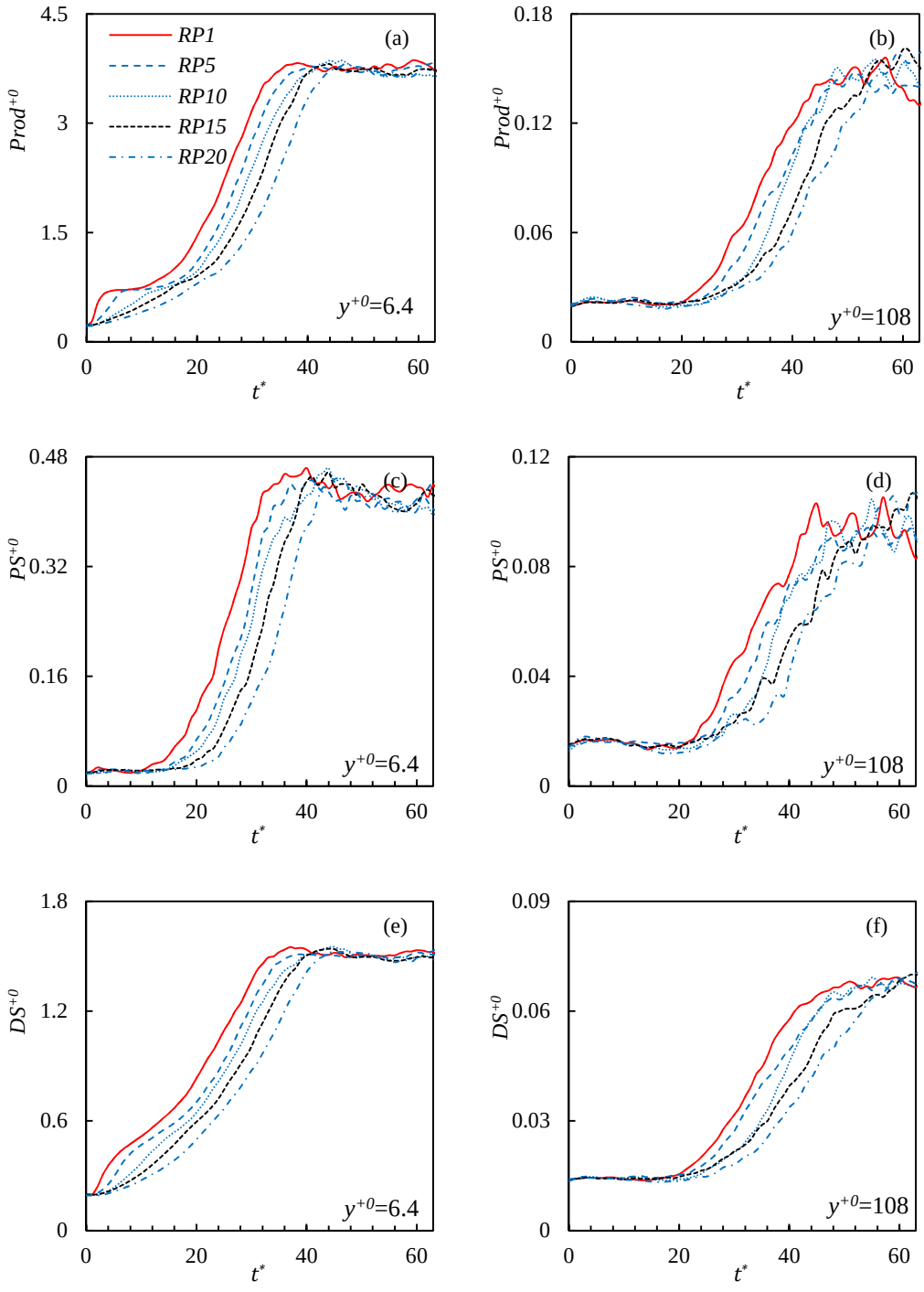

Figure 4.22: The growth of production, pressure strain and dissipation. (a), (c), (e): Production, Pressure strain, Dissipation at y^{+0}=6.4; (b), (d), (f): Production, Pressure strain, Dissipation at y^{+0}=108.

It is worth to check how this linear relationship affected by the slower implemented

accelerations. In Figure 4.23, the data of $RP1$, $RP5$, $RP10$ shows linear or quasi-linear relations. In other two flows, the linear relation is not clear. The length of the linear relation is found different. In $RP1$, this relation breaks at 16.2, which is close to the onset of the transition. Whereas, in $RP5$ and $RP10$, it stops at around t^*=12. After that, the Re_θ starts to decrease but $Re_{v,max}$ remains to grow. The ratio between $Re_{v,max}$ and Re_θ in the linear region of $RP1$, $RP5$ and $RP10$ is found 0.84~0.95. This value is found similar to the step ramp cases (Re_0=2650, Re_1=7362), which shows $Re_{v,max} = 0.99Re_\theta$. As addressed by Langtry (2006), the development of Re_v reflects the growth of disturbance inside the boundary layer. This is confirmed by the observations shown in present study, which shows that, the growth of streaks is stronger in fast ramps than those in slow ramps.

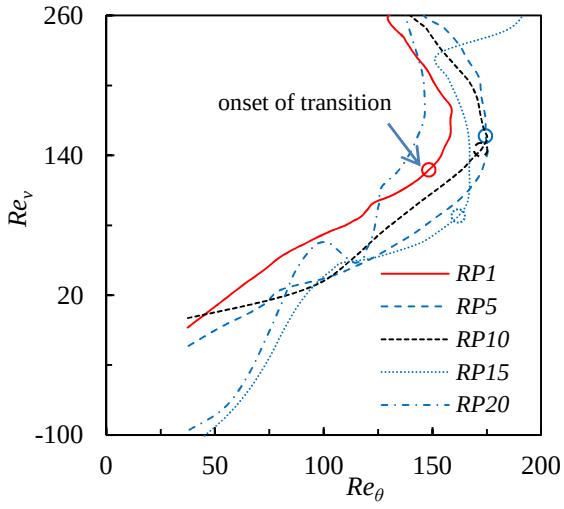

Figure 4.23: The relation of $Re_{v,max}$ and Re_θ in different cases.

4. 4 Conclusions

Through a systematic study on the transient pipe flow subjected to flow rate changes, it is shown that

(1) It is similar to that in a channel, the transient flow in a pipe after a step increase in flow rate is effectively a laminar flow followed by a bypass transition. New turbulence generated through bypass transition mechanisms initially occupies the near wall region; it propagates into the central region following the completion of the transition.

(2) The general trends of the transition in the pipe and channel flows are found to be the same in the near-wall region. The similarities among the two flows are not only in instantaneous flow structures, but also in the ensemble-averaged statistical values. The transition onset prediction formula obtained from channel data works very well for the pipe flow. However, there are detailed differences in the central region between the two flows during the transition stage. The growth of turbulence in the pipe at this stage is faster than that in the channel flow. This is attributed to the stronger mixing effect in the pipe, where the spanwise space becomes narrower as the flow goes closer to the centre.

(3) The developments of the mean velocity profiles, turbulent viscosity, vorticity Reynolds number and budget terms are analyzed. It is found that the growths of the turbulent viscosity and the vorticity Reynolds number are quantitatively different in the two flows, which are attributed to the differences in the velocity gradient developments. These results may provide useful information for the development of turbulence models.

(4) The typical flow response in a bypass transition is the growth and break down of streaks. It is found this scenario in a slow ramp-up flow is not as significant as in a fast ramp-up flow. However, although there is delay effect, the growth of the statistics is similar, disregarding to the slow or fast imposed accelerations.

(5) During the transitional stage, the linear relation of Re_θ and $Re_{v,max}$ is only observed in the fast ramp-up flow. As the ramp-up process is slowed down, the linear region reduces. The slope of linear region in fast ramp-up cases is found between 0.84 and 0.95, contrasting to a typical slope of boundary layer flow 2.193.

Chapter 5

DNS of Turbulent Pipe Flow with Non-uniform Body Force

5.1 Introduction

Mixed convection heat transfer is frequently encountered in thermal energy systems. One of the important factors that influence the heat transfer in mixed convection is buoyancy. The presence of buoyancy in such flow may enhance turbulence production or suppress it, leading to improved or deteriorated turbulence mixing and heat/mass transfer. Buoyancy affects turbulence through structural or external effects (Petukhov & Polyakov 1988). The former is due to density fluctuations directly contributing to the turbulence production or destruction, which is represented as source terms in the transport equations for turbulent kinetic energy and dissipation in the RANS modelling framework. The external effect is the response of turbulence to the distortion of the mean velocity profile. The effect of the non-uniform body force is the phenomenon that we are concerned in this chapter. For vertical flows, this is one of the dominant mechanisms that govern flow behaviours (Jackson 2006; Jackson 2013).

He (2006) conducted exploratory simulations of idealised flows subjected to a prescribed body force specified in a simple form of linear/stepwise distribution to gain

insights into the common characteristics of turbulence in non-equilibrium flows. The results revealed some promising findings regarding to how turbulence and flow respond to a body force. However, the preliminary study was conducted using Reynolds Averaged Navier-Stokes (RANS) approach and there is inevitable limit on the definitive information provided by RANS on flow physics in a basic research such as this. Indeed, the improvement of the performance of turbulence models for simulating non-equilibrium flows was an important aspect of the initial motivation. In the research described here, we intend to carry out a comprehensive study on the generic 'body force phenomena' by performing numerical experiments using Direct Numerical Simulation (DNS) to improve the understanding of the flow behaviour in such non-equilibrium flows and the inherent connections between them, and to provide new data for the improvement of turbulence models.

5.1.1 The prescription of the body force

In this section, it is intended to identify the forms of 'body forces' in selected non-equilibrium flows and to replace them with idealised body forces with simplified distributions and then to study the flow with such body forces. This comprises three steps: i) Extract the real (buoyancy) and the apparent (inertia) body force from physical flows, namely mixed convection in a vertical pipe flow and unsteady flow in a pipe, to; ii) simulates idealised turbulent shear flows subjected to a prescribed body force representing those obtained from (i); and iii) simulate idealised flows with further simplified body force distributions, namely linear-variation or stepwise-changing body forces.

Previous DNS studies of mixed convection flow provide some useful data for the first step. In the DNS study (You $et\ al.$ 2003; Bea $et\ al.$ 2006) of mixed convection heat transfer in a vertical tube, the non-isothermal flow is simplified by applying Boussinesq approximation, in which all the variations of the thermal properties are ignored except for the buoyancy due to the variation of density caused by temperature change. The ensemble averaged buoyancy distribution depends on local mean density or mean temperature, which varies approximately linearly in the near wall region (You $et\ al.$ 2003; Bea $et\ al.$ 2008). As discussed in Chapter 2, the aiding buoyancy force increases the velocity in a region near the wall but decreases the velocity in other part of the flow due to the conservation of mass. It is useful to observe some qualitative and quantitative features of the buoyancy distribution in some mixed convection flows. Figure 5.1(a) shows the local density distributions in a supercritical fluid with mixed convection, representing the distribution of buoyancy (ρg). At a certain distance from the pipe inlet (x=25), a very thin thermal boundary layer is formed, which causes a sharp decrease in density. The thermal boundary layer develops downstream (x =55), resulting in a more gradual variation of density. Figure 5.1(b) shows the density distribution in a strongly heated air flow (at x/R=49), which is different at different heating conditions. In Figure 5.1(c), the density data of both a supercritical fluid and a normal air flow are plotted. For the flow of supercritical fluid, the density change is very steep in certain regions, whereas the density of the normal air changes linearly in the near wall region. These buoyancy distributions result in a flow acceleration in the region near the wall but a flow deceleration in other regions (compared to the force convection flow). Interestingly, the flow with a temporal acceleration studied in chapter 4, is affected by the inertia change ($\rho \frac{du}{dt}$) during the transition, which can be regarded as a special 'body force'. Figure 5.1(d)

shows such terms at different times. The 'body force' is quite large at the beginning, and it reduces to almost 0 at the end of the transition. In the centre of the pipe, it is positive, which reflects the 'plug-like' acceleration of the core flow. In the wall region, the flow slows down at some times (shown in chapter 4, Figure 4.10).

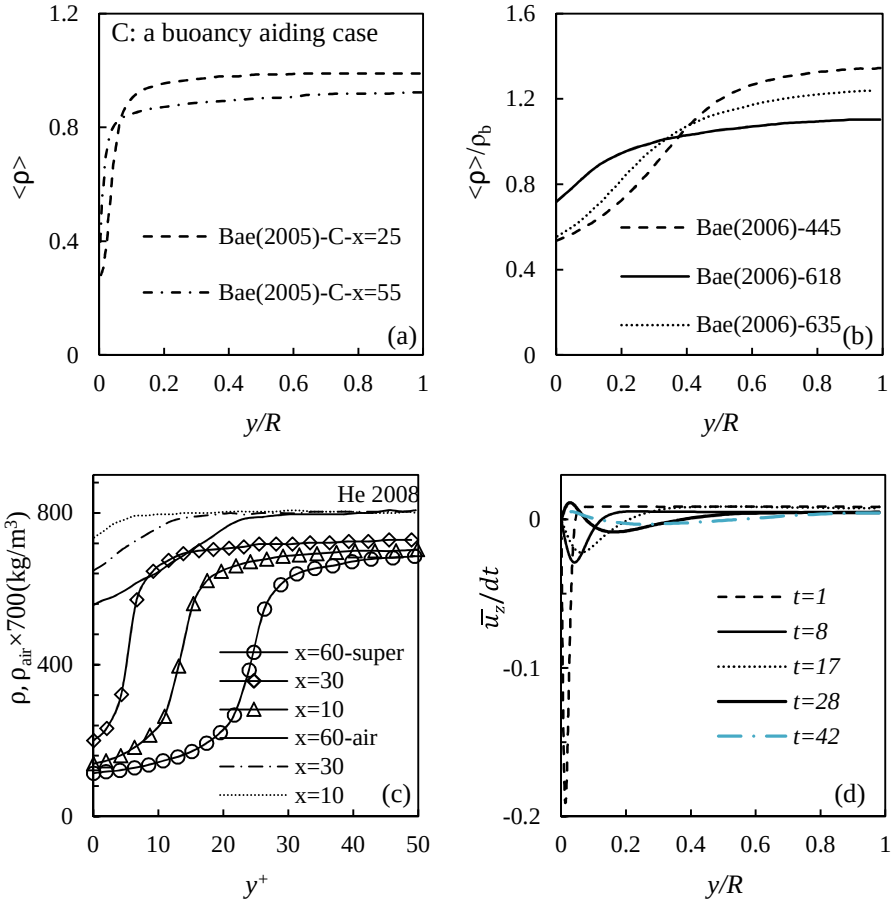

Figure 5.1: The distribution of body force in flows.
of the mean density of (a) Bae *et al*. (2005); (b) Bae *et al*. (2006);
(c) He *et al*. (2008); (d) the inertia term of an acceleration flow (chapter 4).

Above summary of 'body forces' in some physical flows suggests that all of these flows can be represented by turbulent flows with a non-uniform body force, which distorts the mean flow and in turns causes turbulence to change in similar way. The idealized body force distributions are designed to simulate these in Figure 5.1(a), (b), (c), which are further simplified to linear and step change patterns. On the other hand, the total body

force is determined by an integration of the body force over the flow domain ($intbf$), normalized by $\tau_{w0}\pi DL$, that is

$$F = \iiint rbf d\theta dr dz \,/(\tau_{w0}\pi DL) \tag{5.1}$$

where τ_{w0}, D, and L are the shear stress, diameter and the length of pipe, respectively. The total force amplitude F in a real flow mostly depends on parameters, such as Froude number ($1/Fr$, Bae $et\ al.$, 2005). It is evaluated that the amplitude of $1/Fr$ in several DNS studies ranges from 0.003 to 0.081 (0.003-0.015, You $et\ al.$ 2003; 0.027~0.081, Bae $et\ al.$ 2005; 0.01~0.025, Bae $et\ al.$ 2006). Based on the prescribed information, the idealized body force is designed and shown in Figure 5. 2. There are four groups and 22 cases in total. These body forces are parameterized by bf_w (wall amplitude), F (the total force amplitude), body force coverage (y^{+0}, where the body force is positive) and the distribution type of the body force (step or linear). In real flows, the body force is mainly limited to y/R=0~0.5. The coverage of the prescribed body force is limited to this region. In groups A and C, bf_w is fixed but the coverage varies between y^{+0}=15($yv/u_{\tau 0}$, where 0 represents the base flow with $Re_\tau = 180$) and y^{+0}=90. In other regions of the flow, the body force is set to be 0.

Similarly, groups B and D are designed with fixed coverage but different bf_w. The above prescribed body force is added to the right hand side of the streamwise momentum equation (eq.5.2) as a source term throughout the simulation, while the mass flow rate is kept at a prescribed value. The streamwise momentum equation reads:

$$\frac{\partial q_z}{\partial t} + \frac{\partial q_z q_z}{\partial z} + \frac{1}{r}\frac{\partial q_z q_r}{\partial r} + \frac{1}{r^2}\frac{\partial q_z q_\theta}{\partial \theta} = -\frac{\partial p}{\partial z} - \frac{d\bar{P}}{dz} + \frac{1}{Re}\left(\frac{\partial^2 q_z}{\partial z^2} + \frac{1}{r}\frac{\partial}{\partial r}r\frac{\partial q_z}{\partial r} + \frac{1}{r^2}\frac{\partial^2 q_z}{\partial \theta^2}\right) + bf \tag{5.2}$$

where, $bf = bf^* \cdot R^*/(\rho^* * {U_{p0}}^{*2})$ and ${U_{p0}}^*$ is the centre velocity of the laminar flow, where superscript * refers to dimensional parameter and no * is for non-dimensional parameter.

All simulations are conducted on a pipe with a length 20R and the mesh resolution is 600×96×240 (streamwise×wall-normal×spanwise, $z \times r \times \theta$). Other simulation details are summarised in table 5.1. The statistical results are obtained via ensemble averaging in two periodic directions and averaged over 50 independent flow fields after the flow is fully developed.

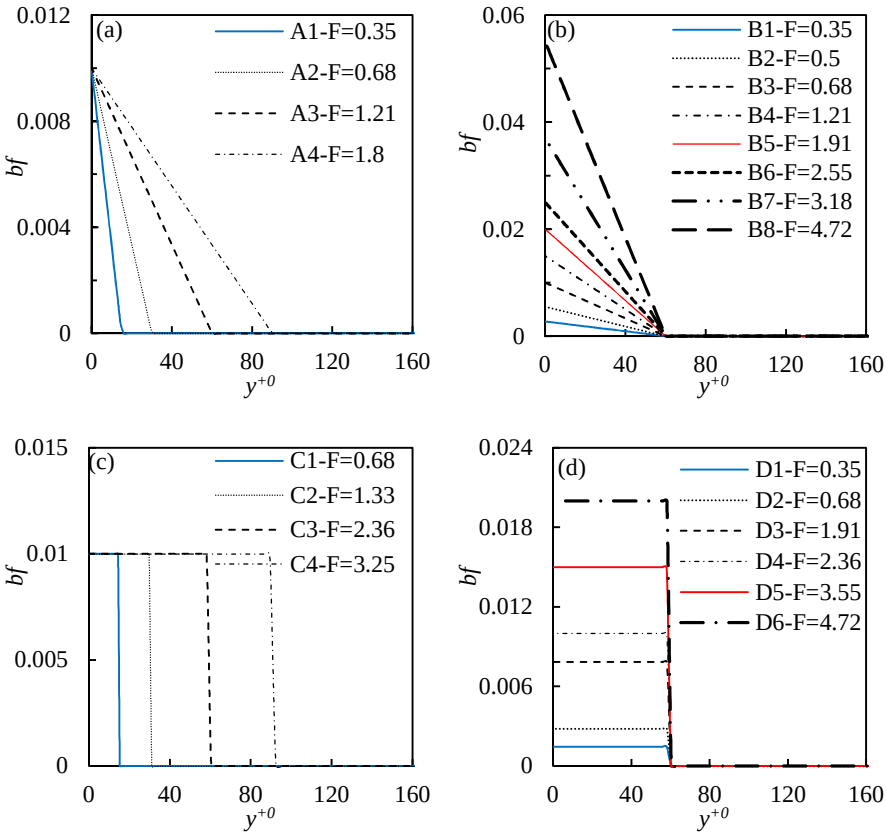

Figure 5.2: The distribution of body force.

Table 5.1 Simulation details

Case	Δz^+	$\Delta(r\theta)_{max}^+$	Δr_{max}^+	Δr_{min}^+	Re_τ	Re_b
Base	6	4.7	3.6	0.14	180	5300
A1~A4	6.2~6.4	4.9~5	3.7~3.9	0.14~0.15	187~193	5300
B1~B8	5.3~9.2	4.1~7.2	3.2~5.5	0.12~0.21	159~276	5300
C1~C4	6.3~6.7	5~5.2	3.8~4	0.15~0.16	191~200	5300
D1~D6	4.8~8.4	3.8~6.5	2.9~5	0.11~0.2	144~231	5300

5.1.2 Turbulent flow with body force abstracted from mixed convection flow

Before we proceed to study the turbulent flow with an idealized body force, it is interesting to check to what extent the turbulent flows with the body force abstracted from some real flow represent original flows. The 3 cases of You *et al*. (2003) are used to do such validation (here after referred to as You1, You2 and You3). The body force extracted from You *et al*. (2003) and similar the corresponding artificial body force used here artificial body force is shown in Figure 5. 3. The body force of You takes a linear form near wall and reduces gradually to zero in the core of the flow contrasts to the sudden change of artificial body force at the out edge of the force coverage. The mean velocity and Reynolds stress results are shown in Figure 5.4. Figures 5.4(a) and (b) show that the simulation results with these extracted body force are very similar to the real flow results. For some cases, like You1, the data of the real flow and the flow with fixed abstracted body force almost completely collapses on top of each other. The small difference between the two flows may be due to the fact that the artificial body force cases neglect the direct effect of buoyancy, which is more significant in strongly laminarized flows. But overall this effect is small. Figure 5.4(c) and (d) shows a comparison of results of

between the flows with linear body force and the three cases of You. These artificial body forces have similar F and body force coverage to that of You's. You1 is slightly laminarized and You2 & You3 are recovery flow. It is shown that although there are detailed differences, the general trend of You's cases are well represented by the flows with linear body force.

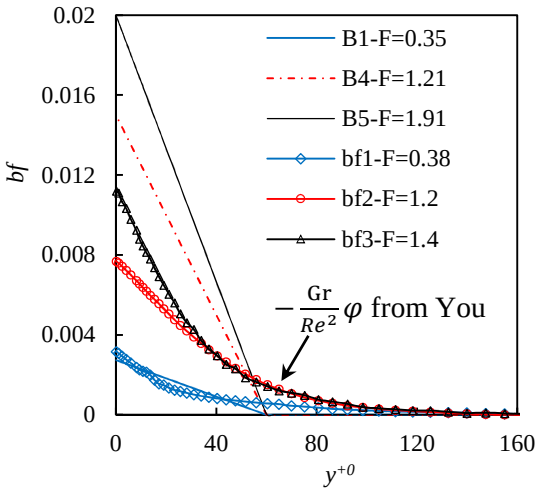

Figure 5.3: The body force of You and three similar artificial body force.

The results in Figure 5.4(a) and (b) illustrate that the effect of non-uniform body force (buoyancy) is the main reason that causes the turbulence and heat transfer deterioration in these flows of You and the direct turbulence production due to buoyancy are small. The comparative study between You's flows and the flows with an artificial body force also demonstrates the possibility to use an artificial body force to study the effect of buoyancy on flow and turbulence.

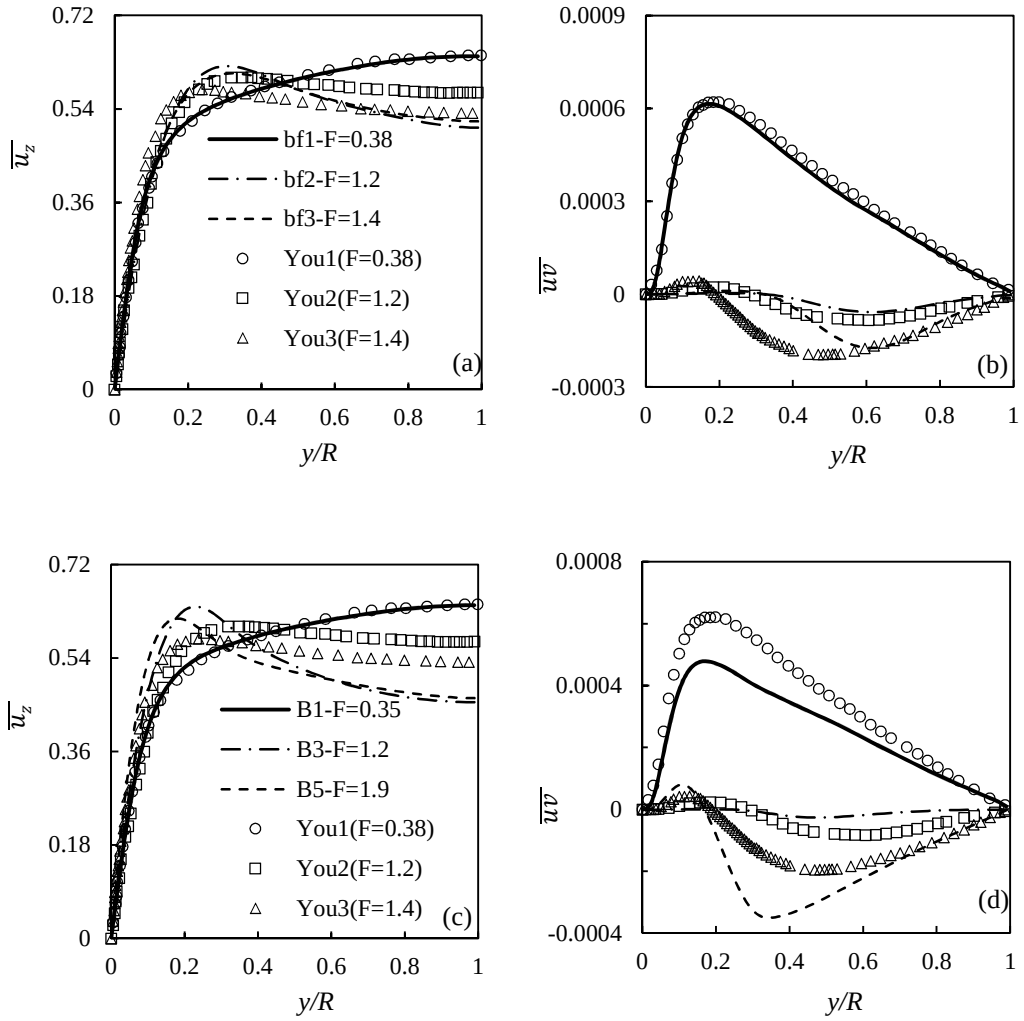

Figure 5.4:Validation of the method based on You's data.

(a) the mean velocity, (b) the Reynolds stress comparison between You's result and the current simulation result with abstracted body force form You1, You1 & You3. (c) the mean velocity, (d) the Reynolds stress comparison between You's result and the current simulation result with similar artificial body force.

5.1.3 General picture of body force effect

Figure 5.5 shows the velocity profiles of all the test cases in linear global coordinates and semi-logarithmic wall coordinates, respectively. With the increase of the body force (F, either through increasing the coverage or the amplitude), the general trends of the variations of the velocity profiles in each of the groups are similar to each other. We will

focus on group B to elucidate such trends but comment on the differences between the groups as appropriate. With a relatively low body force (cases B1 to B3), the velocity profile is only distorted slightly, becoming flattened in the core of the flow. The centreline velocity becomes lower than that of the reference case, and the velocity around say y/R=0.3 becomes higher. The velocity gradient near the wall is always lower than that of the reference flow, and decreasing with the increase of the body force. This is however not always the case in other groups. For example, the velocity gradient adjacent to the wall is higher in A1 and C1 than in the reference flow, and hence under such conditions the friction factor is increased in comparison with the reference flow even though the flow is partially laminarized (see later). Further increasing the body force, the velocity profiles suddenly switch to an M-shape profile, which has been observed in many mixed convection flows (Yoo *et al.* 2003; Bae *et al.* 2005; Bae *et al.* 2008). With the increase of the body force, the velocity in the centre of the pipe reduces and the velocity gradient adjacent to the wall increases, and as a result, the friction factor also increases. The variation of the velocity profiles with increase of body force follows a similar trend in Group D, but in Groups A and C, the velocity gradient near the wall remains largely the same in the various test cases. That is, the overall friction is insensitive to the increase of the imposed body force. This will be discussed further later.

Figures 5.5(e)~(f) show how far the velocity profiles can still be described by the generic logarithmic distribution. For the weaker body force influenced cases (B1 to B3), the velocity is upshifted with increase of the body force, showing increasingly stronger laminarization. There is always a region of logarithmic distribution (linear variation in the semi-log plot) in each case, but the gradient becomes steeper with increase of the body force. In consistent with the observation in Figures 5.5(a)~(d), the profiles of cases A1

and A2 are actually downwards shifted as a result of the increase of the friction velocity. The plots of the M-shaped velocity profiles have little meaning in this style of presentation, the curves follow the 'standard' curve up to y^+~15, and then either curve up or down first before going downwards in the core of the flow.

To illustrate the effect of the body force on turbulence, the turbulent shear stress and kinetic energy are shown in Figure 5.6. When the body force is relatively weak, say, B1 to B3, both turbulent shear stress and kinetic energy reduce progressively with increase of body force. In fact, the flow is effectively completely laminarized in B3, where both $\overline{uv}$ and k are negligibly small. With a further increase in body force, negative shear stresses are generated in the core of the flow, and the magnitude of which increases with the increase of the body force. At the same time, positive shear stress also starts to appear in the wall region. The peak value increases with increase of body force, and its location moves closer to the wall. The production of negative turbulent shear stress stems from the velocity gradient of the M-shaped profile in core region, which has been discussed by various researchers previously (Yoo *et al.* 2003; Bea *et al.* 2005; Bea *et al.* 2008). Along with the increase of $\overline{uv}$, turbulent kinetic energy also increases with increase of body force. There are two peaks in the distribution of k, one is clearly associated with the wall layer (the outer legs of the M) and the other is associated with inner flank of the M (the core of the flow), linked to the negative turbulent shear stress.

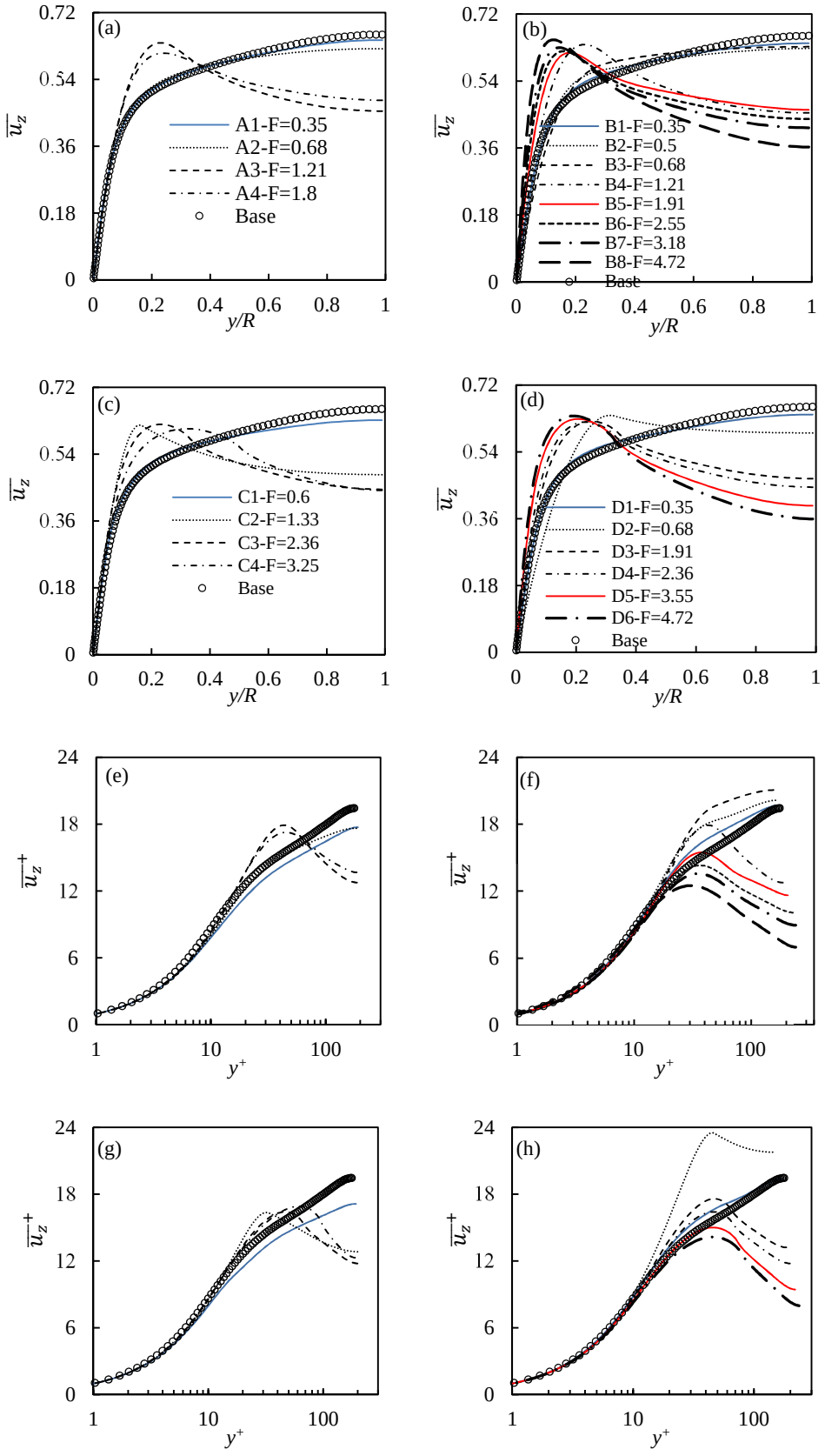

Figure 5.5: Linear and log plot of mean velocity in group A, B, C and D.

(a)~(d): linear plot of A, B, C, D; (e)~(h): log plot of A, B, C, D.

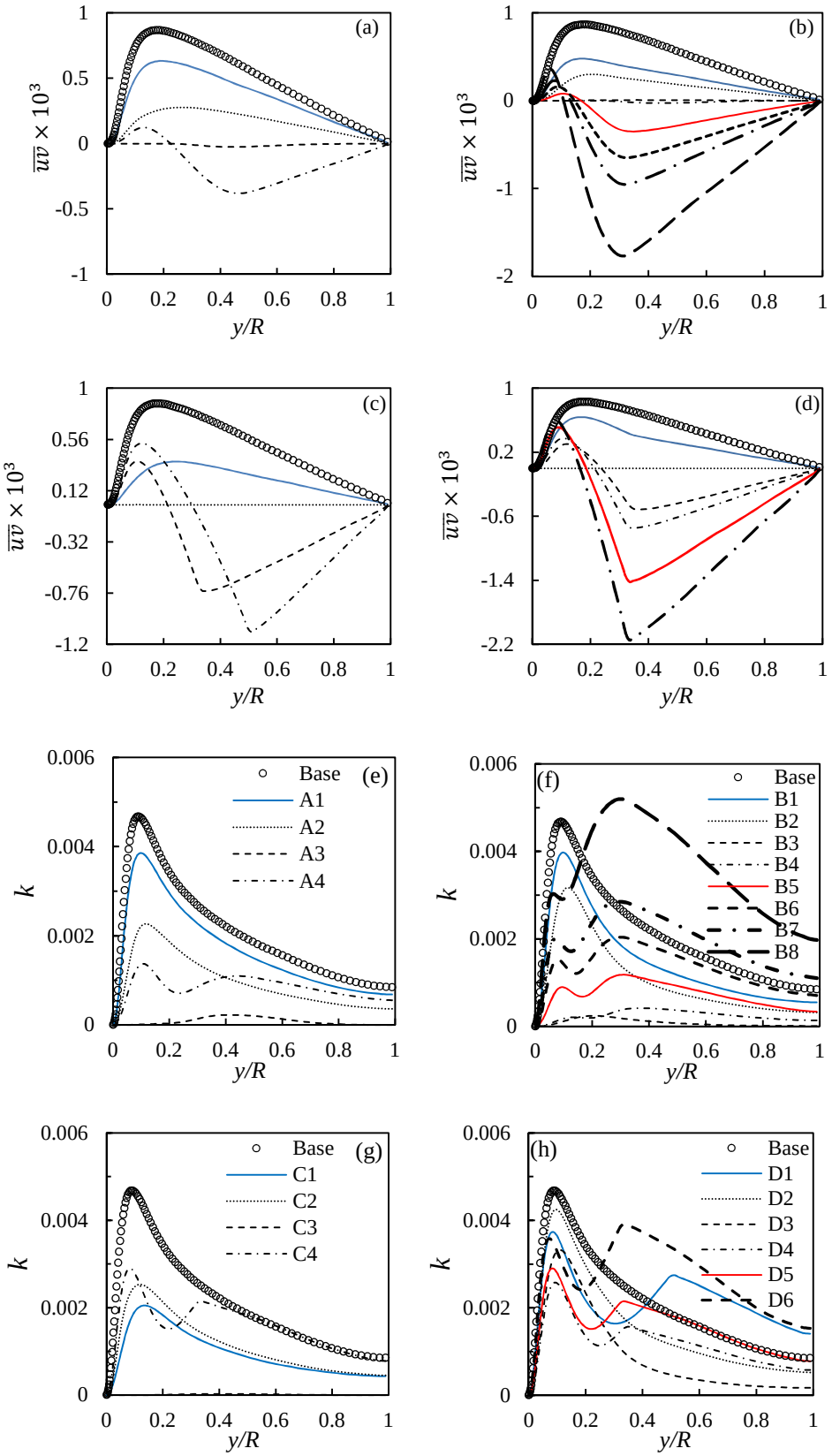

Figure 5.6: Reynolds stress and turbulent kinetic energy of group A, B, C and D. $\overline{uv}$ of A, B, C, D: (a), (c), (e), (g); k of A, B, C, D: (b), (d), (f), (h).

5.1.4 Correlation of turbulent state with boundary layer parameter

It has been shown above that the test cases studied cover all the typical flows encountered in buoyancy influenced flows. Among the many discussions presented above, two are of particular interest: a) the 'physical' body forces can be replaced by simple distributions while keeping the flow behaviour largely the same. Through a systematic study, the quantitative effect of the body force can be studied, which is useful to understand the real flow. b) With suitably selected non-dimensional groups, the influences of all the real and idealised body forces on turbulence, expressed in terms of the reduction/enhancement of heat transfer, friction or other parameters, can be correlated in a similar form. Such a correlation is important in terms of providing the links between the various different cases. The following is devoted to finding such a correlation. The following parameter is used to correlate the data.

Modified friction coefficient:

$$C_f{}' = \frac{\pi DL\tau_w - intbf}{\pi DL\tau_{w0}} \tag{5.3}$$

where $intbf$ an integration of the body force over the flow domain and τ_{w0} is the wall shear of base flow.

Figure 5.7 shows the correlations based on this parameter. Figure 5.7(a) shows that the modified $C_f{}'$ together with F correlates the cases very well. In addition, $C_f{}'$ vs $E_k(=\int_0^R kdr$ also correlates the data. The latter reflects the relationship between friction and the turbulence. The correlations show an interesting turning region (around F=1), which gives a straightforward criterion from where the flow is 'completely' laminarized and where the flow starts to recover. On the left of the turning region, are partially laminarized flows, while, on the other side are the recovery turbulent flows. These features are very

similar to the classic $Nu/Nu_f - Bo$ plot (shown in section 2.1.1). As in a buoyancy aided flow, it is shown that the turbulence state of such flows roughly correlates with F, but see more accurate discussions presented later. It is shown that a fully laminarized flow always coincides with a situation when the friction force roughly balances the applied body force.

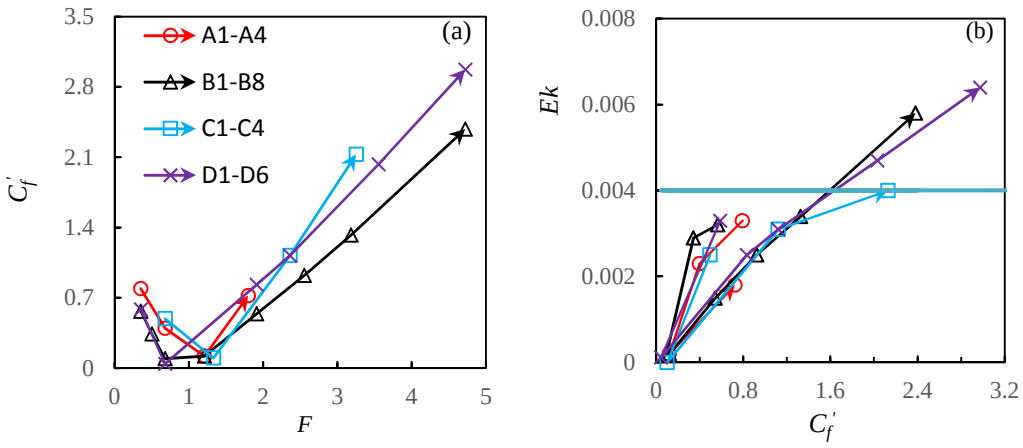

Figure 5.7: Correlation of different boundary parameters with F and integrated kinetic energy (E_k).
(a) $C_f{}' - F$; (b) $E_k - F$.

In order to facilitate further discussion, the flows studied are characterized into four types by the reduction or increase ratio of the Reynolds stress in the outer region (y^{+0}=90) where the Reynolds stress is linear. The classifications are summarized in table 5.2. The flow types I, II, III and IV are partially laminarized flow, 'completely' laminarized flow, partially recovery flow and strongly recovery flow. The velocity profile of regime I flows is flattened in the core of the flow, but is overall only slightly changed from that of the reference flow. The velocity always takes an M-shape in the recovery regime, where the inner flank of the M profile provides the reason for the generation of turbulence in the core of the flow. The velocity profile of a fully laminarized flow can take either of the above shapes. The partially laminarized flows and the fully laminarized flows are

discussed in section 5.2 and section 5.3. The features of recovery flows are analysed in section 5.4 and section 5.5.

Table 5.2 Classification of the flow according to the reduction of $\overline{uv}$ (a $= \frac{\overline{uv}}{\overline{uv}_0}$, *y*/*R*=0.6)

Flow type	*I* (0.3<a<1)	*II* (0<a<0.3)	*III* (-1<a<0)	*IV* (a<-1)
	A1, A2	A3	A4	--
	B1, B2	B3, B4	B5, B6	B7, B8
	C1	C2	--	C3, C4
	D1	D2	D3	D4, D5, D6

5.2 Partially laminarized flow

5.2.1 Turbulence in relaminarization flow-conventional view

Figure 5.8 shows the three components of the turbulent normal stresses normalised using the centreline velocity of the laminar Poiseuille flow and in wall coordinates. It can be seen from Figures 5.8(a)~(c) that the turbulent stresses reduce in all the cases though some of the reductions are stronger than others. More significantly, the reduction in the wall-normal and circumferential components is always much stronger than that in the streamwise component. The cases with the strongest reductions in u'_r and u'_θ are cases A2 and B2, where they reduce to approximately half of that of the reference case. By contrast, the reduction in u'_z is only approximately 10% and 30% in cases A2 and B2 respectively. For case D1 the peak values of the u'_r and u'_θ reduce by about 30%, but the peak value of the u'_z remains more or less the same as that of the reference case near

the wall, even though the values are clearly reduced in the core. As a result of such unequal reduction in the three components, the turbulence becomes strongly anisotropic which is known to be a characteristic of a laminarizing flow (Narasimha & Sreenivasan 1973; Iida & Nagano 1998; Tsukahara *et al*. 2005).

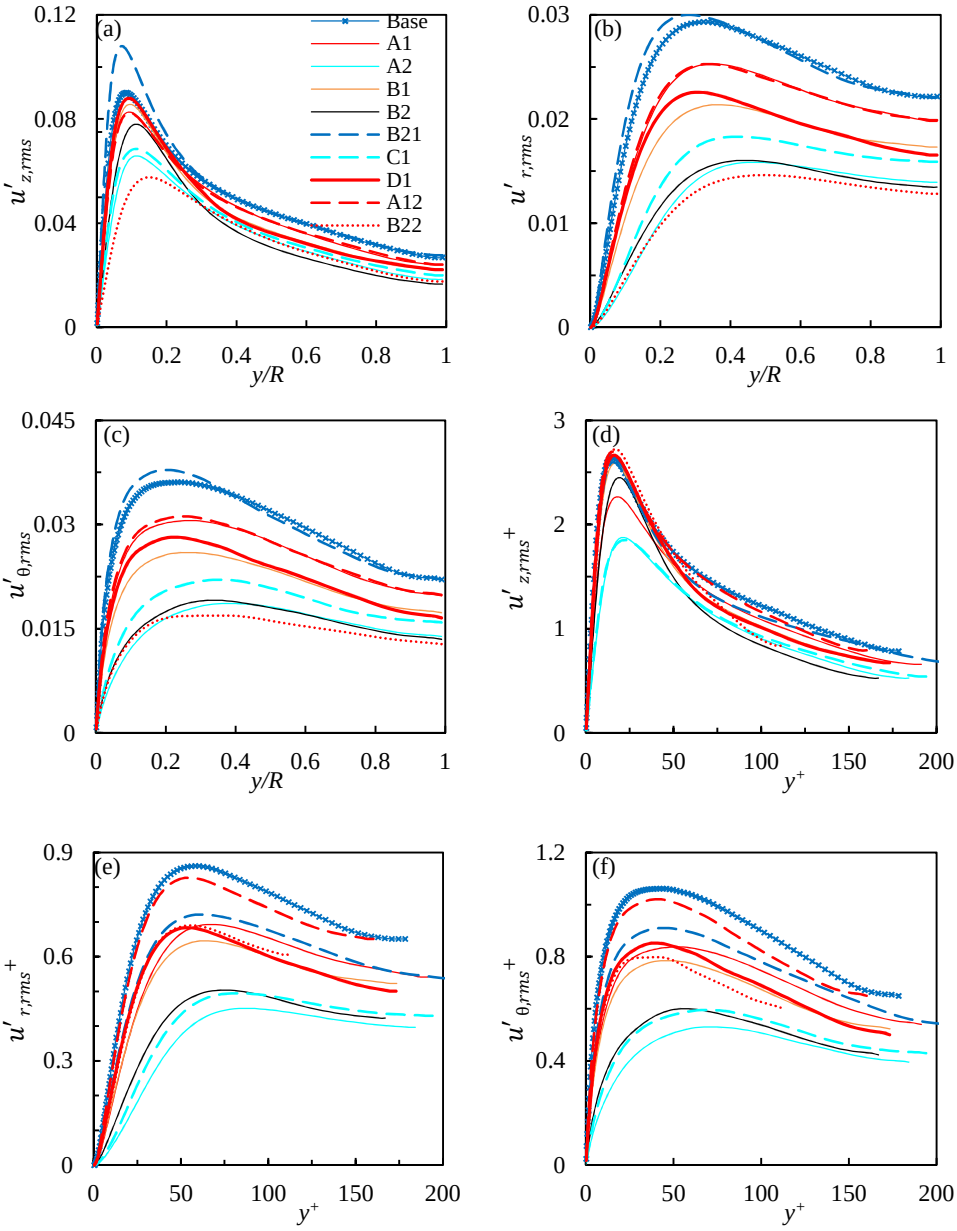

Figure 5.8: The r.m.s of velocity fluctuations in global and wall unit.

In the above, the discussion of turbulence reduction is based on the absolute values. In Figures 5.8(d)~(f), the same results are presented in wall coordinates, which enables us to study how far the turbulence in a laminarizing flow deviates from the generic distribution of an equilibrium flow. Again the turbulence quantities show various levels of reductions in all the cases studied. The reduction is stronger in u'_r and u'_θ and less so in u'_z. However, the percentage of reduction has changed, more significantly in some cases than in others, leading to a change of the order of the severity of laminarization of the flows. For example, the peak value of $u'_{z,rms}$ is lower in B2 than in A1 but the opposite is true in ${u'_{z,rms}}^+$ presentation. Overall, the turbulence reduction can be stronger or less strong in the absolute terms or in wall units depending on the flow conditions, which makes the prediction more difficult. Additionally, the location of the peak ${u'_{z,rms}}^+$ has shifted away from the wall in the laminarized flows which has been observed in the literature (Iida & Nagano 1998; Tsukahara *et al*. 2005).

For a particular type of body force, it is always true that the larger the total body force (F), the stronger the effect in supressing turbulence. However, the criterion as when and how much turbulence is influenced normally comes from empirical correlations from either experimental tests (Launder 1964; Narasimha & Sreenivasan 1973) or computer simulations (Berger *et al*. 2000; You *et al*. 2003). It is even more difficult to compare the effect of different body forces on turbulence.

5.2.2 A new perspective

Ordinarily, comparisons of flows under various flow conditions are based on equal Reynolds numbers, which is the basis of the discussion presented above. For a given flow rate, the turbulence in a flow subjected to a non-uniform body force may be significantly

lower than in the reference flow of the same Reynolds number where the flow is driven by only the pressure gradient. We therefore refer to such flows as partially laminarized, the example of which include, mixed convection in a vertical tube (McEligot *et al.* 2004; Bea *et al.* 2008), accelerating flows (Chung *et al.* 2005; Talha 2012) and some flows subject to certain control mechanisms (Kim 2011), as discussed in the introduction.

Below, we analyse the body-force influenced flows from a new angle which leads to a new theory on laminarizing flows. We will show that this new theory reveals the fundamental characteristics of the body-force influenced flows much more clearly than does the traditional viewpoint and that it enables good predictions of laminarizing flows to be achieved as a result. Taking a Reynolds averaged view of the flow, the governing equation for a statistically steady flow of an incompressible fluid in a pipe, sufficiently away from the entrance is written as:

$$0 = -\frac{dP}{dx} + \frac{1}{r}\frac{\partial}{\partial r}\left[r\left(\frac{1}{Re}\frac{\partial U}{\partial r} - \overline{uv}\right)\right] + bf \tag{5.4}$$

where bf is a body force varying along the radius, but uniform axially and circumferentially, i.e., a function of *r* only. Let us now consider another flow that is driven by a pressure gradient that is the same as that of the body-force influenced flow, but with the body force removed. Using subscript '1' to indicate this flow condition,

$$0 = -\frac{1}{\rho}\frac{dP_1}{dx} + \frac{1}{r}\frac{\partial}{\partial r}\left[r\left(\frac{1}{Re}\frac{\partial U_1}{\partial r} - \overline{uv}_1\right)\right] \tag{5.5}$$

where, $\frac{dP_1}{dx} = \frac{dP}{dx}$. Subtracting Eqn 5.5 from Eqn 5.4,

$$0 = \frac{1}{r}\frac{\partial}{\partial r}\left[r\left(\frac{1}{Re}\frac{\partial U'}{\partial r} - \overline{uv}'\right)\right] + bf \tag{5.6}$$

where $U' = U - U_1$ and $\overline{uv}' = \overline{uv} - \overline{uv}_1$. Introducing the eddy viscosity concept, i.e., $\overline{uv} = -\nu_t \frac{1}{Re}(\partial u/\partial r)$, where ν_t is the turbulent viscosity, the above equation can be written as:

$$0 = \frac{1}{r}\frac{\partial}{\partial r}\left[r\left(\frac{1}{Re}\frac{\partial U'}{\partial r} - \nu_t\frac{1}{Re}\frac{\partial U}{\partial r} - \nu_{t1}\frac{1}{Re}\frac{\partial U_1}{\partial r}\right)\right] + bf \tag{5.7}$$

We now make the following assumption, the validity of which will be demonstrated throughout the remaining part of section 5.2: The addition of the body-force does not change the turbulent mixing characteristics of the flow and in particular, the turbulent viscosity remains unchanged. As a result, Eqn 5.7 becomes:

$$0 = \frac{1}{Re}\frac{1}{r}\frac{\partial}{\partial r}\left[r\left((1+\nu_{t1})\frac{\partial U'}{\partial r}\right)\right] + bf \tag{5.8}$$

where ν_{t1} is the eddy viscosity of the reference flow without any body-force (i.e., from the solution of Eqn 5.5). Consequently, with the solution of the reference flow, the perturbation flow due to the imposed body force can be obtained by simple integration of the above equation. Hereafter we refer to the flow described by Eqn 5.5 to be the dp-based reference flow (with second subscripts 1&2, shown later) of the body-influenced flow that has the same pressure gradient dp/dx. Similarly, we refer to the undisturbed flow (i.e., no body force) of the same Reynolds number to be the Re-based reference flow (with subscript 0).

Integrating Eqn 5.5 resulting in an expression of the force balance in the flow:

$$-\frac{r}{2}\frac{dp}{dx} + \frac{1}{r}\int_0^r rbf\,dr = \overline{uv} - \frac{1}{Re}\frac{\partial U}{\partial r} \tag{5.9}$$

The first and the second terms on the left are the contributions to the total shear stress from the pressure gradient and the body force, noted as, τ_{wp} and τ_{wb}, respectively. Letting r =1, we obtain the total wall shear stress to be $\frac{1}{Re}\left(\frac{\partial U}{\partial r}\right)_{r=R} = -\frac{R}{2}\frac{dp}{dx} + \frac{1}{R}\int_0^R rbf\,dr$, which we denote as $\tau_w = \tau_{wp} + \tau_{wb}$. The total shear stress $\tau_w = \tau_{wp} + \tau_{wb}$ of the body force influenced flow (case B2) together with those of the corresponding Re-based and dp-based reference flows are shown in Figure 5.9 to illustrate the various concepts.

In this particular case, the total wall shear of B2 (τ_w) is greater than that of the Re-based reference case ($\tau_{w,Re}$), but the reverse is true in many other cases. By definition, the wall shear stress of the dp-based reference case (τ_{w0}) and the contribution of the pressure gradient in the body force influenced case (B2 in here) are equal, i.e., $\tau_{w0} = \tau_{wp}$. We define a friction velocity based on pressure gradient component as $U_{\tau p}^* = \sqrt{\tau_{wp}^*/\rho^*}$, which is referred to as the apparent friction velocity, and similarly, $Re_{\tau p} = U_{\tau p}^* R^*/\nu^*$ as the apparent Reynolds number of the flow. These are important parameters in the new framework of analysis.

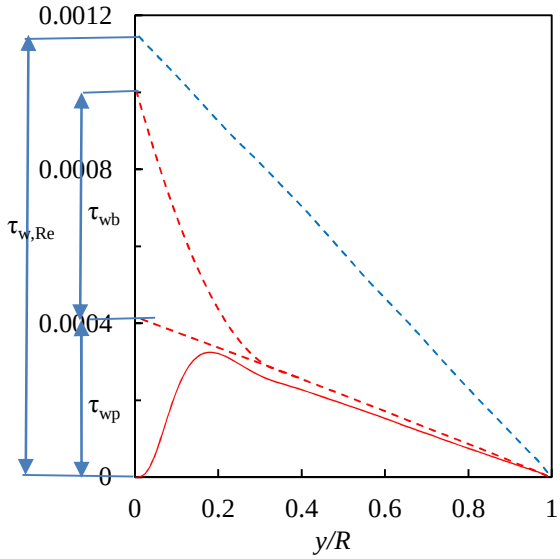

Figure 5.9: The shear stress distribution of B2 and base cases.

We now inspect the turbulent eddy viscosity obtained for the various test cases studied herein, which are shown in Figures 5.10(a) and (b) in wall coordinates based on the complete flow (U_τ^*) and the apparent friction velocity ($U_{\tau p}^*$), i.e., $y^+ = \frac{\sqrt{\tau_w^*/\rho^*}\, y}{\nu}$ and $y^{+1} = \frac{\sqrt{\tau_{wp}^*/\rho^*}\, y}{\nu}$, respectively. It can be seen from Figure 5.10(a) that the turbulent viscosity reduces in the body-force influenced cases in comparison with the Re-based

reference case. B21 is a case with body force B2 and the mean pressure gradient of the base flow. Generally speaking, the larger the body force, the stronger the reduction, which is consistent with the observations on turbulence quantities presented earlier. This is in good accordance with the conventional theory, which explains flow laminarization phenomena (Jackson 2011). By contrast, when the turbulent viscosity is plotted against y^{+1} (Figure 5.10b), the values of the turbulent viscosity in the various cases collapse reasonably closely together near the wall. Away from the wall, the data of the flows with a low apparent Reynolds number deviates from the 'generic' distribution represented by that of case Base; the lower the Re, the earlier the data deviates. This is largely a Reynolds number effect. To verify this, the data obtained from some low Reynolds number flows together with the low Reynolds number data of Tsukahra $et\ al.$ (2005) are shown in the

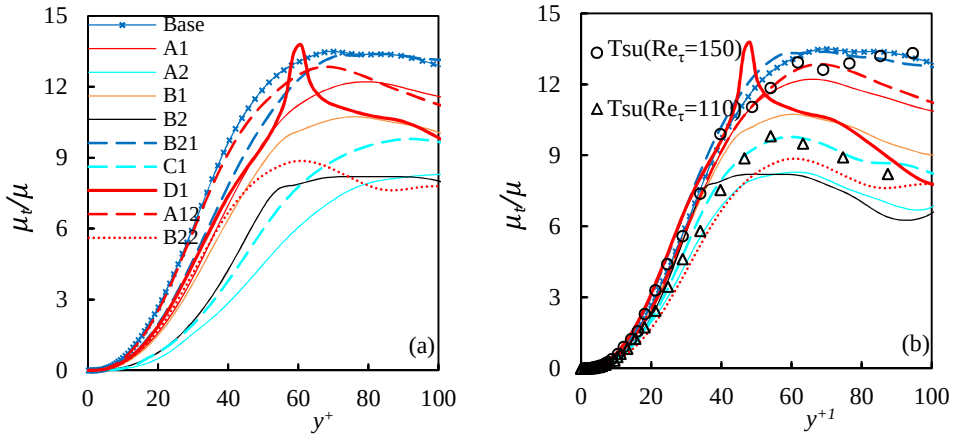

Figure 5.10: The turbulent viscosity (a) nomalized by U_τ^* (b) nomalized by $U_{\tau p}^*$.
(A12: the dp-based cases of A1; B22: the dp-based cases of B2)

figure for comparison. It can be seen that the data from Tsukahara $et\ al.$ (2005) (Re_τ=110, 150) and that of the base (Re_τ =180) provide the lower and higher bounds of the data with only few exceptions. In most cases, the values of the turbulent viscosity of a flow are commensurate to their apparent Reynolds number. In conclusion, these results provide a

good support for the assumption presented early, that is, the values of the turbulent viscosity of the body-force influenced flows are not significantly influenced by the body force and they agree well with those of their corresponding dp-based reference flows.

To further elucidate the idea, next we study the turbulent shear stresses. The total turbulent shear stress and the contribution due to the perturbation flow induced by the body force, calculated from $\overline{uv}_b = \nu_t \frac{\partial U'}{\partial r}$, are shown in Figure 5.11(a). The differences of those two terms are shown in Figure 5.11(b), which are compared with the turbulent shear stress obtained from the corresponding dp-based reference flows (For clarity, the case number is reduced in Figure 5.11b). A12 is the base flow of A2 with dp/dx calculated from A2. B22 is the base flow of B2 with dp/dx calculated from B2. The B21 is the base flow of B2 with dp/dx calculated from base flow (Re_τ=180). The agreement between the two sets of data is strikingly close, which again provides evidence validating the underlining assumption that the turbulence mixing characteristics are not modified by the body force. It can be seen from Figure 5.11(a) that the body-force induced turbulent shear stress ($\overline{uv}_b$) is only limited to the near wall region as expected, and the values vary significantly from case to case. Interestingly, the contribution of $\overline{uv}_b$ is not directly corresponding to the total body force.

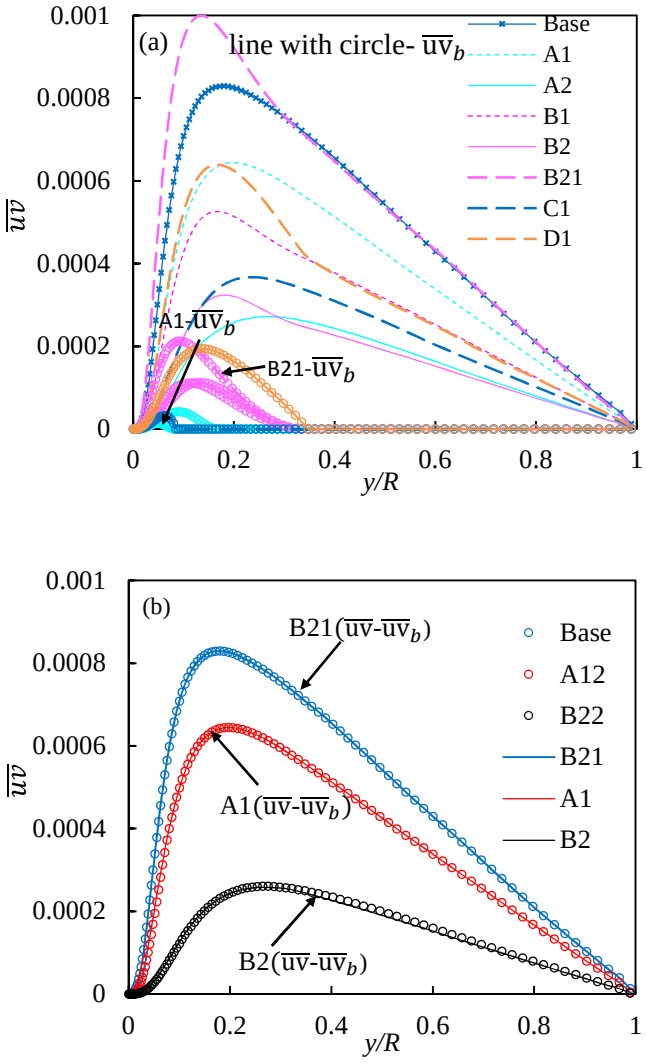

Figure 5.11: The Reynolds stress distribution of different cases.

For example, the body force in A1 and B1 are both 0.35, but $\overline{uv}_b$ is significantly higher in B1 than in A1. Clearly this difference stems from the different coverages of the body force in the two flows. The larger the coverage, the larger the value of $\overline{uv}_b$. In fact, the contribution of $\overline{uv}_b$ to the total turbulent shear stress in A1 is so small that it can be neglected. This has an interesting implication, that is, the body-force induced flow can be seen to be a laminar flow, which makes the analysis even simpler. What is really interesting about this observation is that the total body force does not have to be small; it only requires the coverage to be small. Cases that are in this category are A1, A2 and C1.

Typically, when the coverage of the body force is limited y^+<20, the body-force induced turbulence shear stress ($\overline{uv}_b$) will be negligible.

Next we study the turbulent normal stresses in the new framework. The stresses normalized by the apparent frictional velocity $\sqrt{\tau_{wp}{}^*/\rho^*}$ are plotted againest y^{+1} in Figure 5.12. Before studying the detailed behaviour, we first note that the apparent Reynolds numbers of the most flows studied herein are rather low, and some of them are in the transitional flow regime. The values of the apparent Reynolds number are shown in Table 5. 3 for reference.

Table 5.3 The apparent *Re* for laminarized flows (based on *R*)

Case	A1	A2	B1	B2	C1	D1
$\mathbf{Re}_{\tau,dp}$	160	113	140	110	126	138
$\mathbf{Re}_{b,dp}$	2320	1560	1978	1510	1760	1960

Tsukahara *et al.* (2014) studied low Reynolds number turbulent and transitional flows in a channel with Re_τ between 64 and 180. They have shown that the peak r.m.s. values of the v' and w' at low Reynolds number reduce significantly. Selected data from this reference are included in Figure 5.12 for comparison. It can be seen from Figures 5.12(b) and (c) that ${u'}_{r.rms}{}^{+1}$ and ${u'}_{\theta,rms}{}^{+1}$ in the various test cases do not vary much. The peak values in some of the cases are lower than that of the Re-based reference case, demonstrating a Reynolds number effect for the radial and circumferential turbulence in low Reynolds number flows. These results show that, in contrast to the conclusions drawn earlier based on the conventional approach using wall units based on the total flow, which shows a strong reduction in turbulence, the radial and circumferential turbulence components are not significantly influenced by the imposed body force. In contrast to this

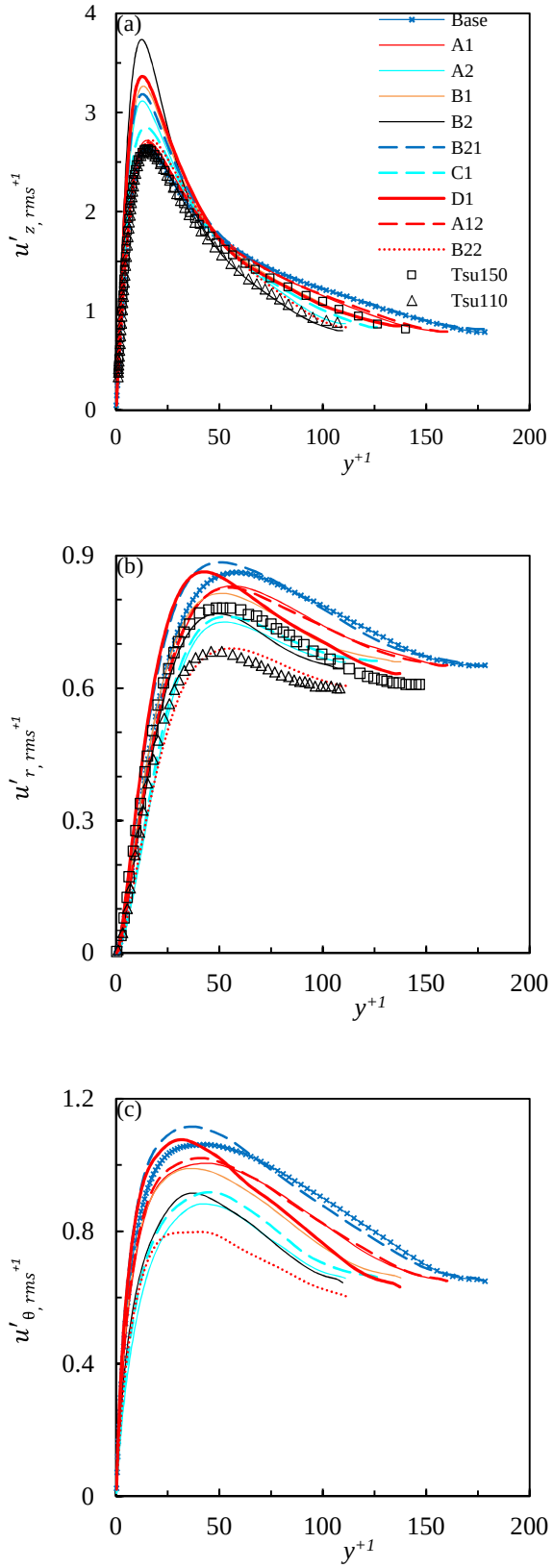

Figure 5.12: The r.m.s of three components normalized by $u_{\tau p}$.

trend (and to the trend demonstrated in conventional plots shown in Figure 5.8), the peak values of the streamwise turbulent velocity in most test cases either remain largely unchanged or are increased, in some cases, significantly. This is despite that the peak values of the corresponding dp-based reference flows remain close to that of the Re-base reference flow. It is noted that the cases in which the peak value of ${u'}_{z,rms}^{+}$ is increased the most does not correspond to that with the minimum ${u'}_{r,rms}^{+}$, which corresponds largely to the lowest $Re_{\tau 1}$.

Instead, the increase of the ${u'}_{z,rms}$ with respect to that of the dp-based reference flow corresponds well with the corresponding increase of the peak value of the body-force induced turbulent shear, that is, $\frac{u_{z,rms,max}-(u_{dp-base})_{z,rms,max}}{(u_{dp-base})_{z,rms,max}} = c\frac{(\overline{uv}_b)_{max}}{(\overline{uv}_{dp-base})_{max}}$, where $u_{z,rms,max}$ is the peak of ${u'}_{z,rms}$. These two ratios are shown in Figure 5. 13, where c is taken to be 1/1.2 to match the two sets of data. It can be seen that the agreement between the two sets of the values are indeed strikingly close in most cases.

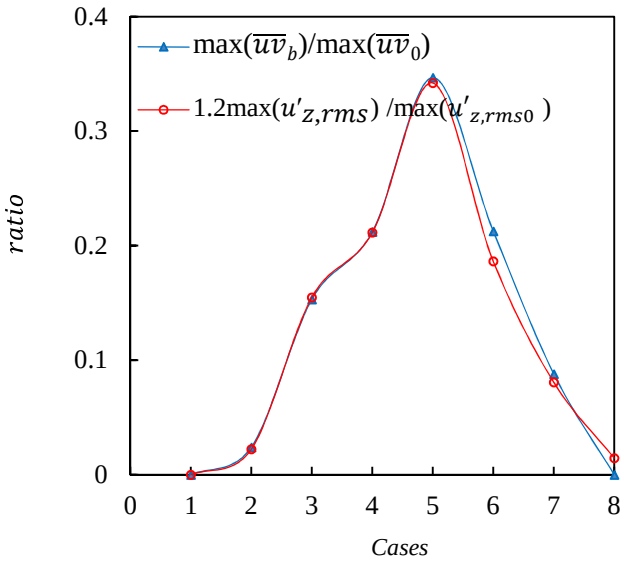

Figure 5.13: The reduction ratio of $\overline{uv}$ and ${u'}_{z,rms}$.

It has been shown earlier that the turbulent eddy viscosity, and the wall-normal and circumferential stresses all remain more or less unchanged from their reference flow values. The question is why $u'_{z,rms}$ is increased. We will show that the increase of $u'_{z,rms}{}^{+1}$ is associated with the enhancement of the streaks in the flow due to the imposition of the body force, which is relevant to a generally accepted turbulence self-sustaining mechanism, as Figure 5.14 shows. It contains 3 important ingredients, namely, streamwise vortices, streaks and streamwise-dependent disturbances. There are three legs connect these important ingredients. The first leg involves the interactions between streamwise vortices ($v(z)$ & $w(z)$) and the mean shear (dU/dy). The transient growth is a well recorded mechanism in terms of streaks formation, which is the second leg. The streamwise vortices will decay if they are not strengthened via the third leg, which is non-linear mechanisms involving streamwise-dependent disturbances. More detailed explanation of this circle can be found in Kim (2011) and many other papers (Walleffe 1997; Jimenez & Pinelli 1999; $etc.$).

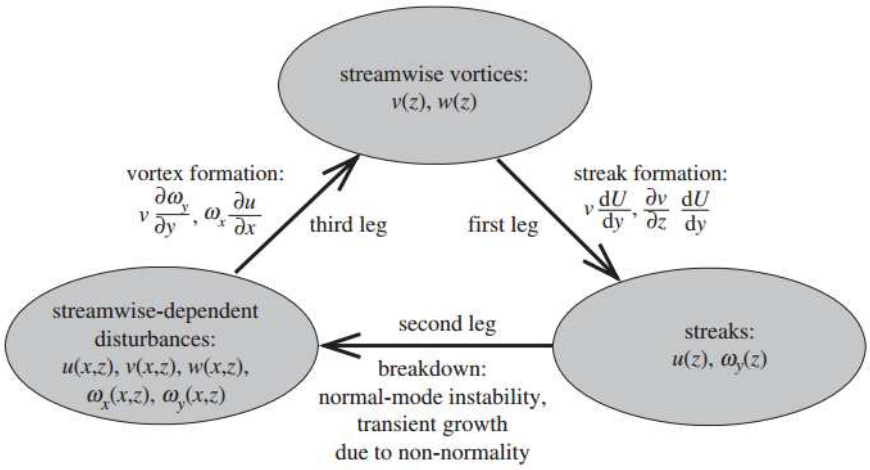

Figure 5.14: The turbulence regeneration circle described by Kim (2011)

Referring to the turbulence regeneration cycle, it appears that the body-force (the boundary layer it induces) enhances the streak generation and transient growth processes (legs 1 & 2), which are linear processes. It does not significantly influence the breakdown of the streaks (nonlinear process – third leg). This will be further discussed later referring to the flow structures.

Before leaving this section, we revisit some interesting features of the mean velocity field. Figures 5.15 (a)~(c) show the profiles of the mean velocity of the perturbation flow induced by the body force (U_{bf}), and the velocity difference, i.e., $U_{diff} = U - U_{bf}$, in outer scaling and wall scaling respectively. The U_{bf} is obtained by a double integration of Eqn 5.6:

$$U_{bf} = Re \int_0^r \frac{1}{\mathrm{r}} \int_0^{\mathrm{r}} bf \; r dr + \int_0^r uv dr \tag{5.10}$$

It is interesting to note that the body force perturbated flow is not necessarily directly proportional to the total body force. The coverage has a significant effect. For example, A1 and B1 have the same total body force, but the flow rate of B1 is more than doubled that in A1. The next thing to note is that the body-force induced perturbation flow is very significant in comparison to the reference flows. The ratios between the two flows are 13% for A1, then around 35% for B1 and B21, around 50% for C1 and D1 and then 70% and 85% for A2 and B2. Thirdly, the differential flow calculated by subtracting the body-force induced flow from the total flow agree extremely well with some corresponding reference flows (B21 & A12 & B22& Tsu (Re_τ=110, 150)) based on DNS simulations of equal pressure gradient. Finally it can be seen from the wall coordinates velocity plot that the profiles of $U_{diff} (= U - U_{bf})$ in most of the cases agree well with the Re-based reference flow profile, clearly exhibiting a region of logarithmic behaviour. There are some cases where the velocity profile shows a relatively strong upshift, which is normally

seen as a sign of laminarization. This occurs in A2 and B2, which corresponds to the lowest U_{diff} and their corresponding dp-based reference flows have the lowest Re_τ.

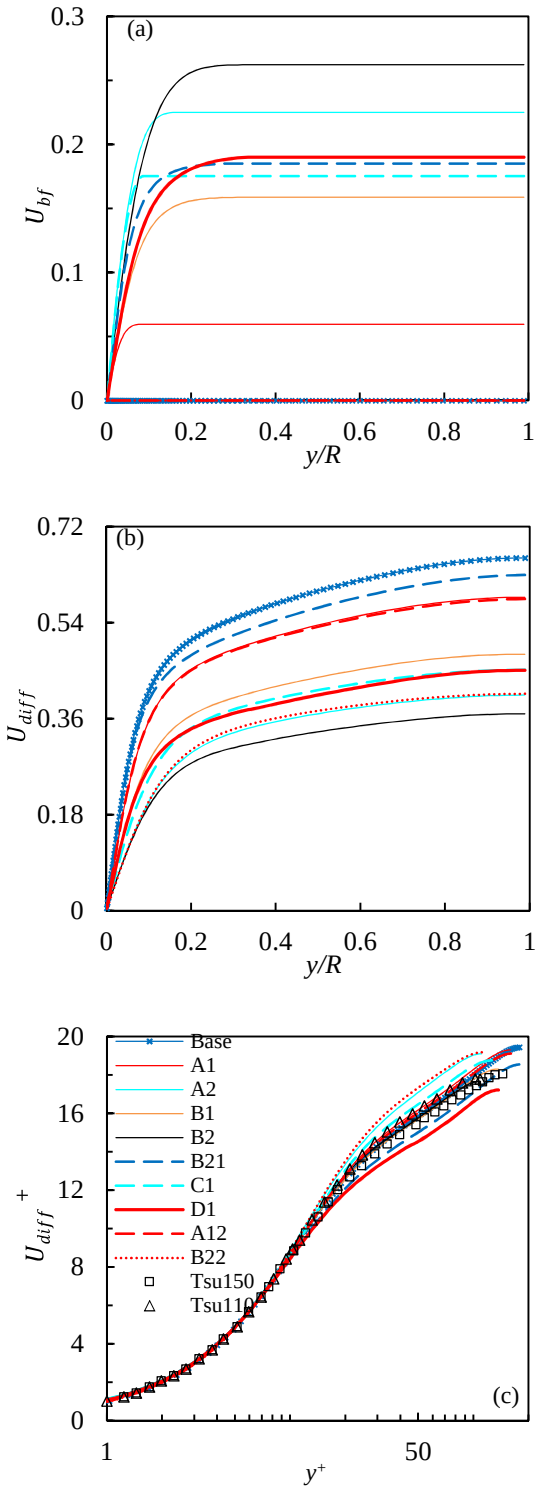

Figure 5.15: The decomposition of the mean velocity (c: U_{diff} normalized by $u_{\tau p}$).

5.2.3 Friction factor and the FIK Identity analysis

Fukagata $et\ al.$ (2002) has introduced a simple but useful analysis of the contributions of different dynamic effects on the friction drag for a turbulent channel, pipe or a boundary layer flow. The local friction is decomposed into laminar, turbulent, inhomogeneous and transient components. This method has been widely used in flow control and drag reduction investigations and is referred to as FIK identity. For flow in a pipe considered here that is described by Eqn 5.5, the FIK expression is,

$$C_f = \frac{16}{Re_b} + 16\int_0^1 2\,r\,\overline{uv}\,rdr + 16\int_0^1 (r^2-1)(bf-F)rdr \qquad (5.11)$$

where $F = 2\int_0^1 bf\ r\ dr$, being the averaged body force. From left to right, the terms represent the contributions due to laminar and turbulent flows, and the body force. To better understand the contribution of the body force, the turbulent contribution is further split into a component due to the $d\bar{P}$-based reference flow ($\overline{uv}_0$) and one due to the perturbation flow induced by the body force ($\overline{uv}_{bf}$):

$$16\int_0^1 2\,r\,\overline{uv}\,rdr = 16\int_0^1 2\,r\,\overline{uv}_0\,rdr + 16\int_0^1 2\,r\,\overline{uv}_{bf}\,rdr \qquad (5.12)$$

The FIK analysis of the various partially laminarized cases is shown in Figure 5.16. It can be seen that the total friction factor in the partially laminarized flows can be higher or lower than that of the Re-based reference flow. The Figure 5.16(a) illustrates that the contribution of the turbulence associated with the perturbation flow due to the body flow is negligible in A1, A2 and C1 and are substantial in the other test cases, which is consistent with earlier observations, referred to Figure 5.10(a) where $\overline{uv}_{bf}$ is shown for example. Comparing A1 with A2 (or B1 with B2), it is noted that the flow is further laminarized as a result of a stronger body force, and hence a less C_f contribution from $\overline{uv}_1$, but the contribution from the body force itself increases. If a reduction of the friction

factor is the objective, increasing the amplitude of the body force is more effective than increasing the coverage, comparing, B1 & B2 with A1 & A2.

Next, we apply the theory established in §5.2.1 to the prediction of the friction factors. We have established that the turbulent viscosity in the body force influenced flows remains little changed from the values of their corresponding dp-based reference flows. Now, in Eqn 5.11, we replace the turbulent shear stress $\overline{uv}_1$ with their corresponding values of the dp-based reference flows, and re-calculate $\overline{uv}_{bf}$ using the turbulent viscosity of the dp-based flows. The following formula is used to predict the C_f.

$$C_f = C_{fp} + C_{fb} \tag{5.13}$$

$$C_{fp} = \frac{16}{Re_b} + 16\int_0^1 2\,r\,\overline{uv}_1\,rdr + 16\int_0^1 2\,r\,\overline{uv}_{bf}\,rdr \tag{5.14}$$

$$C_{fb} = 16\int_0^1 (r^2-1)(bf-F)rdr \tag{5.15}$$

where $\overline{uv}_{bf} = \nu_t \frac{\partial U'}{\partial r}$

The results are shown in Figure 5.16(b). It can be seen that the total friction factors calculated this way are very close to those calculated from the original FIK formulation (Eqn 5.11). Consequently, the friction factor of laminarized flow can be accurately predicted simply using the undisturbed turbulent flow data and the profile of the imposed body force.

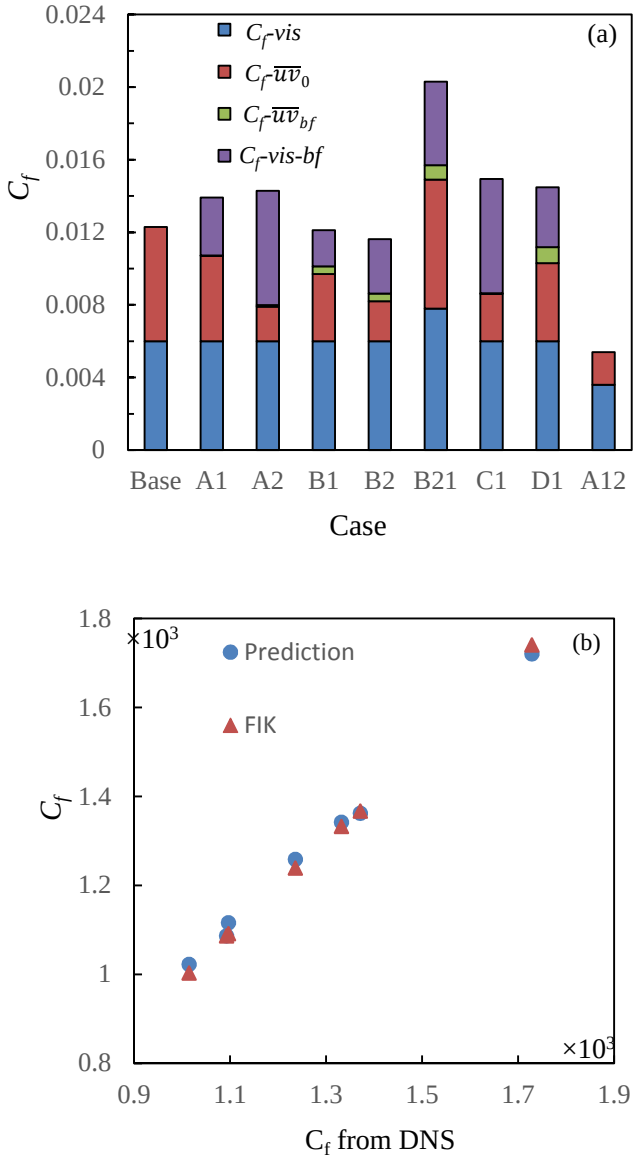

Figure 5.16: The prediction of FIK of laminarized flow.
(a): C_f of different components (b): The C_f predicted by FIK and new theory against the DNS result.

5.2.4 Budget terms

Budget terms are interesting for turbulence modelling and reflect the momentum transfer situation related to the coherent structures. Figures 5.17 to 5.18 show the budget terms for the streamwise and wall-normal stresses normalized by $u_{\tau 0}$. As expected, the terms for both $\overline{u'_z u'_z}$ and $\overline{u'_r u'_r}$ normalized based on $u_{\tau 0}$ are reduced in all test cases, and in

many cases, such as A2, B2 and C1, the reduction is very significant. This is consistent with the traditional view of flow laminarization, demonstrating that turbulence is suppressed due to the presence of the body force.

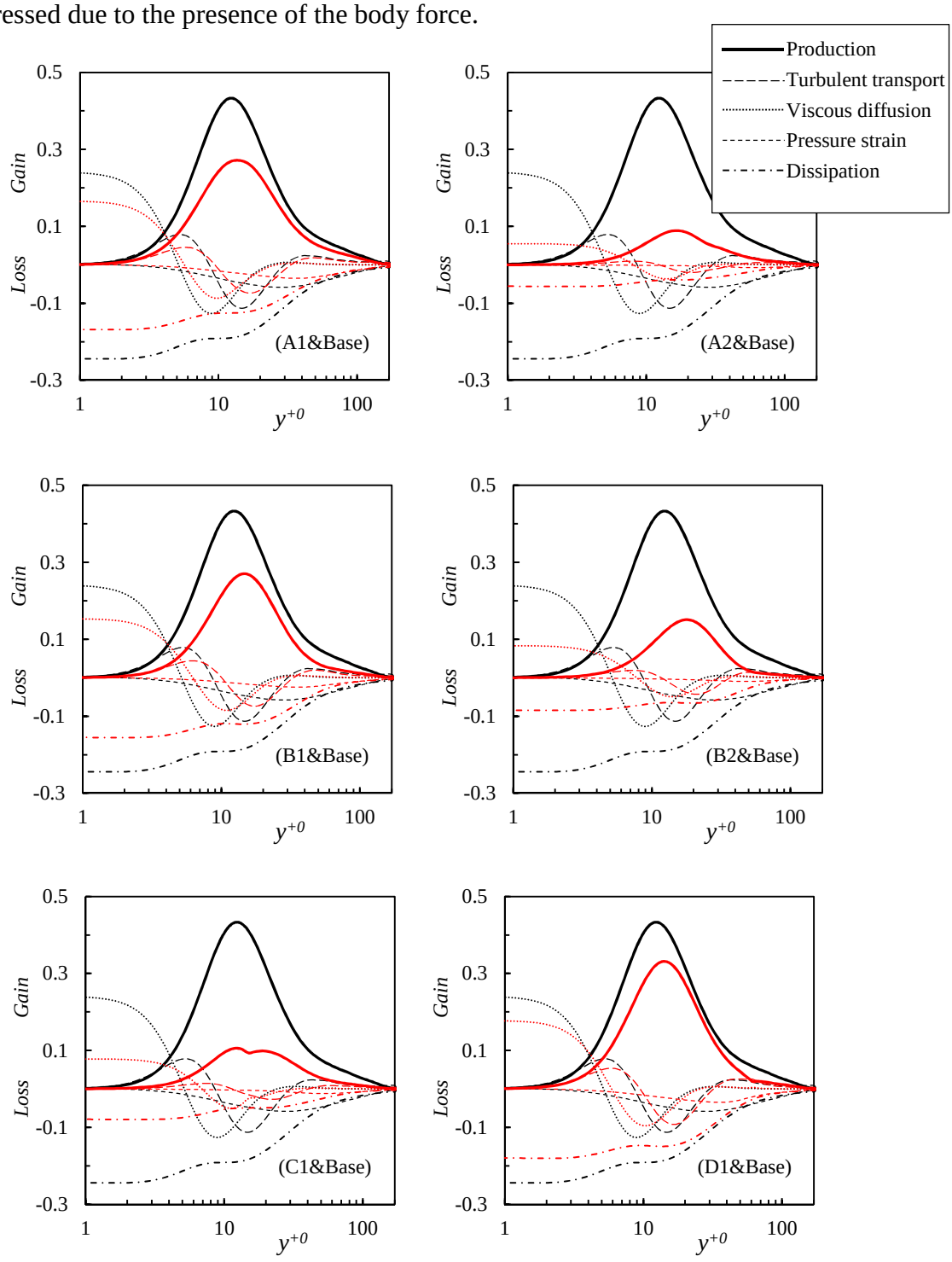

Figure 5.17: The budget terms of $\overline{u'_z u'_z}$ normalized by ${u_{\tau 0}}^4/\nu$.
(Base in black line; Other cases in red line)

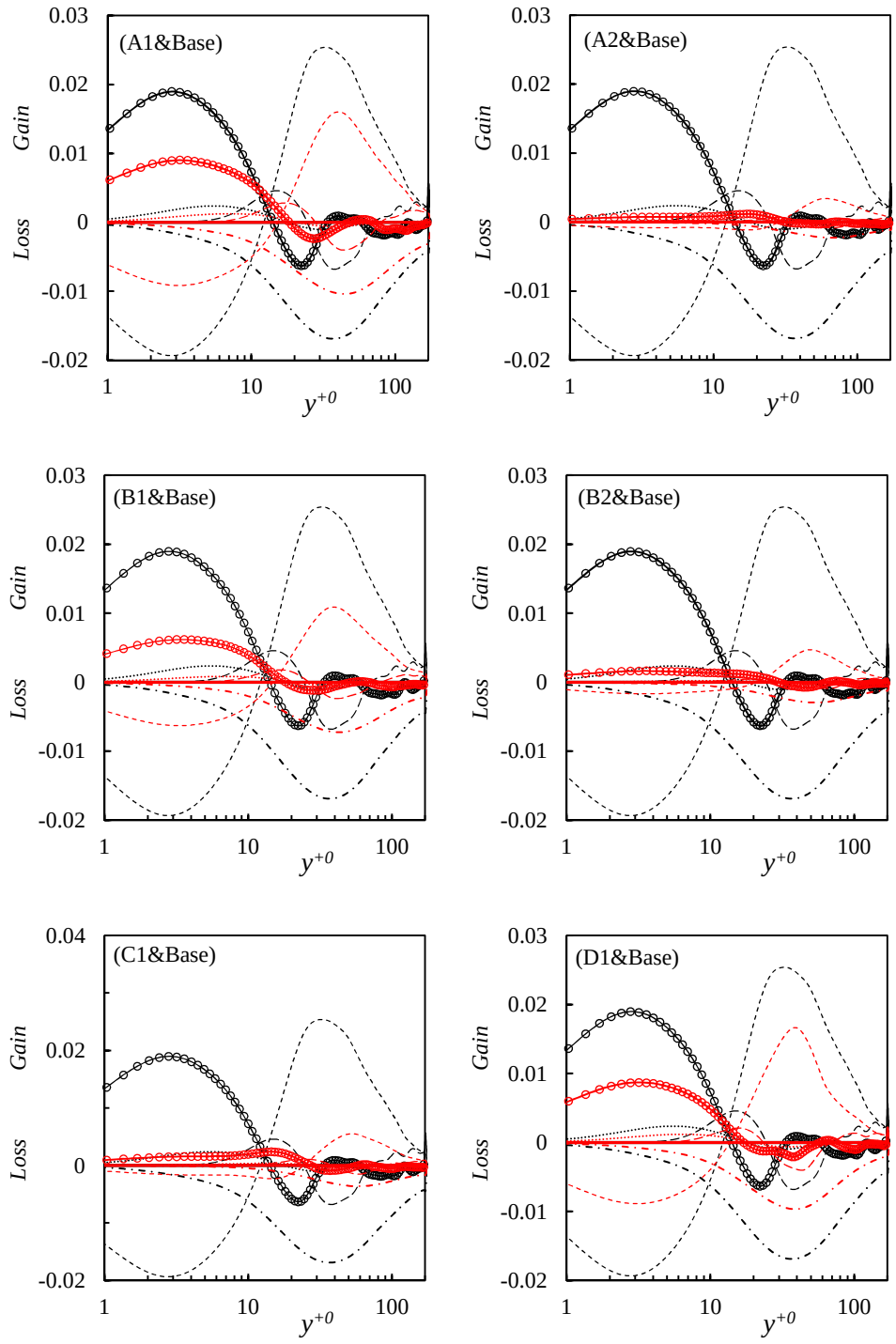

Figure 5.18: The budget terms of $\overline{u'_r u'_r}$ normalized by $u_{\tau 0}{}^4/\nu$.

(Base in black line; Other cases in red line)

Production: ——— ; Turbulent transport: - - - - - ;Viscous diffusion: ·····

Pressure strain: ------- ; Pressure diffusion: —○— ; Dissipation: -·-·-

The picture is very different when the terms are normalized based on $u_{\tau 1}$. For the streamwise component, the budget terms in A1 and C1 agree very well with their corresponding reference values. For the rest of the cases, both the production and the dissipation are increased by various amounts. The above trend is consistent with the observations in Figure 5.12 where $u'_{z,rms}$ is presented. The increase of the production is largely related to the generation of elongated streaks. For the wall-normal component, there is no direction production. The supply of energy comes from the pressure strain term, whereas the sink is the dissipation. In addition, the pressure diffusion term is often also significantly, especially close to the wall. It can be seen from Figure 5. 19 that, overall, the terms in the body force influenced flows agree very well with those of the reference flow (Base), especially considering the deviations shown in the conventional presentation (Figures 5.17 & 5.18). The agreements between the main terms (pressure strain and dissipation) are particularly good for A1 and B1. This is also true for A2 and C1, though the pressure strain and dispersion terms show a strong reduction near the wall (y^{+1}<8). Both terms agree reasonably well with their respective reference data in the core region. Another observation is that the source-term, pressure strain, increases somewhat in several cases, including B21, B2 and D1, and to a lesser extent B1. There are the cases where the body-force induced turbulent shear stress is relatively large. It is worth noting that the general agreement between the body force influenced cases and the reference cases is remarkable considering that in many case the absolute values reduce by several times.

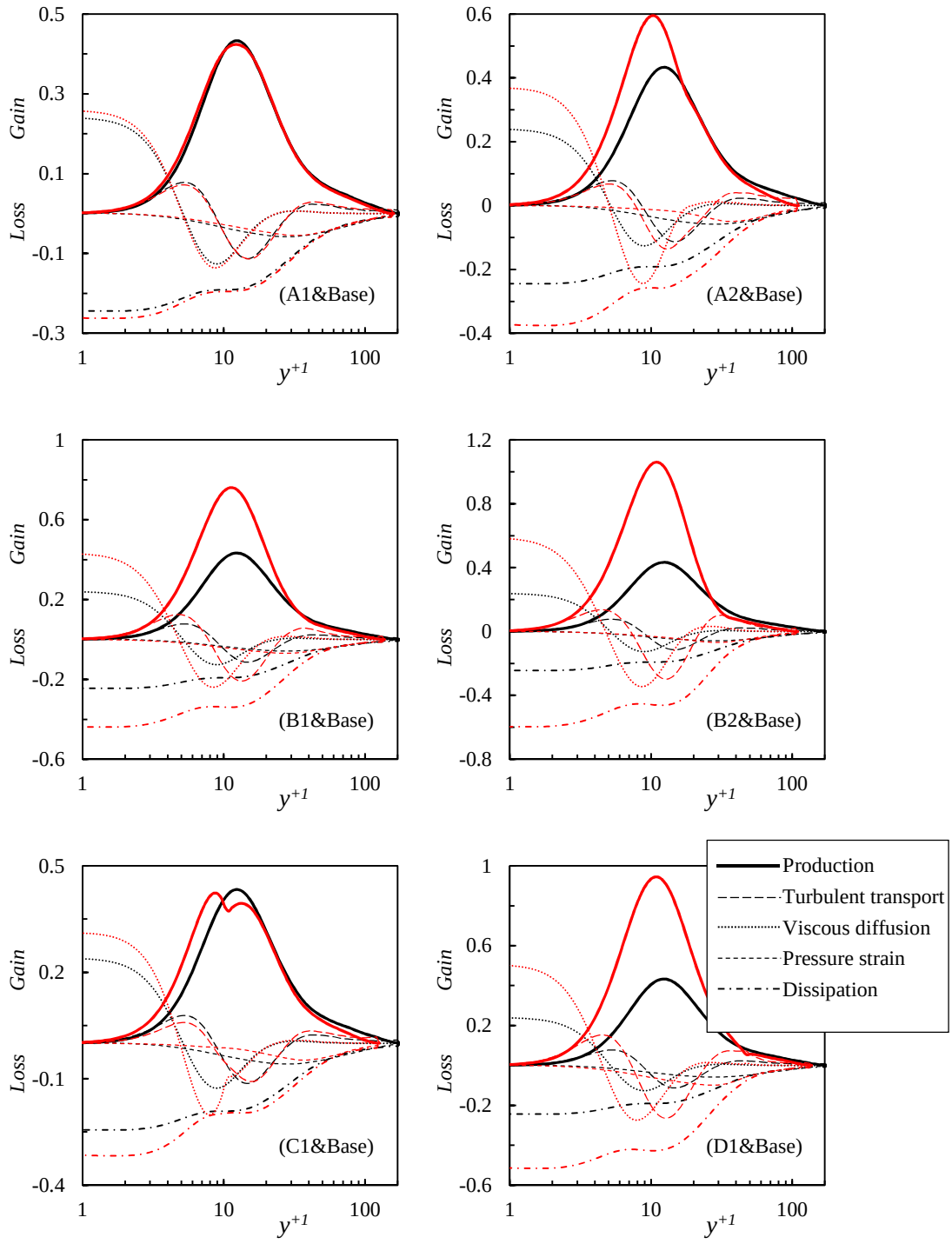

Figure 5.19: The budget terms of $\overline{u'_z u'_z}$ normalized by ${u_{\tau 1}}^4/\nu$.

(Base in black line; Other cases in red line)

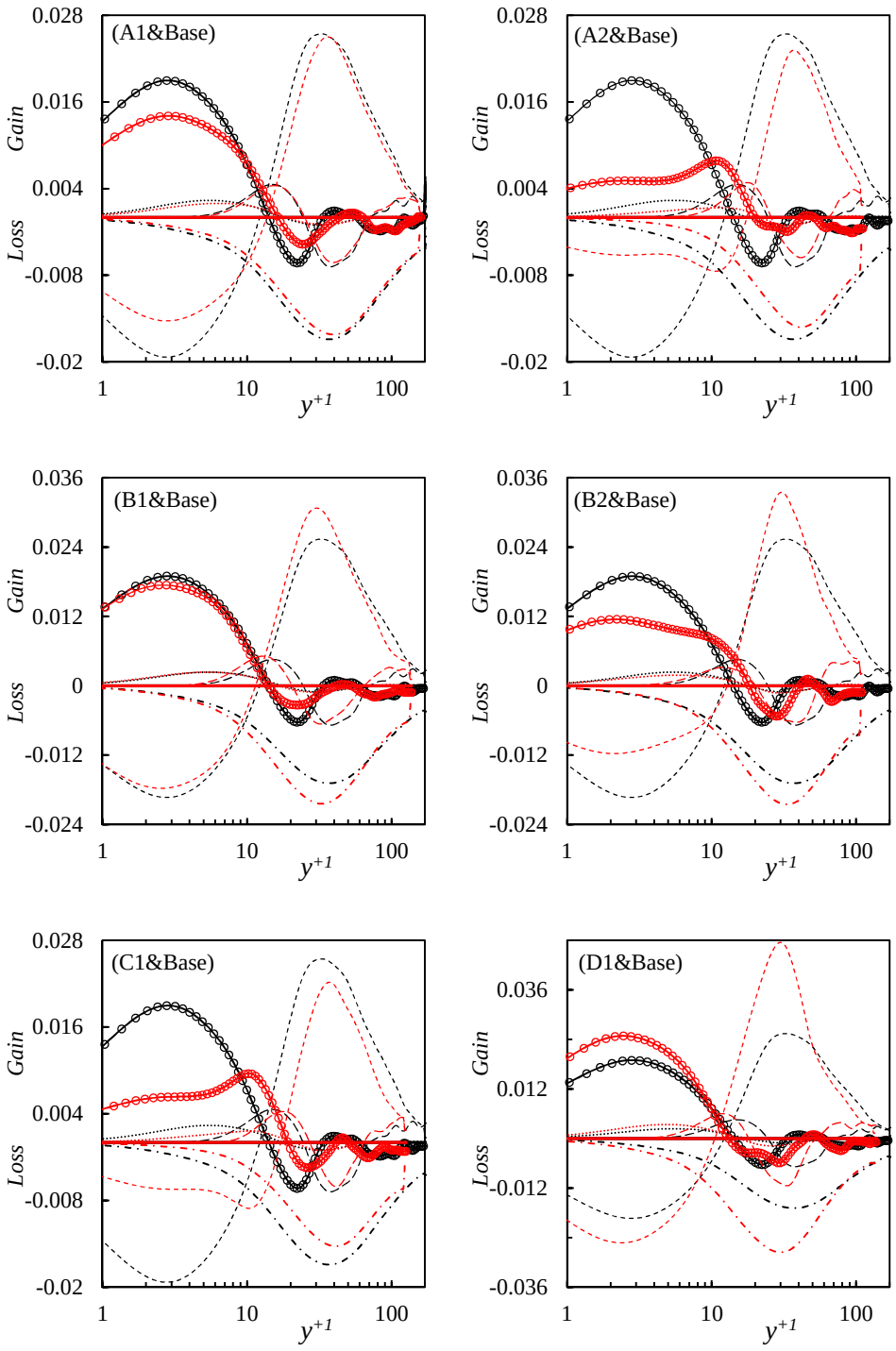

Figure 5.20: The budget terms of $\overline{u'_r u'_r}$ normalized by $u_{\tau 1}{}^4/\nu$.

(Base in black line; Other cases in red line)

Production: ——— ; Turbulent transport: - - - - - ;Viscous diffusion: ·····

Pressure strain: ····· ; Pressure diffusion: —○— ; Dissipation: -·-·-·-

5.2.5 Flow structures

The high and low speed streaks and the vortical cores are visualised in Figure 5.21 using iso-surfaces of fluctuating streamwise velocity u'_z=±0.15 and λ_2=1, respectively. Comparing B1 and B2 with the Re-based reference case, it is clear that both the number of streaks and number of the vortices reduce significantly due to the effect of the body force; and the stronger the body force, the more significant the reduction is. It is interesting to note however, with the increase of the body force, the streaks appear to become longer. This is not surprising since, we noted before, the cases with a stronger body force corresponds to a dp-based reference flow of a lower Reynolds number. It is known that streaks are longer in low Reynolds numbers flows. Next noting that as far as B21 is concerned, the case Base is its dp-based reference case. Comparing these two flows, it appears that the numbers of vortical structures are largely the same in the two flows, whereas there are clearly more streaks in B21 than in Base. This interesting observation is in good accordance with the statistics discussed earlier. The former can be related to the observation that the pressure strain term in the body force influenced cases remains largely unchanged from their corresponding base cases, and in turn the u'_r and u'_θ are also largely unchanged. On the other hand, the increased number of streaks explains the increase in u'_z, even though the vortical structures remain largely changed. The concept of turbulence regeneration cycle has been established over the last couple of decades which successfully explains wall turbulence flow physics and in many cases, flow control and drag reduction applications. Figure 5.14 shows a much simplified sketch illustrating the main processes of the regeneration cycle reproduced from Kim 2011. In leg one, streamwise vortices (primarily consisting of wall-normal and spanwise velocities) interact with the mean shear (dU/dy) generating streaks. This process is often referred

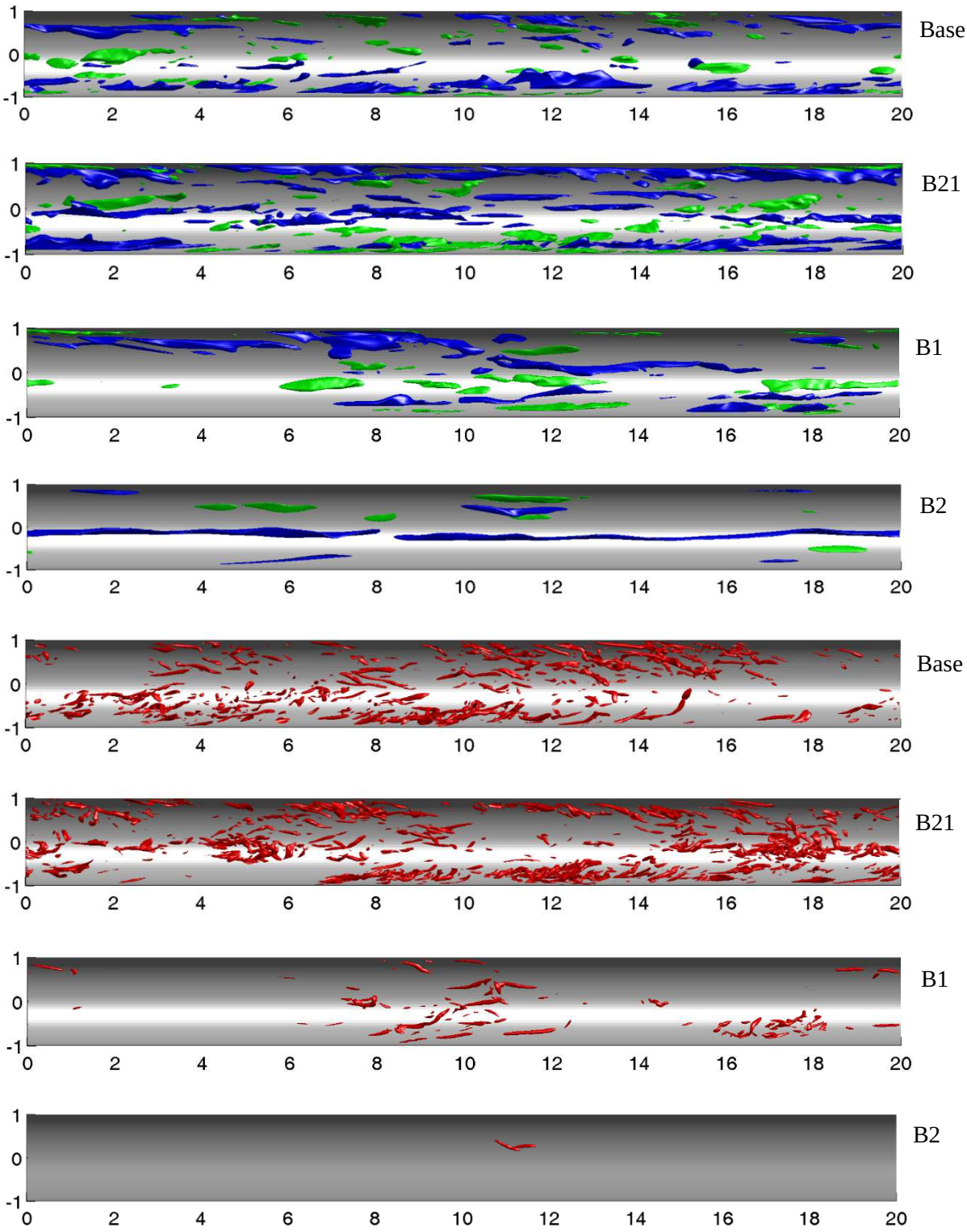

Figure 5.21: The turbulent structures in B2 and its base cases (u'_z=±0.15 and λ_2=1).

to as lift-up. The generated streaks grow as long as the shear is maintained. Later, the streak breaks down due to instability. In leg three, new vortices are formed again resulting from three dimensional disturbances. It is clear that the streamwise vorticity and the wall-normal velocity gradient are two most important factors in turbulence regeneration cycle of a wall shear flow.

Figures 5. 22 (a) and (b) show the r.m.s. of the fluctuating streamwise vorticity in wall coordinates based on the friction velocity of the total flows (u_τ) and the apparent friction velocity ($u_{\tau 1}$), respectively. It can be seen from Figure 5. 22(a) that the vorticity based on the total flow reduces significantly in the various test cases. The reduction is most severe in A2, the value reducing to less than a 1/4 at y^+=1, and the peak away from the wall reducing to about 30% of the reference value. Consequently, the turbulence activities are significantly reduced in the various cases in comparison with the Re-based reference flow. This observation is consistent with the descriptions of laminarization in various scenarios (Iida & Nagano 1998; Willis & Kerswell 2007). The picture is however in strong contrast in Figure 5. 22(b) where the data are normalized using apparent friction velocity. In most cases (except for D1 and B21), the distributions of the streamwise vorticity in the body-force influenced cases agree fair well with their respective bases cases. This implies that the imposition of the body forces does not seem to cause any significant changes in the generation of streamwise vorticity, an important stage in the turbulence regeneration cycle. The increase of the vorticity fluctuations in A2 and D1 can be related to fact that the body force generated turbulent shear stress is larger in those cases, which apparently causes some increase in streamwise vorticity activities. It must be noted however that the increase is still small in comparison to the changes to the flow itself. The imposition of the body force directly results in an increase in the wall-normal

velocity gradient as discussed earlier. Consequently we expect an increase in the velocity of streaks from the imposition of a body force.

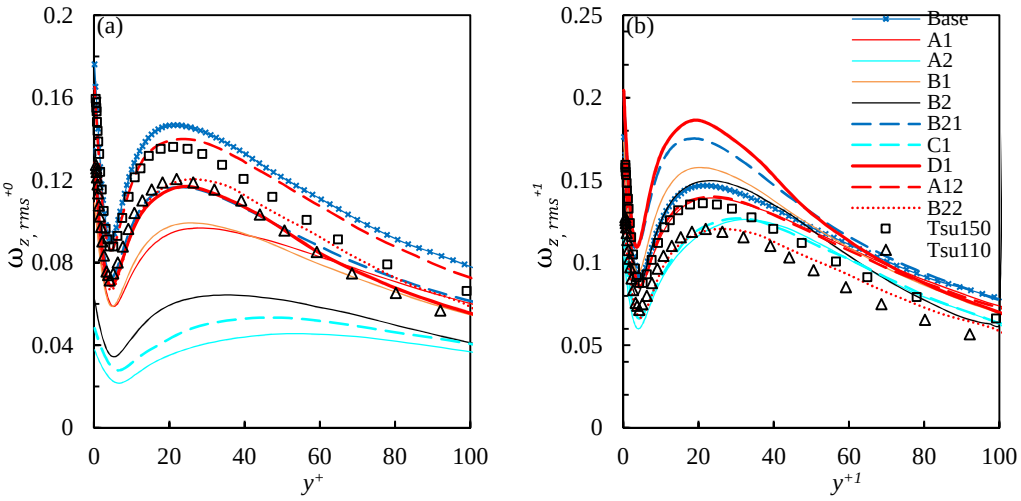

Figure 5.22: The r.m.s of streamwise vorticity normalized by u_τ and $u_{\tau 1}$.

Figure 5.23 shows the contours of the spanwise correlations of the streamwise velocity on the $y-z$ plane in wall coordinates based on the total flow. The data plotted are the amplitude of the negative correlations with the positive correlations set to zero. The location of the peak value (i.e., minimum correlation) provides the following information: $2 \times z_{min}$ is the averaged spacing of the steaks and y_{min} is the averaged wall distance from the centre of the streaks. It can be seen from Figure 5.23 that the averaged spacing of the streaks in the base flow is around 110 ($z_{min}{}^+$= 55) and the wall distance of the averaged streak is $y_{min}{}^+$=14. The streaks spacing in most of the test cases are increased and in some cases, significantly. The largest spacing, occurring in A2, is around z^+= 170. The streak centre also moves away from the wall, and the largest distance is around y^+ =20, occurring in A2 and B2. There are some exceptions to the trends described above: both the streaks spacing and the location do not change significantly in B21 and D1. The same data that shown in the above Figure 5.23 are shown again in Figure 5.24 in the y-

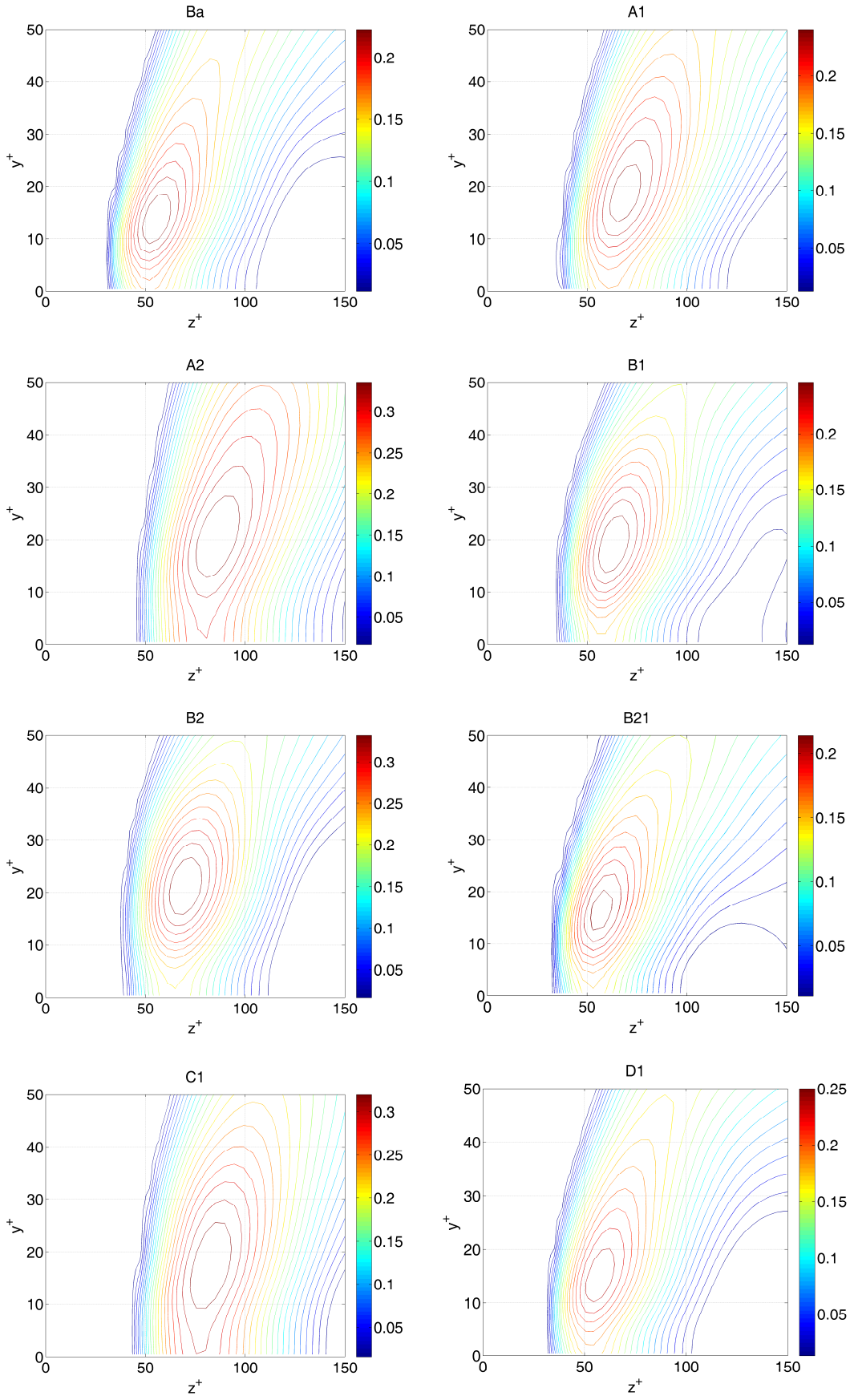

Figure 5.23: The spanwise correlation of u'_z normalized by u_τ.

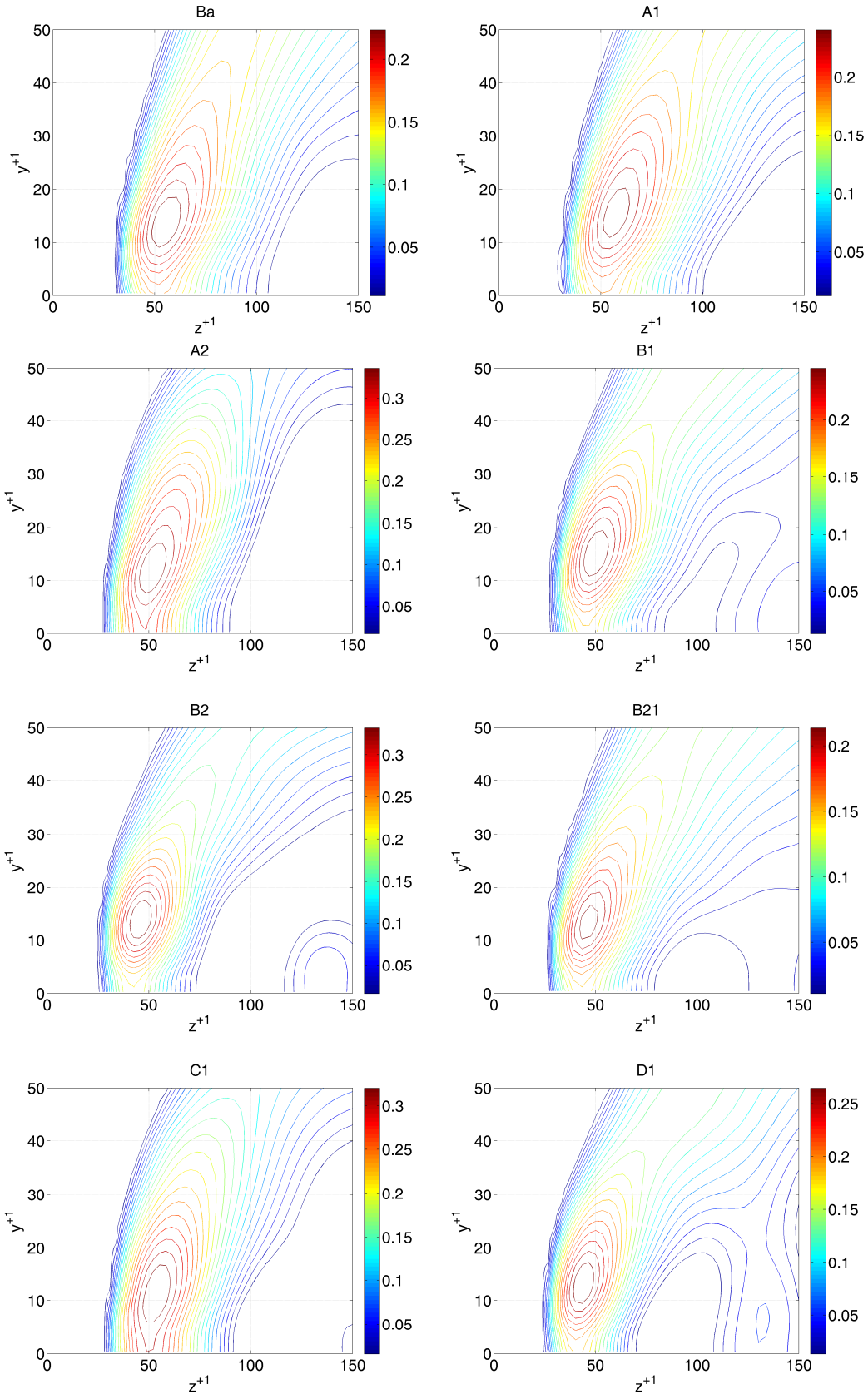

Figure 5.24: The spanwise correlation of u'_z normalized by $u_{\tau p}$.

$-z$ plane wall coordinates based on the apparent friction velocity. In most cases, both the averaged spacing of the steaks ($2 \times z_{min}$) and the wall distance of the streaks centres are similar to those of the reference flow (of the same Re). The exceptions are cases B2, D1 and B21, where the spacing is reduced to about 90 but the vertical locations of the streaks centres are similar to that of the reference flow.

The near wall turbulence structures can be studied through inspecting the ejection and sweep events which are associated with the vortices and streaks (Wallace *et al*. 1972; Kim *et al*. 1987). Quadrant analysis is a useful tool for studying the contribution of various flow events to the total turbulence production. Turbulent events are divided into four groups according to the four quadrants of the $u'-v'$ plane (Q1: $u'>0$ & $v'>0$; Q2: $u'<0$& $v'>0$; Q3: $u'<0$ & $v'<0$; Q4: $u'>0$ & $v'<0$), where u' and v' are streamwise and wall-normal fluctuation velocities respectively. Using the definition of the hyperbolic hole introduced by Lu & Willmarth's (1973), the contribution of each quadrant to $\overline{uv}$ is defined as

$$(\overline{uv})_Q = lim\frac{1}{T}\int_0^T u'v'\, I(t)dt \tag{5.16}$$

where, $I(t)$ is an indicator function defined so that

$$I(t) = \begin{cases} 1, & |u'v'|_Q \geq Hu'_{rms}v'_{rms} \\ 0, & otherwise \end{cases} \tag{5.17}$$

Figures 5.25(a) and (b) show the percentages of the numbers of ejection and sweep of the total turbulent events that create turbulent shear stress, and Figures 5. 26(c) and (d) show the values of the shear stress associated with these two activities. A hyperbolic hole H=1 is used to study those flow events with high amplitude. The H could be a larger integer value like 2, 3, 4, but the features of these plots are similar (not shown here). It is

most interesting to see that the number of the events in the body force influenced cases remains more or less unchanged from their corresponding base cases, while the impact on the shear stress however is significantly increased in the wall region (comparing the Base case and B21). That is, the strength of each event (Q2 & Q4) of B21 is stronger. These can be nicely linked to the observations discussed above on vorticity and streaks. It appears that the imposition of the body force which induces an additional boundary layer near the wall, does not significantly influence the generation of vortices, but for each ejection or sweep event, a larger shear stress is resulted in due to the larger velocity gradient. Additional it is interesting to note that the influence on the ejection events occurs in the region of $10<y^+<60$, where the effect on sweep is restricted to $y^+<30$. This is consistent with previous studies on drag reductions (Choi *et al.* 1994).

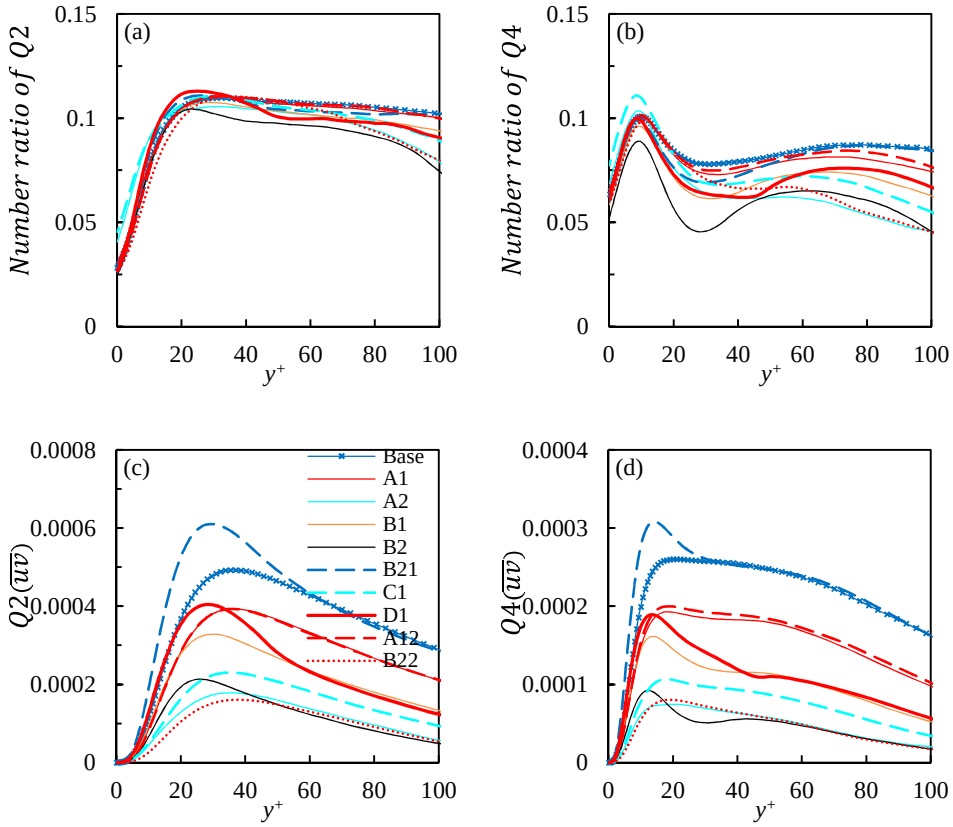

Figure 5.25: The changes of sweeps and ejections.
(y normalized by apparent u_τ)

Next we evaluate the turbulent anisotropy by analysing the anisotropy-invariant map (AIM) of the Reynolds stress anisotropy tensor (b_{ij}):

$$b_{ij} = \frac{\overline{u_i u_j}}{\overline{u_i u_j}} - \frac{\delta_{ij}}{3} \tag{5.18}$$

$$II = -\frac{1}{2}\left({b_{zz}}^2 + {b_{rr}}^2 + {b_{\theta\theta}}^2 + 2{b_{zr}}^2\right) \tag{5.19}$$

$$III = b_{\theta\theta} b_{zz} b_{rr} + b_{\theta\theta} {b_{zr}}^2 \tag{5.20}$$

where $\delta_{ij}$is the Kronecker delta tensor.

The AIM proposed by Tennekes and Lumley (1972) is constructed using the second (II) and the third principal invariants (III), which are independent of the coordinate choice. The Lumley's anisotropic map provides useful information on the streaky structures since they are inherently anisotropic. The AIMs for the various body force influenced cases are plotted on top of that of the Re-bases reference flow in Figure 5.26.

It can be seen clearly that in all cases the profile moves towards the top right vertex, indicating that the flow becomes more one-dimensional and further demonstrating the streaky structures are elongated under the influence of the body force. The stronger the body force, the stronger the one-dimensional feature of the flow. In fact, the profile nearly reaches the top-right vertex in A2 and B2, showing the existence of strong streaks in the flow. The profile in the undisturbed turbulent flow often occurs around y^+=9. It can be seen that this point is only shifted slightly away from the wall in the body force influenced cases even though the strength are significantly decreased. When measured using the wall units based on the dp-base cases, the values actually reduce slightly. In most cases, they remains at y^{+1}=7 (normalized by apparent Reynolds number defined in 5.2.2).

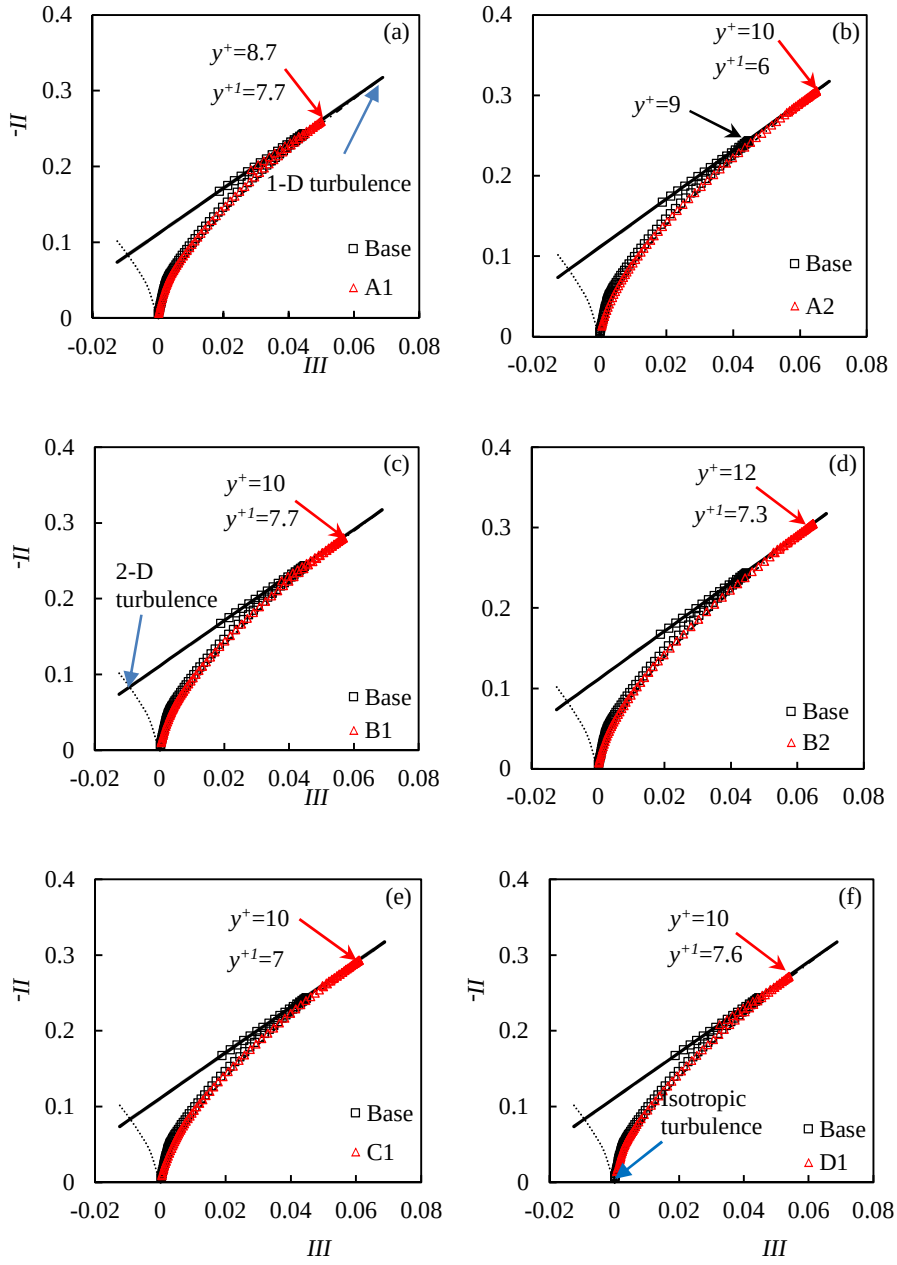

Figure 5.26: The anisotropy-invariant map of partially laminarized flows.

5.3 Completely laminarized flow

5.3.1 Analysis based on the new theory

Consider a turbulent flow at a prescribed Reynolds number subjected to a non-uniformly distributed body force. From the results presented in §5.2, as well as research from the

literature, we know that with the increase of the imposed body force while keeping the Re constant, the turbulence will be more strongly suppressed, that is, the flow is more severely laminarized. The term 'laminarization' refers to a comparison with a reference flow at the same Reynolds number. At some stage, the flow can become fully laminarized, as that in A3 and B3. The above scenario occurs in many applications and one example is the mixed convection, where the flow becomes more and more laminarized with the increase of the buoyancy force (Jackson 2011).

The above process can be described with the new theory presented above in §5.2. The body-force influenced flow can be decomposed into a pressure-driven flow (i.e., the dp-based reference flow) and a perturbation flow due to the body force. The former can be approximated by an undisturbed turbulent pipe flow, whereas the latter is a flow described by Eqn 5.6, which is dependent on the imposed body force and the dp-based reference flow (through ν_{t1}). The dp-based reference flow is the difference between the total flow and the perturbation due to the body force, that is, $Q_{dp} = Q_{tot} - Q_{bf}$. With the increase of the body force (bf) while keeping the total flow constant, Q_{bf} increases and hence Q_{dp} reduces. There will be a point when the Reynolds number of the pressure driven flow is so low that it cannot sustain turbulence any longer, and hence the flow becomes laminar. This critical body force can be calculated using Eqn 5.6 given the critical Reynolds number, say, 2300. Here we can choose to use a laminar flow formulation (i.e., letting $\nu_{t1} = 0$) or a turbulent viscosity. The former will give a higher U_{bf} and hence a lower U_{dp} for a fixed total velocity U_{tot}, and hence a lower critical body force, i.e., giving the lower bound. In reality, the flow under the influence of the critical body force base on $\nu_{t1} = 0$ may still remain turbulent if sufficient disturbances are present.

Following the approach adopted by Fukagata $et\ al.$ (2002), integrating Eqn 5.6 three times and using integration by parts, we can derive the expression for the mean velocity for the perturbation flow driven by the body force:

$$U_{m,bf} = Re_b \left[\frac{1}{2}\int_0^1 (1-r^2) bf\ r dr + \frac{1}{2}\int_0^1 2r\ \overline{uv}_{\mathrm{bf}}\ r dr\right] \tag{5.21}$$

Given the mean velocity, the critical Reynolds number for the pressure driven flow to maintain turbulence is

$$Re_{dp,cr} = \frac{(U_m - U_{m,bf})R}{\nu} > 2300 \tag{5.22}$$

which can be expressed in terms of body-force driven flow Reynolds number,

$$Re_{bf}\left(= \frac{U_{m,bf}R}{\nu}\right) > Re - 2300 \tag{5.23}$$

More specifically, we consider profiles of body forces:

$$bf = \begin{cases} bf_w & y < yc, \text{otherwise } 0 \\ -\frac{bf_w}{yc} r + bf_w & y < yc, \text{otherwise } 0 \end{cases} \tag{5.24}$$

in which, yc is the coverage of the body force.

It is easy to obtain the solution of $U_{m,bf}$ from 5.21. For linear change body force,

$$U_{m,bf} = 0.5 Re_b \left|\frac{a}{3}r^3 - \frac{a}{5}r^5 + \frac{b}{2}r^3 - \frac{b}{4}r^4\right|_{1-yc}^{1} + Re_b \int_0^1 r\ \overline{uv}_0\ r dr \tag{5.25}$$

For step change body force,

$$U_{m,bf} = 0.5 Re_b bf_w \left(\frac{1}{4} - \frac{(1-yc)^2}{2} + \frac{(1-yc)^4}{4}\right) + Re_b \int_0^1 r\ \overline{uv}_0\ r dr \tag{5.26}$$

$$a = \frac{bf_w}{yc} \tag{5.27}$$

$$b = bf_w \left(\frac{yc-1}{yc}\right) \tag{5.28}$$

For facilitating the discussion we drop $Re_b \int_0^1 r\ \overline{uv}_0\ r dr$ first. The requirement of a critical Reynolds stress number should satisfy

$$bf_w \left(\frac{3(1-yc)^5}{60yc} - \frac{10(1-yc)^3}{60yc} + \frac{15(1-yc)}{60yc} - \frac{8}{60yc}\right) > \frac{2300}{{Re_b}^2} \tag{5.29}$$

Let $P = \left(\frac{3(1-yc)^5}{60yc} - \frac{10(1-yc)^3}{60yc} + \frac{15(1-yc)}{60yc} - \frac{8}{60yc}\right)$. The P is plotted against the body force coverage in Figure 5.27. There are 2 qualitative features implied by Figure 5.27 are consistent to the previous DNS results. Firstly, it is seen that as the coverage of the body force increases, for both step change body force and linear change body force, the critical amplitude of them that may completely laminarize the flow reduces. Secondly, the change of coverage of step varying body force has more significant effect on the turbulence than the linear varying body force. It should be noted that it is hard to get the exact critical body force due to the term $Re_b \int_0^1 r\,\overline{uv}_0\,rdr$ is dropped, which is not zero even at very low Reynolds number.

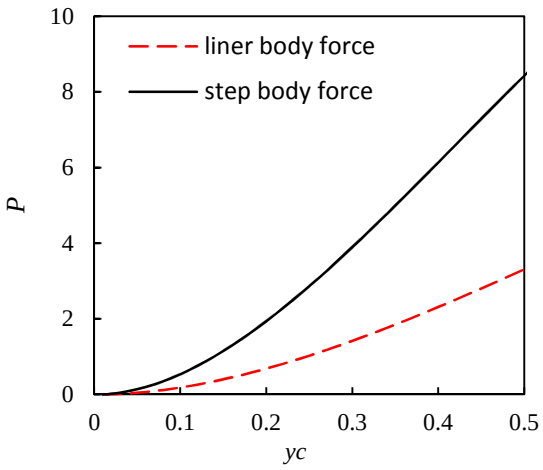

Figure 5.27: The critical body force coverage and amplitude.

It should be noted that for flows at a low but above the critical Reynolds number, the flow is actually in the transitional regime. The flows in several cases (such as A2 and B2) are in this category. Flow laminarization (reverse transition) or the 'forward' transition are not an absolute, definitive event, but to some extent is dependent on the flow conditions. In experiments, the flow can become laminar flow at a rather high Reynolds number if the experimental facility is free from disturbances and noises. In

computer simulations, the initialisation of the flow and the size of the domain will all influence the critical Reynolds number. In the study of Tsukahara $et\ al.$ (2014), they have achieved turbulent/transitional flow in a channel at Re_τ=64. In the present study, we have not attempted systematically increasing the body force to determine the critical flow. However, in Groups A and B, the cases with the highest body force that still remain turbulent are cases A2 and B2, and their Reynolds numbers (Re_p) are 3100 and 2862, (or for Re_τ, 113 and 110), respectively. Cases A3 and B3 are evidently laminarized, but the body force driven flow is significantly greater than the critical value required to just cause flow laminarization.

5.3.2 Flow visualization

Figure 5.28 shows the contours of u'_z of A3 & B3 & C2 & A3. In A3, the contours of u'_z show that there are short and wavy structures, which are away from the wall in the cross-pipe observation. In B3, the structures are smooth and longer than the flow domain. There are very weak structures shown in C2. D2 shows a transitional feature, where the flow structures are like a trace of a turbulent spot. These observations show that the typical coherent structures disappear, which is similar to many other studies on transitional or laminarized flows, or mixed convection flows (Willis & Kerswell 2007; Bae $et\ al.$ 2008).

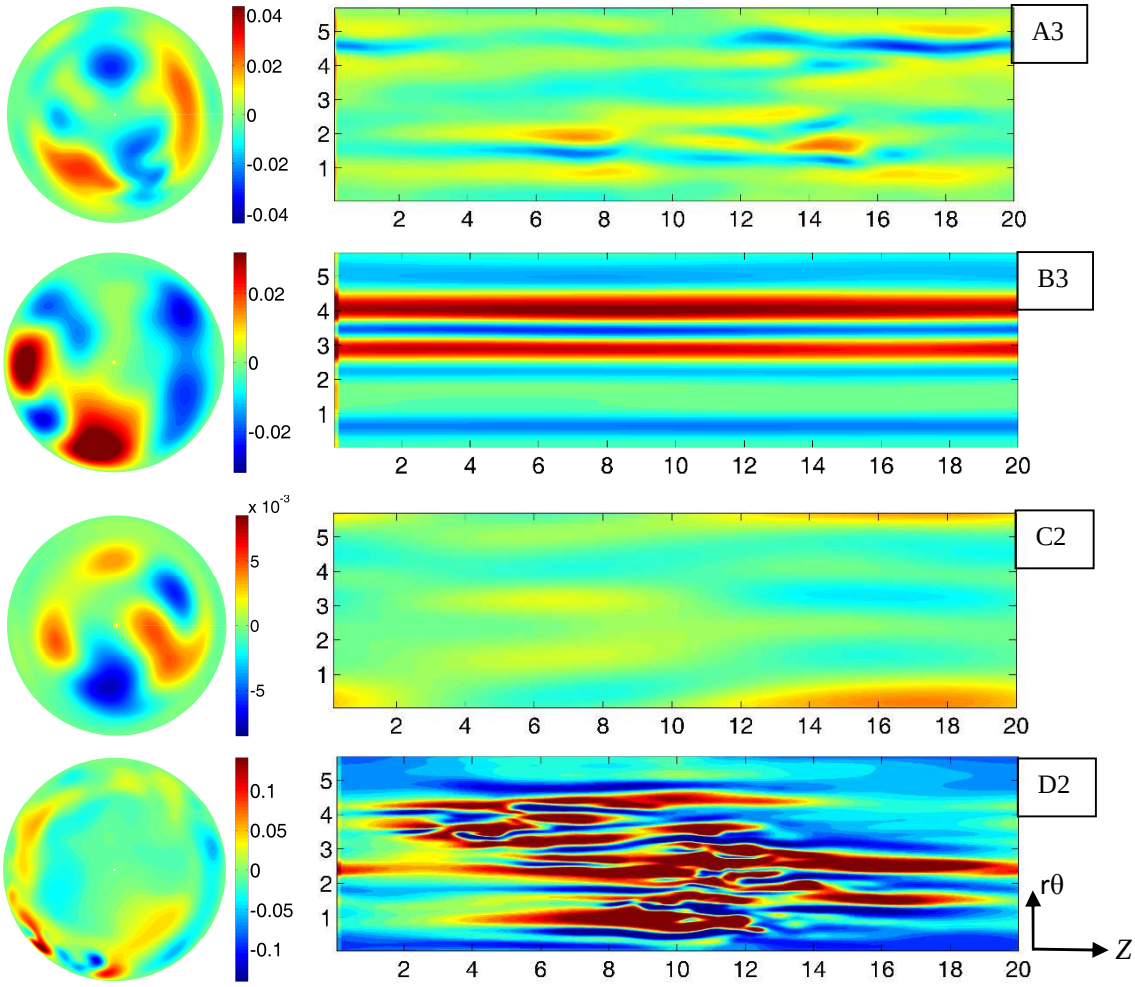

Figure 5.28: Contours of u'_z at z-θ plane (y^{+0}=17) and at r-θ plane (z/*R*=0.3).

$u'_z = \pm 1.5 u_{zrms,p}$

5.4 Partially recovery flow

As the *F* increases, the body force induced mean flow becomes larger than that of base flow, which means that the *dp*– base flow becomes negative in some cases. These flows are more complicated because the turbulence generation at the outer second shear layer influences the inner turbulence generation, which is usually described as a cyclic behaviour (Waleffe 1997). In this section, some basic statistics of these flows are studied to show the physical features of such flows.

5.4.1 The mean and r.m.s velocities

The mean velocities of partially recovery flows are all M-shaped (shown in Figure 5.29). With the increase of F, the peak of the mean velocity profile moves toward the wall. Figure 5.29(b) shows that there are two peaks on in the $u'_{z,rms}$, implying that there are two turbulence generation mechanisms. The outer one is generated by the new shear layers. The inner one is the recovery of the near wall turbulence.

The effects of the amplitude and coverage of the body force on $u'_{z,rms}$ are revealed by comparative study between selected case pairs. For instance, the total force *F* and the coverages of B5 and D3 are the same but the recovery of $u'_{z,rms}$ is found significantly higher in step change case D3. It seems that a step-change body force has a stronger effect on the turbulence causing a greater recovery. Figure 5.30 shows the distribution of body force in A4, B5, C3 and D3. The body force of B5 has the highest near wall force density among these cases and then C3, A4 and D3. The body force density of B5 is higher than that of A4 at y^{+0}<45, therefore, the inner peak of B5 is significantly lower than that of A4. The outer peak of $u'_{z,rms}$ depends on the force density around the new shear layer. The illustrative pairs are B5 & B6, and C3 & D3, where the body force coverage are the same but the value of F different. The outer peaks as well as the inner peaks increase with F. It seems that there is only one peak in $u'_{r,rms}$ but two peaks in $u'_{\theta,rms}$. However, this is due to that the inner peaks of $u'_{r,rms}$ are weak and they merge with the outer ones. This is evident in section 5.5.2 in $u'_{r,rms}$ of C4. The $u'_{r,rms}$ and $u'_{\theta,rms}$ grow with *F* and they are slightly affected by the force distribution pattern. The recoveries of $u'_{r,rms}$ and $u'_{\theta,rms}$, which is shown in Figure 5.29(c) and (d), are not correlated with the growth of $u'_{z,rms}$. For example, the $u'_{z,rms}$ of B6 is lower than D3,

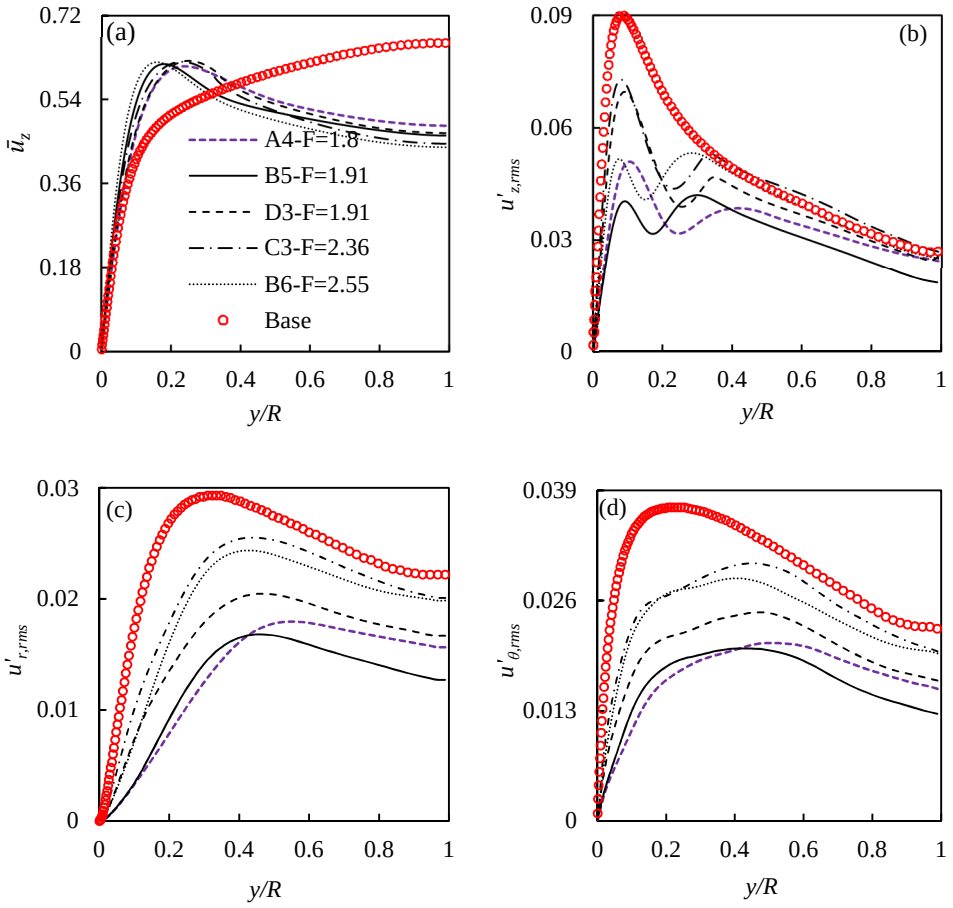

Figure 5.29: Mean and r.m.s velocities of partially recovery flow.

(a) $\overline{u_z}$; (b) $u'_{z,rms}$; (c) $u'_{r,rms}$; (d) $u'_{\theta,rms}$.

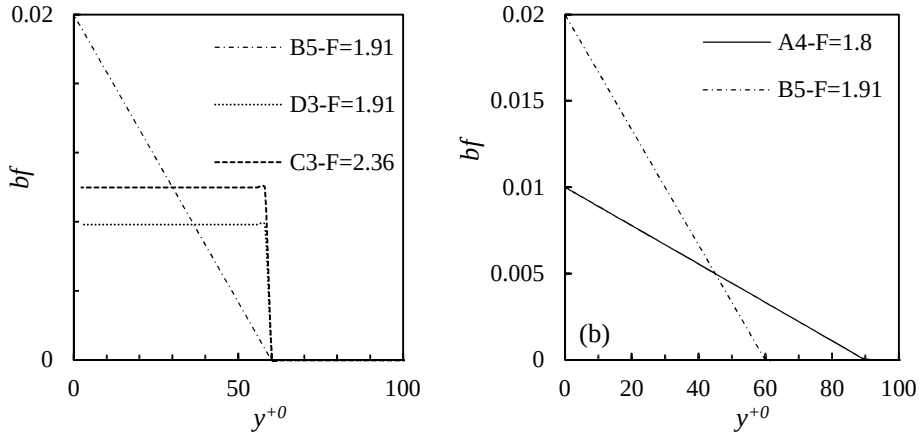

Figure 5.30: The body force distirbution in selected cases.

(a) C3, B5 and D3; (b) A4 and B5.

but the $u'_{r,rms}$ and $u'_{\theta,rms}$ of B6 are higher than that of D3. These data implies that although the higher force density of B6 may suppress the near wall streaks and turbulence generation, the turbulence transported from the outer generation region of B6 is stronger than that of D3. The following discussion is further devoted to reveal the feature of the inner turbulence generation and how the inner turbulence generation mechanism is affected by the outer generation.

5.4.2 The streamwise and spanwise correlations

The streamwise and spanwise correlation of u'_z is useful to characterize the turbulent structures at near wall region. Figure 5.31(a) shows that the length of the near wall structure is reduced in most cases compared to the base case. The spanwise correlation illustrates that the mean spanwise spacing decreases in these cases, which is consistent with the number increase of the streaky structures (shown later). The minimum peak reflects the strength separation between low speed streaks and high speed streaks. It is indicated that the low speed structures are relatively enhanced in B5, C3 and D3.

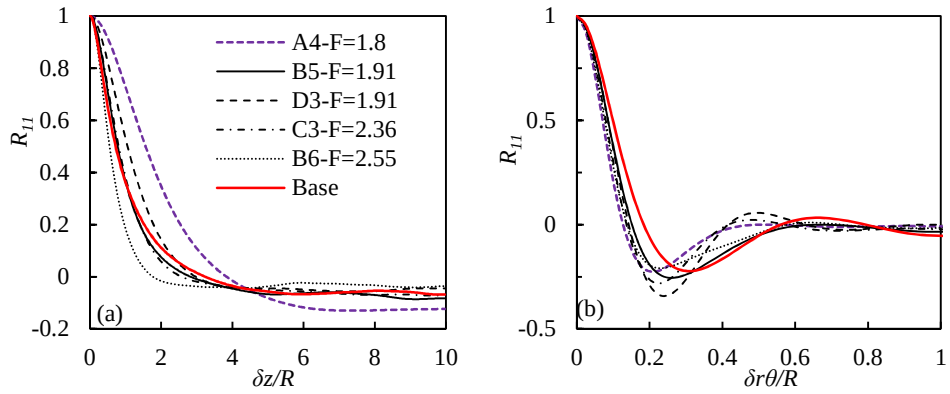

Figure 5.31: The spanwise and streamwise correlations of u'_z of partially recovery flow.
(a) Streamwise correlation; (b) Spanwise correlation(at y^{+0}=6.4).

5.4.3 The 2-D visualization of the flow

The contours of u'_z in Figure 5.32 provide observations on the streaky structures, which show that the low speed streaky structures are recovered strongly in A4, C3 and D3.

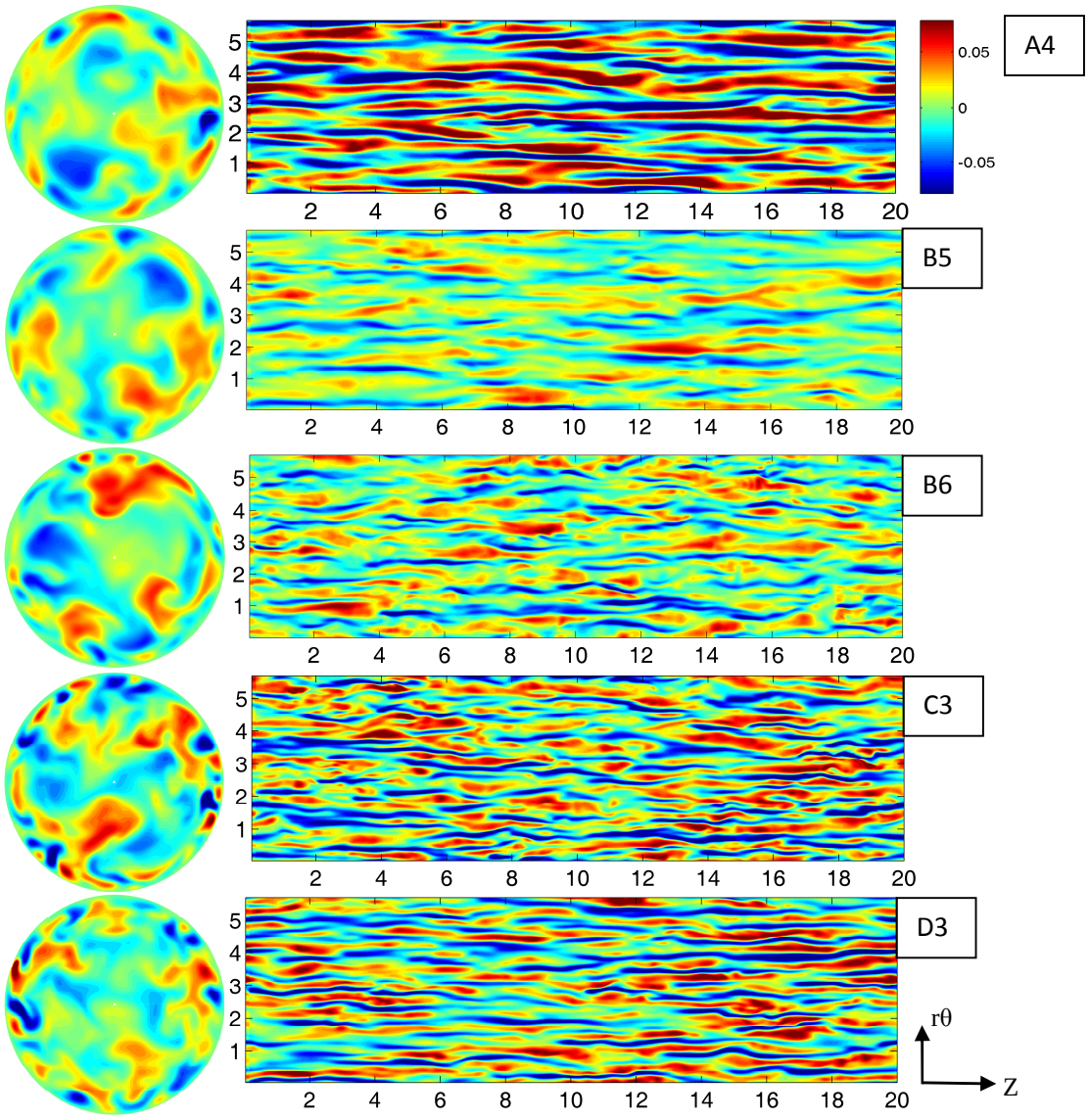

Figure 5.32: Contour of u'_z of partially recovery flow (u'_z=±1.5$u'_{z,rms,p0}$, $u'_{z,rms,p0}$: peak r.m.s of streamwise velocity fluctuation of base flow).

The structures in streamwise as well as in spanwise are similar to those structures in the base flow. The strength of the streaky streaks is weaker in B5 and B6, compared to the other cases. The spanwise flow visualization shows that the structures are not confined to

the wall in A4, B5 and B6. By contrast, there are stronger streaks confined closer to the wall in C3 & D3. As indicated by $u'_{z,rms}$, the streaks are strongly suppressed in B5 & B6.

5.4.4 The 3-D visualization of the flow

The 3-D visualization of streaky and vortical structures are shown in Figure 5.33 by iso-surfaces of u'_z and λ_2. The reference value is based on r.m.s peak of individual flow. Figure 5.33 shows that the number of high speed structures is significantly increased, which is related to the diffusion of outer turbulence. In B5 and C3, there are more high speed structures. The visualization referenced by the local peak of *r.m.s* does not show how strongly the near wall turbulence is recovered compared to the base flow. For completeness, the same visualization based on the peak of *r.m.s* of base flow is shown in Figure 5.34. It shows that the recovery of the turbulence is weak in A4, B5, where no flow structures can be observed. The vortical structures in B6 are stronger but they are detached from the wall and are almost isotropic, indicating that the presence of these structures is more related to the outer shear layer. Only in C3, there are some vortices and the low speed streaks. But these vortices are not as organised as that of base flow. Overall, there are no typical coherent structures in these cases. The coherent structures seem to recover in C3 and D3 but they are weak and influenced by the outer turbulence.

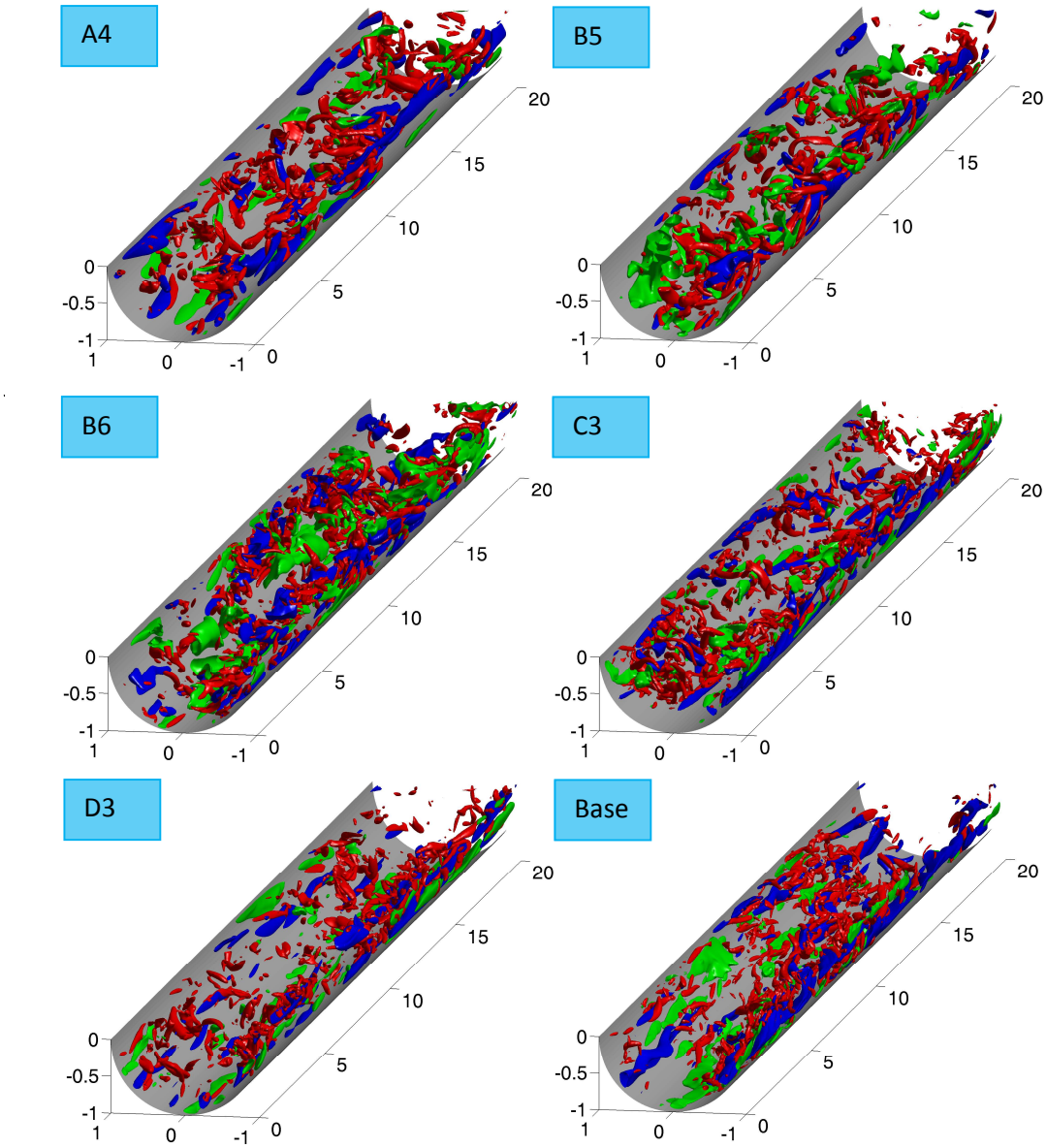

Figure 5.33: The streaky and vortical structure in partially recovery flow.

$u'_z = \pm 1.5 u_{zrms,p}$, $\lambda_2 = \pm 2\lambda_{2_{rms,p}}$

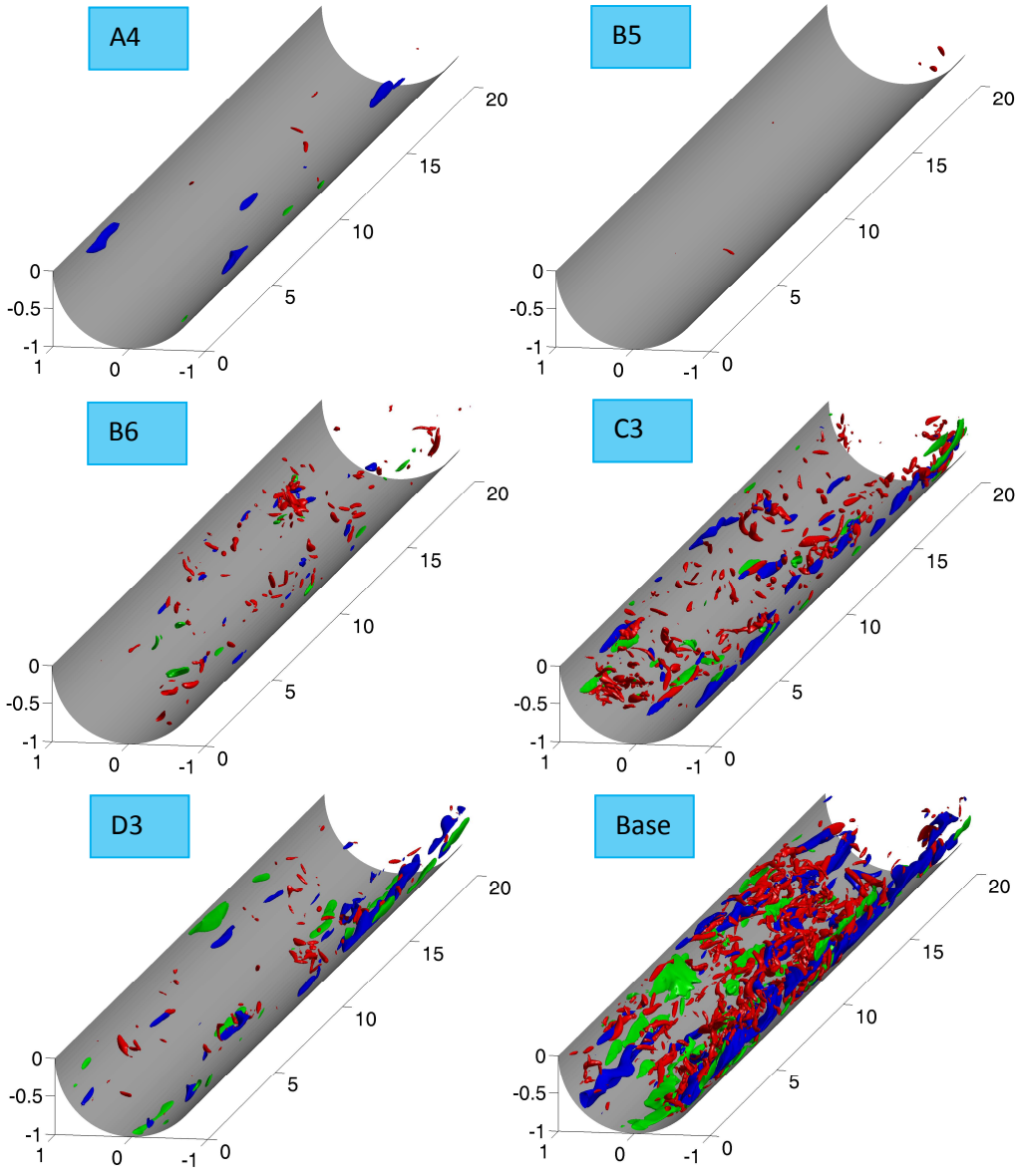

Figure 5.34: The streaky and vortical structure in partially recovery flow.

$u'_z = \pm 1.5 u_{zrms,p0}$, $\lambda_2 = \pm 2\lambda_{2_{rms,p0}}$

5.4.5 Reynolds stress

The Reynolds stress of partially recovery flow shows (Figure 5.35) that the near wall recovery is weak in A4, B5 and B6. The outer recovery is linearly related to the total force amplitude, which is shown by the correlation in section 5. 1. For these cases shown here,

it seems that the amplitude of Reynolds stress at the centre region is influenced by the density of force at this region.

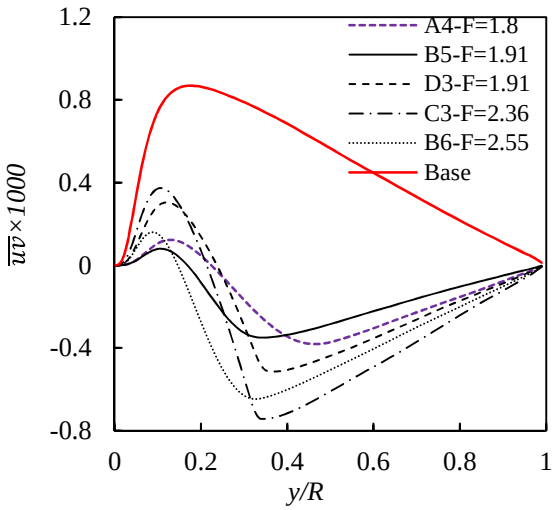

Figure 5.35: The $\overline{uv}$ of partially recovery flow.

5.4.6 Quadrant analysis

As the near wall turbulence recovers, it is interesting to examine if the Reynolds stress structure is still similar to that of base flow. In a standard quadrant analysis, the $\overline{uv}$ contributions from sweeps and ejections reflect the near wall turbulent structures. In Figure 5.36, the data are only showed up to y^+<20, where the Reynolds stress does not change sign. The contributions from sweeps in all cases are reduced. In this region of the base flow, the balance of Reynolds stress is established between sweeps and ejections, where the contribution of sweeps is dominant. The C3 and D3 show similar structure to the base flow but the contribution of sweeps reduces slightly. In A4, B5 and B6, the contributions of sweeps and ejections are similar. This phenomenon shows that the coherent structures are not recovered in these flows.

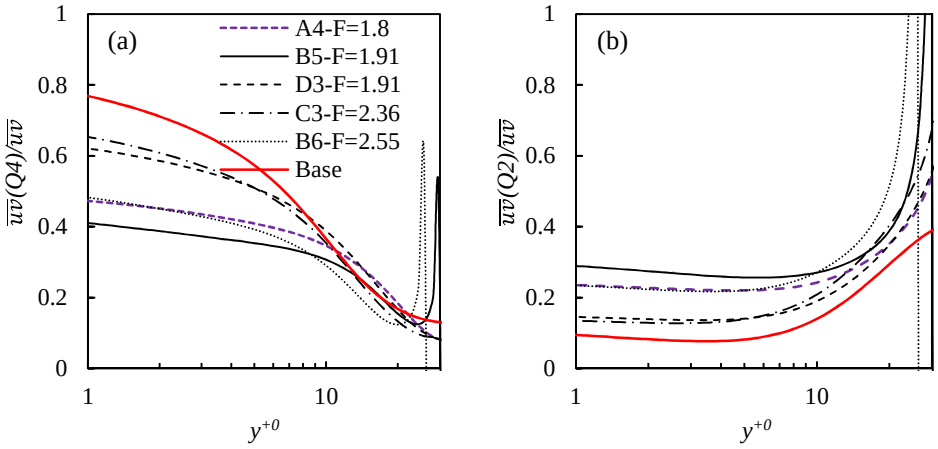

Figure 5. 36: The contribution of sweeps and ejections to $\overline{uv}$.

5.4.7 Flatness and skewness

The flatness and skewness further show that the turbulent structures in partially recovery flow are complicated. They are shown in Figure 5.37. The flatness factors of u'_z and u'_r of base flow, which are equal to 3 at the centre region, assuming a Gaussian distribution. The flatness of u'_θ in the base flow is 3.3, which is also close to a Gaussian distribution. The flatness of u'_z has changed in the recovery flow. In the near wall region (y^{+0}<30), they overshoot the base flow data. The minimum peak is at y^{+0}=15 in the base flow, which is due to the strong separation between low speed and high speed streaks. This structure is changed in body force influenced cases, where there are two peaks. The minimum peaks are roughly at a similar location as that of base flow but their value increases, reflecting the increase of intermittency. The local maximum peaks indicate that the turbulence in this region (15< y^{+0}<60) is a mixture of inner turbulence and outer turbulence. In the centre region, the flatness of u'_z of the partially recovery flow collapses but the value is lower than that of base flow. This indicates that the mixing is better than that of base flow in the centre region. The flatness factors of u'_r of these partially recovery flows are mostly unchanged in the centre region, where the flatness factors of

u'_r still show Gaussian distribution. In a region, 10< y^{+0}<50, the flatness factors of u'_r increase, indicating that the intermittency is enhanced.

The skewnesses of the three components reflect more detailed features of near wall turbulent structures. The skewness of u'_z of the base flow is positive at y^{+0}<12, where the high speed structure is dominant. This feature does not change in these partially recovery flows. The skewnesses of high speed structures are suppressed in B5 and B6.

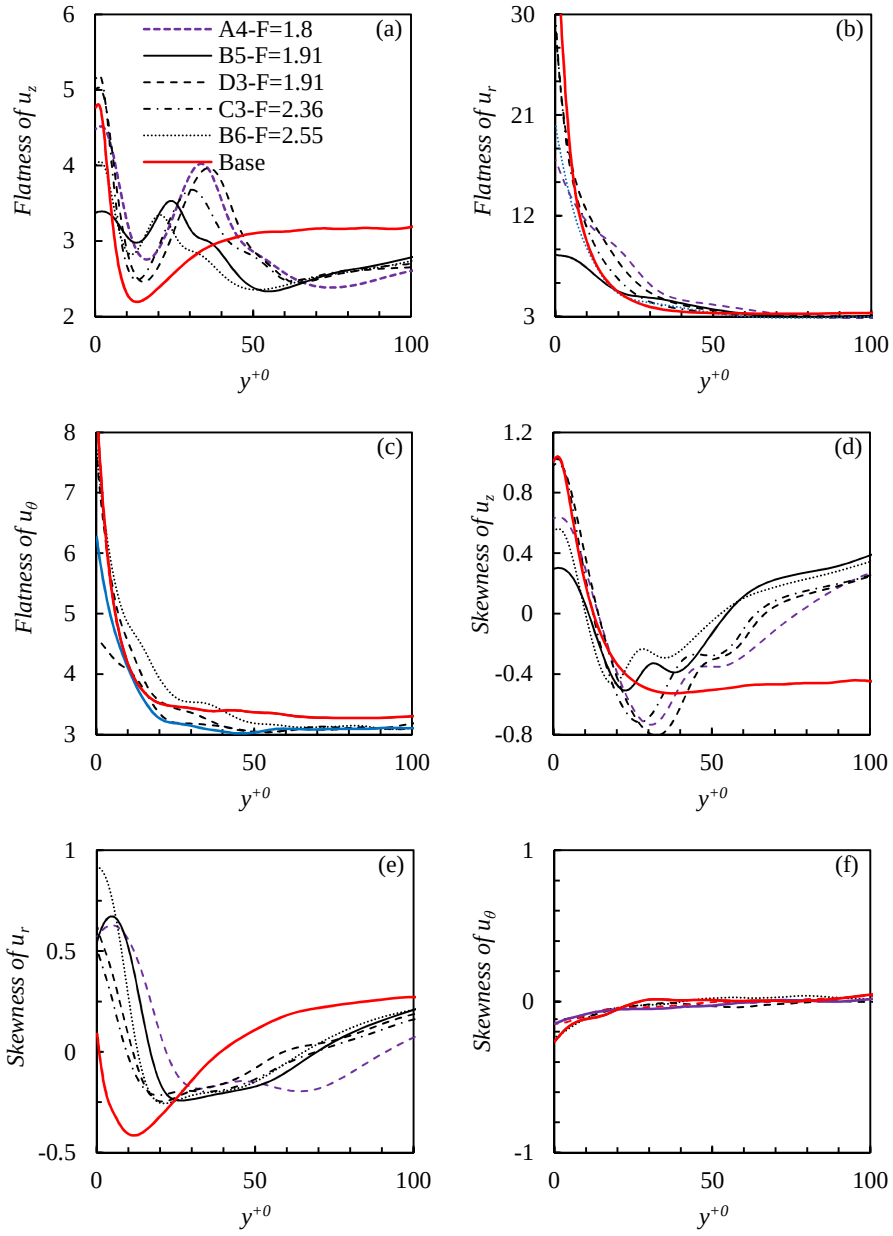

Figure 5.37: The flatness and skewness of partially recovery flow.

The change of skewness is observed at y^{+0}>40. Toward the centre, the low speed structure is still dominant. The high speed structures become dominant at y^{+0}>60 in the flow. Between y^{+0}=12 and y^{+0}=40, the low speed structure is dominant but its value is enhanced (A4, C3 and D4) or suppressed (B5 and B6). These features reflect the complicate interactions between inner turbulence and outer turbulence.

The skewness of u'_r increases near wall, which indicates the existence of strong outward motions. There is a region ($y^{+0} < 2$) in the base flow where the skewness is positive, but this region is extended significantly in the recovery flow, indicating that the outward motions are significantly enhanced. This is attributed to the strong reflection of flow motions induced by the 'splatting' effect (Kim $et\ al.$ 1987; Bradshaw 1994), which is described by Bradshaw (1994) as the process of eddies outside the boundary layer being brought to rest at the wall due to the impermeability condition. In these partially recovery flows, the skewness of u'_r ($20 < y^{+0}$<60) shows a negative flatten region, which illustrates the dominant role of stronger downward motions. These changes in flatness and skewness reflect that the turbulence in the near wall region is 'scratched' by the turbulence from the outer region and trigger the generation of streaks and inner turbulence.

5.4.8 Budget terms

The budgets of $\overline{u'_z u'_z}$ of the partially recovery flow are plotted in Figure 5.38. As expected, the near wall production of C3 and D3 are maximally recovered. Although there is near wall production in A4, B5 and B6, all the terms including the turbulent transport, viscous diffusion, pressure strain and dissipation for y^+<12 are very low. This implies that the near wall turbulence is not recovered in these cases. Figure 5.38(f) shows the balance of the budget of D3 and base flow ($Re_\tau = 180$), where the budget values of base

flow are divided by 5 to facilitate the reading. In D3, the dominant budget terms in y^+<40 are production, dissipation, turbulent transport and viscous diffusion, which is similar to that of the base flow. In the other region, the dominant terms are production, pressure strain, turbulent transport and dissipation, where the production is balanced by the dissipation, pressure strain and turbulent transport. The dissipation has not changed as significantly as the pressure strain and turbulent transport. The latter have sharp peaks.

The budget terms of $\overline{u'_r u'_r}$ show (Figure 5.39) that they recover slightly in y^+<12. The pressure strain (*PS*) is the source term. There is a negative peak on the pressure strain term in y^+<12 of base flow, but this peak is very low for partially recovery flows, implying that the turbulence recovery of this region is weak. It is interesting to see that there is a new negative peak around y^+=30. The region of negative values between y^+=10 and y^+=40 indicates that the pressure strain transfers energy from u'_r to u'_θ. A similar region is only shown in y^+<12 in the base flow. In the outer region (y^+>40), the pressure strain becomes positive, illustrating that the u'_r gains energy from u'_z. The recovery of the dissipation is not significant in the near wall region. The budget balance of u'_r of D3 shows that the balance pattern is actually recovered to that of base flow for y^+ <12. The dominant terms are pressure strain and pressure diffusion. Between $12 < y^+$<40, the pressure strain and pressure diffusion are dominant and they balance each other. For y^+>40, the balance pattern is different to that of the base flow, where the pressure strain and pressure diffusion are enhanced.

The budget of $\overline{u'_\theta u'_\theta}$ is similar to that of the base flow (shown in Figure 5.40), except the existence of outer peaks on pressure strain and pressure diffusion. The pressure strain is positive across the flow, illustrating that this term is always the source term, similar to that of the base flow. The balance is mainly between pressure strain and pressure diffusion.

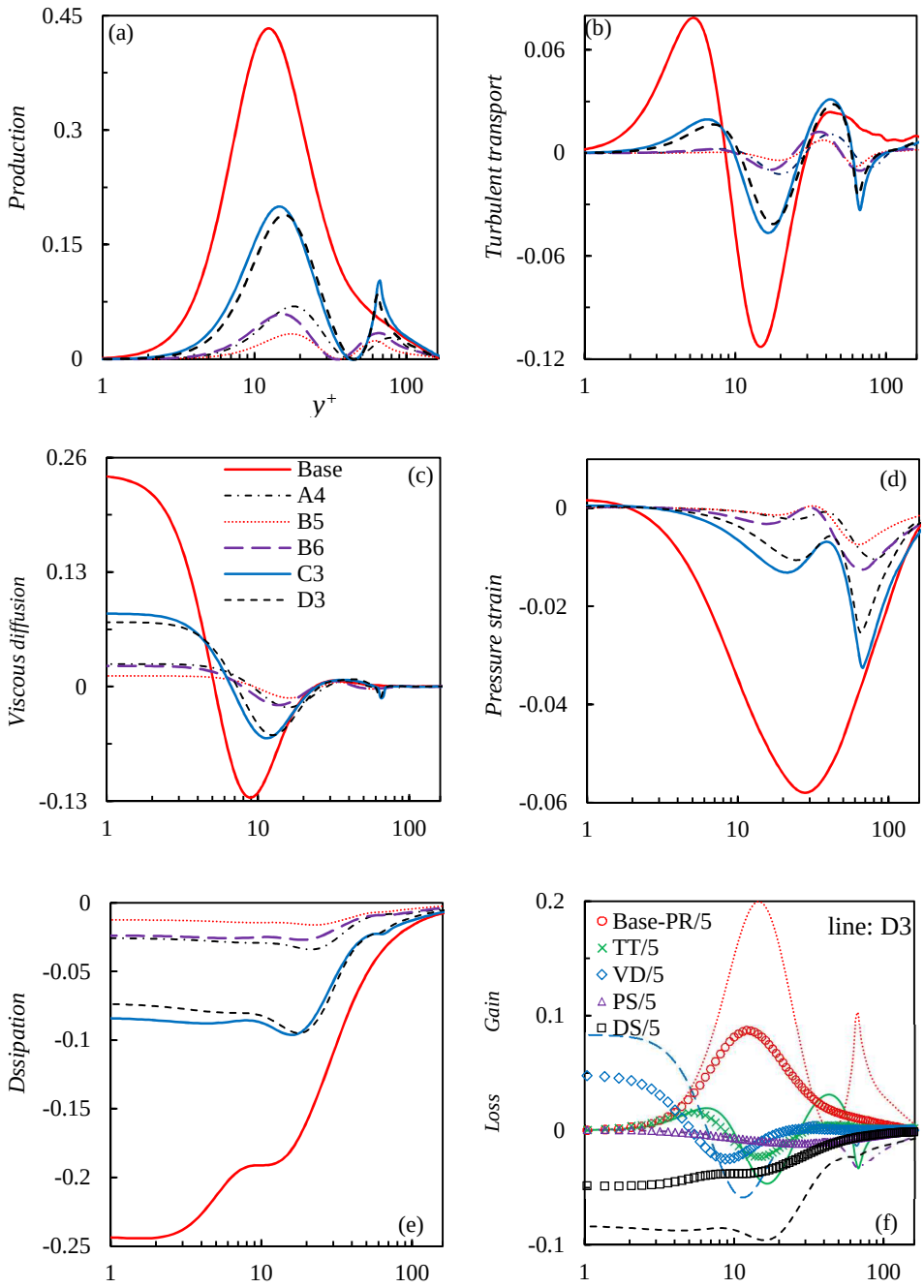

Figure 5.38: Budget of $\overline{u'_z u'_z}$ of partially recovery flow (normalized by $u_\tau{}^4/\nu$).

In (f): PR: production; TT: turbulent transport; VD: viscous diffusion; PS: pressure strain; DS: dissipation.

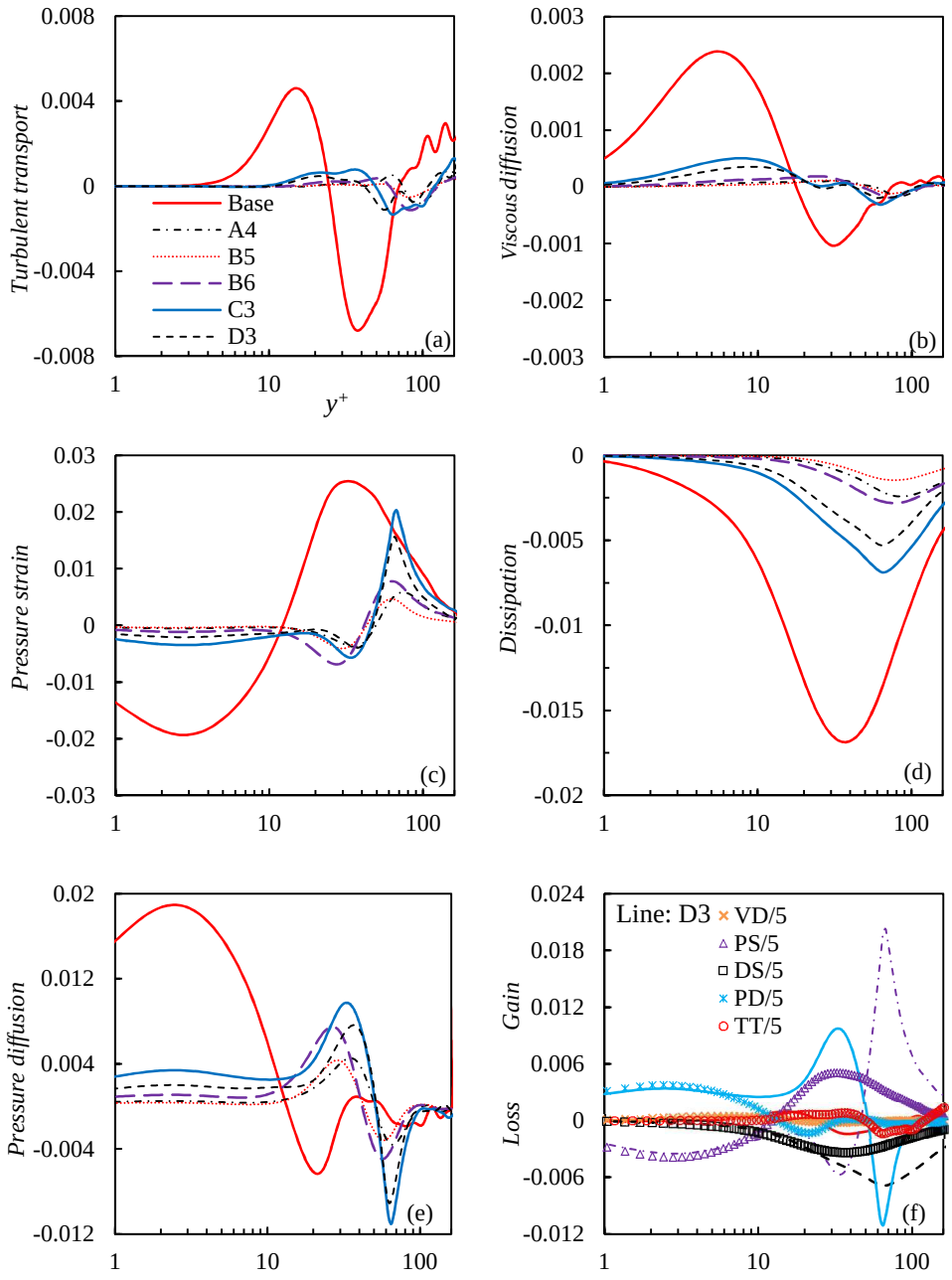

Figure 5.39: Budget of $\overline{u'_r u'_r}$ of partially recovery flow (normalized by $u_\tau{}^4/\nu$). In (f): TT: turbulent transport; VD: viscous diffusion; PS: pressure strain; DS: dissipation; PD: pressure diffusion.

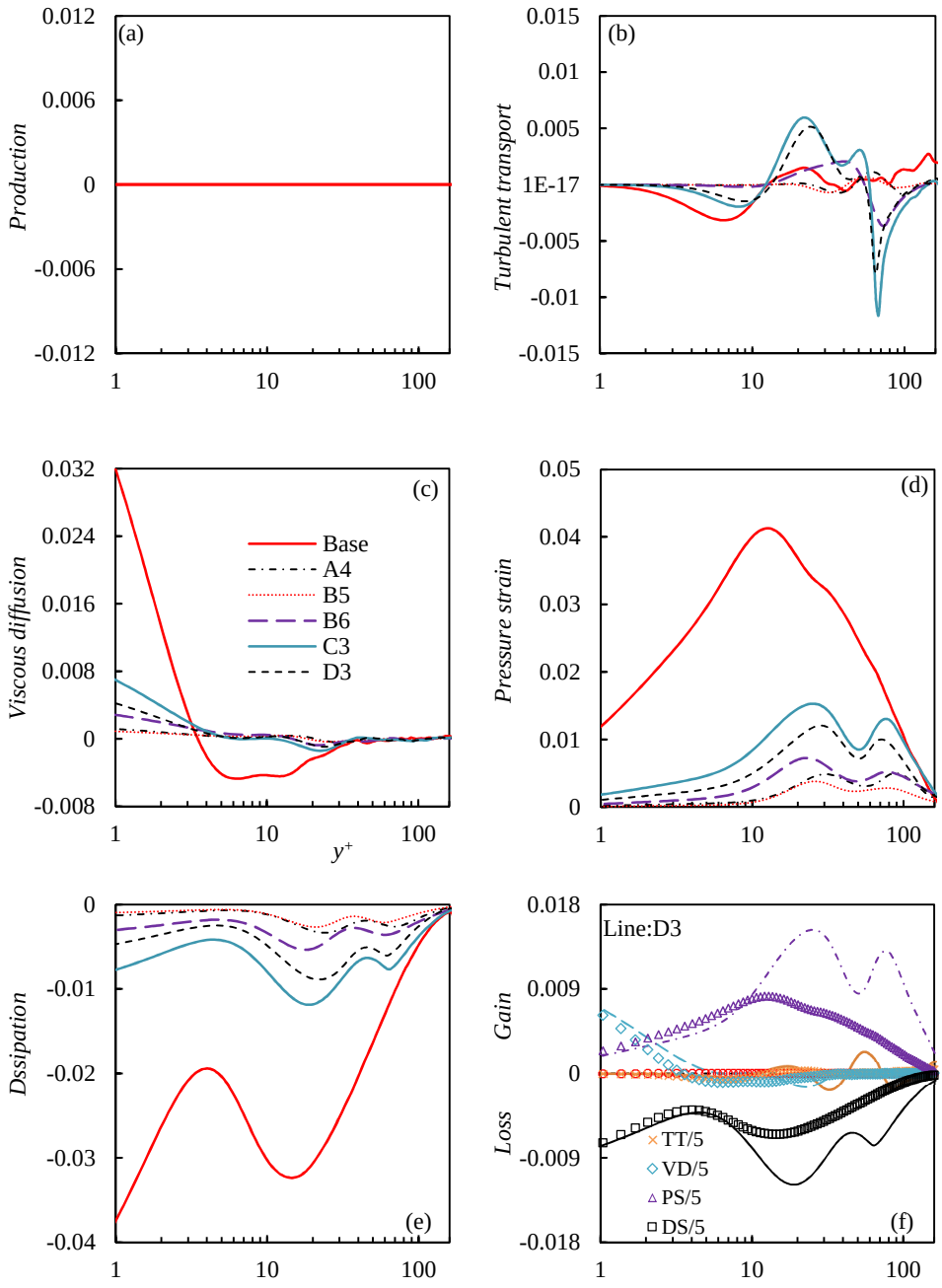

Figure 5. 40: Budget of $\overline{u'_\theta u'_\theta}$ of partially recovery flow (normalized by $u_\tau{}^4/v$).
In (f): TT: turbulent transport; VD: viscous diffusion; PS: pressure strain;
DS: dissipation.

The above study shows that the most important change in partially recovery flow is due to the pressure strain term. In the base flow, the u'_θ gains energy mainly from u'_r and u'_z for y^+<12, but in other regions, both u'_θ and u'_r gain energy from u'_z. The pressure

strain of $\overline{u'_r u'_r}$ of partially recovery flow shows an extended negative region between $y^+ = 12$ and $y^+ = 40$, indicating that both u'_z and u'_r supply energy to u'_θ.

5.5 The strongly recovery flow

The strongly recovery flows show similar features to those of partially recovery flows. Most of the statistics are documented in the appendix. Only the mean velocity and r.m.s of velocity fluctuations are shown in Figure 5.42 and studied to replenish the discussion in section 5.4. The mean velocities of strongly recovery flow show similar features to those of partially recovery flows. As the *F* increases, the near wall gradient of the mean velocity increases. The step change body forces cause less increase in velocity gradient due to the lower force density of them. The $u'_{z,rms}$ overshoots the base flow profile in the outer region. This feature is also found in $u'_{r,rms}$ and $u'_{\theta,rms}$. In the near wall region, the linear body force again shows stronger suppression on the $u'_{z,rms}$. As shown by partially recovery flows, the $u'_{r,rms}$ and $u'_{\theta,rms}$ are not correlated to the growth of $u'_{z,rms}$ in inner wall region. The $u'_{z,rms}$ of D6 is much higher than that of B8. However, their non-streamwise r.m.s of fluctuation velocites collapses. This also indicates that the inner turbulence is strongly affected by the outer turbulence. The $u'_{\theta,rms}$ shows two peaks in most cases, indicating that the near wall turbulence generation is recovered. This recovery is not just due to a single turbulence generation mechanism. As shown in partially recovery flows, the skewness of u'_z and u'_r indicates that the near wall turbulent structures are changed in that the downward motions are enhanced in the region between the inner peak and the outer peak. The near wall turbulence is a mixture of the turbulence produced in the inner and outer regions. The $u'_{r,rms}$ in most cases do not show the second peak. There is an exceptional case C4, as mentioned in section 5.4.1, where the $u'_{r,rms}$

shows two peaks. This is not shown in C3 and other cases, where the outer peak (y^{+0}=60) is too close to the inner one that they coincide with each other.

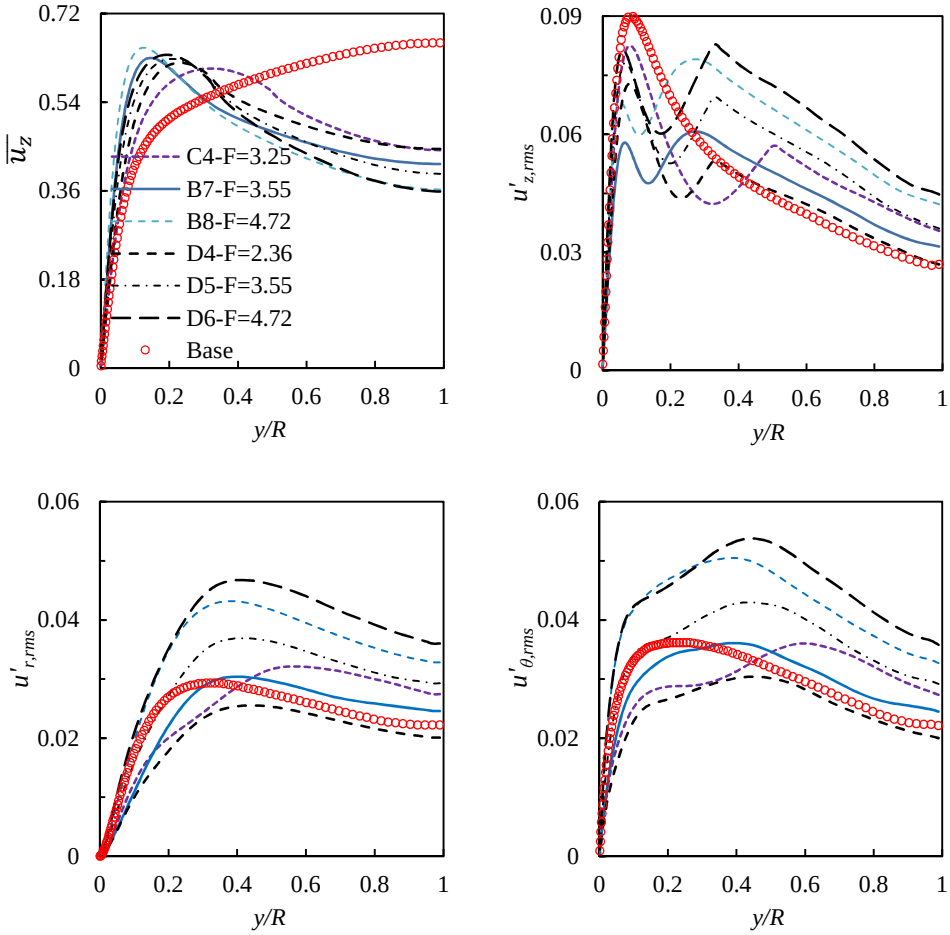

Figure 5. 41: Mean and r.m.s velocities of strongly recovery flow.

(a) $\overline{u_z}$; (b) $u'_{z,rms}$; (b) $u'_{r,rms}$; (b) $u'_{\theta,rms}$.

5.6 Summary and conclusions

Through a systematic DNS study, the effects of non-uniform body force on turbulent pipe flow are carefully examined. The flows are mainly classified into four types, namely, partially laminarized flow, 'completely' laminarized flow, partially recovery flow and

strongly recovery flow. The former two and the later two are discussed in a laminarized flow framework and a recovery flow framework.

For the partially laminarized and 'completely' laminarized flow, a new theory is proposed to explain the 'laminarization phenonmon' due to the imposition of a body force in a turbulent flow. Considerring a turbulent flow of Reynolds number Re_0 driven by a pressure gradient (dp/dx) and an additional non-uniform streamwise body force in the same direction of the flow (body force aided flow). In comparison with the reference flow of the same Reynolds number but without body forces, the turbulence can be significantly reduced. In general, the stronger the body force, the stronger the turbulence reduction is. When the body force is sufficiently strong, the flow can be fully laminarized. This convectional view has been established in the literature for various physical flows. It is also clearly demonstrated by using systematically varied prescribed non-uniform body forces using direct numerical simulation (DNS) herein. In the present study, we have established a new perspective towards such flows. The body-force aided flow can be best interpreted as resulting from imposing a body force to flow driven by a pressure gradient (referred to as the dp-based reference flow). The following are shown in the current study:

(1) The turbulence of the flow remains largely unchanged following the imposition of the body force. Most significantly, the eddy viscosity of the flow remains largely uninfluenced by the imposition of the body force, even though the total flow rate can be significantly increased;
(2) The wall-normal and circumferential turbulent stresses remain largely unchanged and the streamwise turbulent stress is moderately increased. The latter is a result of enhanced high- and low-speed streaks;

(3) The additional flow caused by the imposition of the body force is governed by the following momentum equation,

$$0 = \frac{1}{Re}\frac{1}{r}\frac{\partial}{\partial r}\left[r\left((1+\nu_{t1})\frac{\partial U'}{\partial r}\right)\right] + bf$$

where ν_{t1} is the turbulent viscosity of the dp-based flow and therefore can be seen as known, and the boundary conditions are $U' = 0$ on the wall and $\frac{\partial U'}{\partial r} = 0$ at the pipe centre. The velocity can be obtained from the integration of the above momentum equation. The addition of the body force causes an increase in turbulent shear stress, which can be calculated from the above momentum equation. The total wall shear is the sum of the wall shear of the dp-based flow and that of the body force driven flow obtainable from the above momentum equation;

(4) The body force can be characterized by four parameters, i.e., the total amplitude (F), the wall value, the coverage and the profile. It is found that when the coverage of the body force is small, say, less than y^+<20, the body-force driven flow is effectively a laminar flow. The solution of the total flow is further simplified;

(5) The level of laminarization is associated with the Reynolds number of the dp-based reference flow (Re_τ). When the applied body force is sufficiently large, causing the Reynolds number of the pressure-driven-flow to be sufficiently small and turbulence cannot be sustained and the flow becomes a laminar flow. Consider a series of flow cases of the same total flow rate, but with increasing body forces, e.g., B1, B2, B3. Alternatively, consider a series of flow cases of the same pressure gradient imposed, and with increasing body forces, the turbulent flow is not laminarized at all;

(6) Under the condition of a fixed Reynolds number, the strength of the effect of a body force on the flow in terms of suppressing turbulence and laminarizing the flow is

predominately associated with the flow rate of the perturbation flow it induces. The apparent flow is the total flow takes away the perturbation flow of the body force. Hence, the higher the latter, the smaller the apparent flow; the lower the apparent Reynolds number ($Re_{\tau 0}$) and the stronger the laminarisation. The flow rate of the perturbation flow is linearly proportional to the amplitude of the body force. It also increases with the increase of the coverage when the amplitude is fixed and the relation is described by Eqn 5.21. The profile of the body force distribution only affects the laminarization through flow rate that it causes. For example, with the same amplitude and coverage, the stepwise distribution causes a perturbation flow that is about 2.6 to 3 times higher than that of a linear distribution and hence it is more effective in laminarizing the flow. The ratio between the two total forces in the stepwise and linear distributions is about 1.95.

For the recovery flow, following basical features can be drawn:

(1) The body force can be characterized by four parameters, i.e., the total amplitude (F), the wall value, the coverage and the profile. It is found that the main influential parameters are the total amplitude, which determines the force density. The higher the force density, the more effectively the streamwise turbulent stress is suppressed, but the effect on non-streamwise turbulent stresses is more related to the pattern of the body force, which is determined by both the amplitude and the profile.

(2) The flow visualization shows that many partially laminarized flows are transitional flows. As the F increases, the streaky structures become smooth and the streaky structures are elongated, which are similar to those observations in the transitional region of boundary layer flows. The spanwise and streamwise scales of the streaks

increase. By contrary, for recovery flow, the spanwise and streamwise scales reduce as the F increases and the streaky structures are different from both the base flow and a transitional flow. The vortical structures are organized with the streaky structures in partially laminarized flow but most of vortical structures are not organized and detached from the wall in recovery flow;

(3) The $\overline{uv}$ contributions of ejections and sweeps of the partially recovery flows are similar to that of the base flow at the near wall region. In near wall region (y^+<30) of the base flow, the balance of Reynolds stress are established between sweeps and ejections, where the contribution of sweeps is dominant. The contribution of sweeps reduces slightly but the ejections' contribution increases in recovery flow. Flatness and skewness show that these flows are highly intermittent. Between y^+=10 and new shear layer, the turbulence is a mixture of the inner turbulence and outer turbulence. The skewness data shows that the inward motions are dominant in this region;

(4) The budget terms of recovery flows show a balance pattern different from that of the base flow. There are two production regions shown on the main budget terms. There are many detailed changes on these budget terms, but the most important information can be drawn is from the term for the energy re-distribution between the three components of the turbulent stresses. The pressure strain of $\overline{u'_r u'_r}$ is recovered in the near wall region, which shows two peaks in y^+<40. The peaks at around y^+=5 is due to a 'splatting' effect of the wall and it only exists in strongly recovery flow. The collision of the inward and outward motions creates strong negative peaks on the pressure strain of $\overline{u'_r u'_r}$, which redistributes the energy from u'_r to u'_θ.

Chapter 6

Transient Pipe flow Subjected to a Non-uniform Body Force

In this chapter, the transient flow following the imposition of a non-uniform body force is studied. The body force is prescribed with various amplitudes and coverages. It aims to understand how the turbulence and coherent structures respond to the imposition of these body forces and how the self-sustaining regeneration of the initial turbulent flow is modified. These transient flows share many features with spatially developing flows under the influence of a non-uniform body force. The analysis and knowledge developed in this chapter can be used to understand such real flows. Through the study reported in this chapter, we will answer the following questions:

(1) How do the mean flow and turbulence develop from the initial state to the final state?

(2) How fast are these changes?

(3) How do the changes of body force coverage and amplitude affect the development of the turbulence?

6.1 Simulation setup

The implement of the body force is described in chapter 5. The test cases are shown in Table 6.1. The four body forces of group E1X are shown in Figure 6.1. Group E1X contains E11 & E12 & E13 & E14, which are with the same total amplitude F but varying coverage from y^{+0}=15 to y^{+0}=90. The other groups (E2X, E3X, E4X) are designed in a similar way but the total amplitude of the body force increases (F). The variation of the body force coverage and the F leads to a change of local force density. The computational domain and mesh used in this chapter are the same as that used in chapter 5. The coverage of the body force in each group varies from y^{+0}=15 to y^{+0}=90 (where subscript 0 indicates the friction velocity at t=0 is used). The discussion on the results starts from the general effect of body force coverage and amplitude on turbulence (section 6.2) and then moves to the detailed laminarization and recovery process after the imposition of body force (section 6.3). A brief summary and conclusion are organized into section 6.4.

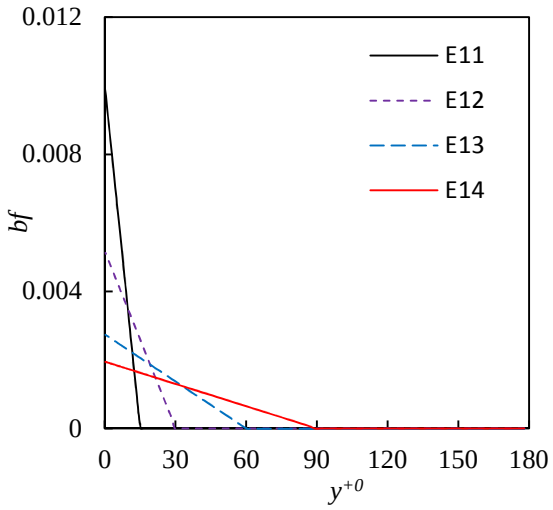

Figure 6.1: The distribution of body force in group E1.

Table 6.1 Summary of body force in all cases

F / Coverage	0.35	0.68	1.28	1.91
15	E11	E21	E31	E41
30	E12	E22	E32	E42
60	E13	E23	E33	E43
90	E14	E24	E34	E44

6.2 General effect of body force coverage and amplitude

The statistics shown here are based on spatial average in the streamwise and spanwise directions. In theory, multiple runs should be carried out to obtain ensemble average to ensure the results to be converged. However, our interest is the general trends of the transient behaviours and hence only single runs are used. Some of oscillations of the statistics are due to lack of data for average.

6.2.1 The time evolution of r.m.s of velocity fluctuations in local coordinate

Figure 6.2 shows the time evolution of the r.m.s of streamwise and wall-normal velocity fluctuations ($u'_{z,rms}$ and $u'_{r,rms}$) at a near wall location (y^{+0}=15) and a centre location (y^{+0}=143), where the velocity is normalized by U_p and t is normalized by H/U_p. The cases E11 & E21 & E31 & E41 are re-grouped together to show the amplitude effect as the coverage kept the same (y^{+0}=15). The amplitude varies from F=0.35 to F=1.91. Similarly, the E12~E42 & E13~E43 & E14~E44 are re-grouped for the coverage y^{+0}=30, 60, 90 respectively. The following discussion covers three parts, namely, the general

decay or recovery features of these r.m.s value in the near wall region and in the central region, and the effect of changing the amplitude or coverage of the body force.

Firstly, let us look at the r.m.s of streamwise velocity fluctuations (Figure 6.2(a) and (c)) at the near wall location. It is shown that the $u'_{z,rms}$ decays monotonically for t<40 in all cases. At certain time, the flows of E11 & E21 & E31 & E12 & E22 reach a quasi-steady state. We refer these flows as PLAM, which means partially laminarized flow. The turbulence oscillates with different frequencies in each flow afterwards. In E11 & E12, the oscillation frequencies are higher than those of other cases. This can be explained by the new perspective developed in chapter 5. It is evaluated that the final apparent Reynolds numbers of E11 & E12 are Re_τ=~140. For the other cases (E31 & E12 & E22), their final apparent Reynolds numbers are below Re_τ =100. These flows are in transitional state. It is known that the transitional flow is highly intermittent and contains turbulence with low frequency fluctuations. In E23 & E24 & E32 & E33 & E41 & E42, the turbulence decays to a very low value and there is no sign of recovery. These flows has completely laminarized final state are referred as CLAM. For E34 & E43 & E44, the $u'_{z,rms}$ experiences a clear re-growth at t=~80 (E43 & E44) and t=~150(E34). These recovering flow are named as REC. The time evolutions of r.m.s of wall-normal velocity fluctuations at a near wall location are shown in Figure 6.2(e) and (g). It is shown that $u'_{r,rms}$ decays monotonically at the beginning. They show similar reduction features as those of $u'_{z,rms}$. However, the reduction rates of $u'_{r,rms}$ are larger in each case.

At the centre location (y^{+0}=143), the $u'_{z,rms}$ (Figure 6.2(b) and (d)) does not reduce monotonically after the imposition of the body force. They reduce first but then increase suddenly at t=~20. In PLAM, they show similar fluctuation features when the flow reaches a quasi-steady state (the apparent larger fluctuations are due to the smaller

samples of the data). In REC, the recovery of $u'_{z,rms}$ is more significant than that of near wall region. The $u'_{r,rms}$ also shows a different response compared to its near wall counterpart. It remains unchanged before t=~20 and then reduces monotonically till reaching quasi-steady state in PLAM. In CLAM, the $u'_{r,rms}$ reduces to almost none and no sign of recovery is observed. For REC, the $u'_{r,rms}$ shows a dramatic recovery at t=~100. This recovery shows different features with that of partially laminarized flow such as E22. For example, the re-growth of $u'_{r,rms}$ of E22 starts from the near wall region at t=120 and the growth is delayed at the centre region. While in REC, the re-growth starts from the outer shear layer region. It is implied that the turbulence re-generation mechanism is different for E22 and the cases of REC.

Figure 6.2 shows that the increase of F or coverage imposes similar effect on the development of turbulence in the flow. Namely, they lead to more significant decrease of the r.m.s values. The flow reaches a quasi-steady state over a different time. For F=0.35 and body force coverage at y^{+0}=15 & 30, the flow reaches a quasi-steady state at t=~40. The time increases with the increase of F and coverage. Most of them reaches a quasi-steady state before t=~200. In some critical conditions (F=0.68, y^{+c0}=60 & y^{+c0}=90 (E23 & E24), F =1.28, y^{+c0}=30 & y^{+c0}=60 (E32 & E33), F =1.91, y^{+c0}=15 & y^{+c0}=30 (E41 & E42)) the flow is completely laminarized.

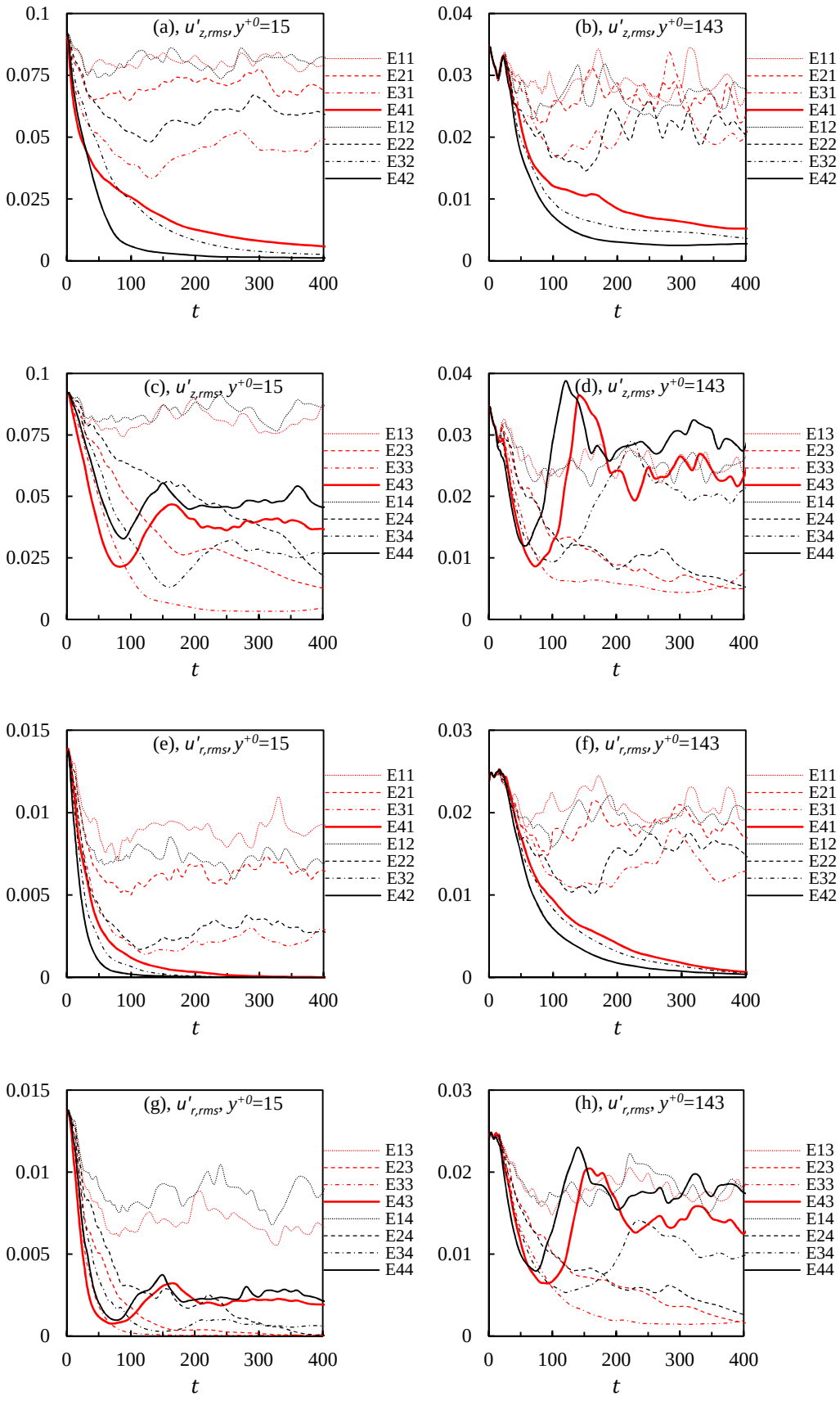

Figure 6.2: The time evolution of r.m.s of streamwise and wall-normal velocity fluctuations.

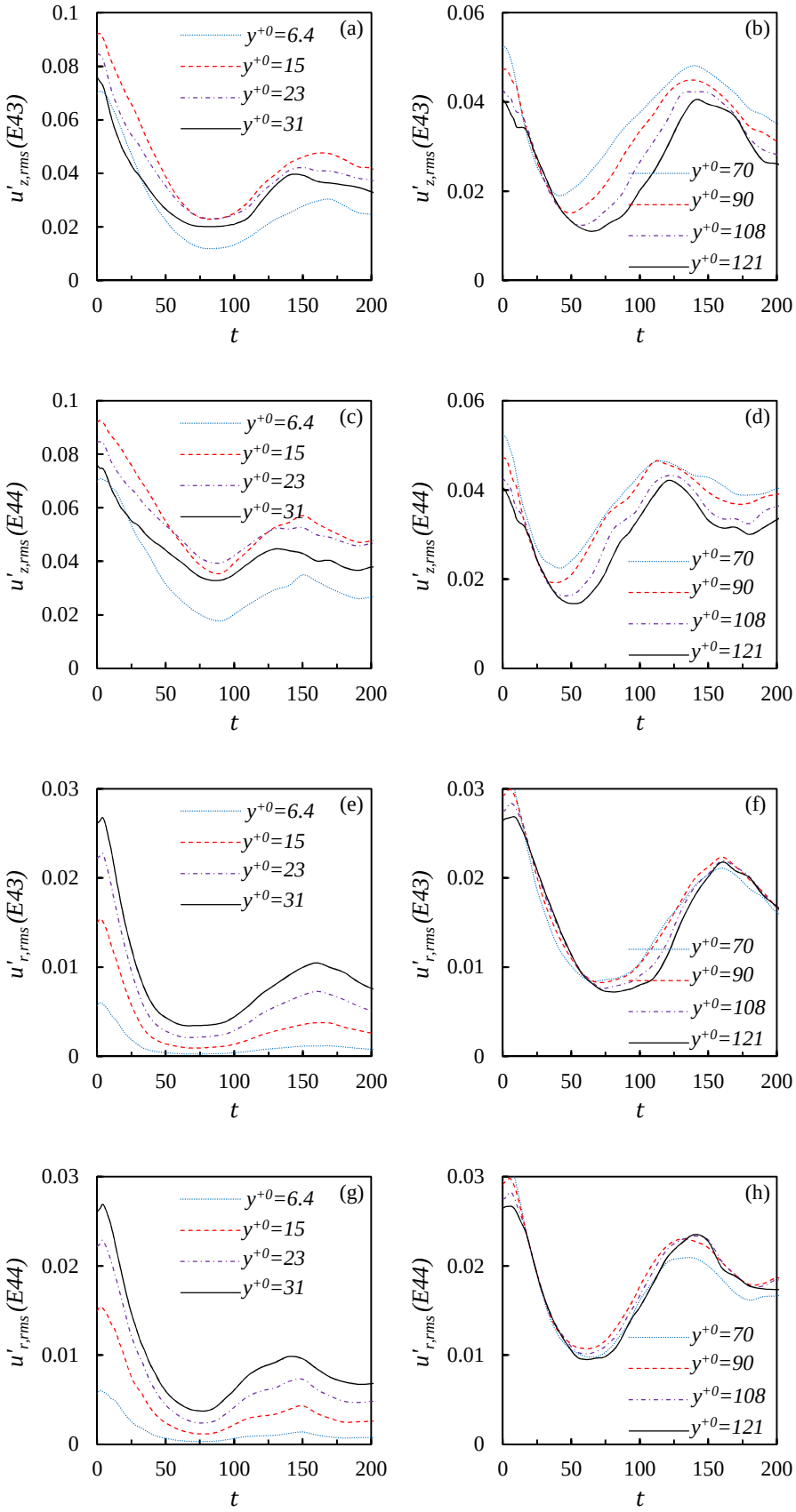

Figure 6.3: The development of turbulence at different wall-normal locations (E43 & E44).

With further increase of F or body force coverage, the recovery of the turbulence is observed in E43 & E44. In order to further study the recovery features of the turbulence, the r.m.s of velocity fluctuations of E43 and E44 at different locations of the pipe are showed in Figure 6.3. It is interesting that the recoveries of $u'_{z,rms}$ and $u'_{r,rms}$ in the near wall region (Figure 6.3(a), (c), (e), (g)) are independent of the locations. The $u'_{z,rms}$ starts to increase at $t = \sim 80$. It is interesting to see that the growth of $u'_{r,rms}$ is slightly earlier. In the central region, as the observation position moves towards the pipe centre, the recoveries of $u'_{z,rms}$ and $u'_{r,rms}$ are delayed. It shows in Figure 6.2(d) & (h) that the increase of body force coverage leads to an earlier recovery of $u'_{z,rms}$ and $u'_{r,rms}$. The recoveries of $u'_{z,rms}$ and $u'_{r,rms}$ in the centre region also show dependence on body force coverage. As the body force coverage increases, the onset of the recovery is pushed forward.

6.2.2 The profiles of r.m.s of the velocity fluctuations in global coordinate

The profiles of the mean velocity, $u'_{z,rms}$ and $u'_{r,rms}$ are plotted in global coordinate at several time sequences in Figures 6.4~6.7. Group E2X and group E4X are selected to show the turbulence decay and recovery features. As indicated in previous discussion, group E1 represents flows that have a lower apparent Reynolds number or in the conventional view, are partially laminarized flows. Group E4X contains both laminarized flows and recovery flows. The mean velocities of E21 and E22 reduce slightly in the centre region of the pipe. In the near wall region, the velocity gradient increases at the beginning and decreases after certain period. The peak values of $u'_{z,rms}$ reduce less than 30% in E21 & E22. The reduction of $u'_{r,rms}$ is similar to that of $u'_{z,rms}$ but the reduction is stronger. In E21, the $u'_{r,rms}$ reduces dramatically before t =~40. After that, the

reduction is slower. There is a clear recovery of $u'_{r,rms}$ between t=~80 and t=~140. It starts in the near wall region and then in the centre region. This is similar to that of $u'_{z,rms}$, whereas the recovery of $u'_{z,rms}$ is earlier (at t=~40). This re-growth scenario is similar to the bypass transition described in chapter 4, in which the growth of $u'_{r,rms}$ is later than that of $u'_{z,rms}$ and it starts at the near wall region. In E22, the recoveries of $u'_{z,rms}$ and $u'_{r,rms}$ are weak. The reduction and recovery of Reynolds stress is similar to that of $u'_{r,rms}$.

The trend of the mean velocity described above becomes more and more significantly as the body force coverage increases. In E23 & E24, the velocity develops a flatten region in the central region. The decays of $u'_{r,rms}$ &$\overline{uv}$ of them are monotonic and stronger. It is shown that the reduction of $u'_{z,rms}$ of E24 at peak location (y^{+0}=15) is 30% at t=160 but the reduction of $u'_{r,rms}$ &$\overline{uv}$ is more than 60%. In group E4 (Figure 6.6 and Figure 6.7), the F increases to 1.91. A monotonic decay of the turbulence is observed in E41 and E42. The peak of $u'_{z,rms}$ is shifted to the wall at the beginning but moves outwardly after t=80. As the body force coverage increases to y^{+0}=60 and y^{+0}=90, the turbulence decays and then recovers. In both E43 and E44 (Figure 6.7), the outer peak of $u'_{z,rms}$ shows at t=~60 and grows dramatically between t=~60 and t=~100. The growth is expanded to the centre of the pipe. The inner peak of $u'_{z,rms}$ decreases till t=80 and stagnates till t =120. After that, it grows with the outer peak. The growth of $u'_{r,rms}$ starts at t=80 across the pipe and the recovery of $u'_{r,rms}$ in the centre region is more significant than that of near wall region. In the beginning, the $\overline{uv}$ reduces dramatically in the region where the body force reduces to zero and it develops negative value there at around t=40.

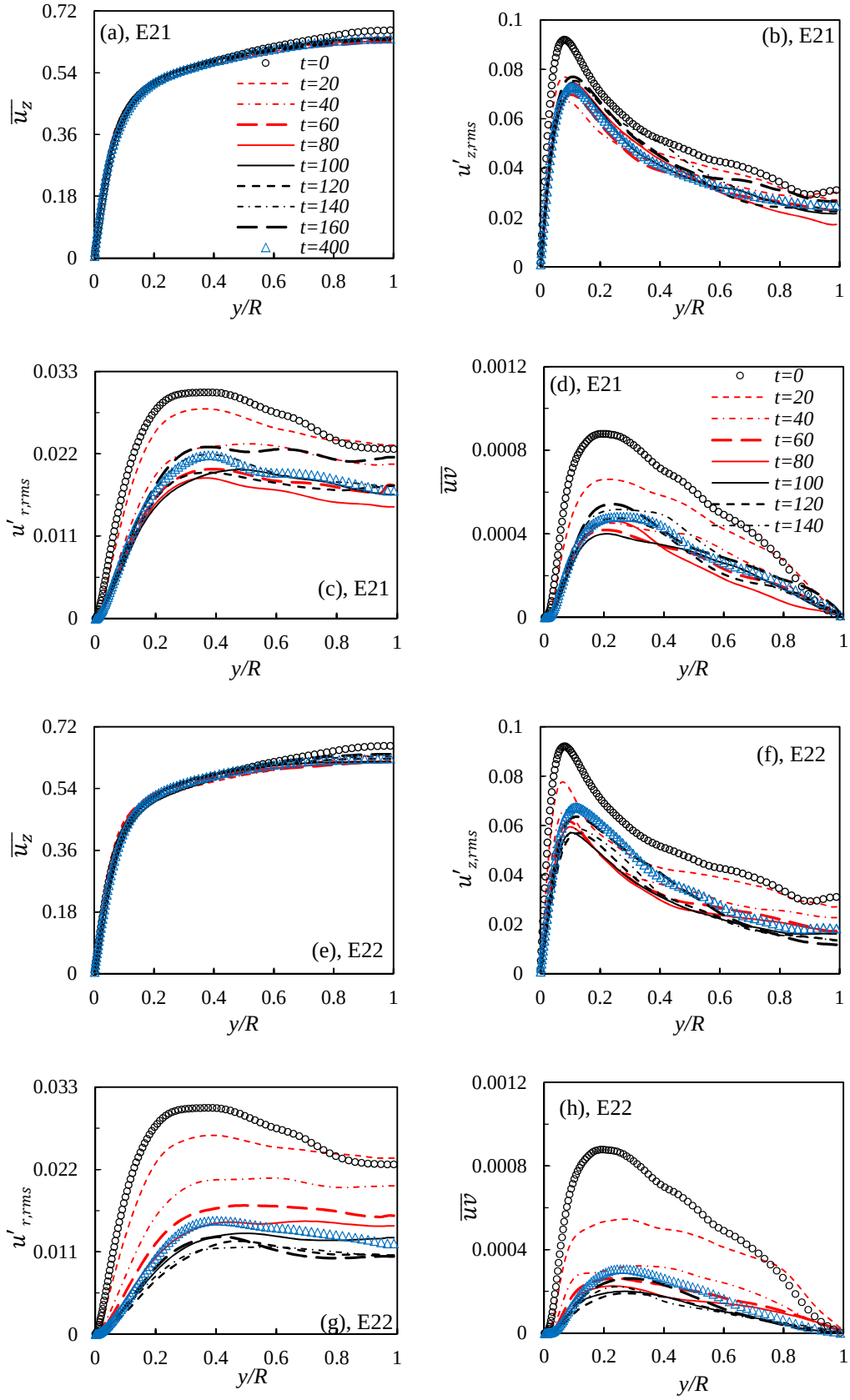

Figure 6.4: The development of $u'_{z,rms}$, $u'_{r,rms}$, $\overline{uv}$ in global coordinate.

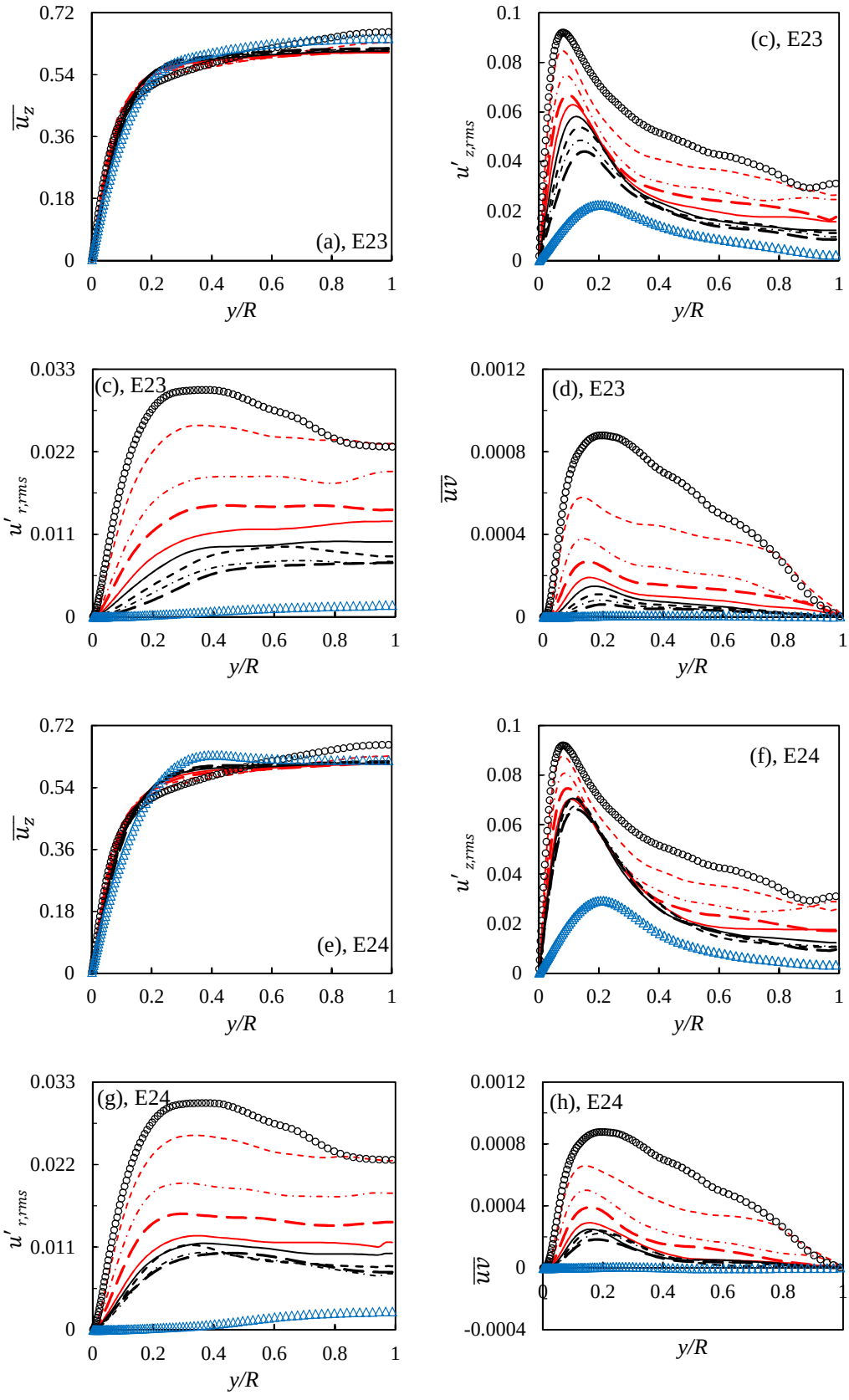

Figure 6.5: The development of $u'_{z,rms}$, $u'_{r,rms}$, $\overline{uv}$ in global coordinate.

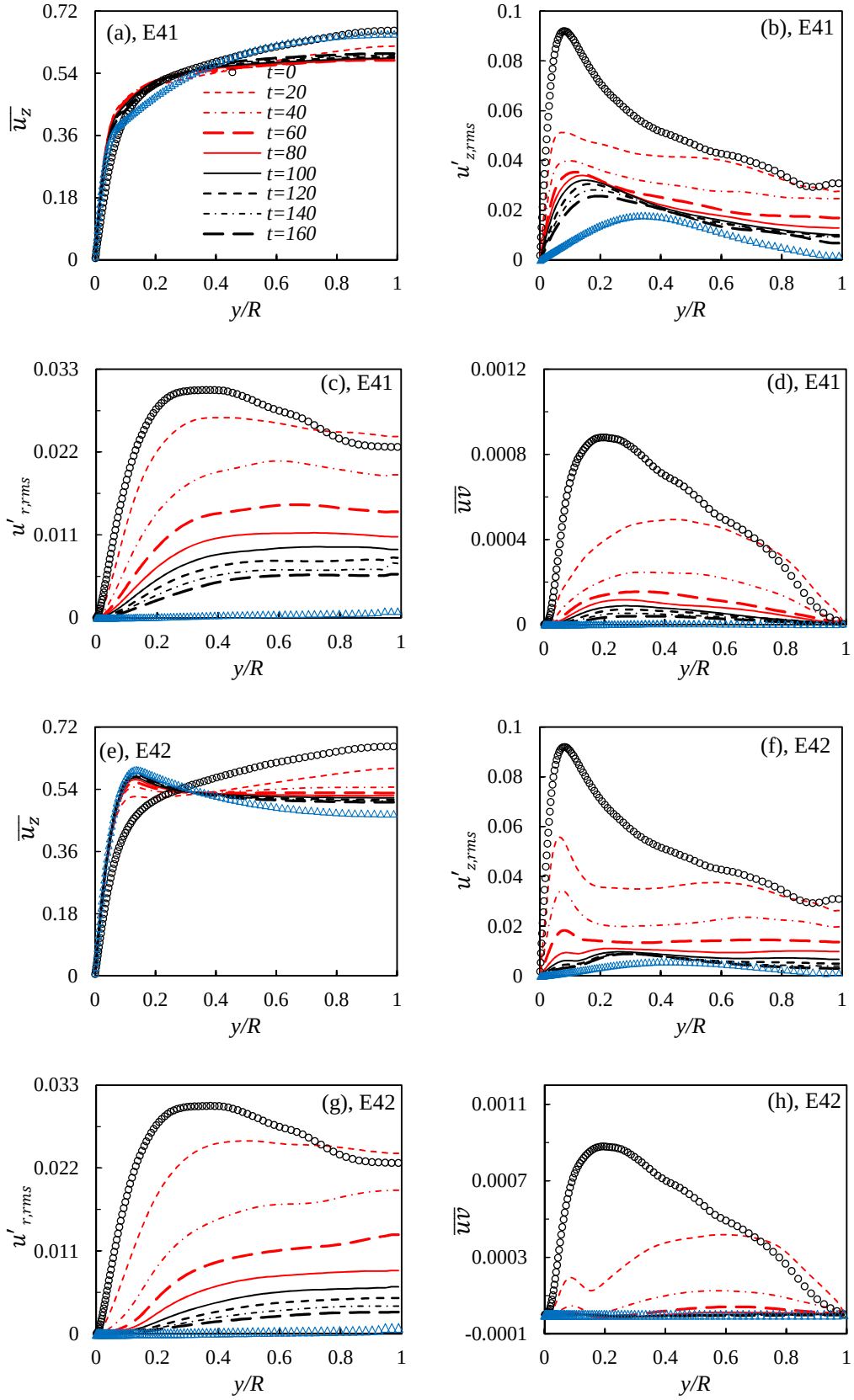

Figure 6.6: The development of $u'_{z,rms}$, $u'_{r,rms}$, $\overline{uv}$ in global coordinate.

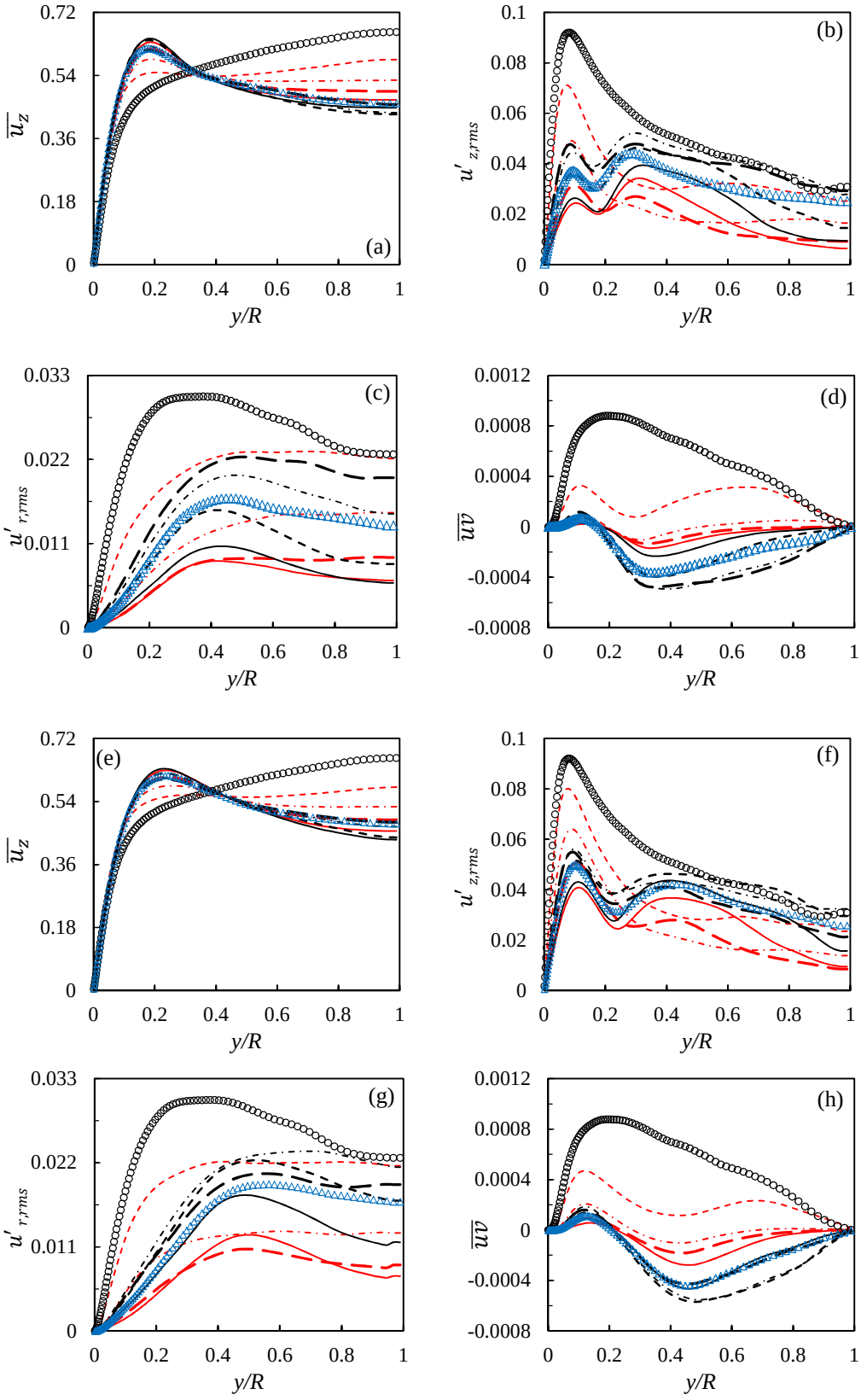

Figure 6.7: The development of $u'_{z,rms}$, $u'_{r,rms}$, $\overline{uv}$ in global coordinate.

The above study shows that although the increase of body force coverage results in a similar effect to that of the body force amplitude, the detailed effect of increasing the body force coverage is more complicated. Figure 6.8 shows the development of ratio of peak values of $u'_{z,rms}$ over $u'_{r,rms}$ against with time. For the coverage at y^{+0}=15(E11 & E21 & E31 & E41), the ratio keeps at ~0.33 during t<200. The increase of F causes almost proportional decay in $u'_{z,rms}$ and in $u'_{r,rms}$. With the coverage at y^{+0}=30, 60 and 90, the increase of F leads to more and more significant decay of $u'_{r,rms}$. The effect is not linear and monotonic. It shows that the decay of $u'_{z,rms}$ depends on the force density in the near wall region. The higher force density in the near wall region more significant is suppression of the $u'_{z,rms}$.

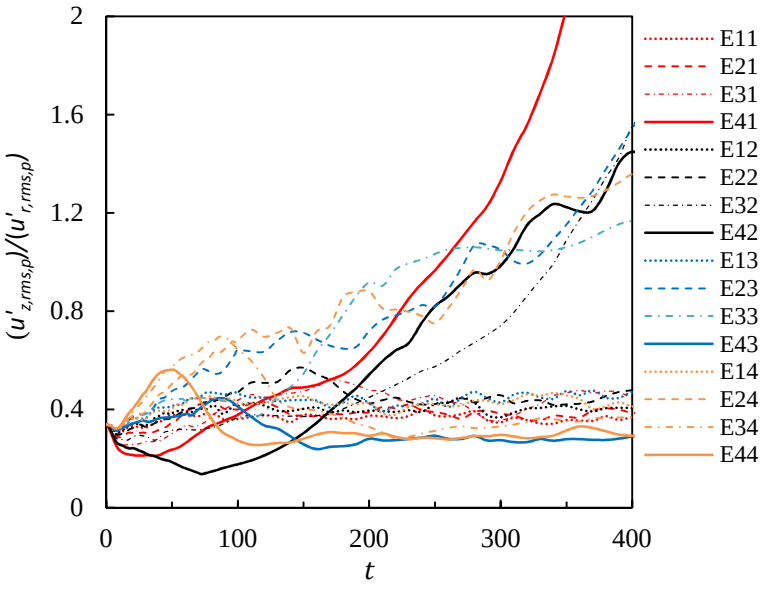

Figure 6. 8: The ratio change of peak value between $u'_{z,rms}$ and $u'_{r,rms}$.

6.3 The laminarization and recovery of a turbulent flow with body force

6.3.1 Flow structures

It is shown in section 6.2 that the change of body force coverage imposes more complicated effect on turbulence. In chapter 5, it shows that the contribution of Reynolds stress from the body force with very narrow coverage (y^{c+0}<20) is negligible, which means the body force induced perturbation flow is largely laminar and the increase of F has a linear effect on the turbulent stress. As the coverage is increased, the turbulence is strongly damped. In this section, E41 and E44 are selected as representative cases with narrow body force coverage and a wide body force coverage. In addition, E41 is a completely laminarized flow and E44 is a recovery flow. The decay features of the coherent structures of them are studied firstly. Figure 6.9 shows the flow structures of E41 and E44 at t=10, 20 and 30 after the imposition of the body force. The high and low speed streaks are in green and blue colour respectively. The vortices are in red colour. From t =10 to t =20, the structures of E41, especially the streaky structures reduce dramatically. The vortical structures depart from the streaky structures at t=30. In E44, the changes of structures scenario show a different picture. At t=10, the low speed and high speed structures are more than that of E41, illustrating that these structures decay faster in E41. At t=20, it is observable that there are more streaky structures in E44 than in E41 but the vortices are fewer in E44. At t =30, sparse vortices and streaky structures remain in E44.

Figure 6.10 shows these structures of E41 and E44 in $r-\theta$ plane, where the change of these structures in wall-normal direction is studied. At t =0, it shows the 3-D visualizations of the flow structures in the base flow. Form t=10 to t=20, the flow structures of E41 reduce significantly in the vicinity of the wall. It seems that the coherent

structures are shift away from the wall during this period. At t =20, the streaky structures disappear but some isolated vortices remain at locations away from the wall. In E44, the change is notable from the outer region. During t =10 and t =30, the structures reduce and they remain at the near wall region. The vortices are organized and mainly around the low speed structures, which is still similar to the typical coherent structure.

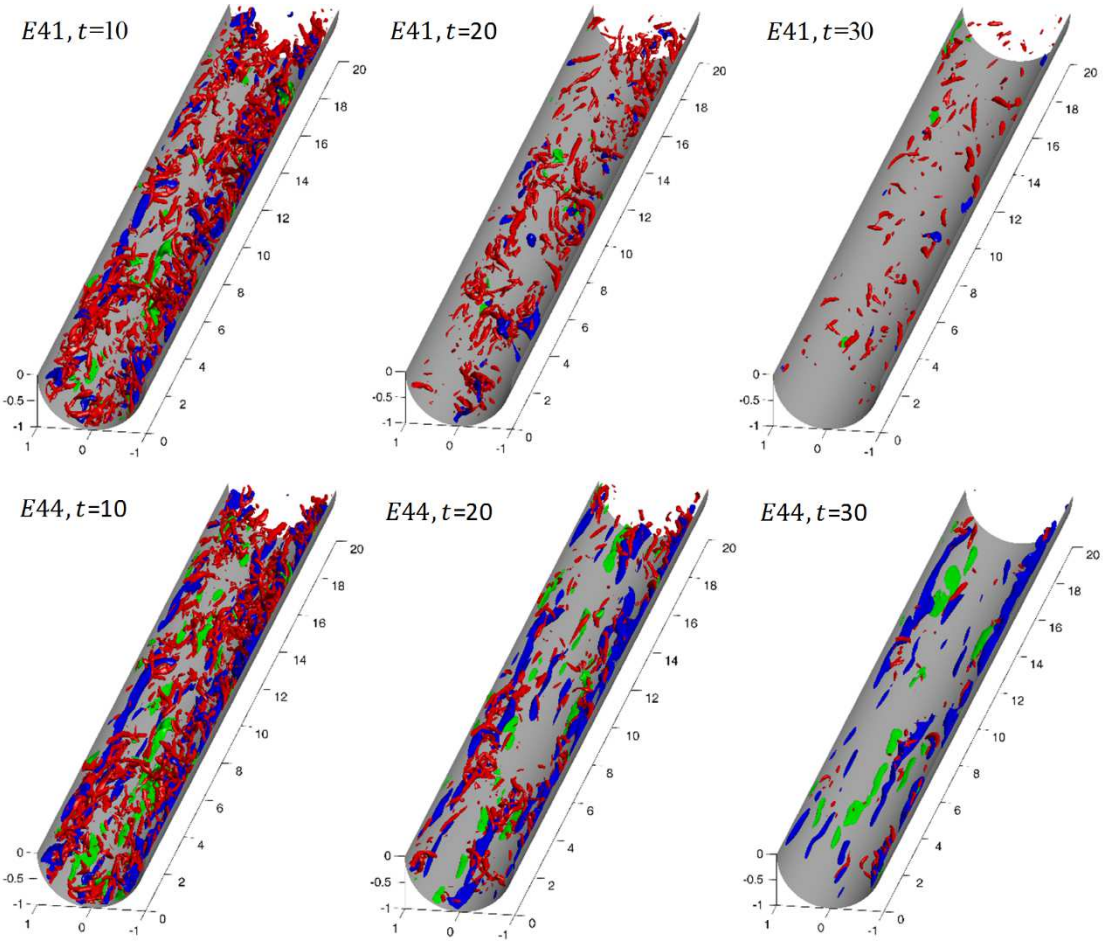

Figure 6.9: The development of flow structure in E41 & E44.
(u'_z=±0.12, λ_2=0.5)

As it is shown in section 6.2.1, the recovery of the turbulence in E34 & E43 & E44 shows different features from those of partially laminarized flow. In this section, the recovery features of E34 & E43 & E44 are furtherly studied by flow visualization. Several

flow fields of E44 from t=70 to t=90 are selected to visualize the recovery of turbulence. At t=70, there are fewer high and low speed structures in the wall region. These structures continue to reduce afterwards and at t=74, some vortical structures show at the location where the positive body force vanish. The red structures grow in size and the number increases significantly after t=78. Among these structures, it shows spot-like high speed and low speed structures also disappear. The streaky structures seem to recover in the near wall region at t=90.

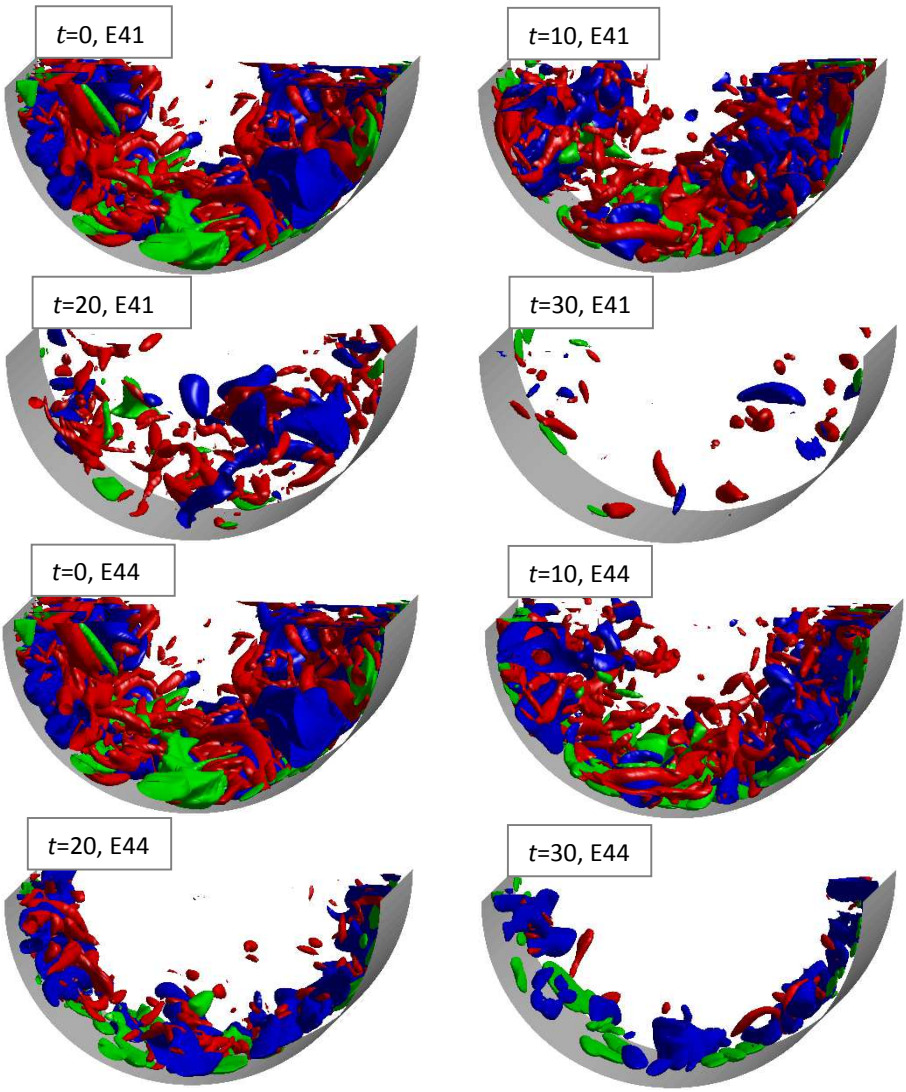

Figure 6.10: The development of flow structures in E41 & E44.
(u'_z=±0.12, λ_2=0.9)

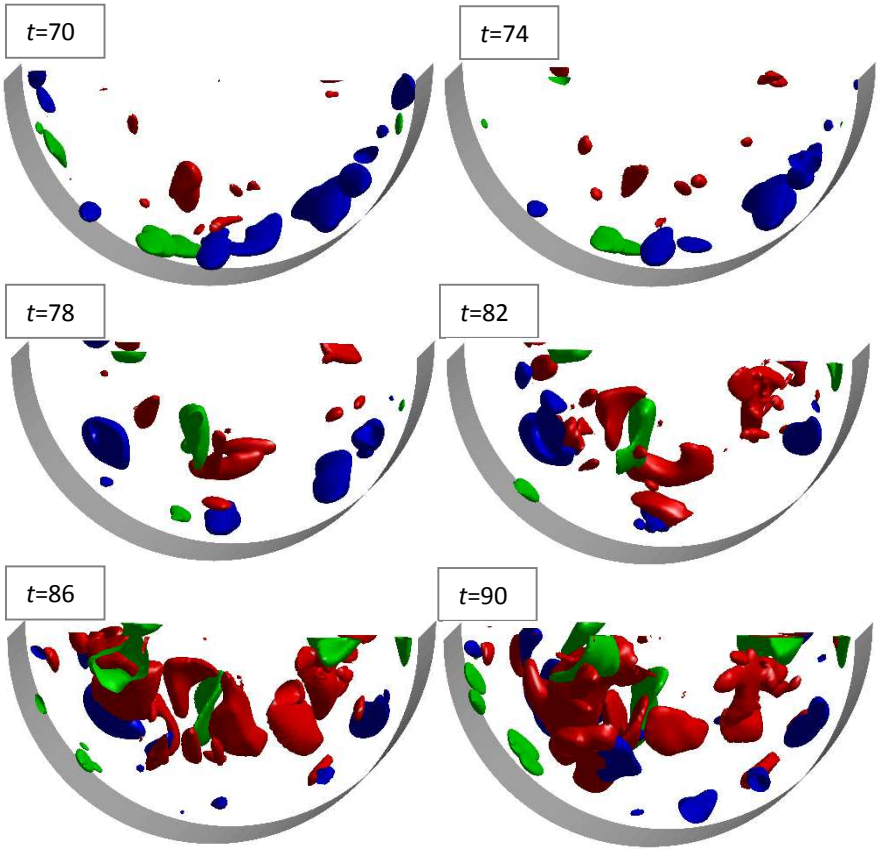

Figure 6.11: The recovery of turbulence in E44.
(u'_z=±0.08, λ_2=-0.06)

6.3.2 The r.m.s of streamwise vorticity fluctuations

Figure 6.12(a) shows the $\omega'_{z,rms}$ of E41. The $\omega'_{z,rms}$ of E41 decreases significantly first in the region y^{+0}=5-40 from t=0 to t=8, after that the reduction is expanded from the wall region to the centre region (8<t<20). For $\omega'_{z,rms}$ of E44 shown in Figure 6.12(b), the change is milder in the wall region. The local peak of E44 in this region remains at t<20, when the positions of the peak starts to move towards the wall, which can be explained by the boundary layer contraction due to the imposition of a body force. As it is disscussed in last section, the local peak position of $\omega'_{z,rms}$ represents the averaged core postions of vortices. This peak is damped quickly and moves slightly away from the

wall in E41. This is consistent with the previous visualization, which shows that the turbulent strutures depart from typical coherent structures in E41. The basical coherent structures of E44 are not changed, therefore the curves of $\omega'_{z,rms}$ are similar to that of the base flow. The recovery of the streamwise vorticity of E44 is shown in Figure 6.12(b). The profiles of $\omega'_{z,rms}$ show two peaks. The inner peak shows at t=~60. The inner peak position of $\omega'_{z,rms}$ of E44 is similar to that of the base flow. The inner peak position of $\omega'_{z,rms}$ of E44 is slightly away from the wall. The positions of the outer peaks are at around y^{+0}=80 (y/R=0.42). The growths of the inner peak and outer peak of $\omega'_{z,rms}$ are simultaneously. They grow to t=120 in E44 and then reduce.

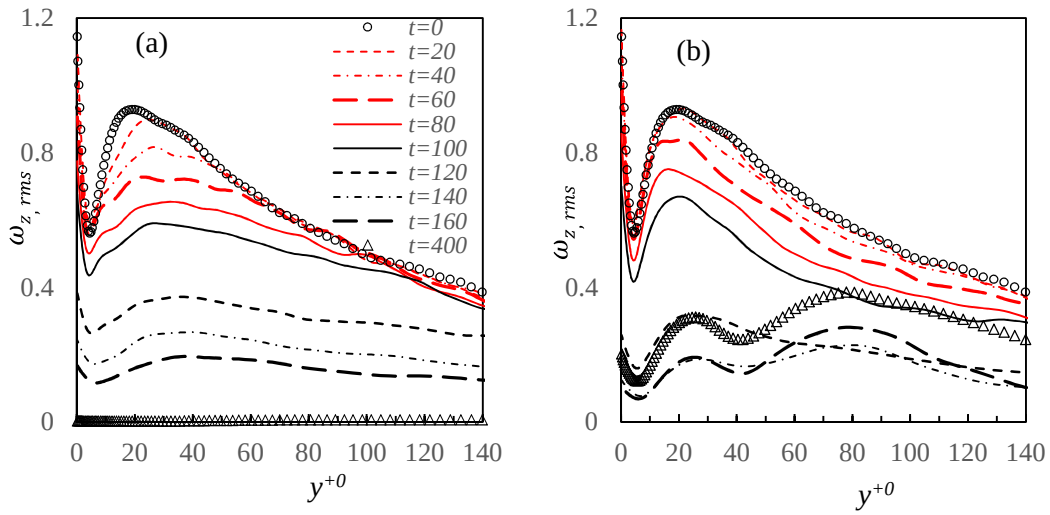

Figure 6.12: The recovery of streamwise vorticity of E41 and E44.
(a) $\omega'_{z,rms}$ of E41; (b) $\omega'_{z,rms}$ of E44.

6.3.3 The streaks

The structural changes, especially the modulation of streaks, shown in section 6.3.1 are reflected on velocity correlations data. The spanwise and streamwise correlations of u'_z of E41 and E44 are shown in Figures 6.13(a), (b), (c) and (d). The minimum peak of

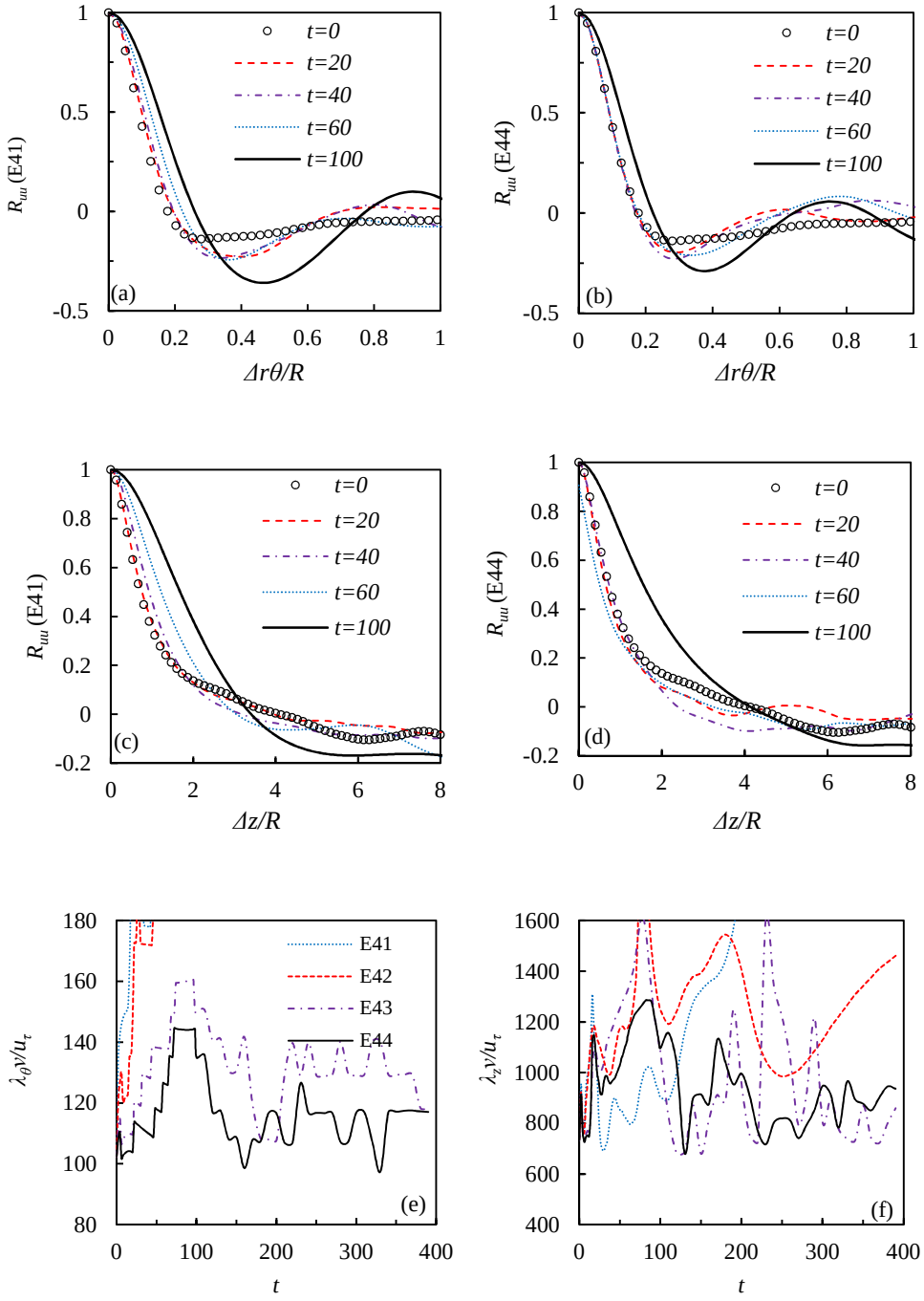

Figure 6.13: Correlations of u'_z of E41 and E44 at y^{+0}=5.4.

spanwise correlation of E41 decreases to -0.36 at t=100. In E44, the minimum value decreases from -0.15 to -0.2 during the laminarization stage (t=0~60). It reduces to -0.29 at recovery stage (t=100). The minimum value reduces due to that the streaks are

enhanced during the flow laminarization. Figure 6.13(e) shows the mean spanwise spacing of streaks, which is 2 times the distance to the first minimum peak. It remains around 100 wall unit ($\nu/u_{\tau 0}$) until t=16, but it increases quickly in E41 and E42 due to the fast decay of the streaks. In E43 and E44, the mean spanwise spacing increases slowly first but it reduces to 110 at t=200.

The streamwise correlation of u'_z is shown in Figures 6.13(c) and (d). The correlation coefficient reduces from 1 to zero at $\Delta z/R$=4.5 at t=0, which represents the averaged streamwise length of the streaky structures. The data in Figure 6.13(f) shows that the length of E41 & E42 & E43 & E44 increases with time. It fluctuates significantly in E41 and E42, which may have little physical meaning due to the fast decay of large scale streaky structures. At t =200, the lengths of the streaky structures of E34 and E44 fluctuate around a typical value 800 of the base flow. The streamwise length of the streaks is elongated in E42 & E43 & E44, which is a typical feature of a transitional flow.

6.3.4 The budget terms

The Figure 6.14 shows the development of profiles of production, pressure strain and dissipation of E21 & E24, which represent partially laminarized flow and 'completely' laminarized flow respectively. It is seen that the production of E21 reduces from t=0 to t=50 but after that the production converges to a steady state. The dissipation and pressure strain of E21 reduces to balance the production term in the wall region. The peak of the production moves inwardly in t<30 and after that it moves outwardly, which indicates the upshifting of the coherent structures. In E24, the reductions of these budget terms are more gradual but they reduce monotonically to small value at t=400. The peaks of the production and pressure strain also move outwardly.

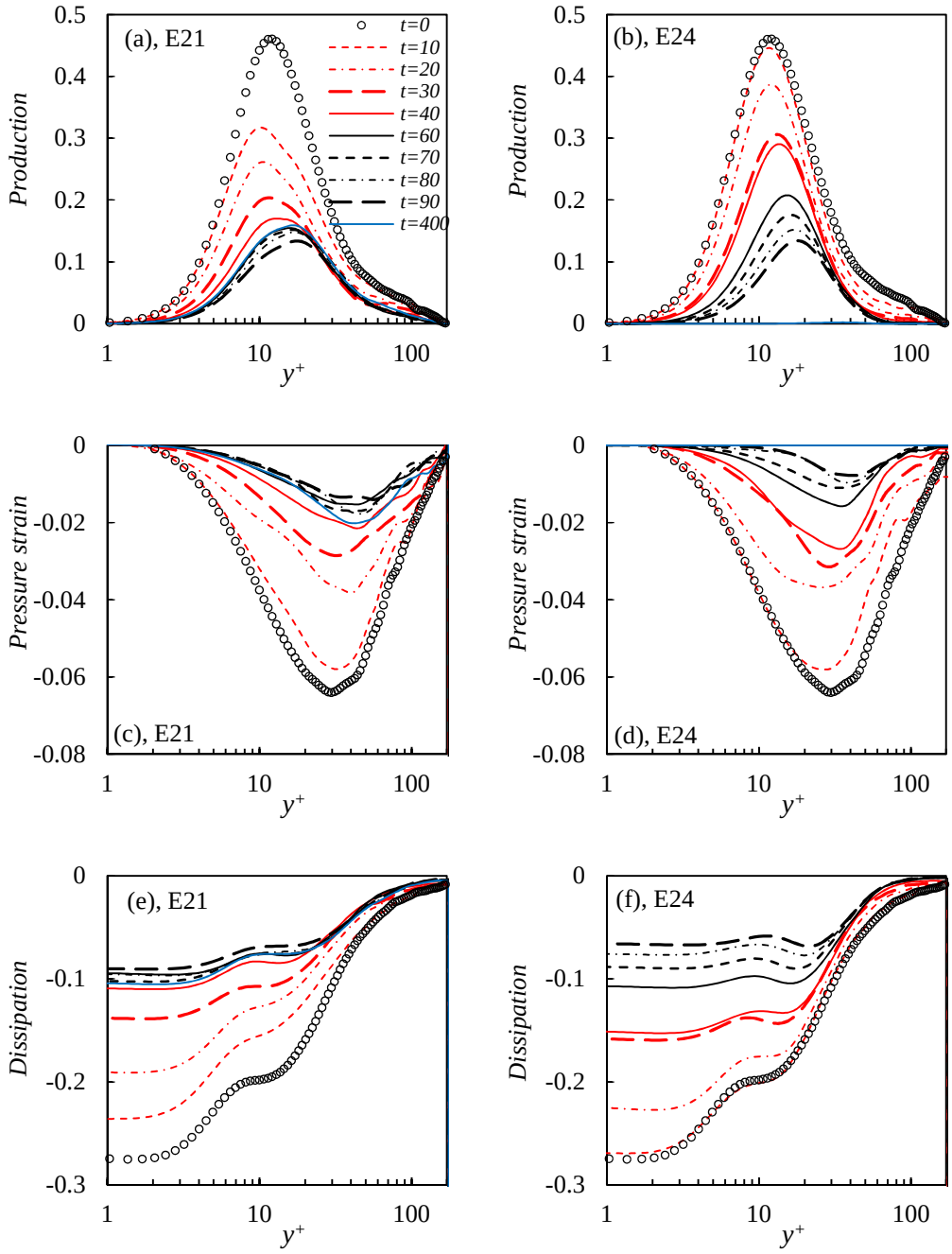

Figure 6.14: Production, pressure strain and dissipation of E21 & E24.

(normalized by $u_\tau{}^4/\nu$)

Figure 6.15 shows the development of profiles of production, pressure strain and dissipation terms of E41 & E44, which belongs to a 'completely' laminarized flow and a recovery flow respectively. The production of E41 is damped quickly during t<20. By

comparison, the production of E44 reduces much slower. The production of E44 shows an outer peak at t=30. Inner peak continues to decrease until t=80, which is consistent to the recovery of inner turbulence which starts at t=~80. The dissipation reduces and the thickness of the viscous layer increases. It is shown that the reduction of the near wall

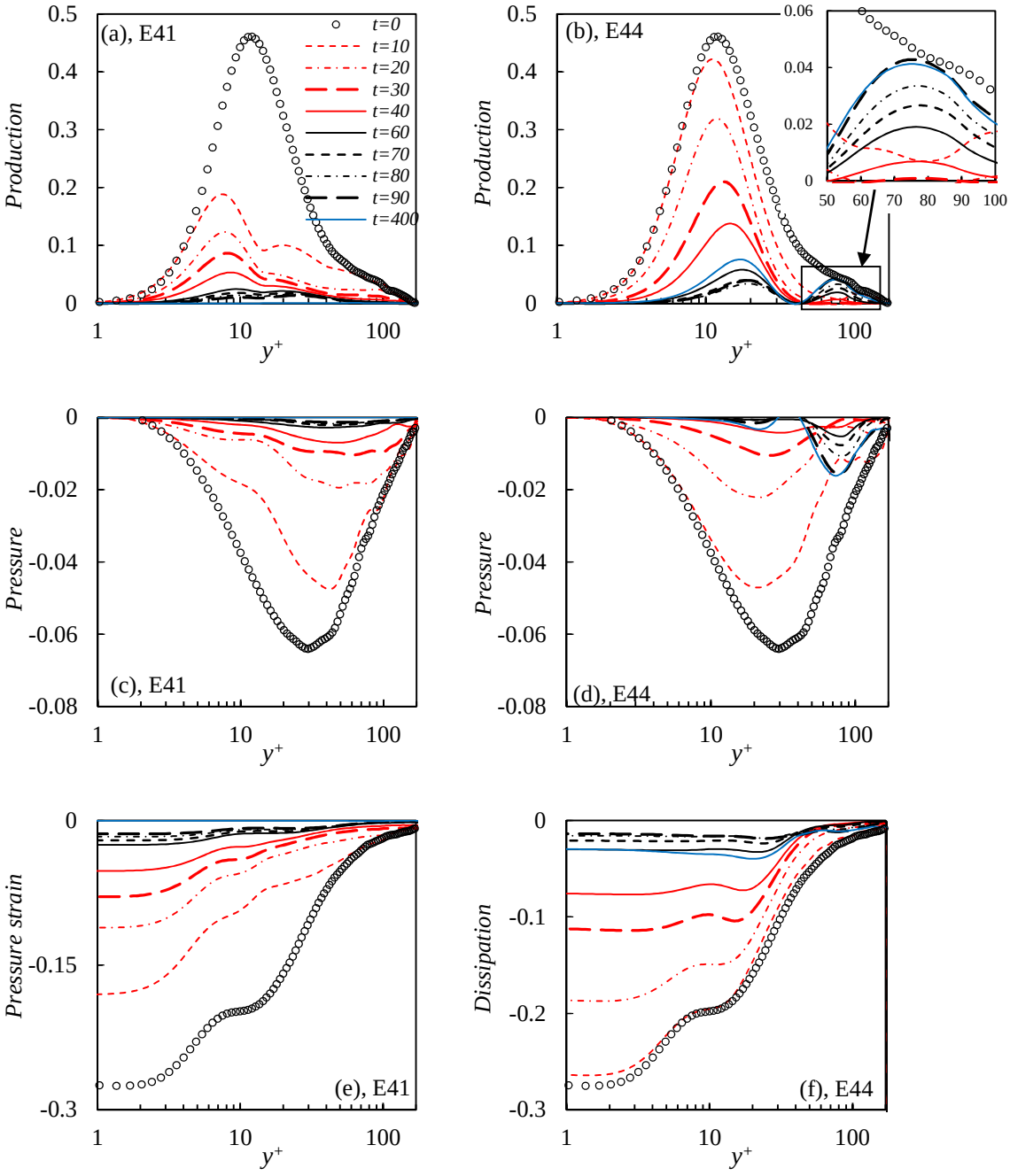

Figure 6.15: Production, pressure strain and dissipation of E41 & E44.
(normalized by $u_\tau{}^4/\nu$)

vortical structures is more significant in E41. The pressure strain of E41 shows that the reduction in t<10 is more significant in the wall region. By comparison, it is more significant in the outer region (y^+>50) for E44. These reduction scenarios are reflected in the visualization of E41 and E44 shown in section 6.3.1.

6.4 Summary and conclusions

The transient response of the development of a turbulent pipe flow after it is subjected to a non-uniform body force with various amplitudes and profiles is studied. It is found that the laminarization of the turbulent flow is a natural response to the change of force balance. Depending on the amplitude and body force coverage, the flow reaches various final quasi-steady states toward the end of the transient process, namely partially laminarized flow, 'completely' laminarized flow and recovery flow. The following conclusions are drawn for the former two:

(1) The turbulence reduction rate is mainly dependent on the total force amplitude (F). The higher force amplitude causes stronger distortion of mean flow and local shear stress.

(2) Although the increase of F and coverage results in similar effects, the latter causes more complicated effects. It is found that the increase of F (the coverage is not changed) leads to monotonic decrease of streamwise and wall-normal turbulent stresses. Increasing the body force coverage (the F is not changed) intensifies the decay of wall-normal turbulent stress but the suppressing effect on the streamwise turbulent stress is reduced.

(3) For the partially laminarized flows, increase of F or increase of coverage leads to a longer transient period of turbulence development. The modulation of the

turbulence includes a reduction stage and a recovery stage. In some cases, the bypass transition scenario is observed during the recovery stage. For some critical F and coverage, the turbulence of the flow decays completely.

(4) The transient turbulence reduction shows two different patterns dependent on the body force coverages. Type one flows are cases with very narrow body force coverage (y^{+0}=15), while type two flows are cases with wider body force coverages (y^{+0}=30, 60, 90). For type one, the turbulence production is damped faster near wall but the body force induced flow is largely laminar. Therefore, increase of F with narrow coverage is less efficient in suppressing the wall-normal turbulence than that with wide coverage. For type two, the turbulence production is damped more gradually but the final reduction is more significant due to that the body force induced flow is turbulent.

The recovery of the turbulence shows the following characteristics:

(1) The recovery of turbulence in the wall region is independent on the wall-normal location, implying that the turbulence recovery in this region is not through a diffusion mechanism. The r.m.s of streamwise and wall-normal velocity fluctuations recover almost simultaneously in this region.

(2) The recovery of turbulence in the central region depends on the wall-normal location, implying that the turbulence recovery in this region is through a diffusion mechanism.

(3) The enlargement of the body force coverage advances the recovery of both near wall turbulence and central turbulence.

Chapter 7

Conclusions and Future Work

7.1 Conclusions

Two typical non-equlibrilum flows, namly a turbulent pipe flow following the increase of flow rate and a turbulent flow subjected to a non-uniform body force are studied systematically. The turbulent pipe flow subjected to a sudden change in flow rate eveloves from an initial state to a final one via a bypass transition mechanism. The results have been comapred with those of a transient channel flow (He & Seddighi 2013, J. Fluids Mech.). The detailed conclusions for this flow are summarized as following

(1) It is similar to that in a channel, the transient flow in a pipe after a step increase in flow rate is effectively a laminar flow followed by a bypass transition. New turbulence generated through bypass transition mechanisms initially occupies the near wall region; it propagates into the central region following the completion of the transition.

(2) The general trends of the transition in the pipe and channel flows are found to be the same in the near-wall region. The similarities among the two flows are not only in instantaneous flow structures, but also in the ensemble-averaged statistical values. The transition onset prediction formula obtained from channel

data works very well for the pipe flow. However, there are detailed differences in the central region between the two flows during the transition stage. The growth of turbulence in the pipe at this stage is faster and earlier than that in the channel flow. This is attributed to the stronger mixing effect in the pipe, where the spanwise space becomes narrower as the flow goes closer to the centre.

(3) The developments of the mean velocity profiles, turbulent viscosity, vorticity Reynolds number and budget terms are analyzed. It is found that the growths of the turbulent viscosity and the vorticity Reynolds number (Re_v) are quantitatively different in the two flows, which are attributed to the differences in the velocity gradient developments. These results may provide useful information for the development of turbulence models.

(4) The typical flow response in a bypass transition is the growth and break down of streaks. It is found this scenario in a slow ramp-up flow is not as significant as in a fast ramp-up flow. However, although there is delay effect, the growth of the statistics is similar, disregarding to the slow or fast imposed accelerations.

(5) During the transitional stage, the linear relation of Re_θ and $Re_{v,max}$ is only observed in the fast ramp-up flow. As the ramp-up process is slowed down, the linear region reduces. The slope of linear region in fast ramp-up cases is found between 0.84 and 0.95, contrasting to a typical slope of boundary layer flow 2.193.

The turbulent flows with a non-uniform body force share similar features to those of real buoancy-aiding flows. The flows with the imposition of body forces are mainly classified into four types, namely, partially laminarized flow, ‘completely’ laminarized

flow, partially recovery flow and strongly recovery flow. The former two and the later two are discussed in a laminarized flow framework and a recovery flow framework.

For the partially laminarized flow and 'completely' laminarized flow, a new theory is proposed to explain the 'laminarization phenonmon' due to the imposition of a body force in a turbulent flow. Considerring a turbulent flow of Reynolds number Re_0 driven by a pressure gradient (dp/dx) and an additional non-uniform streamwise body force in the same direction of the flow (body force aided flow). In comparison with the reference flow of the same Reynolds number but without body forces, the turbulence can be significantly reduced. In general, the stronger the body force, the stronger the turbulence reduction is. When the body force is sufficiently strong, the flow can be fully laminarized. This convectional view has been established in the literature for various physical flows. It is also clearly demonstrated by using systematically varied prescribed non-uniform body forces using direct numerical simulation (DNS) herein. In the present study, we have established a new perspective towards such flows. The body-force aided flow can be best interpreted as resulting from imposing a body force to flow driven by a pressure gradient (referred to as the dp-based reference flow). The following are summarized for the laminarized flow:

(1) The turbulence of the flow remains largely unchanged following the imposition of the body force. Most significantly, the eddy viscosity of the flow remains largely uninfluenced by the imposition of the body force, even though the total flow rate can be significantly increased;

(2) The wall-normal and circumferential turbulent stresses remain largely unchanged and the streamwise turbulent stress is moderately increased. The latter is a result of enhanced high- and low-speed streaks;

(3) The additional flow caused by the imposition of the body force is governed by the following momentum equation,

$$0 = \frac{1}{Re}\frac{1}{r}\frac{\partial}{\partial r}\left[r\left((1+\nu_{t1})\frac{\partial U'}{\partial r}\right)\right] + bf$$

where ν_{t1} is the turbulent viscosity of the dp-based flow and therefore can be seen as known, and the boundary conditions are $U' = 0$ on the wall and $\frac{\partial U'}{\partial r} = 0$ at the pipe centre. The velocity can be obtained from the integration of the above momentum equation. The addition of the body force causes an increase in turbulent shear stress, which can be calculated from the above momentum equation. The total wall shear is the sum of the wall shear of the dp-based flow and that of the body force driven flow obtainable from the above momentum equation;

(4) The body force can be characterized by four parameters, i.e., the total amplitude (F), the wall value, the coverage and the profile. It is found that when the coverage of the body force is small, say, less than y^+<20, the body-force driven flow is effectively a laminar flow. The solution of the total flow is further simplified;

(5) The level of laminarization is associated with the Reynolds number of the dp-based reference flow (Re_τ). When the applied body force is sufficiently large, causing the Reynolds number of the pressure-driven-flow to be sufficiently small and turbulence cannot be sustained and the flow becomes a laminar flow. Consider a series of flow cases of the same total flow rate, but with increasing body forces, e.g., B1, B2, B3.

Alternatively, consider a series of flow cases of the same pressure gradient imposed, and with increasing body forces, the turbulent flow is not laminarized at all;

(6) Under the condition of a fixed Reynolds number, the strength of the effect of a body force on the flow in terms of suppressing turbulence and laminarizing the flow is predominately associated with the flow rate of the perturbation flow it induces. The apparent flow is the total flow takes away the perturbation flow of the body force. Hence, the higher the latter, the smaller the apparent flow; the lower the apparent Reynolds number ($Re_{\tau 1}$) and the stronger the laminarization. The flow rate of the perturbation flow is linearly proportional to the amplitude of the body force. It also increases with the increase of the coverage when the amplitude is fixed and the relation is described by Eqn 5.21. The profile of the body force distribution only affects the laminarization through flow rate that it causes. For example, with the same amplitude and coverage, the stepwise distribution causes a perturbation flow that is about 2.6 to 3 times higher than that of a linear distribution and hence it is more effective in laminarizing the flow. The ratio between the two total forces in the stepwise and linear distributions is about 1.95.

For the recovery flow, following basical features can be drawn:

(1) The body force can be characterized by four parameters, i.e., the total amplitude (F), the wall value, the coverage and the profile. It is found that the main influential parameters are the total amplitude, which determines the force density. The higher the force density, the more effectively the streamwise turbulent stress is suppressed, but the effect on non-streamwise turbulent stresses is more related to the pattern of the body force, which is determined by both the amplitude and the profile.

(2) The flow visualization shows that many partially laminarized flows are transitional flows. As the F increases, the streaky structures become smooth and the streaky structures are elongated, which are similar to those observations in the transitional region of boundary layer flows. The spanwise and streamwise scales of the streaks increase. By contrary, for recovery flow, the spanwise and streamwise scales reduce as the F increases and the streaky structures are different from both the base flow and a transitional flow. The vortical structures are organized with the streaky structures in partially laminarized flow but most of vortical structures are not organized and detached from the wall in recovery flow;

(3) The $\overline{uv}$ contributions of ejections and sweeps of the partially recovery flows are similar to that of the base flow at the near wall region. In near wall region (y^+<30) of the base flow, the balance of Reynolds stress are established between sweeps and ejections, where the contribution of sweeps is dominant. The contribution of sweeps reduces slightly but the ejections' contribution increases in recovery flow. Flatness and skewness show that these flows are highly intermittent. Between y^+=10 and new shear layer, the turbulence is a mixture of the inner turbulence and outer turbulence. The skewness data shows that the inward motions are dominant in this region;

(4) The budget terms of recovery flows show a balance pattern different from that of the base flow. There are two production regions shown on the main budget terms. There are many detailed changes on these budget terms, but the most important information can be drawn is from the term for the energy re-distribution between the three components of the turbulent stresses. The pressure strain of $\overline{u'_r u'_r}$ is recovered in the near wall region, which shows two peaks in y^+<40. The peaks at around y^+=5 is due to a 'splatting' effect of the wall and it only exists in strongly recovery flow. The

collision of the inward and outward motions creates strong negative peaks on the pressure strain of $\overline{u'_r u'_r}$, which redistributes the energy from u'_r to u'_θ.

The transient response of the development of a turbulent pipe flow after it is subjected to a non-uniform body force with various amplitudes and profiles is studied in chapter 6. It is found that the laminarization of the turbulent flow is a natural response to the change of force balance. Depending on the amplitude and body force coverage, the flow reaches various final quasi-steady states toward the end of the transient process, namely partially laminarized flow, 'completely' laminarized flow and recovery flow. The following conclusions are drawn for the former two:

(1) The turbulence reduction rate is mainly dependent on the total force amplitude (F). The higher force amplitude causes stronger distortion of mean flow and local shear stress.

(2) Although the increase of F and coverage results in similar effects, the latter causes more complicated effects. It is found that the increase of F (the coverage is not changed) leads to monotonic decrease of streamwise and wall-normal turbulent stresses. Increasing the body force coverage (the F is not changed) intensifies the decay of wall-normal turbulent stress but the suppressing effect on the streamwise turbulent stress is reduced.

(3) For the partially laminarized flows, increase of F or increase of coverage leads to a longer transient period of turbulence development. The modulation of the turbulence includes a reduction stage and a recovery stage. In some cases, the bypass transition scenario is observed during the recovery stage. For some critical F and coverage, the turbulence of the flow decays completely.

(4) The transient turbulence reduction shows two different patterns dependent on the body force coverages. Type one flows are cases with very narrow body force coverage (y^{+c0}=15), while type two flows are cases with wider body force coverages (y^{+c0}=30, 60, 90). For type one, the turbulence production is damped faster near wall but the body force induced flow is largely laminar. Therefore, increase of *F* with narrow coverage is less efficient in suppressing the wall-normal turbulence than that with wide coverage. For type two, the turbulence production is damped more gradually but the final reduction is more significant due to that the body force induced flow is turbulent.

The recovery of the turbulence shows the following characteristics:

(1) The recovery of turbulence in the wall region is independent on the wall-normal location, implying that the turbulence recovery in this region is not through a diffusion mechanism. The r.m.s of streamwise and wall-normal velocity fluctuations recover almost simultaneously in this region.

(2) The recovery of turbulence in the central region depends on the wall-normal location, implying that the turbulence recovery in this region is through a diffusion mechanism.

(3) The enlargement of the body force coverage advances the recovery of both near wall turbulence and central turbulence.

7.2 Future work

(1) For a transient flow, let us define the turbulence intensity as the initial turbulence over

the final bulk mean velocity, with the increase of the final Reynolds number or the decrease of the initial Reynolds flow, the Tu decreases. An interesting question is that, if the Tu is reduces down to 0.1%, below which T-S wave instability scenario usually shows in boundary layer flow, what is the transition mechanism? The current Reynolds number ranges from 2650-45000. With a large extension of the final Reynolds number it is possible to answer this question.

(2) The non-uniform body forces are imposed on a turbulent flow with a low Reynolds number. In a mixed convection flow, the Reynolds number is usually much larger. Is there any Reynolds number effect on the flow response to a non-uniform body force? Similar studies should be conducted on turbulent flow with higher Reynolds number.

(3) The present study establishes physical models and a database for two typical non-equilibrium flows. The transient flow with sudden change in flow rate is governed by bypass transition mechanism. The database is ideal to test some transitional turbulence models, such as the $\gamma - Re_\theta$ transitional model (Langtry 2006) and laminar kinetic model (Mayle & Schulz 1997). The DNS database of flows with non-uniform body forces can be used to test the performance of RANS models in predicting such flows. More detailed work should be conducted.

References

Andersson, P., Berggren, M., Henningson, D.S., 1999. Optimal disturbances and bypass transition in boundary layers, Phys. Fluids, 11(1), 134-150.

Asai, M., Manigawa, M., Nishioka, M. 2002. The instability and breakdown of near wall low-speed streaks, J. Fluid Mech., 455, 289–314.

Bae, J.H., Yoo, J. Y., Choi, H., 2005. Direct numerical simulation of turbulent supercritical flows with heat transfer, Phys. Fluids, 17, 105104, 1-24.

Bae, J.H., Yoo, J.Y., Choi, H., McEligot, D.M., 2006. Effects of large density variation on strongly heated internal air flows, Phys. Fluids, 18, 075102, 1-25.

Bae, J.H., Yoo, J.Y., McEligot, D.M., 2008. Direct numerical simulation of heated CO2 flows at supercritical pressure in a vertical annulus at Re=8900, Phys. Fluids, 20, 055108, 1-20.

Berger, T.W., Kim, J., Lee, C., Lim, J., 2000. Turbulent boundary layer control utilizing the Lorentz force, Phys. Fluids, 12, 631-649.

Bishop, A.A., Efferding, L.E., Tong, L.S., 1962. A review of heat transfer and fluid flow water during 'once-thru' operation and in the supercritical temperature region, August, WCAP-2040.

Blaisdell, G.A., Coleman, G.N., Mansour, N.N., 1996. Rapid distortion theory for compressible homogenous turbulence under isotropic mean strain, Phy. Fluids, 8(10), 2692-2705.

Bradshaw, P., 1994. Turbulence: the chief outstanding difficulty of our subject, Exp. Fluids, 16, 203–16.

Brandt, L., Schlatter, P., Henningson, D.S., 2004. Transition in boundary layers subject to free-stream turbulence, J. Fluid Mech., 517, 167-198.

Brian, F.F., Petros, J.I., 2012. Dynamics of streamwise rolls and streaks in turbulent wall-bounded shear flow, J. Fluid Mech., 708, 149–196.

Brethouwer, G., Duguet, Y., Schlatter, P., 2012. Turbulent–laminar coexistence in wall flows with Coriolis, buoyancy or Lorentz forces, J. Fluid Mech., 704, 137–172.

Brown, D.L., Cortez, R., Minion, M.L., 2001. Accurate projection methods for the incompressible Navier–Stokes equations, J. Comput. Phys., 168 (2), 464–499.

Butler, K.M., Farrell, B.F., 1992. Three-dimensional optimal perturbations in viscous shear flow, Phys. Fluids A, 4(8), 1637-1650.

Chin, C., OOI, A. S.H., Marusic, I., Blackburn, H.M., 2010. The influence of pipe length on turbulence statistics computed from direct numerical simulation data, Phys. Fluids, 22, 115107, 1-10.

Cheng, X., Kuang, B., Yang, Y.H., 2007. Numerical analysis of heat transfer in supercritical water cooled flow channels, Nucl. Eng. Design, 237, 240–252.

Chin, C., 2011. Numerical study of internal wall-bounded turbulent flows, PhD thesis, The University of Melbourne.

Choi H., Moin, P., Kim J., 1994. Active turbulence control for drag reduction in wall-bounded flows, J. Fluid Mech., 262, 75-110.

Chung, Y.M., 2005. Unsteady turbulent flow with sudden pressure gradient changes, Int. J. for Numer. Methods in Fluids, 47(8-9), 925-930.

Colombo, A.F., Lee, P., Karney, B.W., 2009. A selective literature review of transient- based leak detection methods, J. Hydro-environment Res., 2, 212.

Cossu, C., Pujals, G., Depardon, S., 2009. Optimal transient growth and very large-scale structures in turbulent boundary layers, J. Fluid Mech., 619, 79-94.

Cotton, M.A., Craft, T.J., Guy, A.W., Launder, B.E., 2001. On modelling periodic motion with turbulence closures, Flow Turbul. Combust., 67, 143-58.

Driest, E.V., Blumer, C.E, 1963. Boundary layer transition: Free stream turbulence and pressure gradient effects, AIAA J., 1(6), 1303-1306.

Durst, F., Jovanovic, J., Sender, J., 1995. LDA measurements in the near-wall region of a turbulent pipe flow, J. Fluid Mech., 295, 305-335.

Eggels, J.G. M., Unger, F., Weiss, M.H.J., Westerweel, Adrian, R.T., Friedrich, R., F.T.M., 1994. Fully developed turbulent pipe flow: a comparison between direct numerical simulation and experiment, J. Fluid Mech., 268, 175-210.

Ellingsen, T., Palm, E., 1975. Stability of linear flow, Phys. Fluids., 18, 487-488.

E, W., Liu, J.G. 1996. Projection method I: Convergence and numerical boundary layers, SIAM J. Numer, Anal., 32, 1017–1057.

Ferziger, J.H. and Perié, M., 1996. Computational Methods for Fluid Dynamics, Springer-Verlag Berlin Heidelberg.

Fransson, J.H.M., Matsubara, M., Alfredsson, P.H., 2005. Transition induced by free-stream turbulence, J. Fluid Mech., 527, 1-25.

Fukagata F. and Kasagi, N., 2002. Highly energy-conservative finite difference method for the cylindrical coordinate system, J. Comput. Phys., 181, 478-498.

Fukagata, K., Iwamoto, K., Kasagi, N., 2002. Contribution of Reynolds stress distribution to the skin friction in wall-bounded flows, Phy. Fluids, 14(11), L75-L76.

Ghidaoui, M.S., Zhao, M., McInnis, D.A., Axworthy, D.H., 2005. A Review of Water Hammer Theory and Practice, Appl. Mech. Rev., 58(1), 49-71.

Gilbert, N. and Kleiser, L., 1986. Subcritical transition to turbulence in channel flow, In Direct and Large Eddy Simulation of Turbulence, ed. U. Schumann, R. Friedrich, 1-18. Braunschweig: Vieweg.

Gorji, S., Seddighi, M., Ariyaratne, C., Vardy, A.E., Donoghue, T.O., Pokrajac, D., He, S., 2014. A comparative study of turbulence models in a transient channel flow, Comput. Fluids, 89, 111-123.

Grötzbach, G., 2007. Anisotropy and Buoyancy in Nuclear Turbulent Heat Transfer-Critical Assessment and Needs for Modelling, Karlsruhe Institute of Technology, internal report, FZKA 7363.

Greenblatt, D. and Moss, E.A., 1999. Pipe flow relaminarization by temporal acceleration, Phy. Fluids, 11(11). 3478-3481.

Greenblatt, D. and Moss, E.A., 2004. Rapid temporal acceleration of a turbulent pipe flow, J. Fluid Mech., 514, 65-75.

Guermond, J.L. and Shen, J., 2003. Velocity-correction projection methods for incompressible flows, SIAM J. Numer. Anal., 41 (1), 112–134.

He, S., An, P., Li, J., Jackson, J.D., 1998. Combined heat and mass transfer in a uniformly heated vertical tube with water film cooling, Int. J. Heat and Fluid Flow, 19, 401-417.

He, S. and Jackson, J.D., 2000. A study of turbulence under conditions of transient flow in a pipe, J. Fluid Mech., 408, 1-38.

He, S., Jiang, P.X., Xu, Y.J., Shi, R.F., Kim, W.S., Jackson, J.D., 2005. A computational study of convection heat transfer to CO2 at supercritical pressures in a vertical mini tube, Int. J. Therm. Sci., 44, 521–530.

He, S., 2006. Effects of apparent body forces on turbulence in wall shear flows. Whither Turbulence Prediction and Control, March 26-29, Seoul National University, Seoul, Korea, WTPC.

He, S., Kim, W.S., Bae, J.H., 2008. Assessment of performance of turbulence models in predicting supercritical pressure heat transfer in a vertical tube, Int. J. Heat and Mass Transfer, 51, 4659–4675.

He, S. and Jackson, J. D., 2009. An experimental study of pulsating turbulent flow in a pipe, Eur. J. Mech.-B/Fluids, 28(2), 309-320.

He, S., Aritaratne, C., Vardy, A.E., 2011. Wall shear stress in accelerating turbulent pipe flow, J. Fluid Mech., 685, 440–460.

He, S. and Seddighi, M., 2013. Turbulence in transient channel flow, J. Fluid Mech., 715, 60-102.

He, S. and Seddighi, M., 2015. Transition of transient channel flow after a change in Reynolds number, J. Fluid Mech., 764, 395-427.

Hamilton, J.M., Kim, J., 1993. On the streak spacing in wall-bounded turbulent flows, Stanford University, Annual Research Briefs, pp. 249-257.

Hamilton, J.M., Kim, J., Waleffe, F., 1995. Regeneration mechanisms of near-wall turbulence structures, J. Fluid Mech., 232, 317–348.

Hultgren, L.S, Gustavsson, L.H., 1981. Algebraic growth of disturbances in a laminar boundary layer, Phys. Fluids., 24(6), 1000-1004.

Iido, O. and Nagano, Y., 1998. The Relaminarization Mechanisms of Turbulent Channel Flow at Low Reynolds Numbers, Flow, Turbul. Combust., 60, 193–213.

Jackson, J. D. and Hall, W.B., 1979. Influences of buoyancy on heat transfer to fluids flowing in vertical tubes under turbulent conditions, In Turbulent Forced Convection in Channels and Bundles, ed. S. Kakac, D.B. Spalding, 2, 613–40. Washington, DC: Hemisphere.

Jackson, J.D., Cotton, M.A., Axcell, B.P., 1989. Studies of mixed convection in vertical tubes, Int. J. Heat Fluid Flow, 10(1), 2-15.

Jackson, J.D., 2006. Studies of buoyancy-influenced turbulent flow and heat transfer in vertical passages, Keynote lecture, Proc. 13th Int. Heat Transfer Conf., Sydney, August, 2006.

Jackson, J.D., 2011. Mechanisms for impairment of heat transfer in strongly-heated turbulent flow of air through a tube, 12th UK National Heat Transfer Conference, Leeds, UK, 30 August-1 September.

Jackson, J.D., 2013. Fluid flow and convective heat transfer to fluids at supercritical pressure, Nucl. Eng. Des., 264, 24–40.

Jacobs, R.G. and Durbin, P.A., 2001. Simulations of bypass transition, J. Fluid Mech., 428,185-212.

Jeong, J. and Hussain, F., 1995. On the identification of a vortex, J. Fluid Mech., 285, 69-94.

Jiménez, J. and Moin, P., 1991. The minimal flow unit in near-wall turbulence, J. Fluid Mech., 225, 213–240.

Jiménez, J. and Pinelli, A., 1999. The autonomous cycle of near-wall turbulence, J. Fluid Mech., 389, 335–359.

Kataoka, K., Kawabata, T., Miki, K., 1975. The start-up response of pipe flow to a step change in flow rate, J. Chem. Eng., Japan. 8, 266.

Karniadakis, G.E., Israeli, M., Orszag, S.A., 1991. High-order splitting methods for the incompressible Navier–Stokes equations, J. Comput. Phys., 97, 414–443.

Kasagi, F. and Nishimura, M., 1997. Direct numerical simulation of combined forced and natural turbulent convection in a vertical plane channel, Int. J. Heat Fluid Flow, 18, 88–99.

Khaleghi, A., Pasandideh-Fard, M., Malek-Jafarian, M., Chung Y.M., 2010. Assessment of common turbulence models under conditions of temporal acceleration in a pipe, J. Appl. Fluid Mech., 3, 25-33.

Kim, J. and Moin, P., 1985. Application of a fractional-step method to incompressible Navier–Stokes equations, J. Comput, Phys., 59, 308-323.

Kim, J., Moin, P., Morser, R., 1987. Turbulence statistics in fully developed channel flow at low Reynolds number, J. Fluid Mech., 177, 133-166.

Kim K., Baek S.J., Sung, H.J., 2002. An implicit velocity decoupling procedure for the incompressible Navier-Stokes equations, Int. J. Numer. Meth. Fluids, 38(2): 125-138.

Klebanoff, P.S., Tidstrom, K.D., Sargent, L.M., 1962. The three-dimensional nature of boundary-layer instability, J. Fluid Mech., 12, 1-34.

Kline, S.J., Reynolds, W.C., Schraub, F. A., Runstadler, P. W., 1967. The structure of turbulent boundary layers, J. Fluid Mech., 30, 741-773.

Kleiser, L., Zang, T.A., 1991. Numerical simulation of transition in wall-bounded shear flows, Annu. Rev. Fluid Mech., 23, 495–537.

Koshizuka, S., Takano, N., Oka, Y., 1995. Numerical-analysis of deterioration phenomena in heat-transfer to supercritical water, Int. J. Heat Mass Transfer, 38, 3077–3084.

Kolmogorov, A.N. 1941. The local structure of turbulence in incompressible viscous fluid for very large Reynolds number, Dokl. Akad. Nauk SSSR 30:9–13 (reprinted in Proc. R. Soc. Lond. A 434:9–13, 1991).

Kravchenko, A.G. and Moin, P., 1997. On the Effect of Numerical Errors in Large Eddy Simulations of Turbulent Flows, J. Comput. Phys., 131(2), 310-322.

Kurokawa, J. and Morikawa, M., 1986. Accelerated and decelerated flows in a circular pipe (1st report, velocity profiles and friction coefficient), Bulletin of Japanese Soc. Mech. Engineers, 29, 758-765.

Kurganov, V. A. and Kaptil'ny, A. G., 1992. Velocity and Enthalpy Fields and Eddy Diffusivities in a Heated Supercritical Fluid Flow, Exp. Therm. Fluid Sci., 5, 465-478.

Launder, B. E., 1964. Laminarization of the Turbulent Boundary Layer in a Severe Acceleration, J. Applied Mech., 31(4), 707–708.

Launder, B. E. and Sharma, B. I., 1974. Application of the energy-dissipation model of turbulence to the calculation of flow near a spinning disc, Lett. Heat Mass Trans., 1(2), 131-137.

Langtry, R. B., 2006. Correlation-based transition modelling for unstructured parallelized computational fluid dynamics codes, PhD Thesis, University of Stuttgart.

Landahl, M.T., 1980. A Note on an Algebraic Instability of Inviscid Parallel Shear Flows, J. Fluid Mech., 98, 243–251.

Leonard, A. and Wray, A., 1975. A New Numerical Method for the Simulation of Three-Dimensional Flow in a Pipe, in Fourth Int. Conf. on Numer. Methods in Fluid Dyn., Colorado, Lecture Notes in physics, 135, 335 (Springer-Verlag, New York).

Lefebvre, P. J. and White, F. M., 1989. Experiments on transition to turbulence in a constant-acceleration pipe flow, ASME: J. Fluids Eng., 111(4), 428-432.

Lefebvre, P.J. and White, F.M., 1991. Further experiments on transition to turbulence in constant-acceleration pipe flow, ASME: J. Fluids Eng., 113(2), 223-227.

Li, J.K., 1994. Studies of buoyancy-influenced convective heat transfer to air in a vertical tube, Ph.D. thesis, University of Manchester.

Lu, S.S. and Willmarth, W.W., 1973. Measurements of the structure of the Reynolds stress in a turbulent boundary layer, J. Fluid Mech. 60(03), 481–511.

Luchini, P., 2000. Reynolds-number-independent instability of the boundary layer over a flat surface: Optimal perturbations, J. Fluid Mech., 404, 289–309.

Maruyama, T., Kuribayashi, T., Mizushina, T., 1976. The structure of the turbulence in transient pipe flows, J. Chem. Eng. Japan., 9 (6), 431–439.

Mathur, A., Seddighi, M., He, S., 2015. Effect of high Reynolds number rate on transition of transient channel flow, 8th Turbulence, Heat and Mass Transfer, 15-18, September, Sarajevo.

Mayle, R.E. and Schulz, A., 1997. The path to predicting bypass transition, J. Turbomach., 119, 405-411.

Marusic I., McKeon B.J., Monkewitz, P.A., Nagib H.M., Smits A.J., 2010. Wall-bounded turbulent flows at high Reynolds numbers: Recent advances and key issues, Phys. Fluids, 22, 065103, 1-24.

Mans, J., Kadijk, E.C., de Lange, H.C., Steenhoven, A. A. van., 2005. Breakdown in a boundary layer exposed to free-stream turbulence, Exp. Fluids, 39, 1071–1083.

Mandal, A.C., Venkatakrishnan, L., Dey, J., 2010. A study on boundary-layer transition induced by free stream turbulence, J. Fluid Mech., 660, 114–146.

McEligot, D.M., Coon, C.W., Perkins, H.C., 1970. Relaminarization in tubes. Int. J. Heat Mass Transfer, 9, 1151–1152.

McEligot, D.M. and Jackson, J.D., 2004. Deterioration criteria for convective heat transfer in gas flow through non-circular ducts, Nucl. Eng. Des., 232, 327–333.

Meseguer A. and Trefethen, L.N., 2003. Linearized pipe flow to Reynolds number 10^7, J. Comput. Phys., 186, 178.

Mikielewicz, D.P., Shehata, A.M., Jackson, J. D., McEligot, D.M., 2002. Temperature, velocity and mean turbulence structure in strongly-heated internal gas flows. Comparison of numerical predictions with data, Int. J. Heat Mass Transfer, 45, 4333-4352.

Morinishi, Y., Vasilyev, O.V., Ogi, T., 2004. Fully conservative finite difference scheme in cylindrical coordinates for incompressible flow simulations, J. Comput. Phys., 197, 686–710.

Moretti, P.M., Kays, W.M., 1965. Heat transfer to a turbulent boundary layer with varying free-stream velocity and varying surface temperature—an experimental study, Int. J. Heat Mass Transfer, 8, 1187–1202.

Moser, R.D. and Moin, P., 1987. The effects of curvature in wall-bounded turbulent flows, J. Fluid Mech., 175, 479–510.

Moin, P. and Mahesh, K., 1998. Direct numerical simulation: a tool in turbulence research, Ann. Rev. Fluid Mech., 30, 539–578.

Narasimha, R. and Sreenivasan, K.R., 1973. Relaminarization in highly accelerated turbulent boundary layers, J. Fluid Mech., 63(3), 417-447.

Nagib, H.M. and Chauhan, K.A., 2008. Variations of von Kármán coefficient in canonical flows, Phys. Fluids, 20, 101518, 1-10.

Orlandi, P., 2001. Fluid Flow Phenomena: A Numerical Toolkit. Kluwer.

Orszag, S.A., Israeli, M., Deville, M., 1986. Boundary conditions for incompressible flows, J. Sci. Comput., 1, 75–111.

Orszag, S.A. and Patterson, G.S., 1972. Numerical simulation of turbulence, In Statistical Models and Turbulence. Springer.

Ovchinnikov, V., Choudhari, M.M., Piomelli, U., 2008. Numerical simulations of boundary-layer bypass transition due to high-amplitude free-stream turbulence, J. Fluid Mech., 613, 135-169.

Perkins, K.R., Schade, K.W., McEligot, D.M., 1973. Heated laminarizing gas flow in a square duct, Int. J. Heat Mass Transfer, 16, 897–916.

Petukhov, B.S. and Polyakov, A.F., 1988. Heat Transfer in Turbulent Mixed Convection, Hemisphere, New York.

Quadrio, M. and Luchini,P., 2002. Direct numerical simulation of the turbulent flow in a pipe with annular cross-section, Eur. J. Mech. B, 21, 413–427.

Rai, M.M. and Moin, P., 1991. Direct simulations of turbulent flow using finite-difference schemes, J. Comput. Phys., 96(1), 15-53.

Reynolds, O., 1883. An experimental investigation of the circumstances which determine whether the motion of water in parallel channels shall be direct or sinuous and of the law of resistance in parallel channels, Philos. Trans. R. Soc., 174, 935–82.

Reddy, R.C. and Henningson, D.S., 1993. Energy Growth in Viscous Channel Flows, J. Fluid Mech., 252, 209–238.

Rosenfeld, M., 1996. Uncoupled temporally second-order implicit solver of incompressible Navier-Stokes equations, AIAA. J., 34, 1829-1834.

Satake, S.I., Kunugi, T., Shehata, A. M. McEligot, D.M., 2000. Direct numerical simulation on laminarization of turbulent forced gas flows in circular tubes with strong heating, Int. J. Heat Fluid Flow., 21, 526-534.

Schmid, P.J. and Henningson, D.S., 1994. Optimal energy density growth in Hagen–Poiseuille flow, J. Fluid Mech., 277, 191-225.

Scotti, A. and Piomelli, U., 2001. Numerical simulation of pulsating turbulent channel flow, Phys. Fluids., 13, 67-84.

Schlatter, P., Brandt, L., de Lange, H.C., Henningson, D. S., 2008. On streak breakdown in bypass transition, Phys. Fluids, 20, 101505, 1-15.

Seddighi, M., 2011. Study of turbulence and wall shear stress in unsteady flow over smooth and rough wall surfaces, PhD thesis, University of Aberdeen.

Seddighi, M., He, S., Vardy, A.E., Orlandi, P., 2014. Direct Numerical Simulation of an Accelerating Channel Flow, Flow Turbul. Combust., 92(1), 473-502.

Sharabi, M.B., Ambrosini, W., He, S., 2008. Prediction of unstable behaviour in a heated channel with water at supercritical pressure by CFD models, Ann. Nucl. Energy, 35, 767–782.

Shitsman, M.E., 1963. Impairment of the heat transmission at supercritical pressures, High Temp., 1, 237–244.

Shima, N., 1989. Calculation of a variety of boundary layers with a second-moment closure applicable up to a wall, In: Proceedings of 7th symposium on turbulent shear flows, Stanford University, Paper 5-3.

Shen, J., 1994. Efficient spectral-Galerkin method. I. Direct solvers of second- and fourth-order equations using Legendre polynomials, SIAM J. Sci. Comput., 15, 1489–1505.

Stanaway, S. K., Cantwell, B. J., Spalart, P. R., 1988. NASA the conditions TM 101041, Ph.D. thesis. (unpublished).

Styrikovich, M.A., Margulova T.K., Miropolskiy Z.L., 1967. Problem in the development of designs of supercritical boilers, Teploenergetika, 32 (6), 4-7.

Tanaka, H., Tsuge, A., Hirata, M., Nishiwaki, N., 1973. Effects of buoyancy and of acceleration owing to thermal expansion on forced turbulent convection in vertical circular tubes—Criteria of the effects, velocity and temperature profiles, and reverse transition from turbulent to laminar flow, Int. J. Heat Mass Transfer., 16, 1267–1288.

Talha, T., 2012. A Numerical Investigation of Three dimensional Unsteady Turbulent Channel Flow Subjected to Temporal Acceleration, PhD thesis, University of Warwick University.

Timmermans, L.J.P., Minev, P.D., Van De Vosse, F.N., 1996. An approximate projection scheme for incompressible flow using spectral elements, Int. J. Numer. Methods Fluids, 22, 673–688.

Tennekes, H., Lumley, J.L., 1972. A first course in Turbulence. MIT Press.

Trefethen, L.N., Reddy, A.E., Driscoll, S.C., 1993. Hydrodynamic stability without eigenvalues, Science, 261, 578–584.

Tsukahara, T., Seki, Y., Kawamura, H., Tochio, D. 2005 DNS of turbulent channel flow at very low Reynolds numbers. In Proceedings of Fourth International Symposium on Turbulence and Shear Flow Phenomena (ed. J. A. C. Humphrey et al.), pp. 935–940. Williamsburg, USA.

Vaughan, N.J. and Zaki, T.A., 2011. Stability of zero-pressure-gradient boundary layer distorted by unsteady Klebanoff streaks, J. Fluid Mech., 681, 116–153.

Van Kan J., 1986. A second-order accurate pressure-correction scheme for viscous incompressible flow, SIAM J. Sci. Stat. Comput., 7 (3), 870–891.

Verzicco, R. and Orlandi, P., 1996. A finite difference scheme for three-dimensional incompressible flows in cylindrical coordinates, J. Comput. Phys.,123, 402–413.

Wallace, J.M., Eckelmann, H., Brodkey, R.S., 1972. The wall region in turbulent shear flow, J. Fluid Mech., 54, 39-48.

Waleffe, F., Kim, J., Hamilton., J., 1991. Eds. F. Durst et al., in "Turbulent Shear Flows 8: selected papers from the Eighth International Symposium on Turbulent Shear Flows, Munich, Germany, Sept. 9-11" Springer-Verlag, Berlin, 1993.

Waleffe, F., Kim, J., Hamilton, J.M., 1993. On the origin of streaks in turbulent boundary layers. In Turbulent Shear Flows 8 (ed. F. Durst, R. Friedrich, B. E. Launder, F. W. Schmidt, U. Schumann, J. H. Whitelaw), 3749. Springer.

Waleffe, F., 1997. On a self-sustaining process in shear flows, Phys. Fluids., 9, 883-900.

Willis, A.P. and Kerswell, R.R., 2007. Critical behaviour in the relaminarisation of localised turbulence in pipe flow. Phys. Rev. Lett., 98, 014501, 1-4.

Wosnik, M., Castillo, L., George, W.K., 2000. A theory for turbulent pipe and channel flows, J. Fluid Mech., 421, 115-145.

Wu, X.H., Baltzer, J.R., Adrian, R.J, 2012. Direct numerical simulation of a 30R long turbulent pipe flow at $R^+ = 685$: large- and very large-scale motions, J. Fluid Mech., 698, 235–281.

Wray, A. and Hussaini, Y.M., 1984. Numerical Experiments in Boundary-Layer Stability, Proc. R. Soc. London Ser. A, 392, 373-389.

Yanenko, N. N., 1971. The method of fractional steps. Springer Berlin.

Yamagata, K., Nishikawa K., Hasegawa S., Fujii T., Yoshida S., 1972. Forced Convective Heat Transfer to Supercritical Water Flowing in Tubes, Int. J. Heat Mass Transfer, 15, 2575-2593.

Yang, J., Oka, Y., Ishiwatari, Y., Liu, J., Yoo, J., 2007. Numerical investigation of heat transfer in upward flows of supercritical water in circular tubes and tight fuel rod bundles, Nucl. Eng. Design, 237, 420–430.

Yang, X.B., Su, G.H., Tian, W.X., Wang, J.Y., Qiu, S.Z., 2010. Numerical study on flow and heat transfer characteristics in the rod bundle channels under super critical pressure condition, Annals. Nuclear Energy, 37, 1723–1734.

Youn, B. and Mills, A.F., 1993. Flow of supercritical hydrogen in a uniformly heated circular tube, Numer. Heat Transfer Part A, 24, 1–24.

Yoo, J.Y., 2013. The Turbulent Flows of Supercritical Fluids with Heat Transfer, Annu. Rev. Fluid Mech, 45, 495-525.

You, J.W., Yoo, J. Y., Choi, H., 2003. Direct numerical simulation of heated vertical air flows in fully developed turbulent mixed convection, Int. J. Heat Fluid Flow, 46, 1613.

Zaki, T.A., 2010. Bypass transition to turbulence and the anatomy of turbulent spots, Imperial College London, Final Report, FA8655-07-1-3009.

Zuccher, S., Bottaro, A., Luchini, P., 2006. Algebraic growth in a Blasius boundary layer: Nonlinear optimal disturbances, Eur. J. Mech. -B/Fluids, 25 (1), 1–17.

Appendix

A1. Program diagram

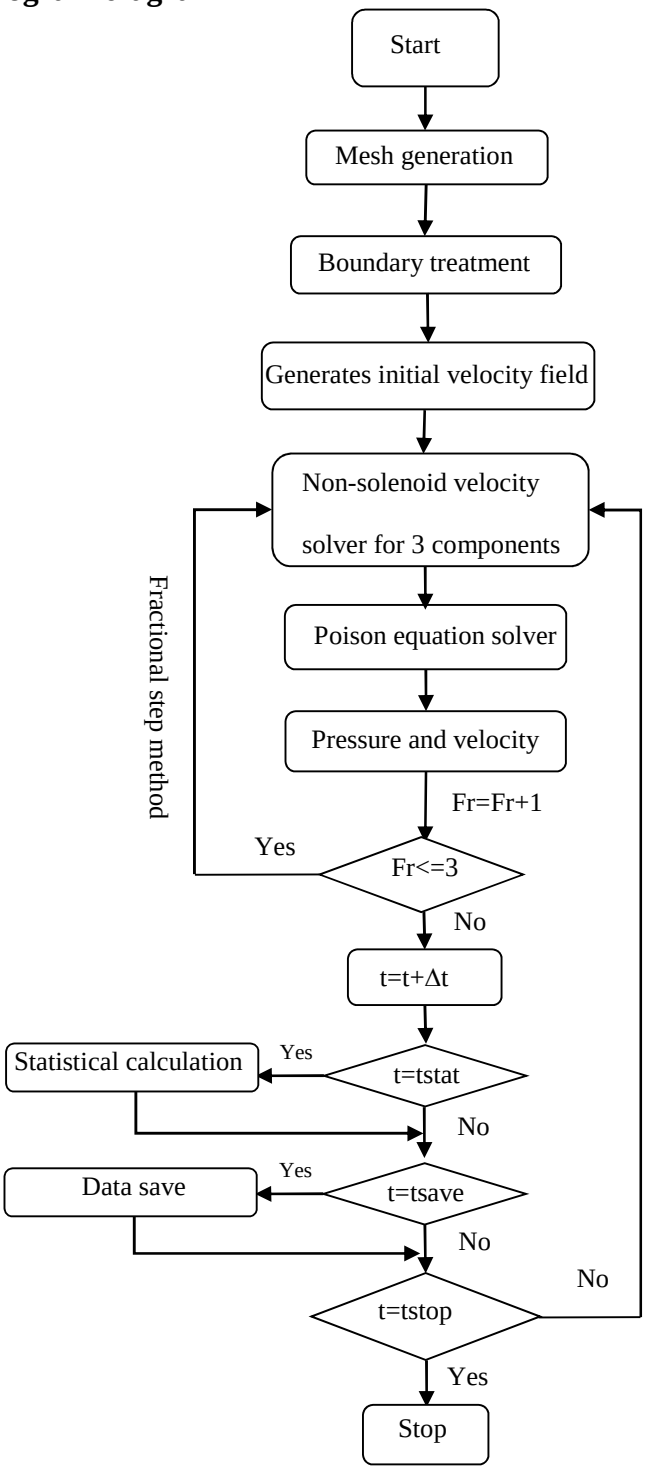

A2. Discretization of the governing equations

Time integration of q_r and q_θ-momentum equations

$$\frac{\widehat{q_r} - {q_r}^k}{\delta t} = \gamma_k {H_r}^k + \beta_k {H_r}^{k-1} - \alpha_k r \frac{\delta p^k}{\delta r} + 0.5\alpha_k \left(\frac{\delta^2(\widehat{q_r} + {q_r}^k)}{\delta z^2} + \frac{1}{r}\frac{\delta^2(\widehat{q_r} + {q_r}^k)}{\delta r^2} + \frac{\delta^2(\widehat{q_r} + {q_r}^k)}{r^2 \delta \theta^2} \right) \quad (8.1)$$

$$\frac{{q_r}^{k+1} - \widehat{q_r}}{\delta t} = -\alpha_k r \frac{\delta \emptyset^{k+1}}{\delta r} \quad (8.2)$$

$$\frac{\widehat{q_\theta} - {q_\theta}^k}{\delta t} = \gamma_k {H_\theta}^k + \beta_k {H_\theta}^{k-1} - \alpha_k \frac{\delta p^k}{\delta \theta} + 0.5\alpha_k \left(\frac{\delta^2(\widehat{q_\theta} + {q_\theta}^k)}{\delta z^2} + \frac{1}{r}\frac{\delta^2(\widehat{q_\theta} + {q_\theta}^k)}{\delta r^2} + \frac{\delta^2(\widehat{q_\theta} + {q_\theta}^k)}{r^2 \delta \theta^2} \right) \quad (8.3)$$

$$\frac{{q_\theta}^{k+1} - \widehat{q_\theta}}{\delta t} = -\alpha_k \frac{\delta \emptyset^{k+1}}{\delta \theta} \quad (8.4)$$

Space discretization of non-linear terms in q_r- and q_θ-momentum equations (all superscript k is ignored)

$$H_r = \frac{\partial q_r q_z}{\partial z} + \frac{\partial q_r q_r / r}{\partial r} + \frac{\partial q_\theta q_r / r^2}{\partial \theta} - \frac{q_\theta q_\theta}{r^2} + \frac{1}{Re_p}\frac{2}{r^2}\frac{\partial q_\theta}{\partial \theta} \quad (8.5)$$

Where,

$$\left.\frac{\partial q_r q_z}{\partial z}\right|_{i,j-1/2,k} = \frac{q_{r,i+\frac{1}{2},j-1/2,k} q_{z,i+\frac{1}{2},\mathrm{j}-1/2,\mathrm{k}} - q_{r,i-\frac{1}{2},j-1/2,k} q_{z,i-\frac{1}{2},\mathrm{j}-1/2,\mathrm{k}}}{\delta z} \quad (8.6)$$

$$\left.\frac{\partial q_r q_r / r}{\partial r}\right|_{i,j-1/2,k} = \frac{\frac{q_{r,i,j,k} q_{r,i,\mathrm{j},\mathrm{k}}}{r_j} - \frac{q_{r,i,j-1,k} q_{r,i,\mathrm{j}-1,\mathrm{k}}}{r_{j-1}}}{r_j - r_{j-1}} \quad (8.7)$$

$$\left.\frac{\partial q_\theta q_r / r^2}{\partial \theta}\right|_{i,j-1/2,k} = \frac{q_{\theta,i,j-1/2,k+1/2}\frac{q_{r,i,j-1/2,k+1/2}}{r_{j+1/2}} - q_{\theta,i,j-1/2,k-1/2}\frac{q_{r,i,j-1/2,k-1/2}}{r_{j+1/2}}}{r_{j-1/2}\delta\theta} \quad (8.8)$$

$$\left.\frac{q_\theta}{r^2}\right|_{i,j-1/2,k} = \frac{\left(q_{\theta,i,j-1/2,k}\right)^2}{{r_{j-1/2}}^2} \quad (8.9)$$

$$\left.\frac{1}{Re_p}\frac{1}{r^2}\frac{\partial q_\theta}{\partial \theta}\right|_{i,j-1/2,k} = \frac{1}{Re_p}\frac{2}{{r_{j-1/2}}^2}\frac{q_{\theta,i,j-\frac{1}{2},k+1/2} - q_{\theta,i,j-\frac{1}{2},k-1/2}}{\delta\theta} \quad (8.10)$$

$$H_\theta = \frac{\partial q_\theta q_z}{\partial z} + \frac{\partial q_r q_\theta / r}{\partial r} + \frac{1}{r^2}\frac{\partial q_\theta q_\theta}{\partial \theta} + \frac{q_\theta q_r}{r^2} - \frac{1}{Re_p}\frac{2}{r^2}\frac{\partial q_r}{\partial \theta} \tag{8.11}$$

$$\left.\frac{\partial q_\theta q_z}{\partial z}\right|_{i,j,k-1/2} = \frac{q_{\theta,i+\frac{1}{2},j,k-1/2}\, q_{z,i+\frac{1}{2},\mathrm{j}+\frac{1}{2},\mathrm{k}-1/2} - q_{\theta,i-\frac{1}{2},j+\frac{1}{2},k-1/2}\, q_{z,i-\frac{1}{2},\mathrm{j}+\frac{1}{2},\mathrm{k}-1/2}}{\delta z} \tag{8.12}$$

$$\left.\frac{\partial q_r q_\theta / r}{\partial r}\right|_{i,j,k-1/2} = \frac{q_{r,i,j+1/2,k}\frac{q_{\theta,i,\mathrm{j}+\frac{1}{2},\mathrm{k}}}{r_{j+1/2}} - q_{r,i,j-1/2,k}\frac{q_{\theta,i,\mathrm{j}-\frac{1}{2},\mathrm{k}}}{r_{j-1/2}}}{r_{j+1/2} - r_{j-1/2}} \tag{8.13}$$

$$\left.\frac{1}{r^2}\frac{\partial q_\theta q_\theta / r}{\partial \theta}\right|_{i,j,k-1/2} = \frac{1}{r_j}\frac{q_{\theta,i,j,k}\frac{q_{\theta,i,\mathrm{j},\mathrm{k}}}{r_j} - q_{\theta,i,j,k-1}\frac{q_{\theta,i,\mathrm{j},\mathrm{k}-1}}{r_j}}{\delta\theta} \tag{8.14}$$

$$\left.\frac{q_\theta q_r}{r^2}\right|_{i,j,k-1/2} = \frac{q_{\theta,i,j,k-1/2}\, q_{r,i,\mathrm{j},\mathrm{k}-1/2}}{{r_j}^2} \tag{8.15}$$

$$\left.\frac{1}{Re_p}\frac{2}{r^2}\frac{\partial q_r}{\partial \theta}\right|_{i,j,k-1/2} = \frac{1}{Re_p}\frac{2}{{r_j}^2}\frac{q_{r,i,j,k} - q_{r,i,j,k-1}}{\delta\theta} \tag{8.16}$$

Space discretization of linear terms in q_r- and q_θ-momentum equations

q_r-momentum equations

$$\left.\frac{\partial^2 q_r}{\partial z^2}\right|_{i,j-1/2,k} = \frac{q_{r,i+1,j-1/2,k} - 2q_{r,i,j-1/2,k} + q_{r,i-1,j-1/2,k}}{(\delta z)^2} \tag{8.17}$$

$$\left.\left(\frac{1}{r}\frac{\partial^2 q_r}{\partial r^2} - \frac{1}{r}\frac{\partial q_r}{\partial r}\right)\right|_{i,j-1/2,k} = \frac{1}{r_{j-\frac{1}{2}}\left(r_j - r_{j-1}\right)}\left[\frac{q_{r,i,j+\frac{1}{2},k} - q_{r,i,j-\frac{1}{2},k}}{\left(r_{j+\frac{1}{2}} - r_{j-\frac{1}{2}}\right)} - \frac{q_{r,i,j-\frac{1}{2},k} - q_{r,i,j-\frac{3}{2},k}}{\left(r_{j-\frac{1}{2}} - r_{j-\frac{3}{2}}\right)}\right] - \frac{1}{r_{j-\frac{1}{2}}}\frac{q_{r,i,j,k} - q_{r,i,j-1,k}}{\left(r_j - r_{j-1}\right)} \tag{8.18}$$

$$\left.\frac{1}{r^2}\frac{\partial^2 q_r}{\partial \theta^2}\right|_{i,j-1/2,k} = \frac{q_{\theta,i,j-\frac{1}{2},k+1} - 2q_{\theta,i,j-1/2,k} + q_{\theta,i,j-\frac{1}{2},k-1}}{{r_{j-1/2}}^2(\delta\theta)^2} \tag{8.19}$$

q_θ-momentum equations

$$\left.\frac{\partial^2 q_\theta}{\partial z^2}\right|_{i,j,k-1/2} = \frac{q_{\theta,i+1,j,k-1/2} - 2q_{\theta,i,j,k-1/2} + q_{\theta,i-1,j,k-1/2}}{(\delta z)^2} \tag{8.20}$$

$$\left.\frac{1}{r}\frac{\partial^2 q_\theta}{\partial r^2} - \frac{q_\theta}{r}\right|_{i,j,k-1/2} = \frac{1}{\left(r_{j+\frac{1}{2}} - r_{j-\frac{1}{2}}\right)r_j}\left(\frac{q_{\theta,i,j+1,k-1/2} - q_{\theta,i,j,k-1/2}}{r_{j+1} - r_j} - \frac{q_{\theta,i,j,k-1/2} - q_{\theta,i,j-1,k-1/2}}{r_j - r_{j-1}}\right) - \frac{q_{\theta,i,j,k-\frac{1}{2}}}{r_j} \tag{8.21}$$

$$\left.\frac{\partial^2 q_\theta}{\partial z^2}\right|_{i,j,k-1/2} = \frac{q_{\theta,i,j,k+1/2} - 2q_{\theta,i,j,k-1/2} + q_{\theta,i,j,k-3/2}}{(\delta\theta)^2} \tag{8.22}$$

A3. The additional data of chapter 5

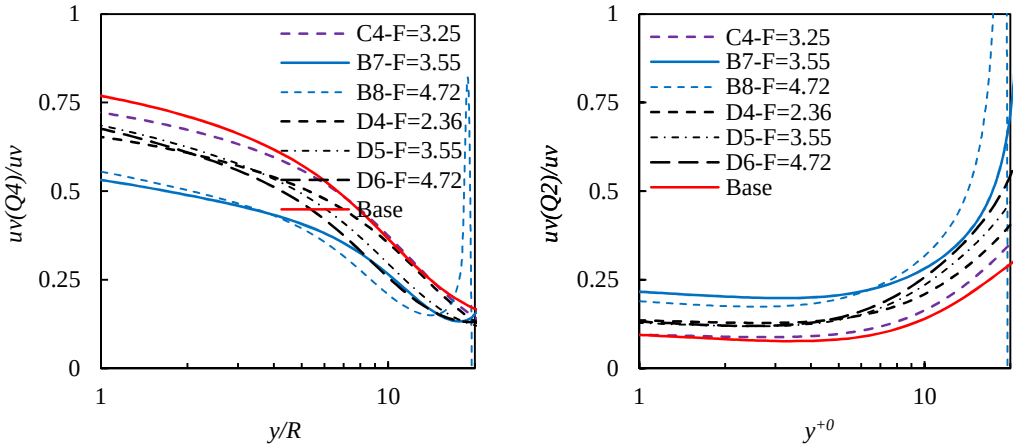

Figure 1 Quadrant of strongly recovery flow.

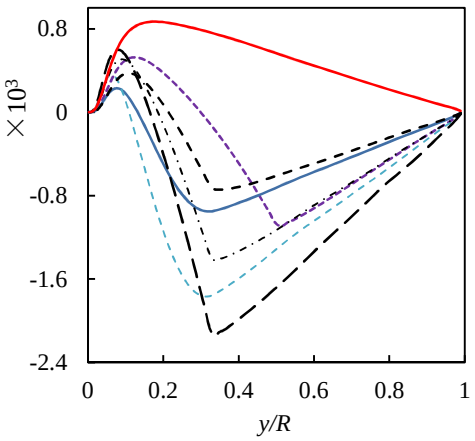

Figure 2 Reynolds stress of strongly recovery flow.

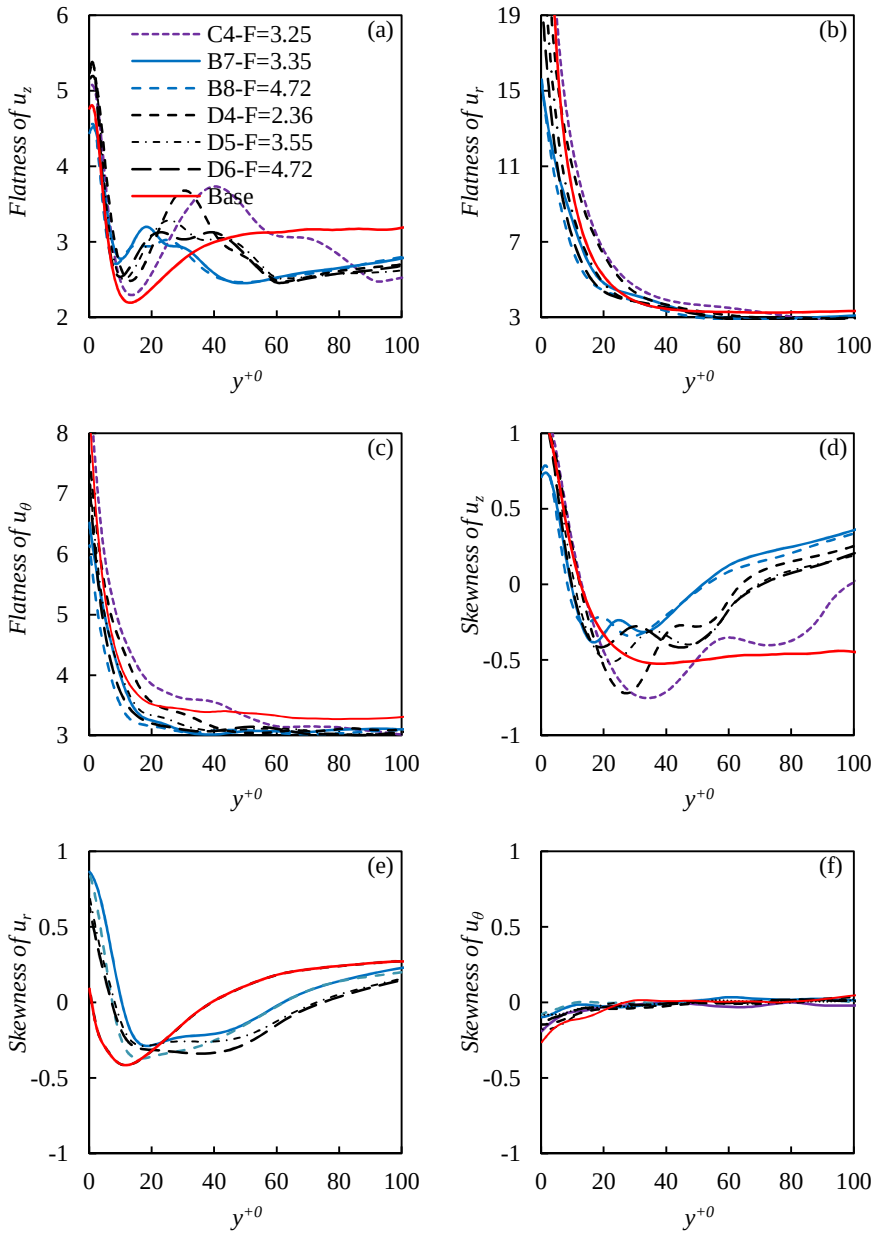

Figure 3 Flatness and skewness of strongly recovery flow.

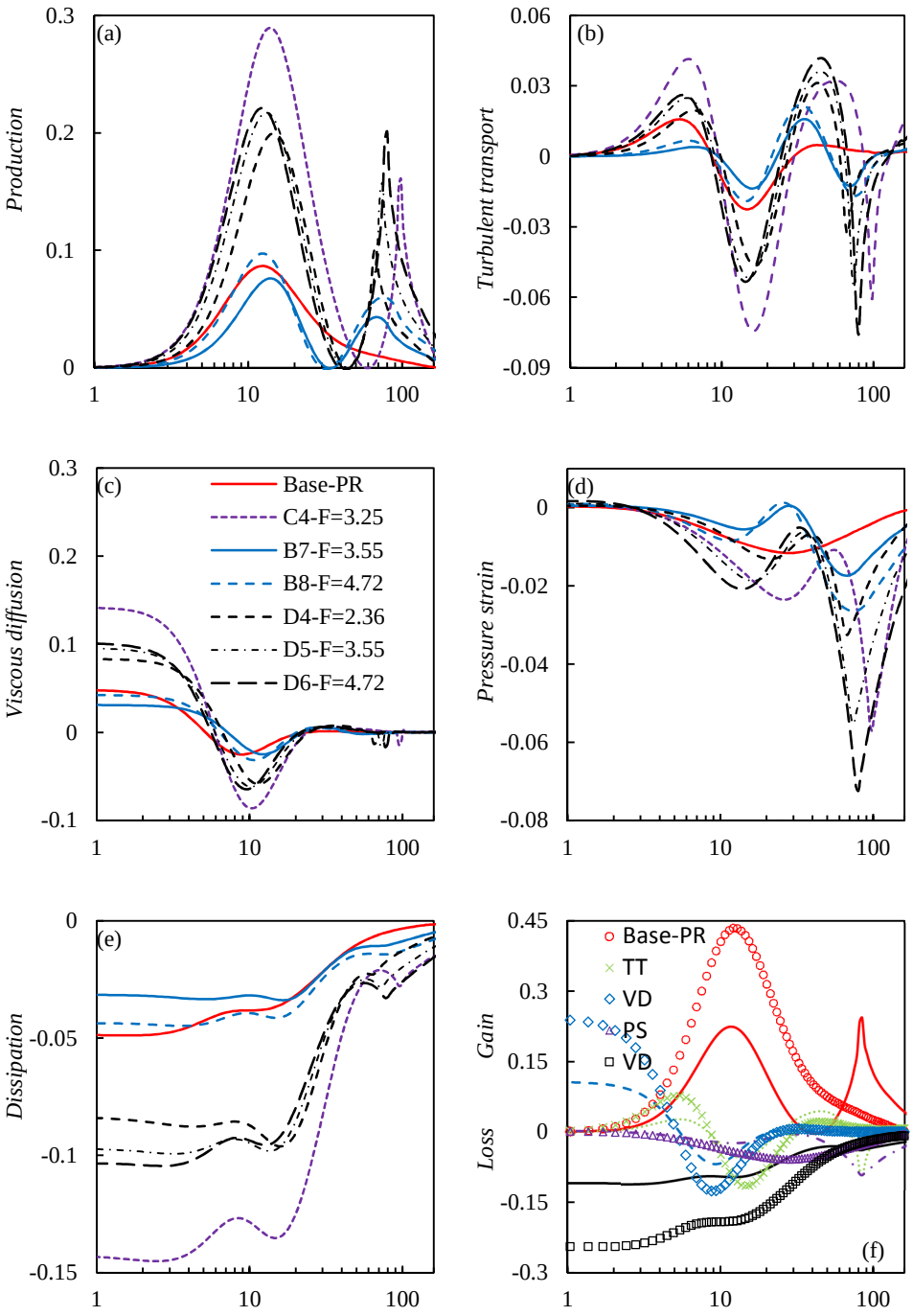

Figure 4 Budget of $\overline{u'_z u'_z}$ of strongly recovery flow (normalized by $u_\tau{}^4/v$).

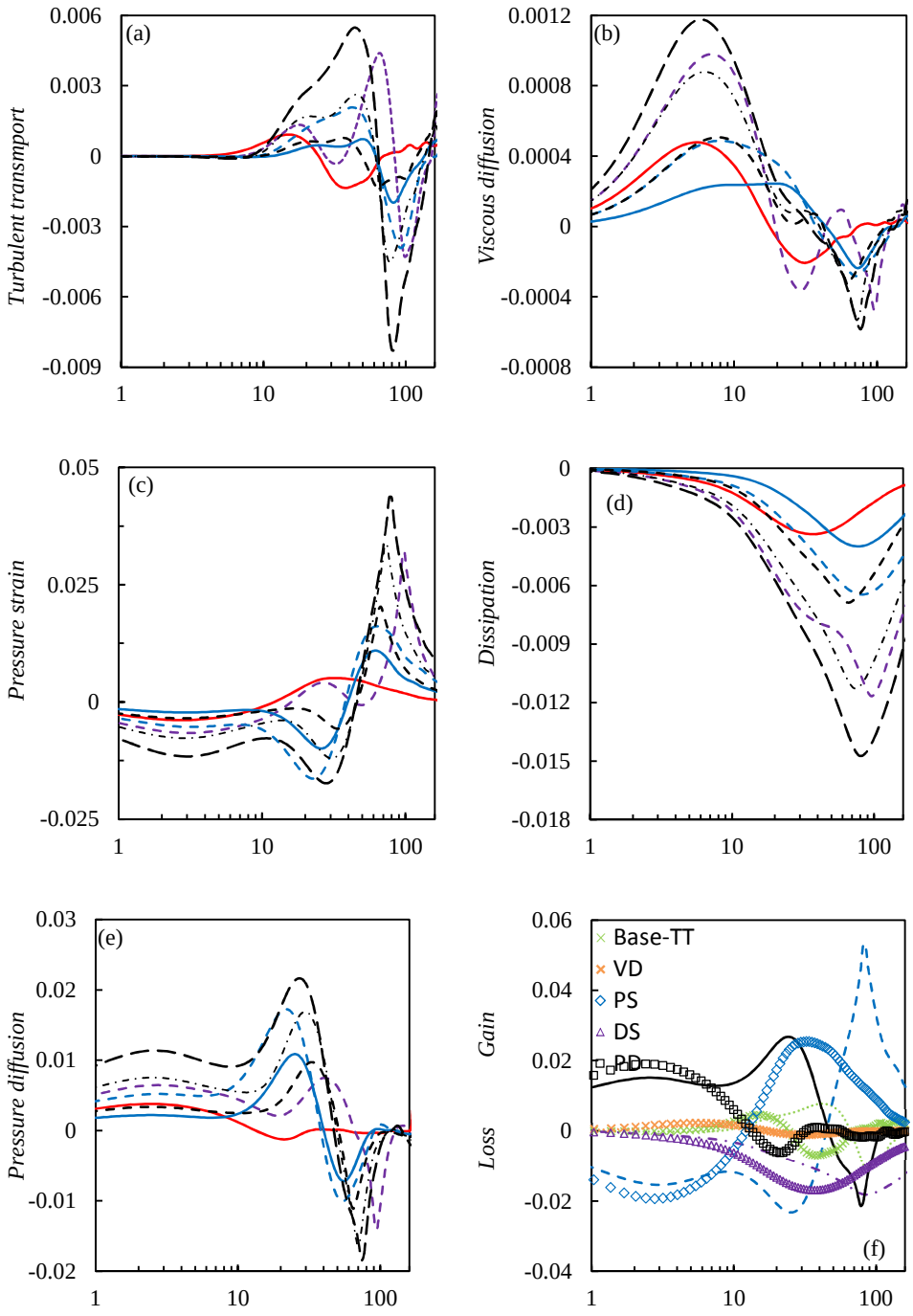

Figure 5 Budget of $\overline{u'_r u'_r}$ of strongly recovery flow (normalized by ${u_\tau}^4/\nu$).

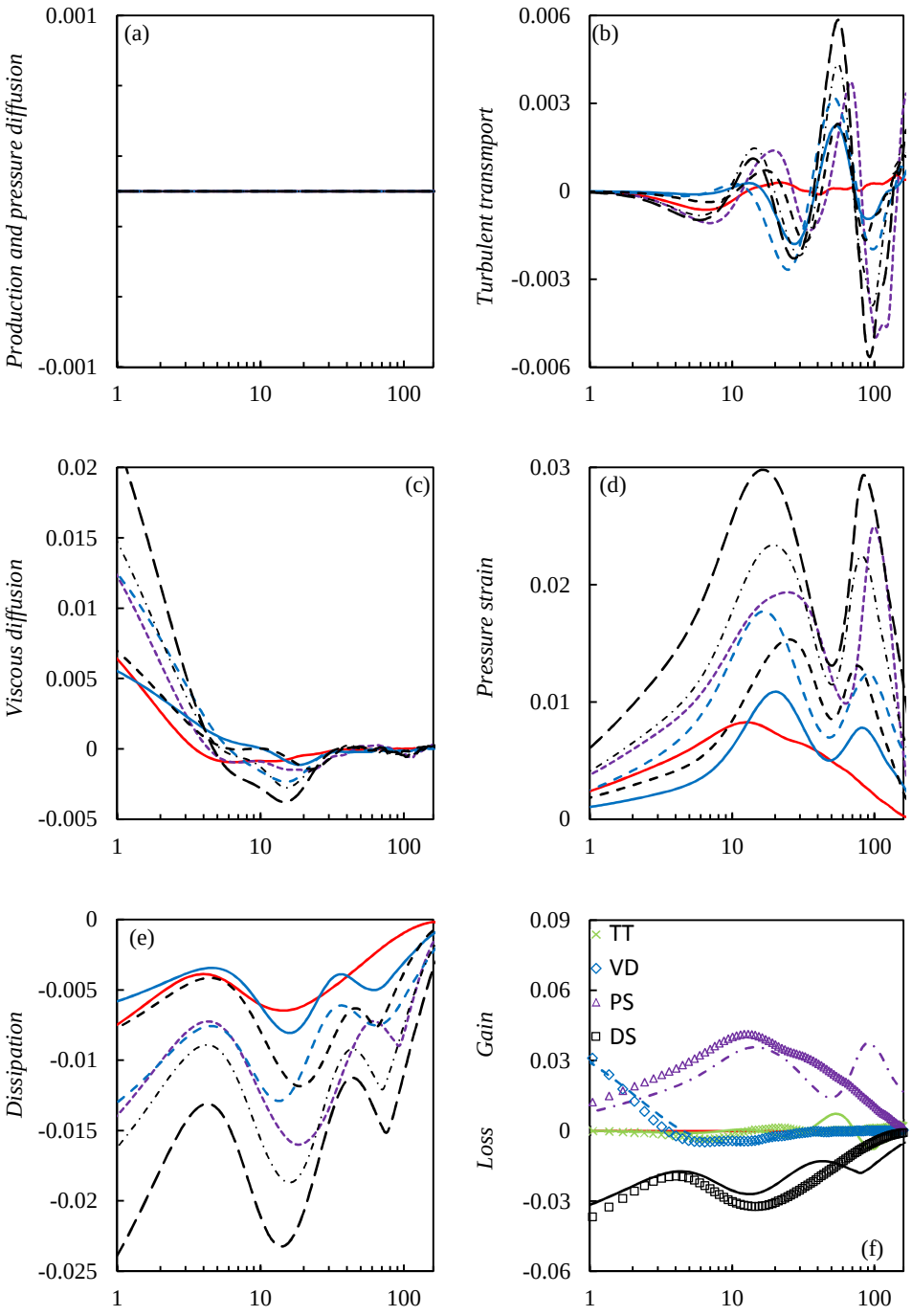

Figure 6 Budget of $\overline{u'_\theta u'_\theta}$ of strongly recovery flow (normalized by ${u_\tau}^4/\nu$).